

# Supersymmetry searches in ATLAS at the LHC

Elena Romero Adam

Dirigida por:  
Vasiliki Mitsou y José Bernabeu Alberola

Doctorado en Física  
Febrero 2017



VNIVERSITAT  
DE VALÈNCIA

Facultat de Física  
Departament de Física Teòrica



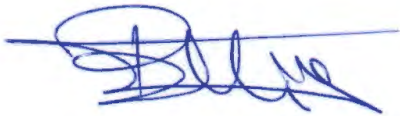
La Dra. **Vasiliki Mitsou**, Científica Titular de Consejo Superior de Investigaciones Científicas, y el Dr. **José Bernabeu Alberola**, Catedrático del Departamento de Física Teórica de la Universitat de València

CERTIFICAN:

Que la presente memoria, "**Supersymmetry searches in ATLAS at the LHC**", ha sido realizada bajo nuestra dirección en el Departamento de Física Teórica de la Universitat de València por Doña Elena Romero Adam y constituye su tesis para optar al grado de Doctora en Física por la Universitat de València.

Y para que así conste, firmamos el presente Certificado.

En Burjassot a 2 de Febrero de 2017.



Vasiliki Mitsou



José Bernabeu Alberola



*Dedicado a mis padres, abuelos y marido, de los que he aprendido todo para  
poder realizar el camino que me ha conducido hasta aquí.  
Gracias por creer en mí y por vuestro amor y apoyo incondicional.  
Y a Lou por haberme devuelto la alegría.*



# Contents

<b>Contents</b>	<b>7</b>
<b>Introduction</b>	<b>11</b>
<b>1 Theoretical framework</b>	<b>15</b>
1.1 Introduction . . . . .	15
1.2 The Standard Model . . . . .	15
1.2.1 Standard Model limitations . . . . .	17
1.3 Supersymmetry . . . . .	20
1.3.1 Supersymmetry at the fundamental level . . . . .	20
1.3.2 $\mathbf{R}$ -parity . . . . .	21
1.3.3 The Minimal Supersymmetric Standard Model . . . . .	22
1.3.4 Supersymmetry breaking . . . . .	23
1.3.5 Specific SUSY models . . . . .	25
1.3.5.1 bRPV-mSUGRA . . . . .	25
1.3.5.2 General Gauge Mediation (GGM) . . . . .	26
<b>2 Experimental framework</b>	<b>29</b>
2.1 Introduction . . . . .	29
2.2 The Large Hadron Collider (LHC) . . . . .	29
2.2.1 The accelerator . . . . .	30
2.2.2 The LHC experiments . . . . .	31
2.2.3 The LHC Computing Grid . . . . .	32
2.3 The ATLAS detector . . . . .	33
2.3.1 Coordinate system . . . . .	34
2.3.2 Inner Detector . . . . .	34
2.3.3 Calorimetry . . . . .	36
2.3.4 Muon system . . . . .	37
2.3.5 Trigger system . . . . .	38
2.4 Summary . . . . .	39
<b>3 One-lepton channel and bilinear RPV SUSY</b>	<b>41</b>
3.1 Introduction . . . . .	41
3.2 Analysis overview . . . . .	42
3.3 SUSY signal models . . . . .	43

3.4	Physics object identification and selection . . . . .	43
3.5	Event selection . . . . .	45
3.6	Background estimation . . . . .	46
3.6.1	$W/Z$ +jets and $t\bar{t}$ control regions . . . . .	47
3.6.2	Reweighting of $W$ + jets and $Z$ + jets simulated samples . . . . .	47
3.6.3	Multijet background . . . . .	48
3.6.4	Other backgrounds . . . . .	49
3.7	Systematic uncertainties . . . . .	49
3.8	Background fit . . . . .	50
3.8.0.1	Background fit validation . . . . .	51
3.9	Results . . . . .	54
3.10	Interpretation . . . . .	56
3.10.1	Limits in the bilinear RPV model . . . . .	56
3.11	Conclusions and outlook . . . . .	59
<b>4</b>	<b><math>Z</math> + jets + <math>E_T^{\text{miss}}</math> analysis</b>	<b>61</b>
4.1	Introduction . . . . .	61
4.2	Analysis overview . . . . .	61
4.3	SUSY signal models . . . . .	64
4.3.1	Gauge-mediated Supersymmetry breaking . . . . .	64
4.3.2	Signal cross-sections . . . . .	68
4.3.3	Branching fractions and masses . . . . .	75
4.4	Physics object identification and selection . . . . .	82
4.4.1	Electrons . . . . .	83
4.4.2	Muons . . . . .	84
4.4.3	Jets . . . . .	85
4.4.4	Overlap removal . . . . .	86
4.4.5	Missing transverse energy . . . . .	87
4.5	Event selection. . . . .	87
4.5.1	Event pre-selection . . . . .	87
4.5.2	Analysis regions . . . . .	89
4.6	Background estimation . . . . .	95
4.6.1	$Z/\gamma^*$ + jets background estimation . . . . .	97
4.6.2	Lepton flavour-symmetric background estimation: $t\bar{t}$ , $WW$ , $Wt$ , $Z \rightarrow \tau\tau$ . . . . .	100
4.6.2.1	Estimation of $N_{e\mu}^{\text{data,corr}}$ . . . . .	100
4.6.2.2	$\alpha$ factor . . . . .	102
4.6.2.3	$k_{ee}$ and $k_{\mu\mu}$ factors . . . . .	102
4.6.2.4	Results from flavour-symmetry method . . . . .	104
4.6.3	Cross-checks on the flavour-symmetry method . . . . .	105
4.6.3.1	MC closure . . . . .	106
4.6.3.2	Cross-check using the side-band fit . . . . .	107
4.6.3.2.1	Test on the stability of $m_{\ell\ell}$ extrapolation . . . . .	108
4.6.3.3	Closure test of the analysis in validation regions	114



4.6.4	Fake-lepton background estimation . . . . .	116
4.6.4.1	Fake leptons background validation . . . . .	118
4.6.4.2	Results of the Fake Leptons estimation . . . . .	122
4.6.5	Estimation of other backgrounds . . . . .	122
4.7	Systematic uncertainties . . . . .	123
4.7.1	Experimental uncertainties . . . . .	123
4.7.1.1	Uncertainties for the data-driven background estimates . . . . .	124
4.7.2	Signal contamination in control and validation regions . . . . .	125
4.7.3	Theoretical uncertainties . . . . .	125
4.7.4	Dominant uncertainties on the background estimates . . . . .	128
4.8	Results . . . . .	128
4.8.1	Comparison of data and MC in unblinded SR before and after the $\Delta\phi$ cut . . . . .	130
4.9	Interpretation . . . . .	137
4.9.1	Model independent upper limits . . . . .	139
4.10	Conclusions and outlook . . . . .	140
<b>5</b>	<b>Conclusions</b>	<b>141</b>
<b>6</b>	<b>Resumen en español</b>	<b>145</b>
	<b>Appendices</b>	<b>155</b>
<b>A</b>	<b>Statistics</b>	<b>157</b>
A.1	Basic concepts . . . . .	157
A.1.1	Probability density functions . . . . .	158
A.1.1.1	Probability models . . . . .	161
A.1.2	The likelihood function . . . . .	162
A.1.3	Auxiliary measurements . . . . .	163
A.2	Measurement as parameter estimation . . . . .	164
A.3	Hypothesis tests . . . . .	165
A.3.1	Null vs alternate hypotheses . . . . .	165
A.3.2	P-value . . . . .	167
A.3.3	Confidence intervals: excluded and allowed regions . . . . .	172
A.3.4	Example: the discovery of a Higgs boson . . . . .	173
A.3.5	The sensitivity problem: the $CL_s$ method. . . . .	177
<b>B</b>	<b>Further studies on the <math>Z + \text{jets} + E_T^{\text{miss}}</math> analysis</b>	<b>179</b>
B.1	Further details on flavour-symmetric backgrounds estimation . . . . .	179
B.1.1	Testing the $N_{ee}^{MC}:N_{\mu\mu}^{MC}:N_{e\mu}^{MC}$ ratio in VRZ.Zsideband . . . . .	180
B.1.2	Testing $m_{\ell\ell}$ distributions: data/MC ratios in the $Z$ -window / $Z$ -side band. . . . .	181
B.2	Study on the impact of a $\Delta\phi(\text{jet}, E_T^{\text{miss}})$ cut on SR. . . . .	187
B.2.1	Applying a $\Delta\phi$ cut on the flavour-symmetry method . . . . .	187
B.2.2	Applying a $\Delta\phi$ cut on the jet-smearing method . . . . .	188

---

B.2.3	Applying a $\Delta\phi$ cut on MC-estimated backgrounds and on fake leptons estimation . . . . .	190
B.2.4	Applying a $\Delta\phi$ cut on GGM signal . . . . .	190
B.2.5	Full background estimation using the flavour-symmetry method . . . . .	192
B.2.6	Full background estimation using the side-band fit . . .	195
B.2.7	Comparison of flavour-symmetric bkg estimation in the previous sections. . . . .	196
B.2.8	Checks in the original SR, before the $\Delta\phi$ cut . . . . .	196
<b>Bibliography</b>		<b>205</b>
<b>List of Figures</b>		<b>219</b>
<b>List of Tables</b>		<b>227</b>

# Introduction

Particle Physics, or High Energy Physics, is the branch of science that studies the elementary building blocks of the Universe and their fundamental interactions. The theory describing these blocks and interactions, known as the Standard Model (SM) [1], was established in the 1960's and 1970's. It describes three of the four fundamental forces of Nature, and puts quarks and leptons as the fundamental building blocks (*particles*). The Standard Model of Particle Physics provides the current most accurate description of the Elementary Particle Physics phenomenology. It has been experimentally tested up to the TeV scale with remarkably successful results. A great success of the SM was the prediction and subsequent discovery of the massive weak interaction  $W^\pm$  and  $Z$  bosons at CERN in 1983 and of the heaviest quark, the top quark, in 1995 at the Tevatron accelerator.

Despite great triumphs, the Standard Model is not considered to be the final fundamental theory of Particle Physics. There are pieces of evidence pointing to some New Physics beyond the SM such as the existence of Dark Matter, the matter-antimatter asymmetry of the Universe, the neutrino masses, or the hierarchy problem. Thus, the SM needs to be extended or included in a more complete theory.

Several theories have been developed in this direction among which Supersymmetry (SUSY) [2] is one of the most favoured. SUSY has been shown to be the only possible extension of the known space-time symmetries of particle interactions. During the first few years of its development, in the early 1970's, it was a purely abstract theory with no physical applications until physicists began to realise that SUSY might indeed solve many of the above-mentioned SM problems. One can say without exaggeration that Supersymmetry is one of the most strikingly beautiful recent ideas in Physics.

The key feature of SUSY's phenomenology is the predicted occurrence of sparticles (supersymmetric particles). Each SM particle gets a supersymmetric partner that differs in spin by half a unit. No SUSY particles have been observed in any experiment so far which indicates that SUSY must be a broken symmetry, therefore the sparticles (if they exist) must be heavier than their SM superpartners. As little is known about the breaking mechanism and the mass spectrum of the new particles, the possible signatures of SUSY are very diverse depending on the particular model realising SUSY.

In experimental Particle Physics very high energy collisions are needed

to produce heavy particles. Therefore, particle accelerators are used to boost two beams of particles to high energies, before these beams are made to collide with each other. The Large Hadron Collider (LHC), operated by the European Laboratory of Particle Physics (CERN) on the Franco-Swiss border, is such an accelerator where energetic collisions between protons take place. With its unprecedented centre-of-mass energy,  $\sqrt{s}$ , and luminosity,  $\mathcal{L}$ , it offers excellent conditions to extend searches for new particles of masses up to the TeV scale and has the potential to also discover very rare production processes. Purpose-built detectors observe and record the results of these collisions, after which the measurements are used to reconstruct each event algorithmically. The ATLAS experiment, whose data is used in this Thesis, is one of the four largest experiments at the LHC that is used to explore the Standard Model and what may lie beyond.

This Thesis presents two different SUSY searches using ATLAS data. The general procedure to perform New Physics searches is based on applying an event selection on several observables in order to minimise the SM backgrounds as much as possible. The amount of SM background surviving the mentioned selection is estimated using either Monte Carlo (MC) simulation or (semi or fully) data-driven methods. Once the background estimation is proved to be correct, it is compared with the real data observation in order to assess if any significant excess of events is produced with respect to the SM expectation. The CLs method is then used to set exclusion limits or claim a discovery.

Supersymmetry can manifest itself in many different ways, depending on the masses of the new particles and their interactions. To avoid getting lost in the wide ocean of possibilities of Supersymmetry, one needs to draw a map and design the routes to search for the SUSY land. With that purpose SUSY searches are organised in analyses looking for different final states to be interpreted in the context of specific SUSY models and scenarios. ATLAS SUSY searches are classified in three main categories according to the production mechanism of the sparticles: strong, electroweak and third generation production. On top of this classification, they are subdivided by their final states characteristics like whether  $R$ -parity is conserved or not and the possibility of SUSY particles being long-lived or prompt.

The analyses presented on this Thesis belong to the category of strong-production searches. These are inclusive searches for gluinos and first- and second-generation squarks.

The first analysis, that will be presented, searches for Supersymmetry in final states containing seven or more jets (“multijets”), one isolated lepton (electron or muon)<sup>1</sup> and missing transverse energy ( $E_T^{\text{miss}}$ ). The search is based on data from the full 2011 data-taking period, corresponding to an integrated luminosity of  $4.7 \text{ fb}^{-1}$  and a centre-of-mass energy  $\sqrt{s} = 7 \text{ TeV}$ . The results of this analysis are interpreted in the context of a bilinear  $R$ -parity violating (bRPV) mSUGRA/CMSSM model.

---

<sup>1</sup>Throughout this document, the term leptons will refer to electrons and muons only, without including the taus, unless it is otherwise stated.

The second analysis is a search for Supersymmetry in final states characterised by a  $Z$  boson that decays to an electron or a muon pair, large  $E_{\text{T}}^{\text{miss}}$  and jets. The proton-proton collision data used in this search were collected at a centre-of-mass energy  $\sqrt{s} = 8$  TeV by the ATLAS detector at the LHC and correspond to an integrated luminosity of  $20.3 \text{ fb}^{-1}$ . The results are interpreted in the context of a GGM supersymmetric model.

Several statistical concepts are key to understand the interpretation of the results of any search analysis, given that all searches in the end can be reduced to hypothesis tests. Thus, in addition to the searches description, this Thesis tries to explain the basic concepts of hypothesis testing, without the detailed mathematical proofs, for the sake of clarity and completeness.

Chapter 1 presents a qualitative description of the Standard Model and Supersymmetry without mathematical details. Chapter 2 describes the layout of the LHC and the ATLAS detector during the 2011 and 2012 data-taking periods. After having seen the motivations and the experimental framework for the realization of this Thesis, the searches description starts in Chapter 3, which depicts the details of the “one lepton + multijets +  $E_{\text{T}}^{\text{miss}}$ ” analysis, whilst Chapter 4 details the “ $Z$  + jets +  $E_{\text{T}}^{\text{miss}}$ ” analysis. Chapter 5 presents the conclusions and perspectives. After that, Appendix A is dedicated to the explanation of hypothesis tests while Appendix B gives additional interesting information to Chapter 4.



# Chapter 1

## Theoretical framework

### 1.1 Introduction

The Standard Model of Particle Physics (SM) provides the current most accurate description of the Elementary Particle Physics phenomenology. It has been experimentally tested up to the TeV scale with remarkably successful results. Nevertheless, there are pieces of evidence pointing to some New Physics beyond the SM such as the existence of Dark Matter [3], the matter-antimatter asymmetry of the Universe [4], the neutrino masses [5], or the hierarchy problem [6–8]. Thus, the SM needs to be extended or included in a more complete theory. Several theories have been developed in this direction among which Supersymmetry (SUSY) is one of the most favoured.

This chapter deals with the theoretical framework in which this Thesis is embedded. A summary of the needed theories without the mathematical formalism behind them will be given. For this purpose, Section 1.2 explains the Standard Model and its principal limitations and Section 1.3 describes Supersymmetry and the two supersymmetric models that are relevant for the next chapters.

### 1.2 The Standard Model

The Standard Model of Particle Physics is the current fundamental theory of elementary particles and their interactions. It was developed in the 20<sup>th</sup> century based on the gauge symmetry guiding principle and on numerous experimental discoveries. Up to the present day, the Standard Model has been tested in hundreds of experiments and its predictions have been verified with very high precision. Nevertheless, the SM has some limitations that will be briefly discussed in Section 1.2.1.

The Standard Model describes three of the four known fundamental forces: the electromagnetic, the weak and the strong interactions. It is a relativistic quantum field theory. The interactions of the SM are defined by the local gauge symmetry  $SU(3)_C \times SU(2)_L \times U(1)_Y$ . Quantum chromodynamics, the quantum theory of the strong force between quarks and gluons, is described

by the gauge group  $SU(3)_C$ . The associated charge quantum number, called colour, assumes three values, denoted red, green and blue, with corresponding anti-colours. The  $SU(2)_L \times U(1)_Y$  group defines the electroweak force which unifies the electromagnetic and weak interactions. The charges belonging to the  $SU(2)_L$  and the  $U(1)_Y$  group are the weak isospin,  $\mathbf{I}$ , and the weak hypercharge,  $Y$ , respectively. The electric charge  $Q$  of a particle is related to the hypercharge and the third component of the weak isospin,  $I_3$ , via  $Q = \frac{Y}{2} + I_3$ .

The fundamental particles of the Standard Model are point-like and can be divided into two classes, fermions with half-integer spin and bosons with integer spin. The three forces in the SM are understood as arising due to the exchange of various spin-one bosons amongst the spin-half particles. Eight spin-one particles, called gluons ( $g^a (a = 1, \dots, 8)$ ), are the mediators of the strong interaction. Any particle that transforms with respect to  $SU(3)_C$ , and so which couples to the gluons, is said to be coloured or to carry colour. Three spin-one particles,  $\mathbf{W}$ , are associated with the factor  $SU(2)_L$ , and one,  $B$ , with the factor  $U(1)_Y$ . The subscript “ $L$ ” is meant to indicate that only the left-handed fermions turn out to transform under the  $SU(2)_L$  factor. The eight gluons are always massless while the three  $W_{1,2,3}$  bosons and the  $B$  boson are massless only in the limit of exact electroweak symmetry. At the weak scale, the  $SU(2)_L \times U(1)_Y$  electroweak symmetry gets spontaneously broken to  $U(1)_{em}$ , which is the electromagnetic group generated by the electric charge  $Q$ . These four bosons ( $\mathbf{W}$  and  $B$ ) are related to the physical bosons that mediate the weak interactions,  $W^\pm$  and  $Z^0$ , and the familiar photon  $\gamma$  through the spontaneous symmetry breaking mechanism.

Leptons are, by definition, those spin-half particles which do not take part in the strong interactions. Six leptons are known which are denoted individually by  $e, \mu, \tau, \nu_e, \nu_\mu$  and  $\nu_\tau$  and collectively by  $\ell$ .

Hadrons, on the other hand, are defined as those colour singlet particles that do take part in the strong interactions through the residual interaction of their constituents. The spectrum of known hadrons is rich and varied but is accounted for as the bound states of six quarks  $u, d, s, c, b$  and  $t$ , denoted collectively as  $q$ .

The quarks and leptons appear in three families or generations. The first family contains the up ( $u$ ) quark and the down ( $d$ ) quark, together with the electron ( $e^-$ ) and the electron neutrino ( $\nu_e$ ). The first family is responsible for all the visible matter in the present Universe. The second family ( $c, s, \mu^-, \nu_\mu$ ) is heavier than the first; and the third ( $t, b, \tau^-, \nu_\tau$ ) is heavier than the second and except for neutrinos, they are unstable under weak interactions.

Tables 1.1 and 1.2 list all the fundamental matter (fermion) and force carrier (boson) particles of the SM. To have a complete picture of the SM particle zoo one would have to mirror Table 1.1 to the *antimatter* world. A particle and its antiparticle have opposite values for all non-zero quantum number labels. As mentioned before, only left-handed fermions transform under the  $SU(2)_L$  factor, which is the meaning of the  $L$ -subscript for the doublets in Table 1.1. The right-handed ( $R$ -subscript) quarks and charged



leptons transform as singlets under the weak interaction.

Family	Fields/Particles			Spin	Electric charge
	1 <sup>st</sup>	2 <sup>nd</sup>	3 <sup>rd</sup>		
<b>Quarks</b>	$(u, d)_L$	$(c, s)_L$	$(t, b)_L$	$(1/2, 1/2)$	$(+2/3, -1/3)$
	$u_R$	$c_R$	$t_R$	$1/2$	$+2/3$
	$d_R$	$s_R$	$b_R$	$1/2$	$-1/3$
<b>Leptons</b>	$(\nu_e, e^-)_L$	$(\nu_\mu, \mu^-)_L$	$(\nu_\tau, \tau^-)_L$	$(1/2, 1/2)$	$(0, -1)$
	$e_R^-$	$\mu_R^-$	$\tau_R^-$	$1/2$	$-1$

Table 1.1: The fermions of the Standard Model listed with their chirality, spin and electric charge.

	Particles	Force	Spin	Electric charge
<b>Gauge bosons</b>	$g$	strong	1	0
	$W^\pm$ and $Z$	weak	1	$\pm 1$ and 0
	$\gamma$	electromagnetic	1	0
<b>Scalar boson</b>	$H$		0	0

Table 1.2: The bosons of the Standard Model listed with their spin and electric charge.

Mass terms for fermions in the SM can only be realized by the Brout-Englert-Higgs mechanism [9]. This mechanism with two scalar doublets spontaneously breaks the electroweak symmetry transforming the originally massless weak interaction bosons into massive bosons (as has been mentioned before) and leaving an extra single physical massive neutral scalar particle, the Higgs boson, while the photon remains massless. In 2012, a Higgs boson was discovered by the LHC experiments ATLAS and CMS with a mass of about 125 GeV [10,11]. Studies about the experimental properties of the found Higgs boson are one of the most important parts of the current physics program of ATLAS and CMS; the present results indicate that it is compatible with the Standard Model Higgs.

### 1.2.1 Standard Model limitations

So far, the Standard Model has remarkable successes at describing the currently known particle phenomena. However, it is still far from a complete theory and has some open questions as it does not explain the limitations summarised below.

- **Gauge hierarchy problem**

The strong interaction starts to play an important role at an energy around 200 MeV, the scale which determines the masses of the hadrons made of light quarks such as the  $\pi^0$ . The energy scale of the electroweak interactions is of the order of the vacuum expectation value of the neutral scalar,  $v_{ev} \approx 246$  GeV [12]. A large gap of the order of  $10^{17}$  GeV is found between the electroweak energy scale and the Planck energy scale ( $\sim 10^{10}$  GeV) where the gravitational effects need to be considered.

The gauge hierarchy problem [6–8], coming from this gap between the energy scales, can be seen in the radiative corrections to the Higgs mass, when allowing the SM to be valid up to the Planck scale. The observable Higgs mass,  $m_{\text{exp},H}$ , is composed of the tree-level Higgs mass,  $m_H$ , and of ‘self energy’ terms coming from virtual particle loops,  $\Delta m_H$ :

$$m_{\text{exp},H}^2 = m_H^2 + \Delta m_H^2. \quad (1.1)$$

However, these radiative corrections are quadratically divergent for scalars because the momentum of those virtual particles can take the highest energy scale at which the theory stops to be valid. For example, if the SM is believed to be suitable up to the reduced Planck scale [2]

$$M_P = (8\pi G)^{-1/2} = 2.4 \times 10^{18} \text{ GeV}, \quad (1.2)$$

where the impact of quantum gravity should be strong, then the radiative corrections  $\Delta m_H \sim M_P$ , and the tree level Higgs mass must become unnaturally large and fine-tuned, as it is known from the experimental measurements that  $m_{\text{exp},H} \simeq (125 \text{ GeV})$ .

As a conclusion, the Standard Model suffers from an unnatural Higgs mass tuning due to the scale hierarchy.

- **Matter-antimatter asymmetry of the Universe**

The observed asymmetry between matter and antimatter in the Universe has not been explained so far within the framework of the SM. *CP*-violation (*CPV*) in the SM through the Cabibbo-Kobayashi-Maskawa Mixing of Quarks predicts matter and antimatter not to behave in the exact same way. However, this *CPV* is too small and still some additional mechanism would be needed to explain the amazing dominance of matter over antimatter in the Universe.

- **Neutrino masses**

Neutrinos are massless particles in the SM. However, the experimental observation of neutrino flavour oscillations requires small but non-zero neutrino masses. Still we do not know whether neutrino mass terms are Dirac or Majorana i.e., conserving or violating by  $\Delta L = 2$  the global lepton number.

- **Cosmological considerations**

Experimental measurements from different sources indicate that the contents of the Universe are distributed as follows: 27% is Dark Matter, 68% is Dark Energy, while Baryonic matter and neutrinos, i.e. Standard Model particles, make up only about 5% of the total energy density of the Universe.

The existence of Dark Matter was first postulated to explain the radial dependence of the rotation speed of galaxies, which requires more gravitational matter than it is visible. More recently, the abundance of Dark Matter has been constrained by precise measurements of the fluctuations in the temperature of the cosmic microwave background radiation. A common hypothesis is that Dark Matter consists of weakly interacting massive particles (WIMPs), although it is not a unique possibility.

Dark Energy was introduced as an explanation for the observed accelerating expansion of the Universe. In general one would expect that the expansion slows down over time due to the attractive gravitational force. However, there is strong evidence that the expansion of the universe is accelerating. The origin of Dark Energy is still unknown.

- **Grand Unification**

Unification of all the fundamental interactions is an attractive concept. In the SM, the strong and electroweak interactions are described independently and their scale dependent ‘running’ coupling strengths do not get unified at any higher energy. A Grand Unifying Theory (GUT) would make these  $SU(3) \times SU(2) \times U(1)$  interactions converge in one universal gauge coupling defined at the grand unification scale.

- **The fermion mass family problem**

The existence of three fermion families has been experimentally tested. Nevertheless, the SM gives no prediction on the number of fermion generations. Furthermore, there is no explanation or prediction of their masses, which are observed to have a hierarchical pattern spanning over six orders of magnitude between the top quark and the electron, or the difference even greater between these two and the neutrinos, which are lighter still by many orders of magnitude. The physics that appears for more than one family is encoded under the name of Flavour Physics.

- **Gravity**

Even though it is one of the fundamental forces of Nature, it is not included in the SM.

Thus, it seems clear that the SM is not the ultimate Theory, but an effective field theory which is able to explain Nature with great accuracy up to a certain energy scale beyond which it will need to be extended or included in a more complete theory. Several theories have been developed in this direction. One of them is Supersymmetry.

## 1.3 Supersymmetry

Supersymmetry (or SUSY in short) [2] is a theoretically attractive extension of the SM that solves some of its outstanding problems. It is a proposed invariance under generalized space-time transformations linking fermions and bosons. One can say without exaggeration that it is one of the most strikingly beautiful recent ideas in Physics.

The key feature of its phenomenology is the predicted occurrence of sparticles (superpartners of the SM particles). For each known elementary particle (including the confined quarks and gluons) there is supposedly at least one sparticle. It differs in spin from the particle by  $1/2$  and is endowed with opposite statistics, a mass difference of the order of  $M_S$  and couplings strictly related to the known particle couplings.

Supersymmetry has been shown to be the only possible extension of the known space-time symmetries of particle interactions. During the first few years of its development, in the early 1970's, it was a purely intellectual theory with no physical applications until people began to realise that SUSY might indeed solve many of the above-mentioned SM problems:

- In the case of  $R$ -parity conservation (to be explained later on), it provides a natural candidate to Dark Matter (DM) [13]: the lightest supersymmetric particle (LSP), which is neutral, weakly interacting, massive and stable (a WIMP). Even in the case when  $R$ -parity is violated there is still the possibility for a DM candidate such as the gravitino [14–19].
- It is a Grand Unification Theory. Including sparticles in the Renormalisation Group Equations (RGEs) for the gauge couplings of the Standard Model would permit them to unify at a very high energy scale [20–25], whereas unification would not occur if only the SM particles were included in the RGEs.
- It stabilises the Higgs mass. Given the fact that fermion loops and boson loops contribute to the Higgs radiative corrections with opposite signs, the large radiative corrections  $\Delta m_H^2$  (mentioned in 1.2.1) would be cancelled by the new loops introduced in Supersymmetry.

### 1.3.1 Supersymmetry at the fundamental level

Supersymmetry implies a symmetry between fermions and bosons. It states that for every particle in the SM there is a corresponding superpartner which differs only in spin by half a unit, but with all other characteristics the same. So a fermion in the SM becomes a boson under the supersymmetric transformation and vice versa. Examining the particle content of the Standard Model in Tables 1.1 and 1.2, one can see that none of them can be each others superpartners. This means that new fields should be introduced in the model, hence ending with twice as many fundamental particles as the SM.

It is customary to apply the supersymmetric transformation to the original SM fields, i.e. before the unification of the electromagnetic and the weak interactions, and before electroweak symmetry breaking leading to definite mass particles. Hence the  $U(1)_Y$   $B$ -field and the  $SU(2)_L$   $W_i$  gauge bosons get their supersymmetric partners, and not the photon or the  $W/Z$  bosons.

Similarly to the situation for SM quarks and leptons, where the weak eigenstates are not identical to the mass eigenstates and are related through a mixing matrix, supersymmetric particles with the same quantum numbers will in general mix to form mass eigenstates. As opposed to the SM quark sector, the mixing of supersymmetric weak eigenstates produces significantly different mass eigenstates that are named differently, as will be discussed in Section 1.3.3.

### 1.3.2 $R$ -parity

$R$ -parity is a multiplicative quantum number defined as:

$$R = (-1)^{3(B-L)+2s} \quad (1.3)$$

where  $B$ ,  $L$  and  $s$  are the baryon number, lepton number and spin, respectively. Hence  $R = +1$  for all Standard Model particles and  $R = -1$  for all SUSY particles.

Most of the scenarios considered within SUSY assume the conservation of both baryon and total lepton number (and therefore  $R$ -parity). However, there is no fundamental reason for  $R$ -parity to be conserved. It is an *ad-hoc* assumption which can be relaxed in several ways. The only firm restriction comes from the proton lifetime: non-conservation of both  $B$  and  $L$  leads to rapid proton decay, however violation of either  $B$  or  $L$  allows a proton decay lifetime compatible with the experimentally measured limit.

The case of  $R$ -parity conserving (RPC) SUSY has three extremely important phenomenological consequences:

- The lightest supersymmetric particle must be absolutely stable. If the LSP is electrically neutral, it interacts only weakly with ordinary matter, and so can make an attractive candidate for the non-baryonic Dark Matter.
- Each particle other than the LSP must eventually decay into a state that contains an odd number of LSPs (usually just one).
- In collider experiments, sparticles can only be produced in even numbers (usually two at a time).

Thus the experimental signatures of RPC signals in colliders involve charged leptons and jets produced in the cascade decays and missing transverse energy ( $E_T^{\text{miss}}$ ) from the two undetected LSPs.

In most  $R$ -parity violating (RPV) supersymmetric models investigated at colliders, only the LSP decays via RPV couplings leaving the pair production

and the cascade decays of the sparticles unchanged compared to RPC. This assumption is motivated by low-energy constraints on the maximum RPV coupling values [26], which suppress RPV decays of other sparticles than the LSP. Due to the fact that the two LSPs of an event decay directly to Standard Model particles, the experimental signature of RPC Supersymmetry of large  $E_T^{\text{miss}}$  is lost in most cases and replaced by additional leptons and jets. However, non-zero  $E_T^{\text{miss}}$  arises in RPV supersymmetric models from neutrinos produced either directly in the LSP decay or upstream in the SUSY cascade decay.

Providing a Dark Matter candidate is one of the strongest advantages of RPC SUSY but also  $R$ -parity violating models exist which may explain dark matter through, for instance, very light gravitinos, axions or axinos [27].

### 1.3.3 The Minimal Supersymmetric Standard Model

The Minimal Supersymmetric Standard Model (MSSM) is the simplest supersymmetric extension of the SM with minimal particle field content and minimal assumptions. For every particle in the SM there is a supersymmetric partner, as can be seen in Table 1.3. The *gauginos* carrying spin 1/2 are superpartners of the gauge bosons, and the superpartners of quarks and leptons carrying spin 0 are called *squarks* and *sleptons*.

In supersymmetric models at least two Higgs doublets ( $H_u, H_d$ ) are needed to generate masses for both up- and down-type quarks<sup>1</sup>. The ratio of their vacuum expectation values (VEVs) is denoted as  $\tan \beta$ . In the same way as in the SM, the weak gauge bosons acquire mass through electroweak symmetry breaking, except that now five scalar Higgs particles appear:  $h^0, H^0, A^0, H^+, H^-$ . Hence the non-supersymmetric Higgs sector is larger in the MSSM models than in the SM. The spartners of the scalar Higgses are spin-1/2 *higgsinos*.

Given that no sparticles have been observed so far, SUSY must be a broken symmetry, as will be shortly discussed in Section 1.3.4, and the sparticles must be heavier than their SM partners. Once SUSY and electroweak symmetry are broken, sparticles in flavour eigenstates will in general mix to form mass eigenstates. All the resulting mass eigenstates are shown in Table 1.3. The only one that stays untouched is the gluino, being the only gaugino with colour charge. The colour neutral gauginos and higgsinos mix to form four charged states called *charginos*  $\tilde{\chi}_{1,2}^\pm$ , and four neutral states called *neutralinos*  $\tilde{\chi}_{1,2,3,4}^0$ , where the number labelling is based on increasing mass. Depending on which of the components makes the dominant contribution to a specific neutralino, they are referred to as higgsino-like, bino-like or wino-like.

As the squarks and sleptons are scalar bosons, the L- and R-handedness does not refer to their helicity state but to that of their SM partner field, though the labels are kept to display the relation. The mixing of sfermions

<sup>1</sup>A single chiral doublet of higgsinos would have gauge anomalies. Introducing two Higgs doublets allows separate Yukawa couplings for up- and down-type quarks, and not using the complex conjugate as in the SM.

happens mainly in the third family, because the mixing matrix off-diagonal contributions are proportional to the SM partner mass [2], hence most relevant for third-family partners. The third-family mass eigenstates are labelled with 1,2 again according to their increasing mass. There can also be flavour mixing of families of sfermions in a super-CKM matrix, but for simplicity it will be ignored.

Names	Spin	$P_R$	Gauge Eigenstates	Mass Eigenstates
<b>Higgs bosons</b>	0	+1	$H_u^0$ $H_d^0$ $H_u^+$ $H_d^-$	$h^0$ $H^0$ $A^0$ $H^\pm$
			$\tilde{u}_L$ $\tilde{u}_R$ $\tilde{d}_L$ $\tilde{d}_R$	(same)
<b>squarks</b>	0	-1	$\tilde{s}_L$ $\tilde{s}_R$ $\tilde{c}_L$ $\tilde{c}_R$ $\tilde{t}_L$ $\tilde{t}_R$ $\tilde{b}_L$ $\tilde{b}_R$	(same) $\tilde{t}_1$ $\tilde{t}_2$ $\tilde{b}_1$ $\tilde{b}_2$
			$\tilde{e}_L$ $\tilde{e}_R$ $\tilde{\nu}_e$	(same)
<b>sleptons</b>	0	-1	$\tilde{\mu}_L$ $\tilde{\mu}_R$ $\tilde{\nu}_\mu$ $\tilde{\tau}_L$ $\tilde{\tau}_R$ $\tilde{\nu}_\tau$	(same) $\tilde{\tau}_1$ $\tilde{\tau}_2$ $\tilde{\nu}_\tau$
<b>neutralinos</b>	1/2	-1	$\tilde{B}^0$ $\tilde{W}^0$ $\tilde{H}_u^0$ $\tilde{H}_d^0$	$\tilde{\chi}_1^0$ $\tilde{\chi}_2^0$ $\tilde{\chi}_3^0$ $\tilde{\chi}_4^0$
<b>charginos</b>	1/2	-1	$\tilde{W}^\pm$ $\tilde{H}_u^\pm$ $\tilde{H}_d^\pm$	$\tilde{\chi}_1^\pm$ $\tilde{\chi}_2^\pm$
<b>gluino</b>	1/2	-1	$\tilde{g}$	(same)
<b>goldstino</b> <b>(gravitino)</b>	1/2 (3/2)	-1	$\tilde{G}$	(same)

Table 1.3: The undiscovered particles in the Minimal Supersymmetric Standard Model (with sfermion mixing for the first two families assumed to be negligible). Anti-sfermion fields have not been listed.

### 1.3.4 Supersymmetry breaking

No supersymmetric particles have been observed so far, so SUSY must be a broken symmetry and the SUSY particles must be heavier than their SM partners. Spontaneous breakdown of Supersymmetry is a theoretically desirable feature, therefore much theoretical proposals have taken place so far regarding the specifics of such a breaking mechanism. A review of such proposals can be found in Ref. [9]. Two broad characteristics can, however, be mentioned here. Spontaneous Supersymmetry Breakdown (SSB) needs to be effected in a sector of fields which are singlets with respect to the SM gauge group and known as the *hidden sector*. SSB can take place there at a distinct scale denoted by  $\Lambda_S$ . Supersymmetry breaking is then transmitted to the gauge nonsinglet observable or *visible sector* by a messenger sector (associated with a typical mass scale  $M_M$  that could, but need not, be as high as the Planck mass);

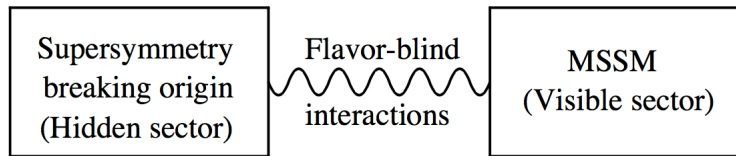


Figure 1.1: The presumed schematic structure for Supersymmetry breaking [2].

this may or may not require the introduction of additional gauge nonsinglet messenger superfields (see Figure 1.1).

It is nonetheless true that this messenger scale must be at least two (and perhaps many more) orders of magnitude above the mass of the MSSM fields. Hence, when the former are integrated out at lower (electroweak) energies, the residual theory is described by the supersymmetric Lagrangian density of the MSSM plus some soft explicit Supersymmetry breaking terms characterized by the supermultiplet splitting mass parameter.

There have been two main competing proposals for what the mediating interactions might be. The first (and historically the more popular) is that they are gravitational. More precisely, they are associated with the New Physics, including gravity, that enters near the Planck scale. This scenario is called *gravity mediated*, or *Planck-scale-mediated Supersymmetry breaking*.

A second possibility are gauge-mediated Supersymmetry breaking (GMSB) models, in which the ordinary gauge interactions, rather than gravity are responsible for the appearance of soft Supersymmetry breaking in the MSSM. The basic idea is to introduce some new chiral supermultiplets, called *messengers* that couple to the ultimate source of SUSY breaking, and also couple indirectly to the (s)quarks and (s)leptons and Higgs(inos) of the MSSM through the ordinary  $SU(3)_C \times SU(2)_L \times U(1)_Y$  gauge boson and gaugino interactions. There is still gravitational communication between the MSSM and the source of Supersymmetry breaking but that effect is here relatively unimportant compared to the gauge interaction effects.

### The goldstino and the gravitino

The spontaneous breaking of *global* Supersymmetry implies the existence of a massless Weyl fermion, the goldstino. Taking into account gravity, Supersymmetry must be promoted to a *local* symmetry. The resulting locally supersymmetric theory is called *supergravity* [28,29]. It necessarily unifies the space-time symmetries of ordinary general relativity with local Supersymmetry transformations. In supergravity, the spin-2 graviton has a spin-3/2 fermion superpartner called *gravitino*.

The gravitino should be thought of as the “gauge” field of local Supersymmetry transformations. As long as Supersymmetry is unbroken, the graviton and the gravitino are both massless, each with two spin helicity states. Once Supersymmetry is spontaneously broken, the gravitino acquires a mass by absorbing (“eating”) the goldstino, which becomes its longitudinal components.



This is called the *super-Higgs* mechanism, and it is analogous to the ordinary Higgs mechanism for gauge theories, by which the  $W^\pm$  and  $Z^0$  gauge bosons in the Standard Model gain mass by absorbing the Goldstone bosons associated with the spontaneously broken electroweak gauge invariance.

In the gravity-mediated Supersymmetry breaking case, the gravitino mass is comparable to the masses of the MSSM sparticles. Its interactions will be of gravitational strength, so the gravitino will not play any role in collider physics, but can be important in cosmology. In contrast, gauge-mediated Supersymmetry breaking models predict that the gravitino is much lighter than the MSSM sparticles as long as  $M_M \ll M_P$ . The gravitino is usually the LSP in this case, and all of the MSSM sparticles will eventually decay into final states that include it. The gravitino inherits the non-gravitational interactions of the goldstino it has absorbed, which means that the gravitino, or more precisely its longitudinal (goldstino) components, can play an important role in collider physics experiments. The mass of the gravitino can generally be ignored for kinematic purposes, as can its transverse components, which really do have only gravitational interactions. Therefore in collider phenomenology discussions one may interchangeably use the same symbol  $\tilde{G}$  for the goldstino and for the gravitino of which it is the longitudinal part.

### 1.3.5 Specific SUSY models

From the huge variety of SUSY models only the ones relevant for this Thesis will be discussed here. Section 1.3.5.1 describes the bRPV-mSUGRA model used to interpret the results from the *1 lepton + multijets analysis* that will be explained in Chapter 3, whereas Section 1.3.5.2 briefly describes the GGM framework, which will be used in the  $Z + E_T^{\text{miss}}$  *analysis* shown in Chapter 4.

#### 1.3.5.1 bRPV-mSUGRA

As mentioned in Section 1.3.2, there is no fundamental reason for  $R$ -parity to be conserved and lepton or baryon number violating terms can appear in the supersymmetric potential as bilinear (involving two supermultiplets) or trilinear (three supermultiplets) terms. Among these possibilities to break  $R$ -parity, there are several reasons to focus on the bilinear one (which violates lepton number). The preferred mechanism to break a symmetry is spontaneously. This also applies to  $R$ -parity, which can be spontaneously broken at high energy scales through the violation of  $L$  while  $B$  is conserved. Hence, breaking  $L$  seems more natural than breaking  $B$ . Furthermore, if RPV is induced by any of the trilinear terms, it is unavoidable for the theory to contain bilinear terms, since they arise from the Renormalisation Group Evolution (RGE) of the trilinears. In contrast, it is perfectly consistent to have an  $R$ -parity breaking through bilinear terms without the presence of trilinear ones [30]. In addition, after the symmetry breaking through bilinear terms, neutrinos naturally acquire masses.

Therefore the simplest way to break  $R$ -parity is to add bilinear terms to the MSSM potential. Besides that, additional bilinear soft SUSY breaking terms are introduced, which include small vacuum expectation values for the sneutrinos. There are nine new parameters introduced in this model. However, after electroweak symmetry breaking and taking into account constraints from neutrino oscillation data, only one free parameter remains.

In the particular bilinear  $R$ -parity violating (bRPV) model that will be considered in this Thesis, the LSP is the lightest neutralino  $\tilde{\chi}_1^0$  [31]. The bRPV terms are embedded in the minimal Supergravity (mSUGRA) model, which imposes some restrictions that reduce the large number of parameters of the MSSM. The number of parameters in mSUGRA is reduced to five, namely  $m_0$ , the scalar mass;  $m_{1/2}$ , the gaugino mass;  $A_0$ , the trilinear scalar coupling;  $\tan\beta$ , the ratio of the Higgs vevs; and  $\text{sign}(\mu)$ , the sign of the higgsino mass parameter.

Therefore, there are six free parameters in the model being considered here. It is stressed that the sparticle spectrum for bRPV-mSUGRA is — within theoretical uncertainties— the same as in RPC mSUGRA; it is the LSP decay modes and its lifetime that depend on the bRPV parameters. The neutralino decays are dominated by leptonic ( $e$ ,  $\mu$ ) or  $\tau$  channels, making lepton-based searches ideal for constraining this model. The fact that in the low- $m_{1/2}$  high- $m_0$  region the  $\tilde{\chi}_1^0$  is slightly long lived opens the possibility to use searches for displaced vertices in order to probe this model at colliders. Lastly, the  $\tilde{\chi}_1^0$  decays to one or two neutrinos give rise to a moderately high  $E_{\text{T}}^{\text{miss}}$ , thus rendering some of the standard  $E_{\text{T}}^{\text{miss}}$ -based analyses pertinent to bRPV. More information on the experimental aspects of bRPV is given in Ref. [32].

### 1.3.5.2 General Gauge Mediation (GGM)

As has been said in Section 1.3.4, one of the possible scenarios to transmit SUSY breaking from the hidden to the visible sector is GMSB. General Gauge Mediation (GGM) [33, 34] is a general approach to formulate gauge mediation in a model-independent way. GGM models maintain the properties common to all GMSB scenarios whilst avoiding any specifics.

The most notable properties of GGM are that the hidden sector decouples from the visible sector as the MSSM couplings approach zero, and that the gravitino  $\tilde{G}$  is always the lightest supersymmetric particle.  $R$ -parity is assumed to be conserved, therefore the LSP is always stable.

Due to the fact that GGM is a GMSB scenario, the next-to-lightest supersymmetric particle (NLSP) defines the phenomenology of these models because it appears at the bottom of every cascade decay and always decays to its SM partner and the gravitino. Depending on the SUSY breaking parameters, the NLSP to LSP decay can be prompt, giving the signature of the prompt SM partner particle plus  $E_{\text{T}}^{\text{miss}}$ , somewhat long-lived, giving a SM particle that does not point back to the primary vertex (displaced vertex) plus  $E_{\text{T}}^{\text{miss}}$ , or

---

long-lived, in which case the NLSP can exit the detector, either leaving a signature, such as a charged track, or being completely invisible, for example if the NLSP is a neutralino.

An important feature of the GGM framework is that it allows almost any superpartner to be the NLSP. In the model investigated in this Thesis, the NLSP is a higgsino-like neutralino. More details about the phenomenology of this specific model can be found in Section 4.3.1. GGM is a very effective “signature generator”: it provides a nice unifying framework through which to view the myriad results at the LHC.



## Chapter 2

# Experimental framework

### 2.1 Introduction

In experimental Particle Physics, very high energy collisions are used to shed light on the laws of Nature that govern the smallest constituents of matter. In order to do this, particle accelerators are used to boost two beams of particles to high energies, before these beams are made to collide with each other or with stationary targets. Purpose-built detectors observe and record the results of these collisions.

This chapter presents the experimental framework (mainly the LHC accelerator and the ATLAS detector) used to perform the searches that will be described in the next chapters<sup>1</sup>. Section 2.2 is dedicated to the LHC and its experiments, in general. Whilst Section 2.3 focuses on the ATLAS detector and its subdetectors.

### 2.2 The Large Hadron Collider (LHC)

The largest international scientific project in the world nowadays is the Large Hadron Collider (LHC) [35]. It includes a hadron accelerator, four huge detectors at its four collision points, together with three smaller experiments, and a Computing Grid project which maintains the data storage and analysis infrastructure.

The LHC, located at CERN near Geneva (Switzerland) has been the first accelerator to explore extensively the TeV scale. Its aim is to allow physicist to test the predictions of new and exciting theories, such as Supersymmetry and Extra Dimensions, and perform precision measurements of already known Standard Model phenomenology. It has already discovered a new particle compatible with the Higgs boson [10, 11] whose properties are currently being measured.

---

<sup>1</sup>The descriptions of the LHC and ATLAS are based on their status before the 2013 shut-down, i.e. when the mentioned analyses were performed. The enhancements implemented to both the accelerator and the detector after the shut-down are beyond the scope of this Thesis.

The proton-proton collision is the primary operation setup, but the LHC also collides protons with lead nuclei and uses lead-lead collisions for other investigations.

Its first research run took place between 2010 and 2011 at an initial energy of 3.5 TeV per beam ( $\sqrt{s} = 7$  TeV), almost 4 times higher than the previous world record for a collider, rising to 4 TeV per beam ( $\sqrt{s} = 8$  TeV) from 2012 to early 2013, when the LHC's first run officially ended and it was shut down for planned upgrades. Its second research run begun on 2015 reaching 6.5 TeV per beam ( $\sqrt{s} = 13$  TeV), the current world record.

### 2.2.1 The accelerator

In order to accelerate the proton beams, the existing CERN accelerator complex is used. The path that the beams follow is shown in Fig. 2.1 and it starts at the LINACs (LINear ACcelerators). There are two kinds of LINACs; LINAC2 which accelerates protons and LINAC3 which accelerates ions. After the LINAC, circular accelerators are used to increase the particle's energy. The beams are first injected into the Proton Synchrotron Booster (PSB), later on through the Proton Synchrotron (PS) and after that into the SPS. The SPS is a 7 km long collider which is operated only as accelerator (only one beam at a time), leading proton beams up to 450 GeV. Finally, the last injection is into the LHC ring which is, nowadays, the longest hadronic accelerator ever built with its 27 km length. Furthermore, the LHC is 100 m below ground.

The LHC has 1232 superconducting dipole magnets which curve the beams through the LHC ring. This kind of magnets uses twin bore magnets which consist of two sets of coils and beam channels within the same mechanical structure and cryostat. This design comes from the fact that the LHC magnets have to accelerate two beams of equally charged particles but in opposite directions and there are obvious room constraints (there were not enough room for two separate magnets in the LHC tunnel). These magnets can generate a bipolar magnetic field up to 8.33 T thanks to their superconductivity capabilities and they fill more than 66% of the LHC ring. The coils are made of niobium-titanium (NbTi) which is a material that allows to reach the superconducting regime at 1.9 K. In addition, there are also radio-frequency cavities for beam acceleration, 392 quadrupolar magnets for beam focusing and beam corrections and also sextupole, octupole and decapole magnets mainly for compensating the systematic non-linearities.

Each beam has an internal structure where the protons are arranged in bunches separated in space. This bunches condense up to  $1.1 \times 10^{11}$  protons. Collisions can have a rate of 40 MHz (i.e. one collision every 25 ns).

Finally, in the LHC ring there are detectors placed at the collision points. A brief description is given in the next section.

## CERN's Accelerator Complex

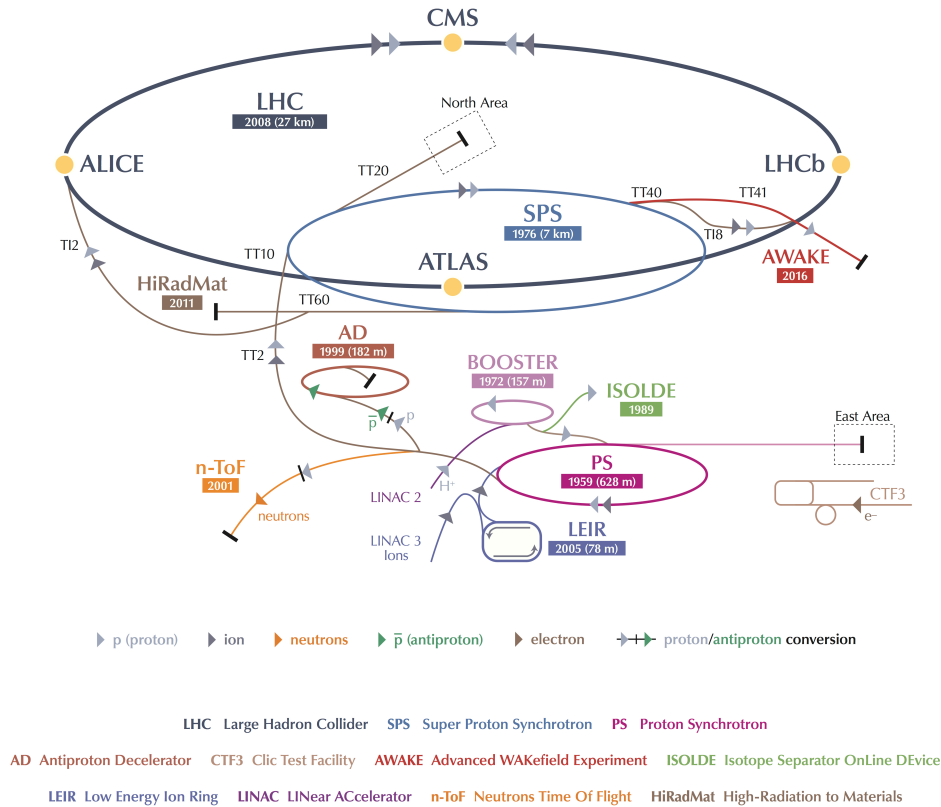


Figure 2.1: Schematic layout of the CERN accelerator complex.

### 2.2.2 The LHC experiments

The LHC has four huge detectors which are located in their corresponding caverns. These detectors are:

- A Toroidal LHC ApparatuS (ATLAS) [36]:** It is a general purpose experiment for high luminosity (up to  $10^{34} \text{ cm}^{-2}\text{s}^{-1}$ ) which performs high precision measurements on SM parameters and the Higgs boson search. It is the largest LHC detector with  $44 \times 25 \text{ m}^2$  of lateral cross section and weighting 7000 tons. It has two magnets: one 2 T solenoid for the inner detector and a toroid which generates up to 6 T/m for the muon spectrometer.
- Compact Muon Solenoid (CMS) [37]:** It is the other general purpose experiment for high luminosity and it has the same discovery potential as ATLAS although its hardware and software design is different to provide different systematic uncertainties. It is smaller than ATLAS

( $21 \times 15 \text{ m}^2$ ) although heavier with 12500 tons and it can generate a unique non-linear magnetic field up to 4 T.

- **Large Hadron Collider beauty (LHCb) [38]:** This experiment is a low luminosity experiment (up to  $10^{32} \text{ cm}^{-2}\text{s}^{-1}$ ) for measuring the parameters of  $CP$  violation in the interactions of B-hadrons. The LHCb detector is a single arm spectrometer stretching for 20 metres along the beam pipe, with its subdetectors stacked one behind the other.
- **A Large Ion Collider Experiment (Alice) [39]:** This experiment is focused on heavy ions and quark-gluon plasma studies. It will operate at a peak luminosity of  $10^{27} \text{ cm}^{-2}\text{s}^{-1}$  for nominal Pb-Pb ion operation.

The LHC also has three smaller experiments:

- **Total cross section based on the Optical Theorem (TOTEM) [40]:** The aim of this experiment is to measure total cross sections, elastic scatterings at small angles and diffractive processes at the LHC at low luminosities (up to  $2 \times 10^{28} \text{ cm}^{-2}\text{s}^{-1}$ ). It shares intersection point with CMS.
- **Large Hadron Collider forward (LHCf) [41]:** It is a special purpose experiment for low luminosity (up to  $2 \times 10^{28} \text{ cm}^{-2}\text{s}^{-1}$ ) which will study neutral pions produced in the forward region of collisions. It shares cavern with ATLAS and consists of two detectors installed at 140 m on either side of the intersection point.
- **Monopole and Exotics Detector At the LHC (MoEDAL) [42, 43]:** The prime motivation of MoEDAL is to directly search for the Magnetic Monopole or Dyon and other highly ionizing Stable (or pseudo-stable) Massive Particles (SMPs) at the LHC. It is installed around the intersection region of the LHCb detector, in the VELO (Vertex LOcator) cavern.

### 2.2.3 The LHC Computing Grid

The last piece of the LHC project is its computing model which has the aim of building and maintaining a distributed data storage and analysis infrastructure, for the entire community that uses the huge amount of data produced by the LHC, based on Grid technologies [44]. This presents several challenges. One is related to the storage, since the LHC produces roughly 15 PB of raw data annually. Another challenge is the fact that around 6000 scientists spread all over the world want to access this huge amount of data almost simultaneously. Moreover this access must be efficient and stable.

In the LHC distributed computing model there is a hierarchy based on sites called Tiers. A primary backup of the LHC data is recorded on tape at CERN, which is the unique Tier0 centre. After the initial processing, these data are distributed to a series of Tier1 centres (11 sites worldwide) which are large



computer centres with sufficient storage and access capacity. The Tier1 centres make data available to the Tier2 centres within their clouds (each Tier1 defines a cloud), each consisting of one or several collaborating computing facilities, which can store sufficient data and provide adequate computing power for specific analysis tasks. Physics groups access these facilities through their closest Tier3 computing resources, which can consist from huge local clusters in their universities to even individual laptops. The main goal of this model is that the computing processes should run where the requested data are, avoiding long data transmission. The Spanish cloud has a multi-experiment Tier1 placed at PIC (Barcelona) and its distributed Tier2s are: CIEMAT (Madrid) and IFCA (Santander) for CMS, IFIC (Valencia), IFAE (Barcelona) and UAM (Madrid) for ATLAS and UB (Barcelona) and USC (Santiago de Compostela) for LHCb.

## 2.3 The ATLAS detector

ATLAS is a general-purpose experiment designed to realize the main physics goals of the LHC. The formal proposal for ATLAS was introduced in 1994 and 10 years later the detector installation in the cavern began. The ATLAS collaboration is quite large with about 2500 physicists scattered around the world.

The ATLAS detector (see Figure 2.2) is nominally forward-backward symmetric with respect to the interaction point. It has cylindrical shape ( $4\pi$  coverage) with layers of subdetectors. It is 44 m long and 25 m high. The closest system to the beam pipe is the tracker or Inner Detector (ID). It operates embedded in a 2 T magnetic field (generated by a thin superconducting solenoid surrounding the ID cavity) and consists of silicon-based subdetectors and drift tubes. This ensures a robust pattern recognition, momentum and charge determination, precise primary and secondary vertex reconstruction as well as particle identification capability. Outside the solenoid are the calorimeters. First, the electromagnetic calorimeter uses liquid argon as an ionization medium, with the absorbers arranged in an accordion geometry. It allows the identification and measurement of electrons and photons. Surrounding the latter is the hadronic calorimeter that uses a scintillating tile technology allowing to measure hadronic jets<sup>2</sup> and helping to determine the missing energy. Outside the calorimeters, ATLAS has a large muon spectrometer, which performs the measurements of muon momenta. It rests inside an air core toroidal magnetic field that is generated by three large superconducting toroids (one barrel and two end-caps) arranged with an eight-fold azimuthal symmetry around the calorimeters. This generates a strong bending power in a large volume within a light and open structure, thereby minimising multiple-scattering effects and allowing to achieve excellent muon momentum resolution with three layers of high precision tracking chambers. The muon momentum

---

<sup>2</sup>A jet is a narrow cone of particles produced by the hadronisation of a quark or gluon.

spectrometer is the outermost part of ATLAS, therefore it defines the overall dimensions of the detector.

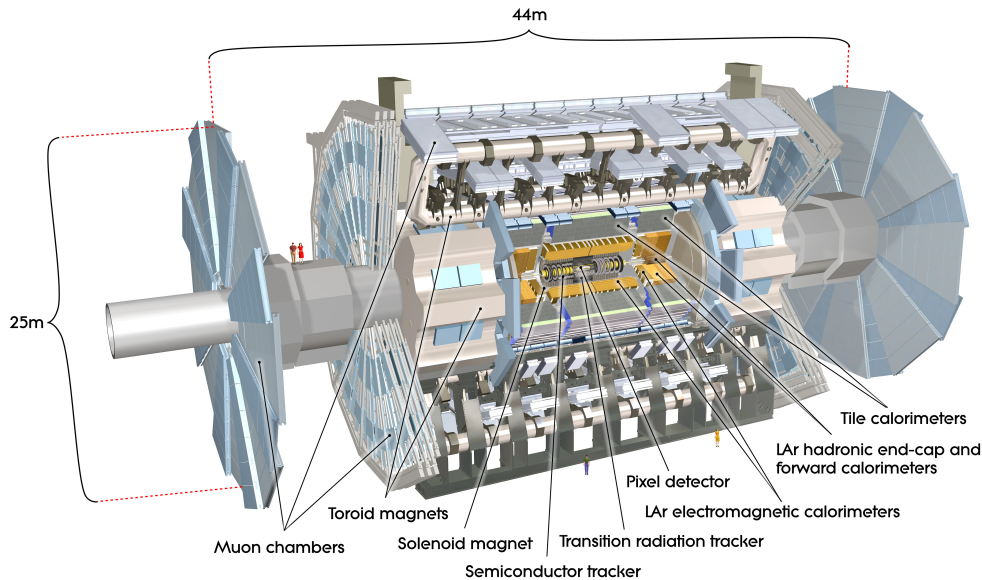


Figure 2.2: Layout of the ATLAS detector.

### 2.3.1 Coordinate system

Before going any further it is useful to briefly summarise the coordinate system and nomenclature used to describe the ATLAS detector and the particles emerging from the proton-proton (pp) collisions.

ATLAS uses a right-handed coordinate system with its origin at the nominal interaction point (IP)<sup>3</sup> in the centre of the detector and the  $z$ -axis along the beam pipe. The  $x$ -axis points from the IP to the centre of the LHC ring, and the  $y$ -axis points upwards. The azimuthal angle  $\phi$  is measured, as usual, around the beam axis, and the polar angle  $\theta$  is the angle from the beam axis. The pseudorapidity is defined as  $\eta = -\ln \tan(\theta/2)$ . The transverse momentum,  $p_T$ , the transverse energy  $E_T$  and the missing transverse energy  $E_T^{\text{miss}}$  are defined in the  $x$ - $y$  plane unless stated otherwise. The opening angle  $\Delta R$  in  $\eta$ - $\phi$  space is defined as  $\Delta R = \sqrt{(\Delta\eta)^2 + (\Delta\phi)^2}$ .

### 2.3.2 Inner Detector

The ATLAS tracker, also known as the Inner Detector (ID), performs the pattern recognition, momentum and vertex measurements together with electron identification, providing a pseudorapidity coverage up to  $\eta < 2.5$ . These

<sup>3</sup>Nominal Interaction point: design position of the IP. Real or physics IP: position where the particles actually collide (also called primary vertex).

capabilities are achieved with a combination of discrete high-resolution semiconductor pixel and strip detectors in the inner part of the tracking volume, respectively the Pixel and the SemiConductor Tracker (SCT), and a straw-tube tracking detector, the Transition Radiation Tracker (TRT), with the capability to generate and detect transition radiation, in its outer part.

The ID operates embedded in a 2T axial magnetic field generated by a solenoid. This magnetic field is used for bending the charged particles and measure their charge and momentum. A three dimensional view of the ID is shown in Figure 2.3 where all its subdetectors are labelled together with its size: 6.2m long and 2.1m width.

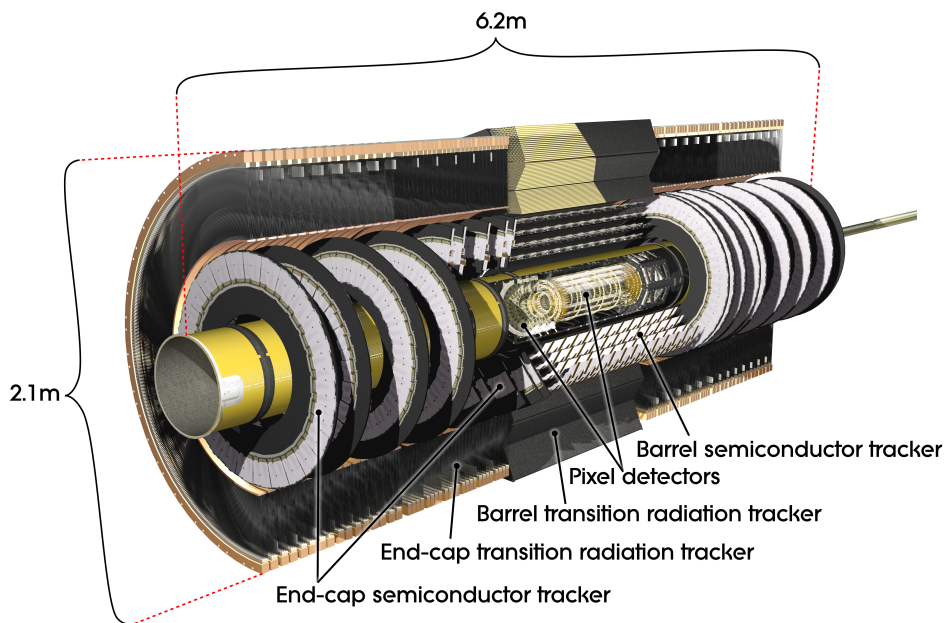


Figure 2.3: Layout of the ATLAS Inner Detector.

Approximately 1500 charged particles will emerge from the collision point and will cross the ATLAS ID every 25 ns at high luminosity ( $10^{34} \text{ cm}^{-2} \text{ s}^{-1}$ ) creating a very large track density in the detector. The ID electronics and all the sensor elements must be fast enough and, of course, radiation hard. In addition, a very fine granularity is needed to handle the particle fluxes and to reduce the influence of overlapping events. For this purpose the ID has 5832 individual silicon modules (with about 86 million readout channels).

The Pixel subdetector is based on silicon pixel technology and it is arranged in three cylindrical barrels and three discs on each side of the central barrel. The pixel elements are  $50 \times 400 \mu\text{m}^2$  resulting in an intrinsic resolution of  $10 \mu\text{m}$  in the transversal direction with a direct 2D readout. This system is designed to provide a very high granularity (with 80.4 million channels) as well as a high precision set of measurements as close as possible to the interaction point.

The SCT is a silicon microstrip based detector which is located just after the Pixel detector. The SCT modules are arranged on four barrel layers and nine end-cap discs on each side. It has been designed to provide eight precision measurements via 4 layers of back-to-back silicon microstrip detector modules with a relative 40 mrad stereo angle. There are five sensor topologies, one for the barrel which has parallel strips with 80  $\mu\text{m}$  pitch and 4 for the end-caps with fan-out structure (54.53 - 90.34  $\mu\text{m}$  pitch). With 80  $\mu\text{m}$  strip pitch on average a SCT module ensures a 17  $\mu\text{m}$  precision in  $r\phi$  and its stereo angle of 40 mrad allows 580  $\mu\text{m}$  in  $z$ . The SCT has 4088 modules.

Finally, the TRT consists of about 300000 gaseous straw tubes arranged in a barrel and two end-caps on each side of this barrel. It has 176 modules, 73 layers in 3 rings in the barrel region and  $2 \times 160$  straw planes in 40 four-plane assembly units in the end-cap regions. The TRT nominal gas mixture Xe/CF<sub>4</sub>/CO<sub>2</sub> (70%/20%/10%) provides an efficient X-ray absorption, a fast charge collection and a stable operation over a sufficient high-voltage range even at high particle rates. Its technology allows to have an intrinsic resolution of 130  $\mu\text{m}$  per straw (i.e. in the direction perpendicular to the wire) where each straw tube has a diameter of 4 mm. From the practical design point of view it has been built to provide in the barrel region and on average  $\sim 30$  TRT hits for tracks coming from the interaction point.

### 2.3.3 Calorimetry

Outside the ID solenoid one can find the calorimeters, which perform energy measurements and particle identification. A view of the sampling calorimeters is presented in Fig. 2.4. These calorimeters cover the range  $|\eta| < 4.9$ , using different techniques in order to fulfil the varying requirements of the physics processes of interest and of the radiation environment over this large  $\eta$ -range. Over the  $\eta$  region matched to the inner detector, the fine granularity of the Electromagnetic Calorimeter (ECAL) is ideally suited for precision measurements of electrons and photons. The coarse granularity of the rest of the calorimeter is sufficient to satisfy the physics requirements for jet reconstruction and  $E_{\text{T}}^{\text{miss}}$  measurements.

The ECAL uses liquid argon (LAr) as an ionization medium (it is also known as LAr calorimeter), with lead absorbers arranged in an accordion geometry [45]. It allows an excellent performance in terms of energy and position resolution as well as in the identification of electrons and photons providing coverage up to  $|\eta| < 3.2$ . It is surrounded by a cryostat as it needs very low temperatures to operate.

Surrounding the latter one finds the Hadronic Calorimeter (HCAL) with a coverage up to  $|\eta| < 4.9$  which measures hadronic jets. A sampling technique with plastic scintillator plates (called tiles) embedded in an iron absorber is used for the hadronic barrel tile calorimeter (also known as TileCal). HCAL is separated into a large barrel and two smaller extended barrel cylinders, one on either side of the central barrel. In the end-caps ( $|\eta| < 1.6$ ), LAr technol-

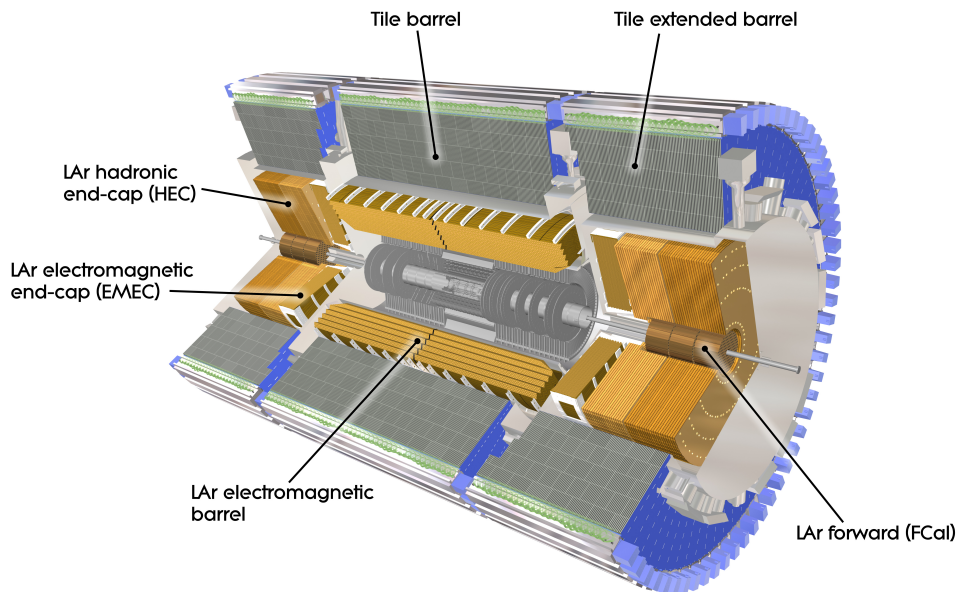


Figure 2.4: Layout of the ATLAS Calorimeters.

ogy is also used for the hadronic calorimeters, matching the outer  $|\eta|$  limits of the end-cap electromagnetic calorimeters. The LAr forward calorimeters provide both electromagnetic and hadronic energy measurements, and extend the pseudorapidity coverage to  $|\eta| < 4.9$ .

### 2.3.4 Muon system

The muon spectrometer (Figure 2.5) is based on the magnetic deflection of muon tracks in the large superconducting air-core toroid magnets, instrumented with separate trigger and high-precision tracking chambers. Over the range  $|\eta| < 1.4$  magnetic bending is provided by the large barrel toroid, which consists of eight flat coils assembled radially and symmetrically around the beam axis. For  $1.6 < |\eta| < 2.7$  muon tracks are bent by two smaller end-cap magnets inserted into both ends of the barrel toroid. Over  $1.4 < |\eta| < 1.6$ , usually referred to as the transition region, magnetic deflection is provided by a combination of barrel and end-cap fields. This magnet configuration provides a field which is mostly orthogonal to the muon trajectories, while minimising the degradation of resolution due to multiple scattering. Tracks are measured with four technologies: Monitored Drift Tubes (MDT), Cathode Strip Chambers (CSC), Resistive Plate Chambers (RPC) and Thin Gap Chambers (TGC). The former two detectors provide high precision momentum measurements for muons, needed to perform the tracking. The latter two detectors are used for triggering.

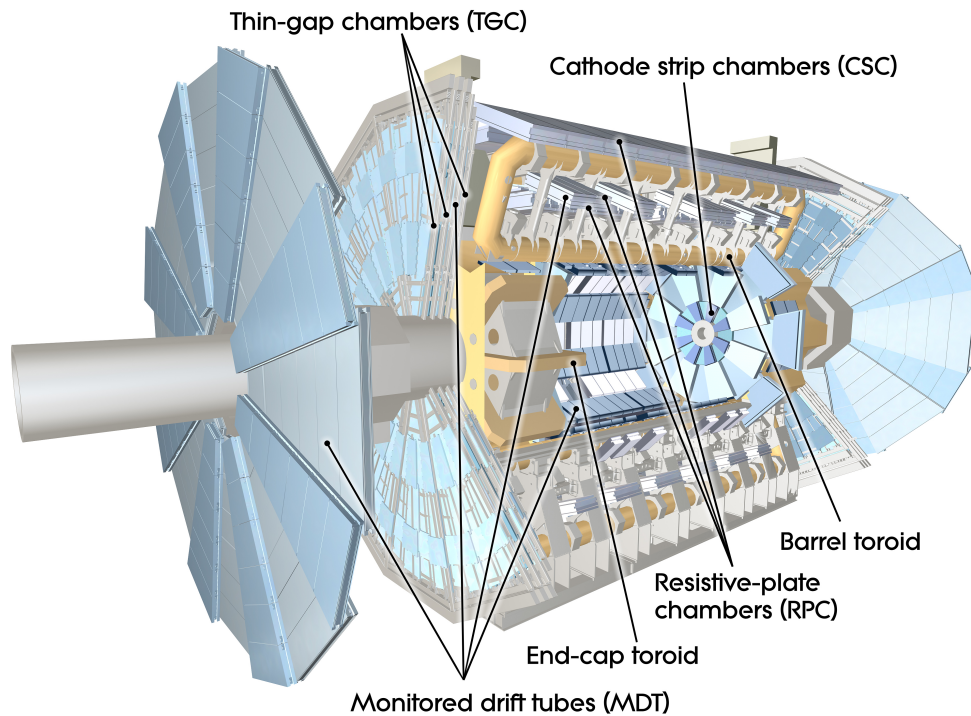


Figure 2.5: Layout of the ATLAS Muon System.

### 2.3.5 Trigger system

The LHC proton bunches can collide at a frequency of 40 MHz, i.e. every 25 ns and at the design luminosity of  $10^{34} \text{ cm}^{-2} \text{ s}^{-1}$  on average about 23 inelastic proton-proton collisions can be produced at each bunch crossing. Therefore, the trigger system needs to efficiently reject a large rate of background events and still select potentially interesting ones with high efficiency. To deal with this great amount of data the ATLAS trigger is based on three levels of online event selection: the level-1 trigger (L1), the level-2 trigger (L2) and the event filter.

Each trigger level refines the event selection done by the previous level applying new criteria. The L1 trigger, which is hardware-based (i.e. it is implemented in custom electronics), searches for high transverse momentum muons, electrons, photons, jets and tau-leptons decaying into hadrons, as well as large missing and total transverse energy. It is responsible for the first level of event selection, reducing the initial event rate to less than 75 kHz. It uses a limited amount of the total detector information to make a decision in less than  $2.5 \mu\text{s}$ . The two higher levels, collectively known as the High Level Trigger (HLT) are software-based and access more detector information for a final rate of up to 200 Hz. On the one hand, the L2 trigger decides in  $O(10)$  ms if the event should be rejected making use, at full granularity and precision, of all the available detector data within the regions of interest. The L2 menus

---

are designed to reduce the trigger rate to approximately 3.5 kHz. On the other hand, the final stage of the event selection is carried out by the event filter, which reduces the event rate to roughly 200 Hz. Its selections are implemented using offline analysis procedures within an average event processing time of the order of four seconds.

## 2.4 Summary

This chapter is a brief description of the LHC and the ATLAS detector as they were at the time when the relevant analyses for this Thesis were performed, i.e. before the 2013-2014 long technical stop. It is worth mentioning that all the ATLAS subdetectors are necessary for these analyses given that leptons, jets and  $E_T^{\text{miss}}$  are used.





## Chapter 3

# One-lepton channel and bilinear RPV SUSY

### 3.1 Introduction

This chapter presents an inclusive search for Supersymmetry by the ATLAS experiment at the LHC in proton-proton collisions at a centre-of-mass energy  $\sqrt{s} = 7$  TeV in final states containing seven or more jets (“multijets”), one isolated lepton (electron or muon) and  $E_{\text{T}}^{\text{miss}}$ . The search is based on data from the full 2011 data-taking period, corresponding to an integrated luminosity of  $4.7 \text{ fb}^{-1}$ .

Among the possible SUSY scenarios, bilinear R-parity violating SUSY is particularly interesting. At low energies, R-parity breaking is explicit through bilinear lepton number violating terms which lead to neutrino masses and to the decay of the lightest supersymmetric particle (LSP). When the R-parity violating couplings are embedded in a mSUGRA/CMSSM production model the LSP decay modes involving muons or neutrinos have relatively large Branching Ratios (BRs) and hence, muons and some amount of  $E_{\text{T}}^{\text{miss}}$  are expected in the final states. Therefore, the results of the analysis are interpreted in the context of this bRPV mSUGRA/CMSSM scenario.

A full description of this search, together with other interpretations, can be found in Ref. [46]. This analysis is an extension to higher jet multiplicity of the “1-lepton + 3- and 4-jets +  $E_{\text{T}}^{\text{miss}}$ ” channels described in Ref. [47]. Searches for new phenomena in channels with high jet multiplicity and  $E_{\text{T}}^{\text{miss}}$  (vetoing on leptons) have also been reported by the ATLAS Collaboration in Refs. [48] and [49].

This chapter starts with an overview of the setup of the analysis. A brief description of the SUSY signal model considered for interpretation follows in Section 3.3. The physics object identification and event selection are presented in Sections 3.4 and 3.5, followed by the description of the background estimation methods in Section 3.6 and the systematic uncertainties in Section 3.7. In Section 3.8 the background fit is discussed. Finally, Sections 3.9, 3.10 and 3.11 are dedicated to the results, interpretation and conclusions, respectively.

## 3.2 Analysis overview

This section briefly introduces the main concepts of the SUSY analysis considering strong production with one lepton in the final state. The general procedure to perform New Physics searches starts with the definition of Signal Regions (SRs), which are sets of selection requirements (*cuts*), on some observables, that enhance the signal over background ratio. In this search, a combination of three discriminating variables in the beam transverse plane (after lepton and jet kinematic selection) is used to define the SR:

- the missing transverse energy ( $E_T^{\text{miss}}$ ), vectorial sum of lepton, jets and other calorimeter activity,
- the transverse mass, defined later in Eq. (3.1), and
- the inclusive effective mass, defined later in Eq. (3.2).

The one lepton selection in the signal region requires exactly one isolated electron or muon in the final state. This veto on additional leptons ensures the orthogonality to the two lepton selections used in some control regions (CRs).

The background estimate in the signal region is obtained using a semi-data-driven approach, in which the dominant backgrounds are normalized to the data in dedicated control regions, which are all orthogonal to the SR. The normalised Monte Carlo prediction is then used to extrapolate the background components from these CRs to the SR. The definition of the control regions is discussed in Section 3.6. The background enriched CRs are also useful to reduce the systematic uncertainties on the background estimation in the SR.

The main background processes in the SR are top quark production (mostly semi- and fully-leptonic  $t\bar{t}$  pairs, but also single top to a lesser extent) and the production of  $W$  and  $Z$  bosons in association with jets (where the  $W/Z$  boson decays leptonically,  $W \rightarrow \ell\nu$  or  $Z \rightarrow \ell\ell$ ). In addition, an estimate on the QCD jet production is required in the SR, since large uncertainties affect both the theory and the lepton fake rates.

To validate the background extrapolation from control to signal region, different validation regions (VRs) are defined having dominant contributions from one background source. Usually requirements on the same variables also used in the definition of the signal regions are applied to select the events in the validation regions. These VRs are located between the control and signal regions. Their exact definitions are given in Section 3.8.0.1.

A profile likelihood fit is applied to extract all background contributions in the different control, validation and signal regions. For the discovery fit, only the control regions are used to predict the background in the signal region. For the exclusion setup, also the signal region itself is included in the fit. All validation regions are only used as cross check and do not constrain the backgrounds. The various systematic uncertainties discussed in Section 3.7 are taken into account by the fit.

The background prediction in the SR is compared to the experimental observation in order to assess if any significant excess of events is produced with respect to the SM expectation. The CLs method (described in Section A.3.5) is then used to set exclusion limits in a bRPV-mSUGRA model.

### 3.3 SUSY signal models

The benchmark SUSY model considered here allows for bilinear R-parity violating terms in the superpotential [50]. The R-parity violating couplings are embedded in a mSUGRA/CMSSM SUSY production model, which is characterized by five parameters: the universal scalar and gaugino mass parameters  $m_0$  and  $m_{1/2}$ , a universal trilinear coupling parameter  $A_0$ , the ratio of the vacuum expectation values of the two Higgs doublets  $\tan\beta$ , and the sign of the Higgsino mass parameter  $\mu$ . In this analysis, the values of  $m_0$  and  $m_{1/2}$  are scanned between  $100 \text{ GeV} \leq m_0 \leq 1400 \text{ GeV}$  and  $260 \text{ GeV} \leq m_{1/2} \leq 1000 \text{ GeV}$ . The other parameters are fixed as follows:  $\tan\beta = 10$ ,  $A_0 = 0$  and  $\mu$  is taken to be positive [51]. For this chosen set of mSUGRA parameters, the bilinear R-parity violating parameters are determined under the tree-level dominance scenario [52] by fitting them to the neutrino oscillation data as described in Ref. [53]. The neutralino LSP is unstable and decays within the detector through decay modes that include neutrinos [54]. Such decays along with the presence of neutrinos in SUSY decay chains such as  $\tilde{\chi}_j^\pm \rightarrow \ell^\pm \nu \tilde{\chi}_i^0$  lead to significant  $E_T^{\text{miss}}$ .

### 3.4 Physics object identification and selection

Three types of triggers were used to collect the data: electron, muon and  $E_T^{\text{miss}}$ . The electron trigger selects events containing one or more electron candidates, based on the presence of a cluster in the electromagnetic calorimeter, with a shower shape consistent with that of an electron. The muon trigger selects events containing one or more muon candidates based on tracks identified in the MS and ID. The  $E_T^{\text{miss}}$  trigger is used only for selecting events for the background validation tests described in Section 3.8.0.1.

The reconstructed primary vertex [55] is required to be consistent with the beam spot envelope and to have at least five associated tracks; when more than one such vertex is found, the vertex with the largest summed  $|p_T|^2$  of the associated tracks is chosen.

Electrons are reconstructed from energy clusters in the electromagnetic calorimeter matched to a track in the ID [56]. Preselected electrons are required to have  $|\eta| < 2.47$  and pass a variant of the “medium” selection defined in Ref. [56] that differs mainly in having a tighter track-cluster matching in  $\eta$ , stricter pixel hit requirements, additional requirements in the TRT, and tighter shower-shape requirements for  $|\eta| > 2.01$ . These requirements provide background rejection close to the “tight” selection of Ref. [56] with only a

few percent loss in efficiency with respect to “medium”. Preselected electrons are further required to have  $p_T > 10$  GeV. No explicit requirements are made on the distance of closest approach to the event primary vertex; however, the electron reconstruction restricts the distance in the transverse plane to approximately less than 2 mm.

Muons are identified either as a combined track in the MS and ID systems, or as an ID track matched with a MS segment [57, 58]. Requirements on the quality of the ID tracks are identical to those in Ref. [59]. Preselected muons are required to have  $|\eta| < 2.4$  and a  $p_T > 10$  GeV.

Jets are reconstructed using the anti- $k_t$  algorithm [60, 61] with a distance parameter  $R = 0.4$ . Jets arising from detector noise, cosmic rays or other non-collision sources are rejected [62]. To account for the differences between the calorimeter response to electrons and hadrons,  $p_T$ - and  $\eta$ -dependent factors, derived from simulated events and validated with test beam and collision data, are applied to each jet to provide an average energy scale correction [62] back to particle level. Preselected jets are required to have  $p_T > 20$  GeV and  $|\eta| < 4.5$ . Since electrons are also reconstructed as jets, preselected jets which overlap with preselected electrons within a distance  $\Delta R = \sqrt{(\Delta\eta)^2 + (\Delta\phi)^2} = 0.2$  are discarded.

For the final selection of signal events, “signal” electrons are required to pass a variant of the “tight” selection of Ref. [56], providing 1-2% gain in efficiency and slightly better background rejection. Signal electrons must have  $p_T > 25$  GeV,  $|\eta| < 2.47$  and a distance to the closest jet  $\Delta R > 0.4$ . Signal electrons are required to satisfy isolation criteria: the scalar sum of the  $p_T$  of tracks within a cone of radius  $\Delta R = 0.2$  around the electron (excluding the electron itself) is required to be less than 10% of the electron  $p_T$ .

Muons in the final selection (“signal” muons) are required to have  $p_T > 20$  GeV,  $|\eta| < 2.4$  and  $\Delta R > 0.4$  with respect to the closest jet. Further isolation criteria (over and above the isolation implied by the requirement that the muon be separated from the nearest jet by  $\Delta R > 0.4$ ) are imposed: the scalar sum of the  $p_T$  of tracks within a cone of radius  $\Delta R = 0.2$  around the muon candidate (excluding the muon itself) is required to be less than 1.8 GeV. The distance of closest approach to the event primary vertex in the transverse plane ( $d_0$ ) and in the  $z$  direction ( $z_0$ ) are required to be less than 2 mm and 5 mm, respectively.

Signal jets are required to have  $p_T > 25$  GeV and  $|\eta| < 2.5$ . In addition, they are required to be associated with the hard-scattering process, by demanding that at least 75% of the scalar sum of the  $p_T$  of all tracks associated with the jet come from tracks associated with the primary vertex of the event. Jets with no associated tracks are rejected. The above requirements are applied to cope with the pileup conditions of the 2011 data taking.

The missing transverse momentum is computed as the negative of the vector sum of the  $p_T$  of all preselected electrons, preselected muons and preselected jets (after removing those overlapping with preselected electrons), and all calorimeter clusters with  $|\eta| < 4.9$  that are not associated with any of the

above-mentioned objects.

For approximately 20% of the 2011 data-taking period, an electronics failure created a region in the electromagnetic calorimeter, located at  $0 < \eta < 1.4$  and  $-0.8 < \phi < -0.6$ , where the signal readout was compromised. Events with an electron in this region are vetoed for the entire dataset, leading to an acceptance loss of less than 1% for signal events in the signal region. For jets, the amount of transverse energy ( $E_T$ ) lost in the dead region can be estimated from the energy deposited in the neighbouring calorimeter cells. If this lost  $E_T$  projected along the  $E_T^{\text{miss}}$  direction amounts to more than 10 GeV and constitutes more than 10% of the  $E_T^{\text{miss}}$ , the event is rejected. The effect of the electronics failure is described in the detector simulation, and the loss of signal acceptance from this requirement is negligible.

Jets arising from  $b$ -quarks are identified using information about track impact parameters and reconstructed secondary vertices [63]; the  $b$ -tagging algorithm is based on a neural network using as input the output weights of algorithms defined in Refs. [64, 65].

### 3.5 Event selection

Two variables, derived from the kinematic properties of the reconstructed objects, are used in the event selection. The transverse mass ( $m_T$ ) computed from the momentum of the lepton ( $\ell$ ) and the missing transverse momentum ( $\mathbf{p}_T^{\text{miss}}$ ), defined as

$$m_T = \sqrt{2p_T^\ell E_T^{\text{miss}}(1 - \cos(\Delta\phi(\ell, \mathbf{p}_T^{\text{miss}}))}, \quad (3.1)$$

is useful in rejecting events containing a single  $W$  boson. The inclusive effective mass ( $m_{\text{eff}}^{\text{inc}}$ ) is the scalar sum of the  $p_T$  of the leptons, the jets and  $E_T^{\text{miss}}$ :

$$m_{\text{eff}}^{\text{inc}} = \sum_{i=1}^{N_{lep}} p_{T,i}^\ell + \sum_{h=1}^{N_{jet}} p_{T,h}^{\text{jet}} + E_T^{\text{miss}} \quad (3.2)$$

where the index  $i$  runs over all the signal leptons and  $j$  runs over all the signal jets in the event. The inclusive effective mass is correlated with the overall mass scale of the hard-scattering process and provides good discrimination against the SM background, without being too sensitive to the details of the SUSY decay cascade.

In the signal region, the number of signal leptons with  $p_T > 25(20)$  GeV for electrons (muons) is required to be exactly one. Events containing additional signal leptons (but with the  $p_T$  threshold lowered to 10 GeV) are rejected. Events containing a muon that failed the requirement on  $d_0$  or  $z_0$  are also rejected. The number of signal jets is required to be  $\geq 7$ , with a leading jet satisfying  $p_T > 80$  GeV and the other jets having  $p_T > 25$  GeV. In addition, the following conditions are imposed:  $m_T > 120$  GeV,  $E_T^{\text{miss}} > 180$  GeV, and  $m_{\text{eff}}^{\text{inc}} > 750$  GeV. The selection criteria are summarized in Table 3.1

	SR	3-jet $W$ CR	3-jet $t\bar{t}$ CR	7-jet $W$ CR	7-jet $t\bar{t}$ CR	$Z$ + jets CR	dileptonic $t\bar{t}$ CR
Trigger	Single electron or muon (+jet)						
$N_\ell$	1	1	1	1	1	$\geq 2$	$\geq 2$
$p_T^{\ell_1}$	$> 25$ (20)	$> 25$ (20)	$> 25$ (20)	$> 25$ (20)	$> 25$ (20)	$> 25$ (20)	$> 25$ (20)
$p_T^{\ell_2}$	$< 10$	$< 10$	$< 10$	$< 10$	$< 10$	$< 10$	$< 10$
$N_{jet}$	$\geq 7$	$\geq 3$	$\geq 3$	$\geq 7$	$\geq 7$	$\geq 2$	$\geq 2$
$p_T^{jet}$	$> 80, 25,$ $\dots, 25$	$> 80, 25,$ $25$	$> 80, 25,$ $25$	$> 80, 25,$ $\dots, 25$	$> 80, 25,$ $\dots, 25$	$> 80, 50$ or $50, 50, 50, 50$	$> 80, 50$ or $50, 50, 50, 50$
$N_{b-jet}$	—	0	$\geq 1$	0	$\geq 1$	—	$\geq 1$
$E_T^{\text{miss}}$	$> 180$	[40, 150]	[40, 150]	[40, 120]	[40, 120]	$< 50$	[30, 80]
$m_T$	$> 120$	[40, 80]	[40, 80]	[40, 80]	[40, 80]	—	—
$m_{\text{eff}}^{\text{inc}}$	$> 750$	$> 500$	$> 500$	$> 400$	$> 400$	—	—
$m_{\ell\ell}$	—	—	—	—	—	[81, 101]	$< 81$ or $> 101$

Table 3.1: Overview of the selection criteria for the signal and control regions in this analysis. The  $p_T$  selections for leptons are given for electrons (muons). All mass and momentum requirements are in units of GeV.  $\ell_1$  is the leading lepton,  $\ell_2$  the subleading lepton and  $m_{\ell\ell}$  the invariant mass of the two leading leptons.

### 3.6 Background estimation

The dominant source of background in this analysis is the production of semi- and fully-leptonic  $t\bar{t}$  events, and the production of  $W$ +jets where the  $W$  decays leptonically. Other background processes which are considered are multijets, single-top, dibosons and  $t\bar{t}$  plus vector boson.

The major backgrounds are estimated by isolating each process in a control region, normalizing the simulation to data in that control region, and then using the simulation to extrapolate the background expectations into the signal region. The multijet background is estimated entirely from data by a matrix method described below. All other (smaller) backgrounds are estimated entirely from the simulation, using the most accurate theoretical cross section available. To account for the cross-contamination of physics processes across control regions, the final estimate of the background is obtained with a simultaneous, combined fit to all the control regions, as described in Section 3.8.

Several correction factors are applied to the simulation. As described in Section 3.6.2, the  $p_T$  of the  $Z$  boson is reweighted based on a comparison of data with simulation in an event sample enriched in  $Z$  + jets events. The same correction factor is applied to  $W$  boson production and improves the agreement between data and simulation in the  $E_T^{\text{miss}}$  distribution. Other correction factors are derived during the combined fit. The relative normalization of the

$W + \text{jets}$ ,  $Z + \text{jets}$  and  $t\bar{t}$  samples simulated with ALPGEN with different numbers of partons ( $N_{\text{parton}}$ ) in the matrix element is adjusted by comparing the jet multiplicity distribution in data and simulation in the 3-jet control regions. A common set of corrections is obtained for the  $W + \text{jets}$  and  $Z + \text{jets}$  samples, and a separate set of common corrections is obtained for  $t\bar{t}$  decays.

### 3.6.1 $W/Z + \text{jets}$ and $t\bar{t}$ control regions

The  $W + \text{jets}$  and  $t\bar{t}$  processes are isolated in control regions defined by the following requirements. In the 3-jet control regions, three or more signal jets are required, with a leading jet  $p_{\text{T}} > 80$  GeV. The lepton requirements are the same as in the signal region. The  $E_{\text{T}}^{\text{miss}}$  is required to be between 40 and 150 GeV while the transverse mass is required to be between 40 and 80 GeV. The  $m_{\text{eff}}^{\text{inc}}$  requirement is relaxed to  $m_{\text{eff}}^{\text{inc}} > 500$  GeV. In order to gauge the sensitivity of the analysis to the choice of control region, an alternate set of control regions with seven or more signal jets is defined with a leading jet  $p_{\text{T}} > 80$  GeV. The  $E_{\text{T}}^{\text{miss}}$  is required to be between 40 and 120 GeV. The  $m_{\text{eff}}^{\text{inc}}$  requirement is relaxed to  $m_{\text{eff}}^{\text{inc}} > 400$  GeV. All other requirements are the same as in the 3-jet control regions. The  $W + \text{jets}$  and  $t\bar{t}$  CRs are distinguished by requirements on the number of  $b$ -tagged jets. For the  $W + \text{jets}$  control region, events are rejected if any of the three highest  $p_{\text{T}}$  jets is  $b$ -tagged; the rejected events then define the  $t\bar{t}$  control region.

Control regions for  $Z + \text{jets}$  and dileptonic  $t\bar{t}$  are also defined in order to provide additional constraints when fitting the normalization factors for the  $W + \text{jets}$  and  $t\bar{t}$   $N_{\text{parton}}$  bins (described in Section 3.8). A  $Z + \text{jets}$  control region is defined by requiring two or more signal leptons of opposite charge and same flavour (where the  $p_{\text{T}}$  requirement on the second lepton is lowered to 10 GeV), a dilepton mass consistent with that of the  $Z$  boson,  $E_{\text{T}}^{\text{miss}} < 50$  GeV, and two or more signal jets with the leading jet above 80 GeV, and sub-leading jets above 50 GeV. In events with four or more jets, the leading jet threshold is lowered to 50 GeV. A dileptonic  $t\bar{t}$  CR is defined with the same requirements as the  $Z + \text{jets}$  CR, except that leptons of different flavour are allowed, and the dilepton mass is required to be inconsistent with that of the  $Z$  boson. The  $E_{\text{T}}^{\text{miss}}$  requirement is changed to  $30 \text{ GeV} < E_{\text{T}}^{\text{miss}} < 80 \text{ GeV}$ , and one or more jets is required to be  $b$ -tagged. Table 3.1 summarizes the control region definitions.

### 3.6.2 Reweighting of $W + \text{jets}$ and $Z + \text{jets}$ simulated samples

As in Ref. [47], the samples of simulated  $W + \text{jets}$  and  $Z + \text{jets}$  events are reweighted as a function of the generated  $p_{\text{T}}$  of the vector boson. A common set of corrections to the  $p_{\text{T}}$  of the vector boson, applied to both  $W + \text{jets}$  and  $Z + \text{jets}$  samples, is found to improve the agreement between data and simulation for a number of variables ( $E_{\text{T}}^{\text{miss}}$ ,  $m_{\text{eff}}^{\text{inc}}$ , and jet  $p_{\text{T}}$ ).

The  $p_{\text{T}}^Z$  distribution is measured in data by selecting a sample with two oppositely-charged, same-flavour leptons with an invariant mass between 80 GeV

and 100 GeV,  $\geq 3$  signal jets with  $p_T > 25$  GeV, and  $m_{\text{eff}}^{\text{inc}} > 400$  GeV. The  $p_T^Z$  distribution in five bins of reconstructed  $p_T$  is compared to the ALPGEN simulation in five bins of generated  $p_T$  ( $p_T^{Z,\text{gen}}$ ), with the first four bins ranging from 0 to 200 GeV and the last bin integrated above 200 GeV; the ratio of the two distributions is taken as the  $p_T^{Z,\text{gen}}$ -dependent weight factor. The simulation used here uses the cross sections as stated in Ref. [46]. Only the systematic uncertainty from the jet energy scale is considered (in addition to statistical uncertainties) when computing the uncertainty on the weighting factors.

### 3.6.3 Multijet background

Multijet events become a background when a jet is misidentified as an isolated lepton or when a real lepton appears as a decay product of hadrons in jets, for example from  $b$ - or  $c$ -jets, and is sufficiently isolated. In the following, such lepton-like objects are collectively referred to as misidentified leptons from now on. The multijet background in the signal region, and in the  $W + \text{jets}$  and  $t\bar{t}$  control regions, where it is more significant, is estimated from the data following a matrix method similar to that employed in Ref. [59].

The multijet background from all sources (but separated by lepton flavour) is determined collectively. In the single-lepton channels, the multijet process is enhanced in a control sample with all the SUSY signal region criteria applied except that the lepton isolation criteria are not imposed and the shower shape requirements on electrons are relaxed. Defining  $N_{\text{pass}}$  and  $N_{\text{fail}}$  as the number of leptons in such a loose sample passing or failing the final lepton selection criteria, and defining  $N_{\text{real}}$  and  $N_{\text{misid.}}$  as the number of real and the number of misidentified leptons, the following equations hold:

$$N_{\text{pass}} = \epsilon_{\text{real}} N_{\text{real}} + \epsilon_{\text{misid.}} N_{\text{misid.}}, \quad (3.3)$$

$$N_{\text{fail}} = (1 - \epsilon_{\text{real}}) N_{\text{real}} + (1 - \epsilon_{\text{misid.}}) N_{\text{misid.}}, \quad (3.4)$$

where  $\epsilon_{\text{real}}$  is the relative identification efficiency for real leptons, and  $\epsilon_{\text{misid.}}$  is the misidentification efficiency for misidentified leptons. Solving the equations leads to:

$$N_{\text{misid.}}^{\text{pass}} = \epsilon_{\text{misid.}} N_{\text{misid.}} = \frac{N_{\text{fail}} - (1/\epsilon_{\text{real}} - 1) N_{\text{pass}}}{1/\epsilon_{\text{misid.}} - 1/\epsilon_{\text{real}}}, \quad (3.5)$$

The efficiency  $\epsilon_{\text{real}}$  is measured from data samples of  $Z \rightarrow \ell\ell$  decays. The lepton misidentification efficiency is obtained using events containing at least one electron (muon) satisfying the relaxed criteria, and at least one signal jet with  $p_T > 30$  (60) GeV. In addition for the electron case,  $E_T^{\text{miss}} < 30$  GeV is required. For the muon case, the event is required to contain exactly one muon with  $|d_0|/\sigma_{d_0} > 5$  where  $\sigma_{d_0}$  is the uncertainty on the transverse impact



parameter measured with respect to the primary vertex. The electron misidentification efficiency is evaluated separately for samples enhanced (depleted) in heavy-flavour contributions by requiring (vetoing) a  $b$ -tagged jet in the event.

### 3.6.4 Other backgrounds

The backgrounds from single-top, diboson and  $t\bar{t}$  + vector boson production are estimated almost purely from simulation. The background from cosmic-ray muons overlapping a hard-scattering event is estimated from a control sample with large  $z_0$ . Extrapolating to the signal region  $|z_0| < 5$  mm, the contribution is found to be negligible.

## 3.7 Systematic uncertainties

Systematic uncertainties have an impact on the expected background and signal event yields in the control and signal regions. These uncertainties are treated as nuisance parameters in a profile likelihood fit described in Sec. 3.8. The following systematic uncertainties on the reconstructed objects are taken into account. The jet energy scale (JES) uncertainty has been determined from a combination of test beam, simulation and in-situ measurements from 2010  $pp$  collision data [62]. Additional contributions from the higher luminosity and pileup in 2011 are taken into account. Uncertainties on the lepton identification, momentum/energy scale and resolution are estimated from samples of  $Z \rightarrow \ell^+\ell^-$ ,  $J/\psi \rightarrow \ell^+\ell^-$  and  $W^\pm \rightarrow \ell^\pm\nu$  decays in data [56–58]. The uncertainties on the jet and lepton energies are propagated to the  $E_T^{\text{miss}}$ ; an additional  $E_T^{\text{miss}}$  uncertainty arising from energy deposits not associated with any reconstructed objects is also included [66]. Uncertainties on the  $b$ -tagging efficiency are described in Refs. [63, 67, 68], while uncertainties on the light-flavour and charm mis-tag rate are derived in Refs. [69] and [70] respectively.

Uncertainties in the matrix method for the determination of the multi-jet background include the statistical uncertainty in the number of events available in the various control samples, the difference in misidentification efficiency for electrons from heavy- versus light-flavoured jets, the dependence of the misidentification efficiency on the jet multiplicity, and the uncertainty in the subtraction of other backgrounds from the samples used to estimate the misidentification efficiency.

Uncertainties from the identification efficiency for jets associated with the primary vertex and from the overlay of pileup in simulated events are both found to be negligible. The theoretical modelling uncertainties in the simulation are described in Ref. [46]. The uncertainty in the signal cross section is taken from an envelope of cross section predictions using different PDF sets (including the  $\alpha_s$  uncertainty) and factorization and renormalization scales, as described in Ref. [71].

The impact of these systematic uncertainties on the background yields and signal estimates are evaluated via an overall fit, described in Sec. 3.8 and 3.9.

### 3.8 Background fit

The background in the signal region is estimated with a fit based on the profile likelihood method [72, 73] (see Appendix A). The inputs to the fit are as follows:

- The observed numbers of events in the  $Z + \text{jets}$ , dileptonic  $t\bar{t}$ , 3-jet  $W + \text{jets}$  and 3-jet  $t\bar{t}$  control regions, and the numbers expected from simulation. These are separated into 7 jet-multiplicity bins, ranging from 3 to 9 jets for the 3-jet  $W + \text{jets}$  and  $t\bar{t}$  control regions. Eight jet-multiplicity bins, ranging from 2 to 9 jets are used for the  $Z + \text{jets}$  and dileptonic  $t\bar{t}$  control regions.
- Transfer factors (TF), derived from simulation, are multiplicative factors that propagate the event counts for  $W + \text{jets}$  and  $t\bar{t}$  backgrounds from one control region to another, or from one control region to the signal region.
- The number of multijet background events in all control and signal regions, as derived from the data.
- Expectations from simulation for the number of events from the minor backgrounds (single-top, diboson,  $t\bar{t}$ +boson) in all control and signal regions.

The event count in each bin of the control region is treated with a Poisson probability density function. There are 30 control region bins in total. Each lepton flavour is treated separately in the likelihood function. The statistical and systematic uncertainties on the expected yields are included in the probability density function as nuisance parameters, constrained to be Gaussian with a width given by the size of the uncertainty. Approximately 150 nuisance parameters are included in the fit and are detailed in Ref. [46]. Correlations in the nuisance parameters from bin to bin are taken into account where necessary. The Poisson probability density functions also include free parameters, for example to scale the expected contributions from the major backgrounds; these are described in more detail below. A likelihood is formed as the product of these probability density functions and the constraints on the nuisance parameters. The free parameters and nuisance parameters are adjusted to maximize the likelihood.

The free parameters considered in the fit are as follows:

- $t\bar{t}$  background: Each  $t\bar{t}$  sample, divided into  $N_{\text{parton}}$  bins (from 0 to 3, with the last being inclusive), is scaled by a free parameter. For each  $N_{\text{parton}}$  bin, a common parameter is used for semi-leptonic and dileptonic  $t\bar{t}$  samples.
- $W + \text{jets}$  background: each  $W + \text{jets}$  sample, again divided into  $N_{\text{parton}}$  bins from 2 to 5 is scaled by a free parameter. The  $N_{\text{parton}} = 6$  bin

for  $W$ +light-flavoured jets shares its fit parameter with  $N_{\text{parton}} = 5$ . The vector boson plus heavy-flavour samples share the same relative normalization parameters as the light-flavour samples. Only  $N_{\text{parton}}$  bins between two and five are allowed to float, as the lower multiplicity bins contain only a small number of events due to the jet and effective mass requirements.

The backgrounds from multijets and the sub-dominant backgrounds from single-top, diboson, and  $t\bar{t}$ +boson production are allowed to float in the fit within their respective uncertainties.

### 3.8.0.1 Background fit validation

The background fit is cross-checked in a number of validation regions, situated between the control and signal regions, where the results of the background fit can be compared to observation. These validation regions are not used to constrain the fit.

- The  $W$  + jets validation region is identical to the 7-jet  $W$  + jets control region except that the  $E_{\text{T}}^{\text{miss}}$  requirement is changed to  $120 \text{ GeV} < E_{\text{T}}^{\text{miss}} < 180 \text{ GeV}$ .
- Similarly, the  $t\bar{t}$  validation region is identical to the 7-jet  $t\bar{t}$  control region except that the  $E_{\text{T}}^{\text{miss}}$  requirement is changed to  $120 \text{ GeV} < E_{\text{T}}^{\text{miss}} < 180 \text{ GeV}$ .
- The high transverse mass, low  $E_{\text{T}}^{\text{miss}}$  validation region is identical to the signal region except that the  $E_{\text{T}}^{\text{miss}}$  requirement is changed to  $40 \text{ GeV} < E_{\text{T}}^{\text{miss}} < 180 \text{ GeV}$ . This region tests the validity of the background yields from dileptonic  $t\bar{t}$  events.
- The high  $E_{\text{T}}^{\text{miss}}$ , low transverse mass validation region is identical to the signal region except that the requirement on the transverse mass is changed to  $40 \text{ GeV} < m_{\text{T}} < 120 \text{ GeV}$ .
- The high transverse mass, low lepton  $p_{\text{T}}$  validation region is identical to the signal region except that the lepton  $p_{\text{T}}$  requirement is changed to  $10 \text{ GeV} < p_{\text{T}}^{\ell} < 20 \text{ GeV}$ . The events in this region are collected with the  $E_{\text{T}}^{\text{miss}}$  trigger.
- The low transverse mass, low lepton  $p_{\text{T}}$  validation region is defined by  $40 \text{ GeV} < m_{\text{T}} < 120 \text{ GeV}$  and  $10 \text{ GeV} < p_{\text{T}}^{\ell} < 20 \text{ GeV}$ . All other requirements are identical to the signal region. The events in this control region are collected with the  $E_{\text{T}}^{\text{miss}}$  trigger.

The definitions of the validation regions are summarized in Table 3.2.

The results of the fit to the control regions, as well as the comparison of observed versus predicted event counts in the validation region, are summarized

	$W + \text{jets}$	$t\bar{t}$	<b>Low</b> $E_T^{\text{miss}}$ <b>High</b> $m_T$	<b>High</b> $E_T^{\text{miss}}$ <b>Low</b> $m_T$	<b>Low</b> $p_T^{\ell_1}$ <b>High</b> $m_T$	<b>Low</b> $p_T^{\ell_1}$ <b>Low</b> $m_T$
Trigger	Single electron or muon (+jet)			$E_T^{\text{miss}}$	$E_T^{\text{miss}}$	
$N_\ell$	1	1	1	1	1	1
$p_T^{\ell_1}$	>25 (20)	>25 (20)	>25 (20)	>25 (20)	[10, 20]	[10, 20]
$p_T^{\ell_2}$	<10	<10	<10	<10	<10	<10
$N_{jet}$	$\geq 7$	$\geq 7$	$\geq 7$	$\geq 7$	$\geq 7$	$\geq 7$
$p_T^{jet}$	> 80, 25, ..., 25	> 80, 25, ..., 25	> 80, 25, ..., 25	> 80, 25, ..., 25	> 80, 25, ..., 25	> 80, 25, ..., 25
$N_{b-jet}$	0	$\geq 1$	—	—	—	—
$E_T^{\text{miss}}$	[120, 180]	[120, 180]	[40, 180]	> 180	> 180	> 180
$m_T$	[40, 80]	[40, 80]	> 120	[40, 120]	> 120	[40, 120]
$m_{\text{eff}}^{\text{inc}}$	> 400	> 400	> 750	> 750	> 750	> 750

Table 3.2: Overview of the selection criteria for the validation regions in this analysis. The  $p_T$  selections for leptons are given for electrons (muons). All mass and momentum requirements are in units of GeV.  $\ell_1$  is the leading lepton and  $\ell_2$  the subleading lepton.

in Fig. 3.1. The difference between the observed and predicted event counts is normalized by the total (statistical and systematic) uncertainty on the prediction. The agreement between predicted and observed yields is reasonable. Figure 3.2 shows the  $m_{\text{eff}}^{\text{inc}}$  distribution in the  $t\bar{t}$  validation region after the fit.

As a crosscheck of the modelling of the backgrounds at high jet multiplicity, the background fit is performed to the 7-jet control regions rather than the 3-jet regions. The difference seen in the top background predictions, amounting to 16% (53%) in the electron (muon) channel, is assigned as an additional systematic uncertainty; the difference in the uncertainty between the electron and muon channels is consistent with a statistical fluctuation in the low number of events in the 7-jet control region.

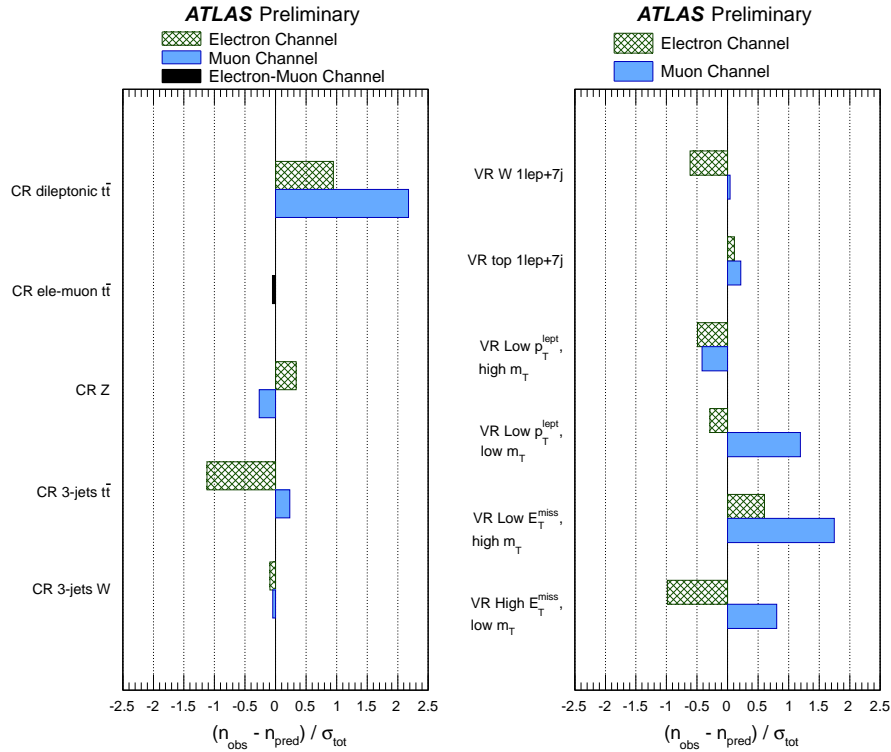


Figure 3.1: Summary of the fit results in the control regions (left) and validation regions (right). The difference between the observed and predicted number of events, divided by the total (statistical and systematic) uncertainty on the prediction, is shown for each control and validation region.

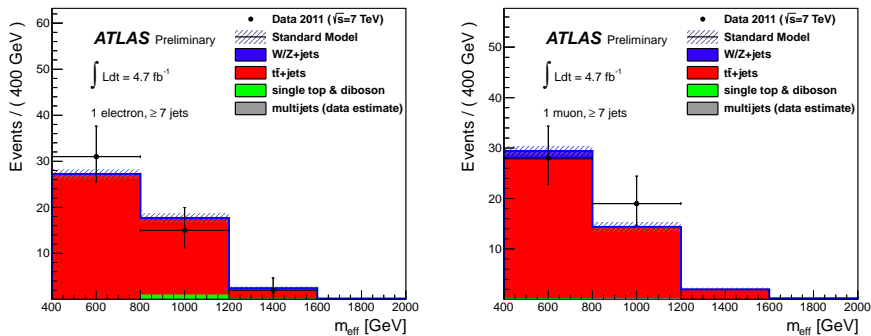


Figure 3.2: Distribution of  $m_{\text{eff}}^{\text{inc}}$  in the  $t\bar{t}$  validation region for the electron (left) and muon (right) channels. The SM expectation shown here is the output of the final fit. The uncertainty band around the SM expectation combines all statistical and systematic uncertainties except for the multiparton uncertainty.

Number of events	<b>Electron</b>	<b>Muon</b>
Observed	7	7
Fitted background	$4.3 \pm 1.2$	$2.2 \pm 1.1$
Fitted top	$3.1 \pm 0.7$	$1.9 \pm 1.0$
Fitted $W/Z$ + jets	$0.3 \pm 0.5$	$0.3 \pm 0.5$
Fitted other background	$0.2 \pm 0.2$	$< 0.05$
Fitted multijet	$0.6 \pm 0.7$	$< 0.05$
MC expectation SM	$6.0 \pm 2.4$	$3.7 \pm 2.4$
MC expectation top	$4.5 \pm 1.8$	$3.4 \pm 2.2$
MC expectation $W/Z$ + jets	$0.3 \pm 0.4$	$0.3 \pm 0.4$
MC expectation other background	$0.5 \pm 0.7$	$0.0 \pm 0.2$
Data-driven multijet	$0.6 \pm 0.7$	$< 0.05$

Table 3.3: The observed numbers of events in the electron and muon signal regions, and the background expectations from the fit. The inputs to the fit are also shown; these consist of the data-driven multijet background estimate and the nominal expectations from simulation (MC), normalized to theoretical cross sections. The errors shown are the statistical plus systematic uncertainties on the mean of the Poisson function describing the background probability density.

### 3.9 Results

The predicted background in the signal regions and the observed numbers of events are shown in Table 3.3. No significant discrepancy is seen between the observed yields and the SM expectations. The deviation in the muon (electron) channel has a  $p$ -value of 0.019 (0.13), amounting to approximately a  $2.1\sigma$  ( $1.1\sigma$ ) effect. Combining the two channels, the deviation has again a  $p$ -value of 0.019.

The dominant background uncertainty is the multiparton uncertainty (described in Ref. [46]). The limited number of events in the background simulation samples in the signal region also contributes significantly. For the signal prediction, the dominant uncertainties at the highest excluded SUSY masses arise from the PDFs (30 – 40%) and the JES (10 – 20%); the former reflect the uncertainty in the gluon distribution at high values of  $x$ .

The distributions of jet multiplicity and transverse mass after all selection requirements (except those on jet multiplicity and transverse mass, respectively) are shown in Figures 3.3 and 3.4. The SM expectation shown is the sum of the fitted values for each of the SM background components.

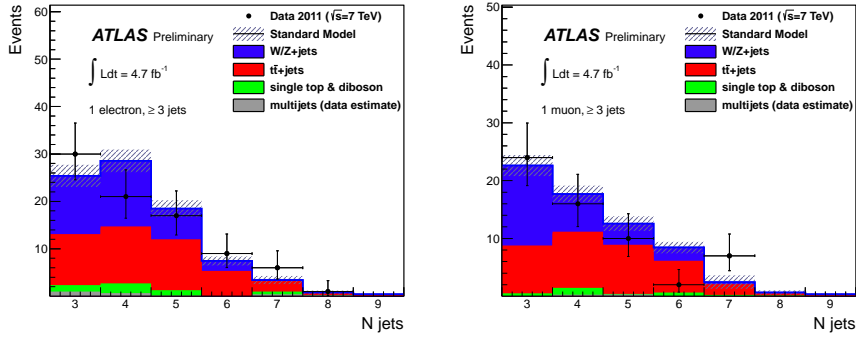


Figure 3.3: Distribution of the jet multiplicity in the electron (left) and muon (right) channels after all selection requirements except for that on the jet multiplicity. The last bin includes all overflows. The SM expectation shown here is the sum of the fitted values for each of the SM background components. The uncertainty band around the SM expectation combines all statistical and systematic uncertainties except for the multiparton uncertainty, which is included only for  $N_{\text{jet}} \geq 7$ .

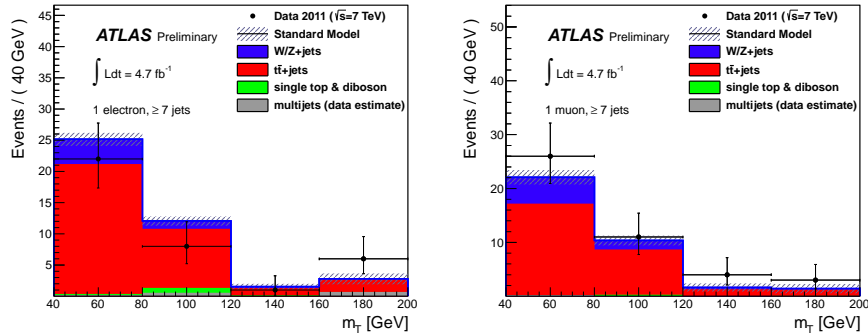


Figure 3.4: Distribution of the transverse mass in the electron (left) and muon (right) signal regions after all selection requirements except for that on the transverse mass. The last bin includes all overflows. The SM expectation shown here is the sum of the fitted values for each of the SM background components. The uncertainty band around the SM expectation combines all statistical and systematic uncertainties except for the multiparton uncertainty, which is included only for  $m_T > 120$  GeV.

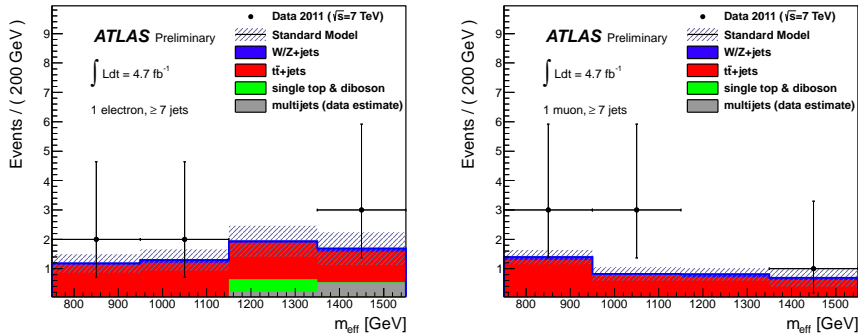


Figure 3.5: Distribution of  $m_{\text{eff}}^{\text{inc}}$  in the electron (left) and muon (right) signal regions after all selection requirements. The last  $m_{\text{eff}}^{\text{inc}}$  bin includes all overflows. The SM expectation shown here is the input to the final fit, and is entirely derived from simulation, normalized to the theoretical cross sections. The uncertainty band around the SM expectation combines the statistical uncertainty on the simulated event samples with the systematic uncertainties on the jet energy scale and resolution, lepton efficiency and resolution, luminosity, multijet background and  $b$ -tagging.

### 3.10 Interpretation

In this section, the results of the previous section will be used to set limits in the mSUGRA model with bilinear RPV [74] described in Sec. 3.3. The limit setting procedure uses the “exclusion fit” configuration, which proceeds in the same way as the background fit except that in this case the signal contamination in control regions is taken into account as further input to the fit. In addition, the likelihood fit makes use of the  $m_{\text{eff}}^{\text{inc}}$  shape information in the signal region as a further discriminant. The likelihood is extended to include bin-by-bin  $m_{\text{eff}}^{\text{inc}}$  information by dividing the signal region into four bins in  $m_{\text{eff}}^{\text{inc}}$ . Examples of these distributions (as input to the fit) are shown in Fig. 3.5.

#### 3.10.1 Limits in the bilinear RPV model

The implications of the analysis for a mSUGRA model with bRPV are studied here. An overview of the phenomenological aspects and determination of model parameters, together with a more detailed definition of the bRPV grid used in previous analysis rounds, has been given in Ref. [75]. In summary, bRPV signal points are based on mSUGRA input parameters supplemented by bilinear RPV parameters. The latter are determined by the spectrum generator SPheno [76, 77] to be consistent with neutrino oscillation results. The mSUGRA parameters in this analysis are defined as follows:

- $100 \text{ GeV} \leq m_0 \leq 1400 \text{ GeV}$



- $260 \text{ GeV} \leq m_{1/2} \leq 1000 \text{ GeV}$
- $A_0 = 0 \text{ GeV}$
- $\tan \beta = 10$
- $\text{sign}(\mu) = +1$

For  $m_{1/2} \lesssim 250 \text{ GeV}$  the increasing LSP lifetime results in a loss of acceptance from the requirements on the muon impact parameter. This region is not considered in the present analysis.

The parameter space is extended significantly with respect to the previous analysis in Refs. [59, 78], where input masses in the ranges  $100 \text{ GeV} \leq m_0 \leq 800 \text{ GeV}$  and  $200 \text{ GeV} \leq m_{1/2} \leq 600 \text{ GeV}$  were considered. Progress in simulation of bRPV signal points has been made in updating PYTHIA6-based event generation. Moreover, all underlying SLHA spectrum files have been updated using an improved version of SPheno. Note that these improvements lead to a more consistent simulation, in particular for late decays of the neutralino LSP. The grid model points used for bRPV exclusion limits have been produced in full simulation for late decays of the LSP, while ATLFast-II has been used otherwise.

The exclusion limits are shown in Fig. 3.6. They are obtained from the combination of the hard one lepton (muon plus electron) and seven jets signal regions. The reach of the analysis is extended significantly in comparison to the previous limit, which was based on the hard one muon plus four tight jets signal region of Ref. [59].

Apart from the improved fit setup and increased luminosity, several effects enhance the sensitivity with respect to the 2011 analysis:

- The statistical combination of different channels yields increased exclusion potential. This is particularly pronounced for bRPV analysis combining the electron and muon (plus multiple jets) signal regions since the previous result was based only on the 4 tight jets plus *muon* selection.
- An enhancement of the sensitivity with respect to R-parity conserving mSUGRA is expected since bRPV also leads to LSP decays involving jets. Due to the high number of jets in this model, high jet multiplicity selection essentially only reduces background.
- Studying the cut-flows for signal points indicates that relaxing the  $E_T^{\text{miss}}$  cut to 180 GeV improves the efficiency significantly. Also removing the  $E_T^{\text{miss}}/m_{\text{eff}}$  cut (used in the previous analysis) for this analysis strongly enhances the sensitivity, while it typically reduced the number of events by 40% in previous selections.

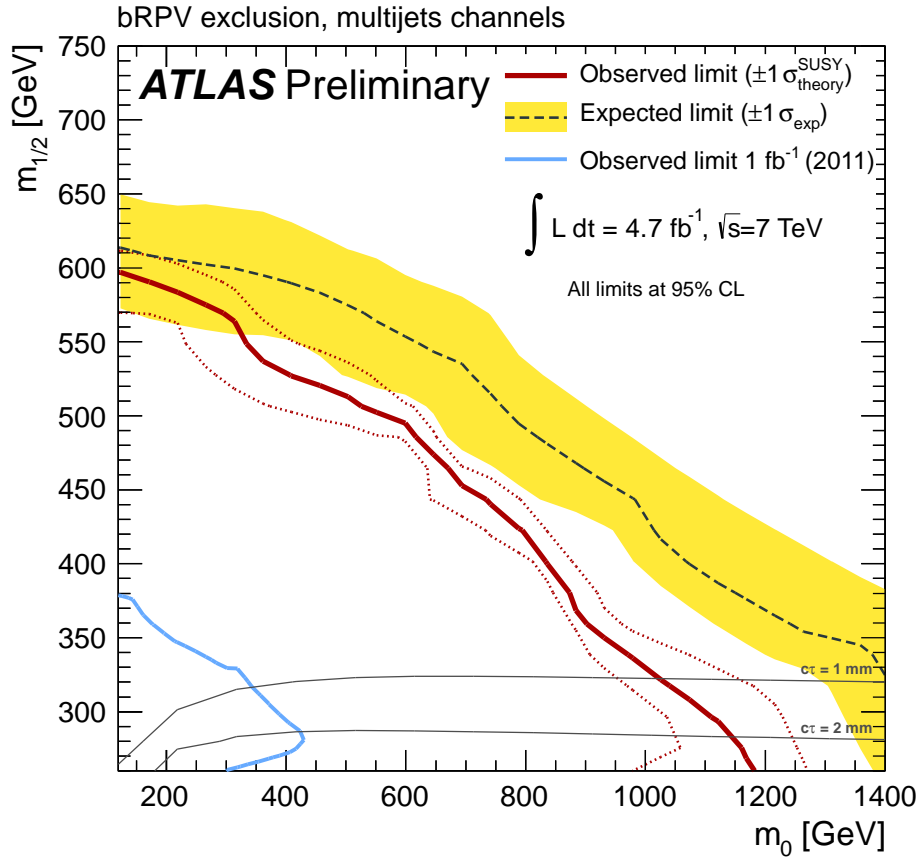


Figure 3.6: Expected and observed 95% CL exclusion limits in the bilinear R-parity violating model. The results are obtained by combining the electron and muon channels. The band around the median expected limit shows the  $\pm 1\sigma$  variations on the median expected limit, including all uncertainties except the theoretical uncertainties on the signal. The dotted lines around the observed limit indicate the sensitivity to  $\pm 1\sigma$  on these theoretical uncertainties. The thin solid black contours show the LSP lifetime. The result from the previous ATLAS search [59] for this model is also shown (in blue).

### 3.11 Conclusions and outlook

A search with the ATLAS detector for SUSY in final states containing seven or more jets, one isolated lepton (electron or muon) and  $E_T^{\text{miss}}$  has been presented. Data from the full 2011 data-taking period, corresponding to an integrated luminosity of  $4.7 \text{ fb}^{-1}$  and a  $\sqrt{s} = 7 \text{ TeV}$ , have been analysed. Observations are consistent with SM expectations and 95% CL exclusion limits have been placed on a bilinear R-parity violating model embedded in a mSUGRA/CMSSM production model. These limits greatly extend the previous results [59] from ATLAS.

Beyond the scope of this Thesis, several analyses have continued to probe bRPV mSUGRA/CMSSM models with  $\sqrt{s} = 8 \text{ TeV}$  data with an integrated luminosity of  $20 \text{ fb}^{-1}$ . For this purpose, the model presented in this chapter has been modified to accommodate the measured mass of the Higgs boson particle found in 2012. Three analyses show great sensitivity to this model: (chronologically) the first one dedicated to final states with “two same-sign leptons or three leptons + jets +  $E_T^{\text{miss}}$ ” (*SS-search*) [79], the second with “at least one tau lepton + jets +  $E_T^{\text{miss}}$ ” (*tau-search*) [80], and the third with “one or two isolated leptons + jets +  $E_T^{\text{miss}}$ ” (*1-lepton-search*) [81].

The statistical combination of the results of the three analyses has been performed in Ref. [82]. These searches at 8 TeV extend the parameter space probed and the exclusion limits. For  $m_0$  values smaller than approximately 750 GeV the sensitivity is dominated by the tau-search which excludes  $m_{1/2}$  values up to 680 GeV. At high  $m_0$  values the best sensitivity is provided by the SS-search, which excludes values of  $m_{1/2}$  between 200 GeV and 490 GeV. For  $m_0$  values below 2200 GeV, signal models with  $m_{1/2} < 200 \text{ GeV}$  are not considered because the lepton acceptance is significantly reduced due to increased LSP lifetime in that region.



## Chapter 4

# $Z + \text{jets} + E_{\text{T}}^{\text{miss}}$ analysis

### 4.1 Introduction

This chapter describes a search for Supersymmetry in final states characterised by a  $Z$  boson that decays to an electron or a muon pair, large missing transverse energy ( $E_{\text{T}}^{\text{miss}}$ ) and jets. This final state is motivated by SUSY models where at least one superpartner decays preferably to a  $Z$  boson, in particular by a generalised gauge-mediated Supersymmetry-breaking model where the gravitino is the lightest supersymmetric particle and the next-to-lightest SUSY particle is a higgsino-like neutralino.

The proton-proton collision data used in this search were collected at a centre-of-mass energy  $\sqrt{s} = 8$  TeV by the ATLAS detector at the LHC and correspond to an integrated luminosity of  $20.3 \text{ fb}^{-1}$ .

The chapter starts with an overview of the analysis in Section 4.2. Subsequently, the supersymmetric signal models that will be probed are explained in Section 4.3 which is followed by the physics object identification and selection in Section 4.4. The event selection is described in Section 4.5. Section 4.6 is dedicated to the background estimation while the systematic uncertainties are shown in Section 4.7. Finally, the analysis results, interpretations and conclusions are presented in Sections 4.8, 4.9 and 4.10 respectively.

### 4.2 Analysis overview

This section briefly introduces the main concepts of this SUSY analysis. The search region definition can be summarized as containing a light lepton pair from a  $Z$  boson decay accompanied by jets and large missing transverse energy.

A great effort has been made to accurately estimate the number of SM events that are expected to survive the signal region selection cuts. The dominant background processes and those that are expected to be most difficult to model using MC simulation are estimated using data-driven or semi-data-driven techniques. For this, dedicated control regions and seed regions are defined. To check the background extrapolation from control to signal re-

gions, the estimated background is compared to data in pre-defined validation regions. An overview of all the control, validation and signal regions for all background estimation methods is given in Table 4.1. The control and validation regions mimic the SR jet multiplicity and other kinematic cuts as much as possible.

A brief description of the considered backgrounds and their estimation methods is given below, whereas the detailed information can be found in Section 4.6.

The so-called “flavour-symmetry” method is used to estimate the di-leptonic  $WW$ ,  $t\bar{t}$ ,  $Wt$  and  $Z \rightarrow \tau\tau$  backgrounds, amongst which  $t\bar{t}$  production is the dominant contribution. This method is detailed in Section 4.6.2 and begins from the assumption that for these flavour-symmetric backgrounds the true ratio of  $ee:\mu\mu:e\mu$  events is 1:1:2. Therefore  $e\mu$  control regions (CRe $\mu$ ), where a different flavour lepton pair is required, can be used to estimate these backgrounds in the signal regions in which a lepton pair of the same flavour is required. The measured ratio of events is affected by differences in trigger requirements and reconstruction efficiencies for electrons and muons; these effects are accounted for in the final estimation.

As a cross-check to the flavour-symmetry method a side-band fit is performed, which is documented in Section 4.6.3.2. For this cross-check, dedicated  $t\bar{t}$  enriched control regions (CRT) are defined in which the MC expectation for  $t\bar{t}$  events is fitted to the data. With the normalization factors retrieved from the fit, the  $t\bar{t}$  contribution is extrapolated to the signal regions. A set of validation regions (VRT) is defined to check the results of the fit.

Diboson backgrounds with real  $Z$  boson production ( $WZ$  and  $ZZ$ ) as well as “Rare Top” backgrounds, which include  $t\bar{t} + W$ ,  $t\bar{t} + Z$  and single top ( $tZ$ ) processes are estimated from MC directly, with the appropriate experimental and theoretical uncertainties being applied.

Processes with “fake leptons”, i.e. jets mis-reconstructed as leptons, are estimated using the Matrix Method, as described in Section 4.6.4.

Finally, there is the special case of the  $Z/\gamma^* + \text{jets}$  background. Although Standard Model events with a  $Z$  boson decaying into light charged lepton pairs do not contain any real  $E_{\text{T}}^{\text{miss}}$ , these events can enter the signal region when the mis-measurement of associated jets leads to high  $E_{\text{T}}^{\text{miss}}$  (usually called instrumental or fake  $E_{\text{T}}^{\text{miss}}$ ). Considering that the  $Z/\gamma^* + \text{jets}$  background could mimic a possible signal, particular care has been taken to suppress it as much as possible and to estimate its remaining, although negligible, contribution as precisely as possible. To perform this estimation, given the difficulties of modelling the instrumental  $E_{\text{T}}^{\text{miss}}$  in MC simulation, the data-driven “jet smearing” method is applied. For this method the jets in “seed events” from specific regions with low  $E_{\text{T}}^{\text{miss}}$  are smeared with a function modelling the detector jet response to retrieve an estimation for the fake  $E_{\text{T}}^{\text{miss}}$  distribution. The extrapolation to the signal regions is double-checked in appropriate validation regions (VRZ). The jet smearing method provides an estimate for the contribution from events containing both fake  $E_{\text{T}}^{\text{miss}}$ , from object mis-measurement,

Region	$E_T^{\text{miss}}[\text{GeV}]$	$H_T[\text{GeV}]$	$n_{\text{jets}}$	$m_{\ell\ell} [\text{GeV}]$	SF/OF	$E_T^{\text{miss}}$ sig. [ $\sqrt{\text{GeV}}$ ]	$f_{\text{ST}}$	$\Delta\phi(\text{jet}_{1,2}, E_T^{\text{miss}}) > 0.4$
Signal regions								
SR	$> 225$	$> 600$	$\geq 2$	$81 < m_{\ell\ell} < 101$	SF	-	-	$\checkmark$
Jet smearing method								
SeedR	-	$> 600$	$\geq 2$	$81 < m_{\ell\ell} < 101$	SF	$< 0.9$	$< 0.6$	-
VRZ	$< 150$	$> 600$	$\geq 2$	$81 < m_{\ell\ell} < 101$	SF	-	-	-
Flavour-symmetry method								
CRe $\mu$	$> 225$	$> 600$	$\geq 2$	$81 < m_{\ell\ell} < 101$	OF	-	-	$\checkmark$
Combined fit								
CRT	$> 225$	$> 600$	$\geq 2$	$m_{\ell\ell} < 81$ OR $m_{\ell\ell} > 101$	SF	-	-	$\checkmark$
VRT	$150 < E_T^{\text{miss}} < 225$	$> 500$	$\geq 2$	$m_{\ell\ell} < 81$ OR $m_{\ell\ell} > 101$	SF	-	-	$\checkmark$
VRTZ	$150 < E_T^{\text{miss}} < 225$	$> 500$	$\geq 2$	$81 < m_{\ell\ell} < 101$	SF	-	-	$\checkmark$
VRT_highHT	$150 < E_T^{\text{miss}} < 225$	$> 600$	$\geq 2$	$m_{\ell\ell} < 81$ OR $m_{\ell\ell} > 101$	SF	-	-	$\checkmark$
VRTZ_highHT	$150 < E_T^{\text{miss}} < 225$	$> 600$	$\geq 2$	$81 < m_{\ell\ell} < 101$	SF	-	-	$\checkmark$
VRT_highMET	$> 225$	$400 < H_T < 600$	$\geq 2$	$m_{\ell\ell} < 81$ OR $m_{\ell\ell} > 101$	SF	-	-	$\checkmark$
VRTZ_highMET	$> 225$	$400 < H_T < 600$	$\geq 2$	$81 < m_{\ell\ell} < 101$	SF	-	-	$\checkmark$

Table 4.1: Overview over all signal, control, seed and validation regions used in this analysis. More details are given in the text in the specific sections. The  $E_T^{\text{miss}}$  significance and the Soft Terms fraction  $f_{\text{ST}}$  needed in the seed regions for the jet smearing method are defined in Section 4.6.1. The dilepton pair flavour is denoted as either SF for same flavour or OF for opposite flavour.

and real  $E_{\text{T}}^{\text{miss}}$ , from neutrinos in heavy flavour quark decays. All the details can be found in Section 4.6.1.

The resulting background estimates are compared to the observed event yields to calculate a significance (the local probability for the background estimate to produce a fluctuation greater than or equal to the observed data) using pseudo-experiments.

The results are interpreted in the context of a generalised gauge-mediated Supersymmetry-breaking model where the gravitino is the lightest supersymmetric particle (LSP) and the next-to-lightest SUSY particle (NLSP) is a higgsino-like neutralino.

### 4.3 SUSY signal models

The most relevant phenomenological aspects of the SUSY models considered for interpretation are summarized in this section.

#### 4.3.1 Gauge-mediated Supersymmetry breaking

One popular scenario that provides a formalism to explain the mechanism of SUSY breaking, which in turn gives rise to the superpartner masses and interactions, is gauge-mediated Supersymmetry breaking (GMSB). In GMSB models [83–88], SUSY is broken in a hidden sector and the SUSY breaking is propagated to the visible sector via SM-like  $SU(3)_C \times SU(2)_L \times U(1)_Y$  gauge boson and gaugino interactions of some new chiral supermultiplets, called messengers, and the MSSM particles. The main advantage of GMSB models relative to the minimal supergravity and anomaly-mediated SUSY breaking models is that scalars with the same gauge quantum numbers, but different flavours, have identical soft SUSY breaking masses. As a result, flavour-changing neutral currents (FCNC) are suppressed, thus solving the so-called “flavour problem”.

In GMSB, the gravitino ( $\tilde{G}$ ) is the LSP (in general  $m(\tilde{G}) \ll 1 \text{ keV}$ ), which escapes detection, leading to missing transverse momentum (denoted  $\mathbf{p}_{\text{T}}^{\text{miss}}$ ). The phenomenology of GMSB models is determined by the nature of the next-to-lightest supersymmetric particle (NLSP), which for a large part of the GMSB parameter space is the lightest neutralino  $\tilde{\chi}_1^0$ .

Neutralinos are mixtures of gaugino ( $\tilde{B}, \tilde{W}^0$ ) and higgsino ( $\tilde{H}_u^0, \tilde{H}_d^0$ ) eigenstates, and therefore the lightest neutralino decays to a  $\tilde{G}$  and either a  $\gamma$ ,  $Z$ , or  $h$ . If the  $\tilde{\chi}_1^0$  is bino-like, the main decay mode is  $\tilde{\chi}_1^0 \rightarrow \gamma\tilde{G}$ . If the  $\tilde{\chi}_1^0$  is higgsino-like, it decays as  $\tilde{\chi}_1^0 \rightarrow h\tilde{G}$ . In addition, since the longitudinal polarisation component of the  $Z$  boson is also a Goldstone mode of the Higgs field, a higgsino-like neutralino can also decay as  $\tilde{\chi}_1^0 \rightarrow Z\tilde{G}$ . Consequently, a  $\tilde{\chi}_1^0$  pair produced in a collider can give rise to the diboson final states  $(hh, h\gamma, hZ, Z\gamma, ZZ, \gamma\gamma) + E_{\text{T}}^{\text{miss}}$ . The scenarios considered for interpretation of this analysis are the ones with at least one  $Z$ -boson in the final state, i.e.  $ZZ$  and  $Zh$ , plus two  $\tilde{G}$ . Hence, the case where the  $BR(\tilde{\chi}_1^0 \rightarrow h\tilde{G})$  is not



negligible is also covered. The analysis is also in principle sensitive to  $Z\gamma$  signal events, but these are rare in the models considered here.

In recent years, the effort to formulate GMSB in a model-independent way has led to the development of general gauge mediation (GGM) [33, 34]. GGM includes an observable sector with all the MSSM fields, together with a hidden sector that contains the source of SUSY breaking. In GGM, there need not be any hierarchy between coloured and uncoloured states, and therefore there is no theoretical constraint on the coloured-states mass, thus raising the feasibility of GGM discovery even with early LHC data. Both ATLAS and CMS have performed searches for GGM models with bino-like  $\tilde{\chi}_1^0$ 's [89, 90]. CMS also performed a search for wino-like  $\tilde{\chi}_1^0$  GGM [90–92]. ATLAS has performed a search for higgsino-like  $\tilde{\chi}_1^0$  GGM [93, 94] with  $5.8 \text{ fb}^{-1}$  of  $\sqrt{s} = 8 \text{ TeV}$  data. No excesses above the SM background expectations were observed.

The search for the higgsino-like  $\tilde{\chi}_1^0$  GGM SUSY models, suggested in Refs. [95, 96], was performed in Ref. [94] and is updated in this analysis. In these models the gluino mass,  $m(\tilde{g})$ , and the higgsino mass parameter,  $\mu$ , are treated as free parameters. The higgsino mass parameter was chosen to be positive to ensure that  $\tilde{\chi}_1^0 \rightarrow Z\tilde{G}$  is the dominant NLSP decay. The  $U(1)$  and  $SU(2)$  gaugino mass parameters ( $M_1$  and  $M_2$ , respectively) are fixed to 1 TeV. All other sparticle masses are fixed at  $\sim 1.5 \text{ TeV}$ , which leads to gluino pair production via strong interactions being the dominant production mode. The gluinos then cascade-decay into final states involving the NLSP  $\tilde{\chi}_1^0$  and jets. In this particular region of parameter space, the two lightest neutralinos ( $\tilde{\chi}_1^0$  and  $\tilde{\chi}_2^0$ ) and lightest chargino ( $\tilde{\chi}_1^\pm$ ) become higgsino-like. In the limit ( $M_1, M_2$ )  $\rightarrow \infty$ , the exact relations  $m(\tilde{\chi}_1^0) = m(\tilde{\chi}_2^0) = m(\tilde{\chi}_1^\pm) = \mu$  hold true. In practice,  $M_1$  and  $M_2$  are never infinite, and therefore the effect of neutralino and chargino mixing will push the masses of  $\tilde{\chi}_1^0$ ,  $\tilde{\chi}_2^0$  and  $\tilde{\chi}_1^\pm$  (which can be seen in Sec. 4.3.3) away from  $\mu$ . Two different values of  $\tan\beta$  were selected in this analysis. A  $\tan\beta$  value of 1.5 was chosen to ensure  $\tilde{\chi}_1^0 \rightarrow Z\tilde{G}$  is the dominant NLSP decay ( $BR(\tilde{\chi}_1^0 \rightarrow Z\tilde{G}) \sim 97\%$ ) [95]. Since the large values of  $\tan\beta$  increase the  $BR(\tilde{\chi}_1^0 \rightarrow h\tilde{G})$  up to 40%, a  $\tan\beta$  value of 30 was chosen to investigate models with mixture of  $\tilde{\chi}_1^0 \rightarrow Z\tilde{G}$  and  $\tilde{\chi}_1^0 \rightarrow h\tilde{G}$  final states. Figure. 4.1 shows the branching fraction for  $\tilde{\chi}_1^0 \rightarrow h\tilde{G}$  and  $\tilde{\chi}_1^0 \rightarrow Z\tilde{G}$  as a function of  $\mu$ . In these models,  $h$  is the lightest CP-even SUSY Higgs boson, with  $m_h = 126 \text{ GeV}$  and SM-like branching fractions. The values of the parameters of the models considered here are summarized in Table 4.2.

Finally, the NLSP decay length is constrained to be  $c\tau_{\text{NLSP}} < 0.1 \text{ mm}$  for all input values of  $\mu > 120 \text{ GeV}$ . A summary of the relations between the lifetime of NLSP neutralino and gravitino parameters can be found in Ref. [95].

The three-body gluino decays  $\tilde{g} \rightarrow q\bar{q}\tilde{\chi}_1^0$  and  $\tilde{g} \rightarrow q\bar{q}\tilde{\chi}_2^0$  followed by the higgsino-like  $\tilde{\chi}_2^0$  decay  $\tilde{\chi}_2^0 \rightarrow \tilde{\chi}_1^0 f\bar{f}$  and  $\tilde{\chi}_1^0$  decay  $\tilde{\chi}_1^0 \rightarrow Z\tilde{G}$  are expected to lead into final states that are characterised by the presence of at least one  $Z$  boson, which decays to a pair of electrons or muons, and large  $E_{\text{T}}^{\text{miss}}$ , induced from the undetected gravitinos. Example decay modes are shown in the Feynman diagrams of Fig. 4.2.

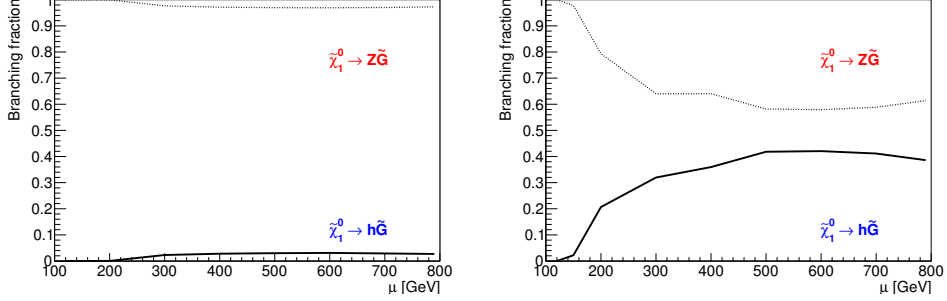


Figure 4.1: The branching fraction for  $\tilde{\chi}_1^0 \rightarrow h\tilde{G}$  and  $\tilde{\chi}_1^0 \rightarrow Z\tilde{G}$  processes as function of  $\mu$  for GGM grid models characterised by the following parameters:  $M_1 = 1 \text{ TeV}$ ,  $M_2 = 1 \text{ TeV}$ ,  $m(\tilde{g}) = 800 \text{ GeV}$ ,  $\tan\beta = 1.5$  (left),  $\tan\beta = 30$  (right).

Parameters	$M_1$	$M_2$	$\tan\beta$	$c\tau_{\text{NLSP}}$	$\mu$	$m(\tilde{g})$	All other sparticle masses
Values	1 TeV	1 TeV	1.5 or 30	$< 0.1 \text{ mm}$	vary	vary	$\sim 1.5 \text{ TeV}$

Table 4.2: Parameters of the GGM models used for the signal production. The constraint  $c\tau_{\text{NLSP}} < 0.1 \text{ mm}$  is fulfilled for all input values of  $\mu > 120 \text{ GeV}$ .

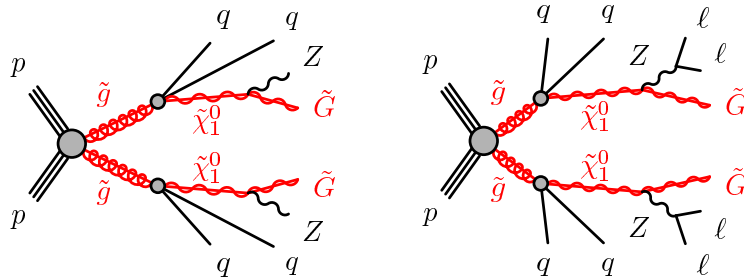


Figure 4.2: Example of Feynman diagrams for signal processes, also indicating leptonic  $Z$  decays.

The mechanisms for sparticle production in the signal points can be grouped into two categories: strong production ( $\tilde{g}\tilde{g}$ ,  $\tilde{q}\tilde{g}$  and  $\tilde{q}\tilde{q}$ ), and electroweak production ( $\tilde{\chi}_1^0\tilde{\chi}_2^0$ ,  $\tilde{\chi}_1^\pm\tilde{\chi}_1^\mp$ ,  $\tilde{\chi}_1^0\tilde{\chi}_1^\pm$ ,  $\tilde{\chi}_2^0\tilde{\chi}_1^\pm$ ). At high  $\mu$  values gluino production is enhanced as can be seen in Fig. 4.3, resulting in increasingly boosted  $Z$  bosons. This has an impact on the signal acceptance, with leptons becoming less isolated and their isolation cones beginning to overlap. The effect is more pronounced in the muon channel, which have absolute isolation requirements (described in Section 4.4). (The resulting asymmetry between the electron and muon channel signal acceptance is discussed in detail in Appendix F.2 of Ref. [97].)

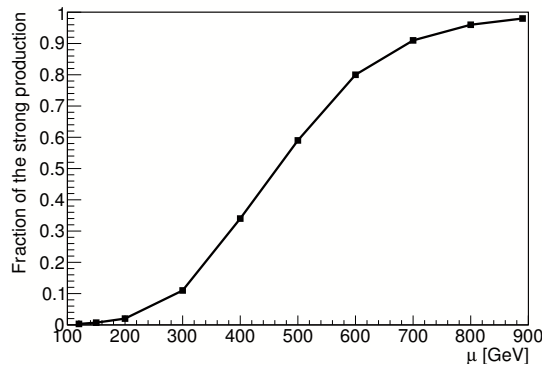


Figure 4.3: The fraction of the  $\tilde{g}\tilde{g}$  processes as function of  $\mu$  for GGM grid models characterised by the following parameters:  $M_1 = 1$  TeV,  $M_2 = 1$  TeV,  $m(\tilde{g}) = 900$  GeV,  $\tan\beta = 1.5$ .

A result from the search for at least four leptons [98] based on full 2012 data has constrained part of the parameter space in the GGM models investigated: For very large gluino masses, the electroweak production of lightest charginos and/or light neutralinos becomes dominant, and values of  $\mu$  between 200 GeV and about 230 GeV are excluded for any gluino mass at  $\tan\beta = 1.5$ . For larger value of  $\tan\beta = 30$ , the limits are weaker, see Ref. [98] for more details.

The SUSY mass spectra, gluino branching ratios, and the gluino decay width for the GGM scenarios are calculated using SUSPECT 2.41 [99] and SDECAY 1.3 [100]. As an example of the GGM signal samples generated, the full SUSY particle mass spectrum for the model with  $\tan\beta = 1.5$ ,  $m(\tilde{g}) = 700$  GeV and  $\mu = 200$  GeV is listed in Table 4.3.

The MC signal samples are generated using PYTHIA 6.423 [101] with the MRST2007 LO\* [102] parton distribution functions (PDF) set. Signals are normalised to cross sections calculated at next-to-leading order (NLO) in the strong coupling constant ( $\alpha_s$ ), including the resummation of soft gluon emission at next-to-leading-logarithmic accuracy (NLO + NLL) [103–107]. The nominal cross-section and the uncertainty are taken from an envelope of cross-section predictions using different PDF sets and factorisation and renormalisation scales, as described in Ref. [71]. More details about signal production

Names	Mass Eigenstates	m [ GeV]
squarks	$\tilde{u}_L \tilde{u}_R$	$\approx 1500$
	$\tilde{d}_L \tilde{d}_R$	
	$\tilde{s}_L \tilde{s}_R$	
	$\tilde{c}_L \tilde{c}_R$	
	$\tilde{t}_1 \tilde{t}_2$	
	$\tilde{b}_1 \tilde{b}_2$	
sleptons	$\tilde{e}_L \tilde{e}_R$	$\approx 1500$
	$\tilde{\mu}_L \tilde{\mu}_R$	
	$\tilde{\tau}_1 \tilde{\tau}_2$	
neutralinos	$\tilde{\chi}_1^0$	190.1
	$\tilde{\chi}_2^0$	200.3
	$\tilde{\chi}_3^0$	1000.0
	$\tilde{\chi}_4^0$	1010.2
charginos	$\tilde{\chi}_1^\pm$	192.6
	$\tilde{\chi}_2^\pm$	1007.8
Higgs bosons	$\tilde{h}^0$	126.0
	$\tilde{H}^0$	2004.0
	$\tilde{A}^0$	2000.0
	$\tilde{H}^\pm$	2002.1

Table 4.3: SUSY particle mass spectrum for the higgsino-like NLSP GGM model which is characterised by the following parameters:  $M_1 = 1$  TeV,  $M_2 = 1$  TeV,  $\tan\beta = 1.5$ ,  $c\tau_{\text{NLSP}} < 0.1$  mm,  $\mu = 200$  GeV,  $m(\tilde{g}) = 700$  GeV.

cross-sections will follow in Section 4.3.2.

As SUSY simulated events will only be selected if they contain at least one  $Z$  boson that decays to a pair of electrons or muons, a specific filter is used at generator level. The usage of this filter means that only events with at least one  $Z$  decaying to a pair of electrons, muons or taus will be simulated to save computing resources and time. This filter has an efficiency of  $18.8 \pm 0.5\%$  for models with  $\tan\beta = 1.5$ . The filter efficiency for the models with  $\tan\beta = 30$  is dependent on  $\mu$ , because  $BR(\tilde{\chi}_1^0 \rightarrow h\tilde{G})$  increases with  $\mu$  for these models. The filter efficiency for each generated GGM point can be seen in Figs. 4.5 and 4.7.

### 4.3.2 Signal cross-sections

Signal cross sections are calculated to next-to-leading order (NLO) in the strong coupling constant, adding the resummation of soft gluon emission at next-to-leading-logarithmic accuracy (NLO+NLL) [103–107]. To obtain the nominal cross-section and the uncertainty, the approach agreed by CMS and

ATLAS has been used. This approach consists in the following:

- Vary CTEQ Parton Distribution Functions (PDFs)
- Vary MSTW PDFs
- Vary renormalisation/factorisation scale with CTEQ central value PDF
- Vary renormalisation/factorisation scale with MSTW central value PDF
- Vary strong coupling using CTEQ PDFs,

where CTEQ and MSTW are two different PDF sets.

This results in asymmetric CTEQ and MSTW PDF uncertainties, asymmetric scale uncertainties for both CTEQ and MSTW central value PDF, and an asymmetric strong coupling uncertainty. From these variations the best value for the cross-section is obtained as follows:

$$\begin{aligned} \text{CTEQ\_ERROR}_{\text{up}} &= \sqrt{\text{CTEQ\_PDF}_{\text{up}}^2 + \text{CTEQ\_SCALE}_{\text{up}}^2 + (\alpha_s)_{\text{up}}^2} \\ \text{CTEQ\_ERROR}_{\text{down}} &= \sqrt{\text{CTEQ\_PDF}_{\text{down}}^2 + \text{CTEQ\_SCALE}_{\text{down}}^2 + (\alpha_s)_{\text{up}}^2} \\ \text{MSTW\_ERROR}_{\text{up}} &= \sqrt{\text{MSTW\_PDF}_{\text{up}}^2 + \text{MSTW\_SCALE}_{\text{up}}^2} \\ \text{MSTW\_ERROR}_{\text{down}} &= \sqrt{\text{MSTW\_PDF}_{\text{down}}^2 + \text{MSTW\_SCALE}_{\text{down}}^2} \end{aligned}$$

$$\begin{aligned} A &= \max(\text{CTEQ} + \text{CTEQ\_ERROR}_{\text{up}} * \text{CTEQ} , \\ &\quad \text{MSTW} + \text{MSTW\_ERROR}_{\text{up}} * \text{MSTW}) \\ B &= \min(\text{CTEQ} - \text{CTEQ\_ERROR}_{\text{down}} * \text{CTEQ} , \\ &\quad \text{MSTW} - \text{MSTW\_ERROR}_{\text{down}} * \text{MSTW}) \end{aligned}$$

Best value for the cross-section:

$$0.5(A + B)$$

And the upper and lower uncertainties on this cross-section:

$$(A - B)/(A + B)$$

This is a symmetric uncertainty.

The calculated cross-sections are applied per process to the signal samples at truth level. For example, every  $\tilde{g}\tilde{g}$  event is reweighted by the  $\tilde{g}\tilde{g}$  NLO (NLL+NLO) cross-section divided by the number of  $\tilde{g}\tilde{g}$  events in the specific sample. And the same is done for every production process. In the same fashion, the theoretical uncertainty is also applied per process.

The SUSY signal cross-sections and their uncertainties computed by the ATLAS SUSY group have two sources. For strong production the interpolation tool NLL-FAST [108] has been used to obtain NLL+NLO cross-sections. For other processes, and masses outside of the NLL-FAST range, PROSPINO 2.1 [109] is used.

The total cross-sections for each signal point are shown in Figs. 4.4 and 4.6, together with their uncertainties. The generation filter efficiencies and the effective cross-sections (generator filter efficiency times cross-section) can be seen in Figs. 4.5 and 4.7. All processes are considered for NLO and NNLL calculations.

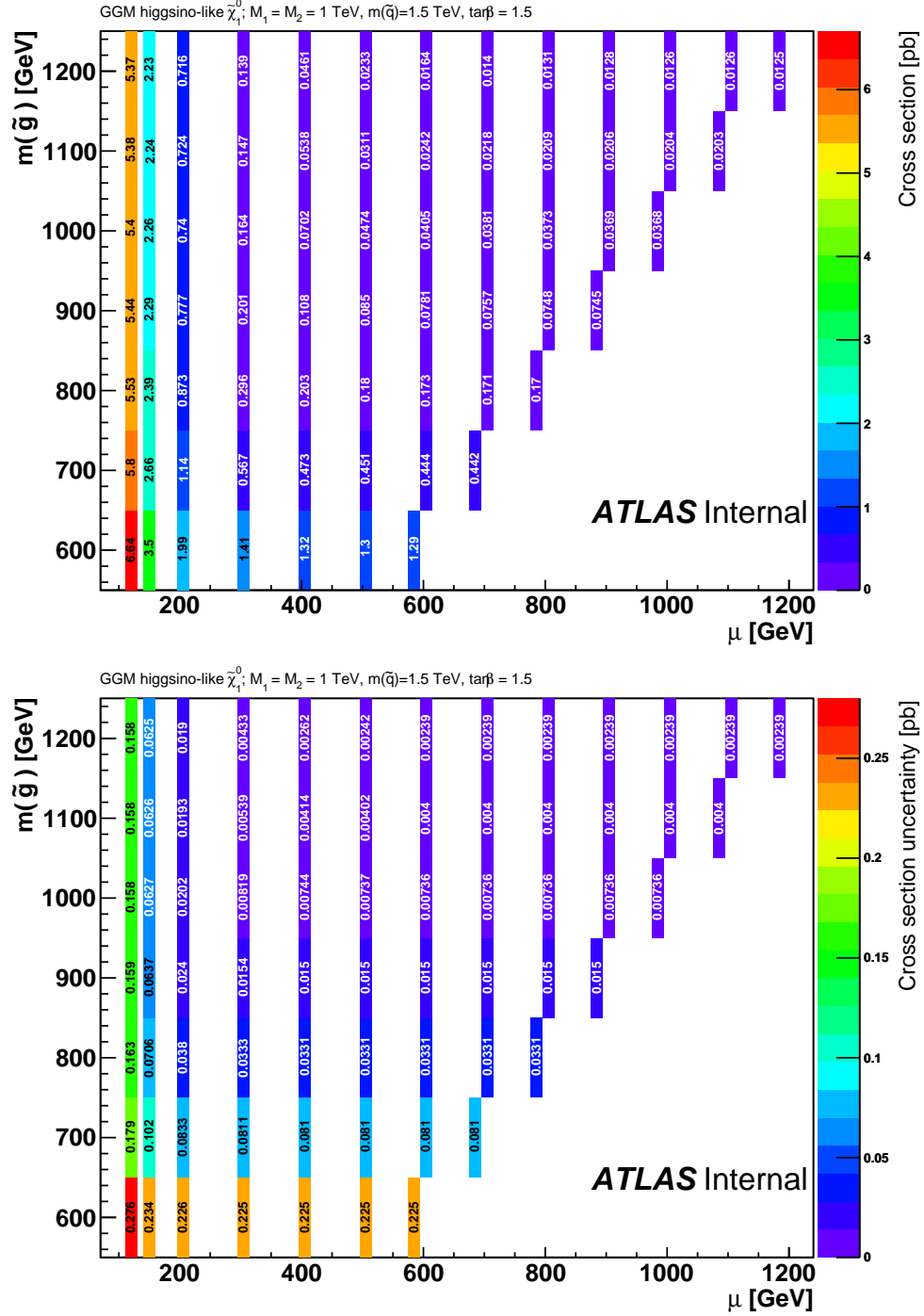


Figure 4.4: Total production cross-section (top) and uncertainty in the cross-section estimation (bottom) for the GGM model with  $\tan\beta = 1.5$ .

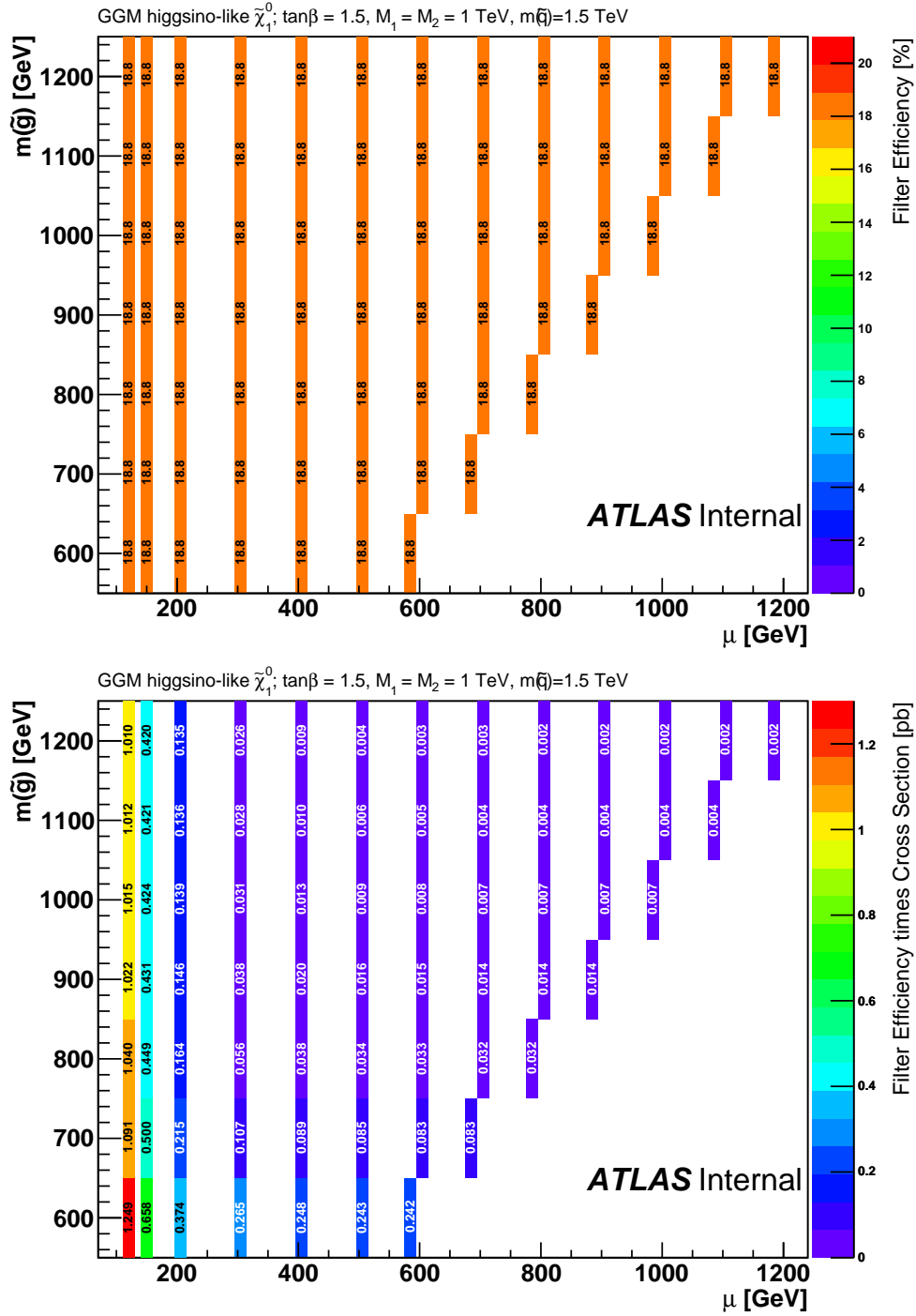


Figure 4.5: Generation efficiency (top) and effective cross-section (bottom) for the GGM model with  $\tan\beta = 1.5$ .



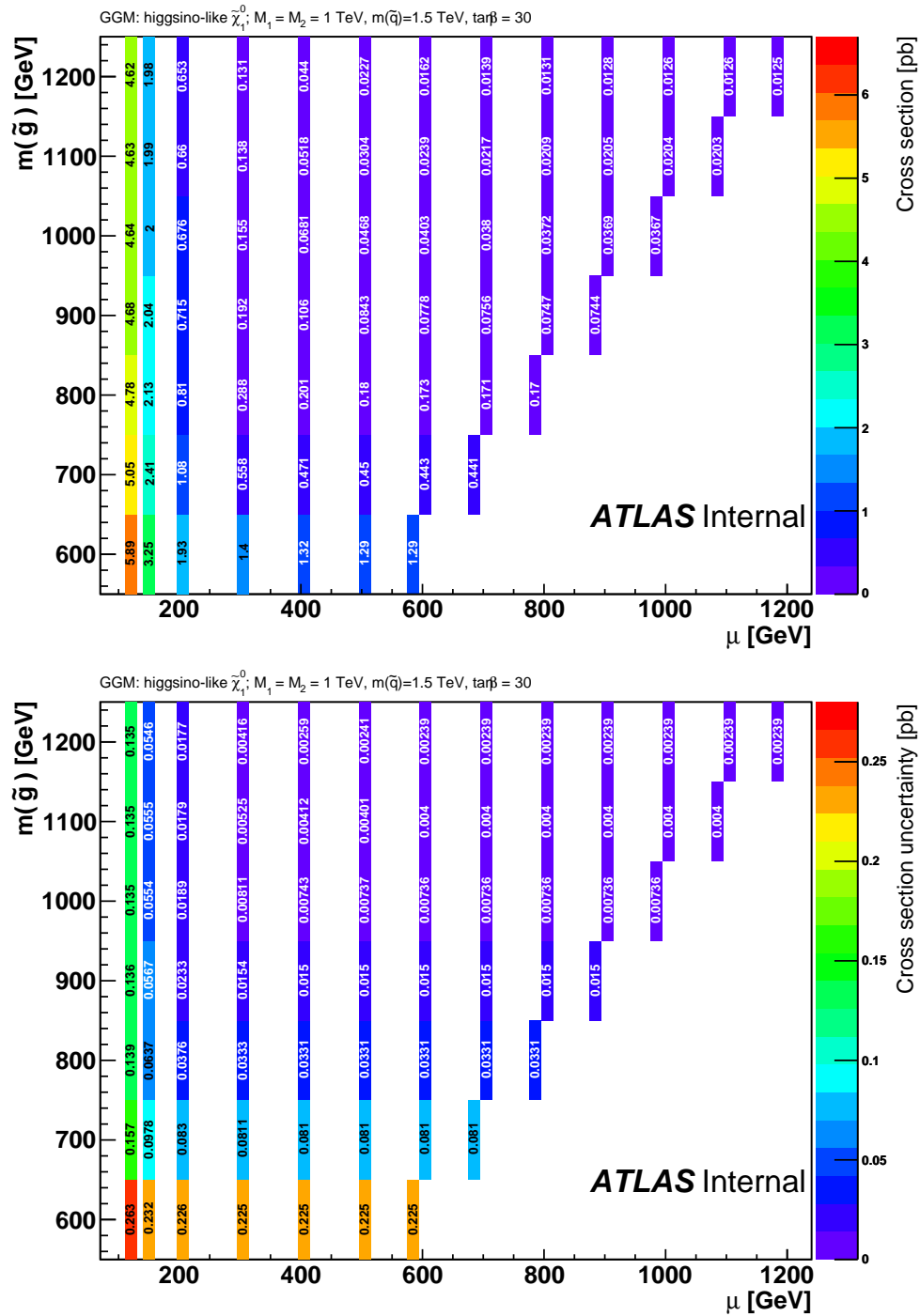


Figure 4.6: Total production cross-section (top) and uncertainty in the cross-section estimation (bottom) for the GGM model with  $\tan\beta = 30$ .

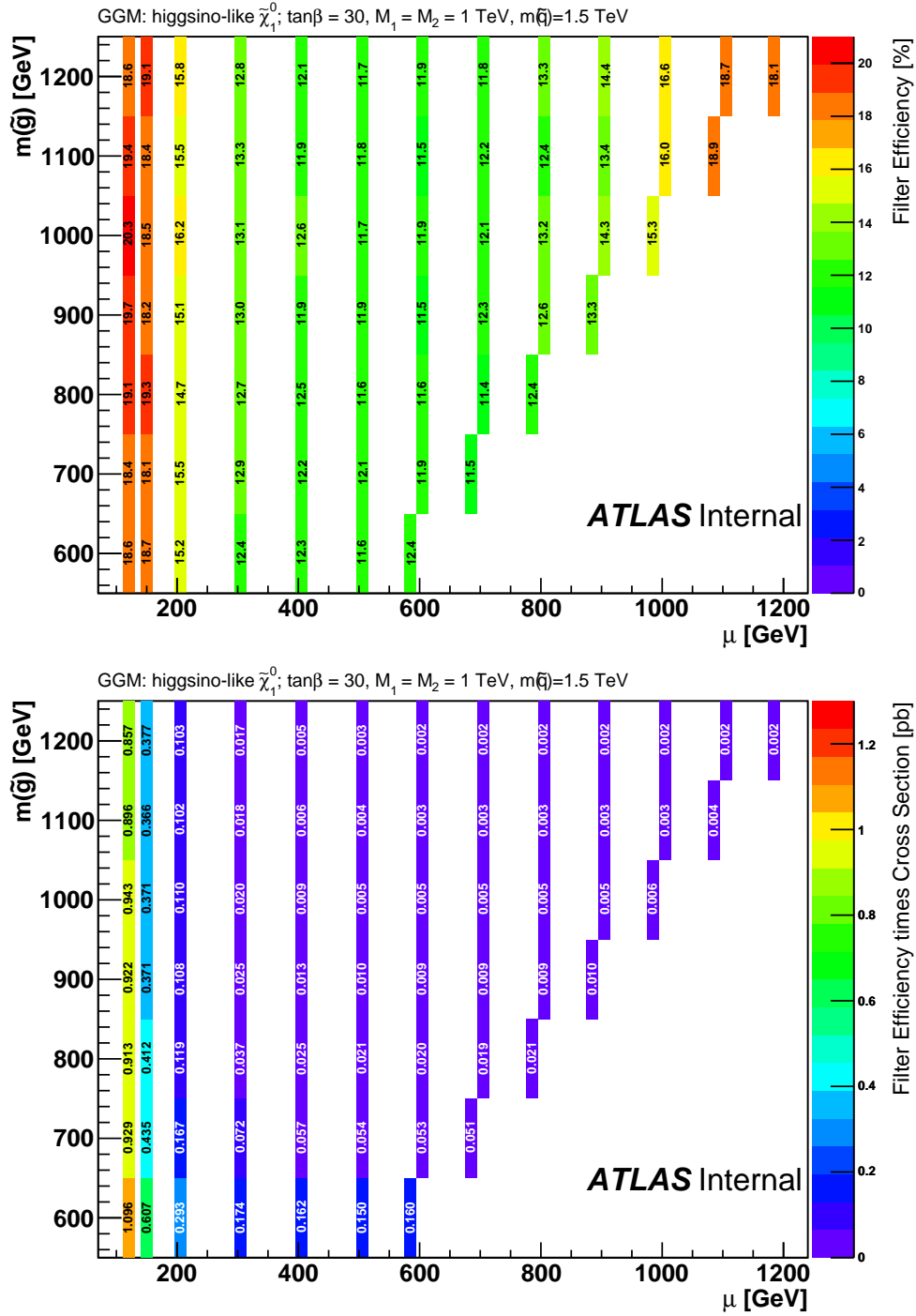


Figure 4.7: Generation efficiency (top) and effective cross-section (bottom) for the GGM model with  $\tan\beta = 30$ .

### 4.3.3 Branching fractions and masses

For the sake of completeness the values of some interesting model parameters will be shown in this section.

As mentioned before, the mechanisms for sparticle production in the signal points can be grouped into two categories: strong production ( $\tilde{g}\tilde{g}$ ,  $\tilde{q}\tilde{q}$  and  $\tilde{q}\tilde{q}$ ), and electroweak production ( $\tilde{\chi}_1^0\tilde{\chi}_2^0$ ,  $\tilde{\chi}_1^\pm\tilde{\chi}_1^\mp$ ,  $\tilde{\chi}_1^0\tilde{\chi}_1^\pm$ ,  $\tilde{\chi}_2^0\tilde{\chi}_1^\pm$ ). A study of the contribution from each production process in each point of the grid follows, showing the fraction of the total cross section due to the various main production processes, for each GGM point in Figures 4.8–4.11. All processes are considered for NLO and NNL calculations. The processes shown are: gluino pair production, squark pair production, squark-gluino and the sum of the main electroweak processes ( $\tilde{\chi}_1^0\tilde{\chi}_1^0$ ,  $\tilde{\chi}_2^0\tilde{\chi}_2^0$ ,  $\tilde{\chi}_1^+\tilde{\chi}_1^-$ ,  $\tilde{\chi}_1^0\tilde{\chi}_1^+$ ,  $\tilde{\chi}_1^0\tilde{\chi}_1^-$ ,  $\tilde{\chi}_2^0\tilde{\chi}_1^+$ ,  $\tilde{\chi}_2^0\tilde{\chi}_1^-$ ). Squarks do not include stops in this section.

In addition, the masses of  $\tilde{\chi}_1^0$ ,  $\tilde{\chi}_2^0$  and  $\tilde{\chi}_1^\pm$  are shown in Figures 4.12–4.13 as they are main input parameters for the models. Furthermore, the branching fractions for  $\tilde{\chi}_1^0 \rightarrow h\tilde{G}$  and  $\tilde{\chi}_1^0 \rightarrow Z\tilde{G}$  are shown in Figures 4.14–4.15.

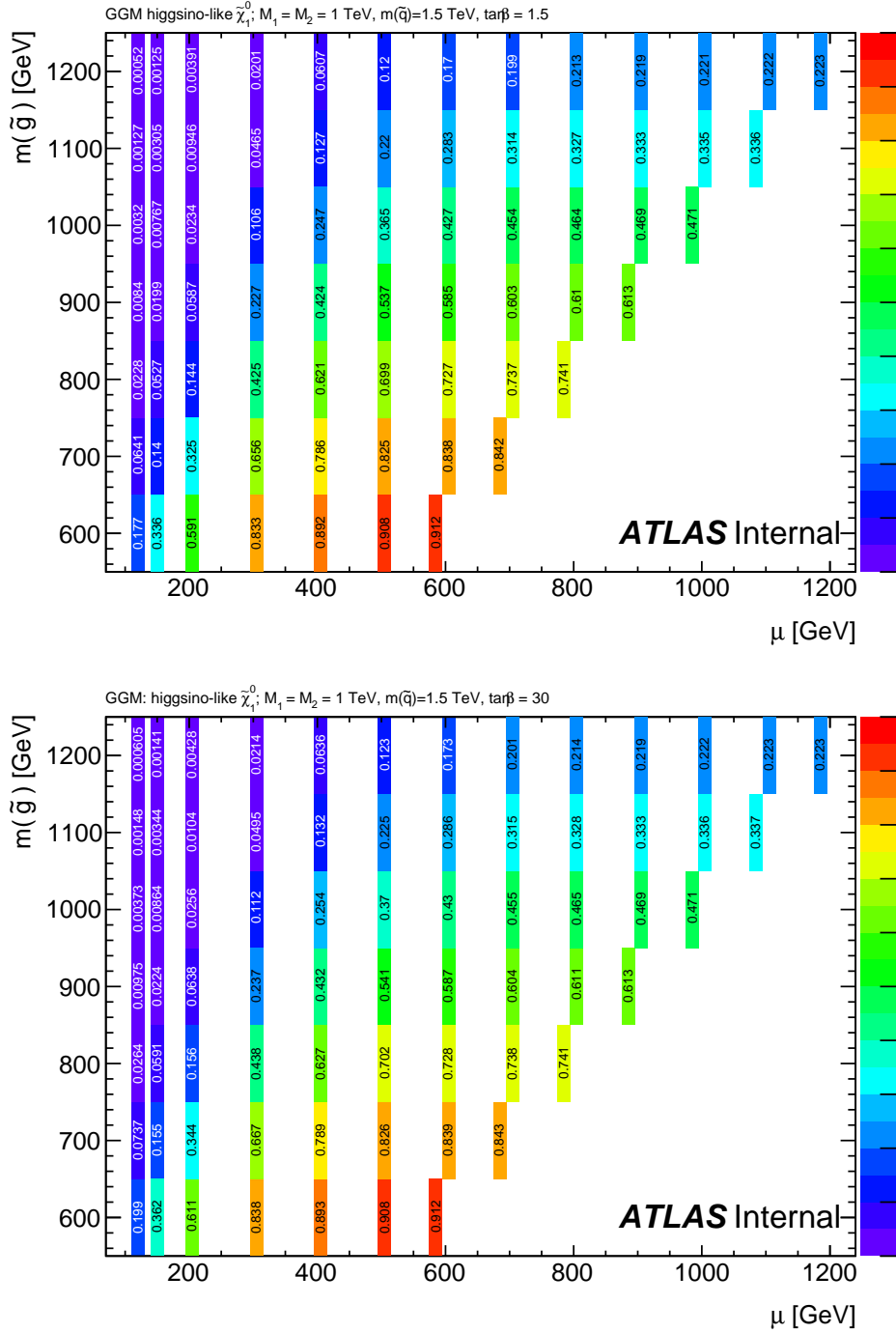


Figure 4.8: Fraction of total cross section due to gluino–gluino production for the GGM model with  $\tan\beta = 1.5$  (top) and GGM model with  $\tan\beta = 30$  (bottom).

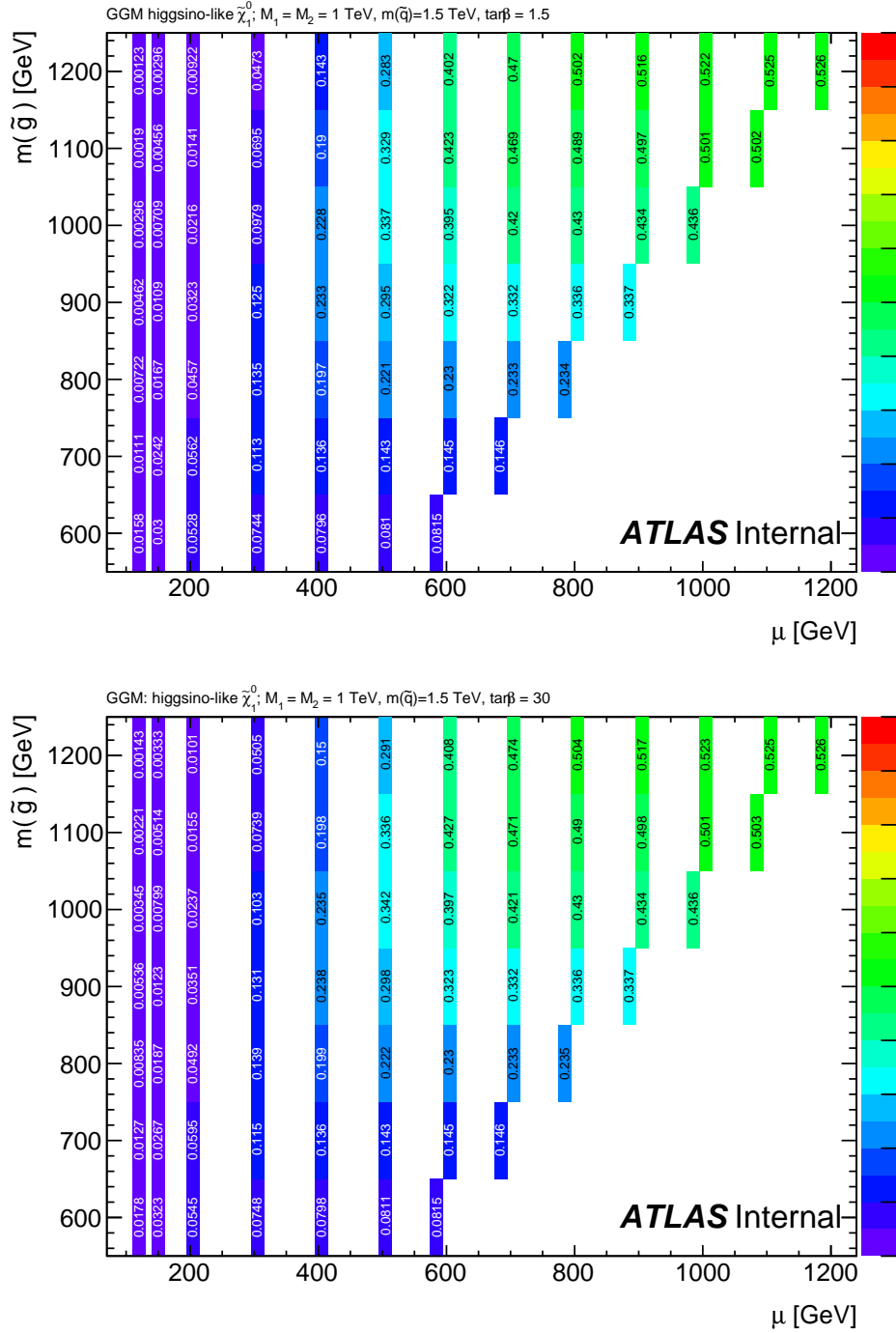


Figure 4.9: Fraction of total cross section due to squark–gluino production for the GGM model with  $\tan\beta = 1.5$  (top) and GGM model with  $\tan\beta = 30$  (bottom).

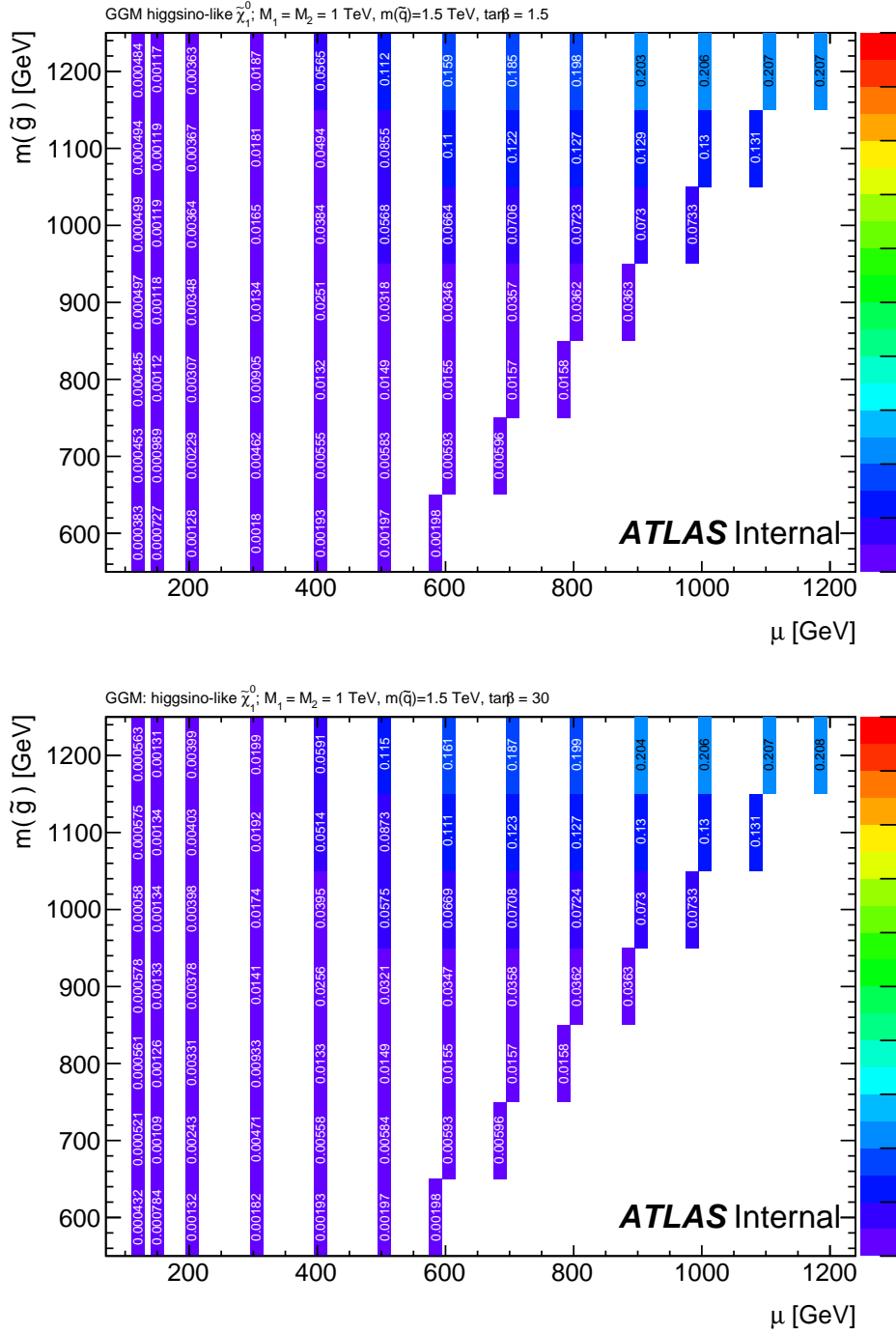


Figure 4.10: Fraction of total cross section due to squark pair production for the GGM model with  $\tan\beta = 1.5$  (top) and GGM model with  $\tan\beta = 30$  (bottom).

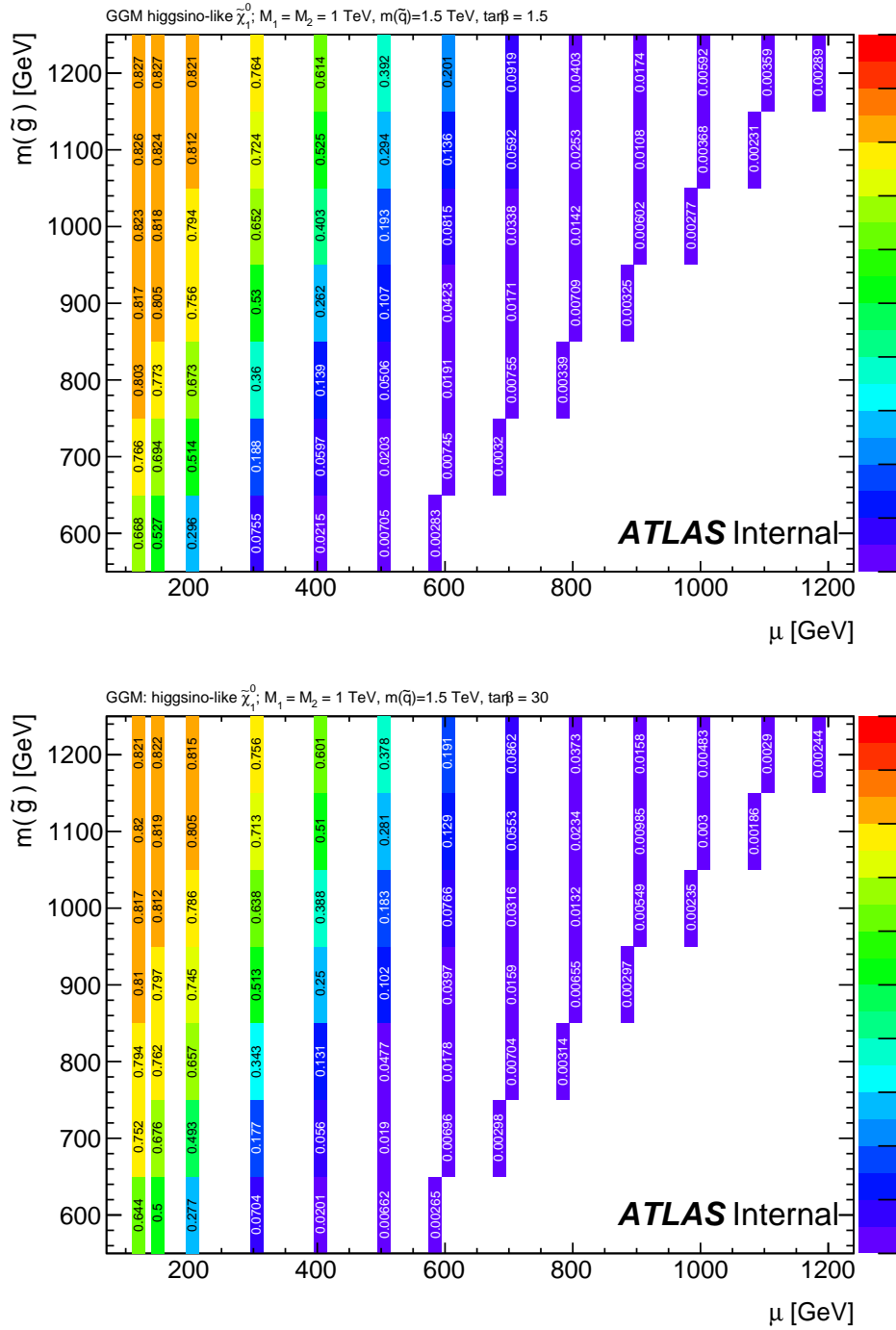


Figure 4.11: Fraction of total cross section due to EW production for the GGM model with  $\tan\beta = 1.5$  (top) and GGM model with  $\tan\beta = 30$  (bottom).

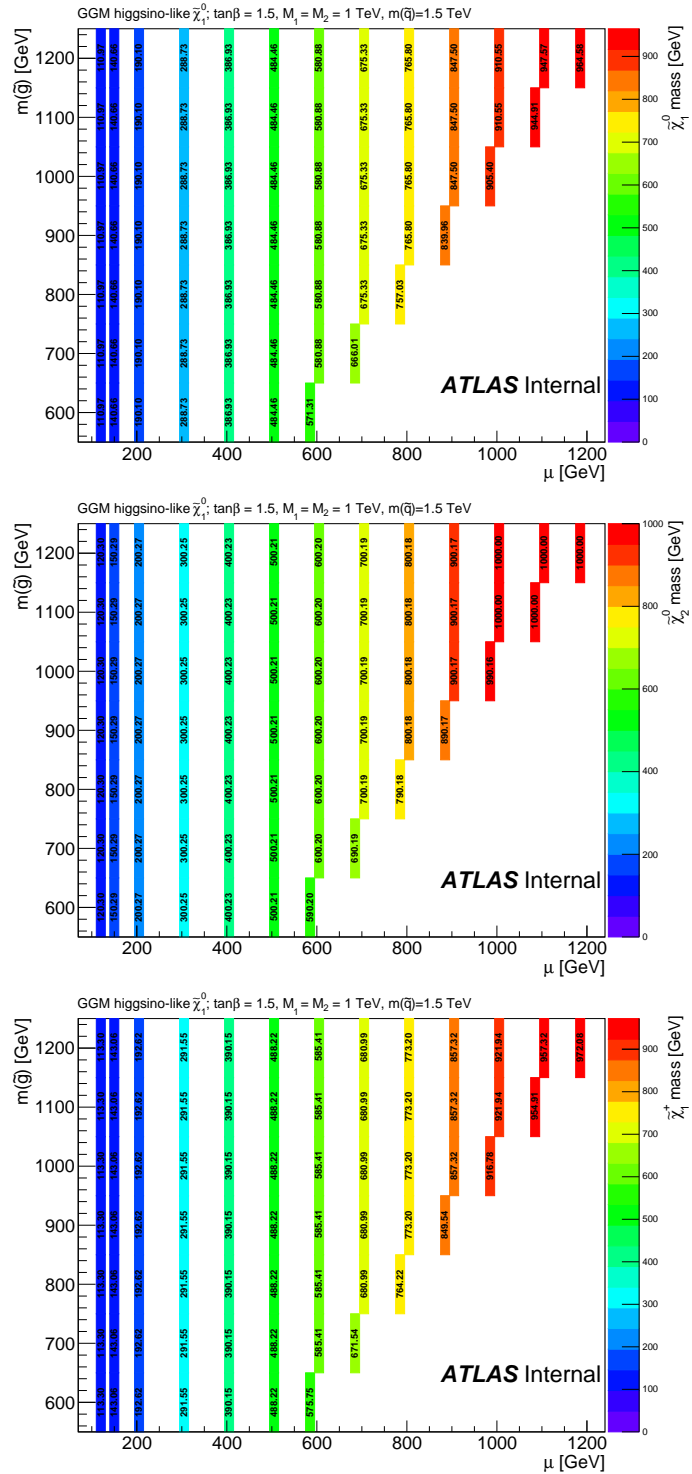


Figure 4.12: Masses of  $\tilde{\chi}_1^0$  (top),  $\tilde{\chi}_2^0$  (middle) and  $\tilde{\chi}_1^+$  (bottom) for the GGM model with  $\tan\beta = 1.5$ .



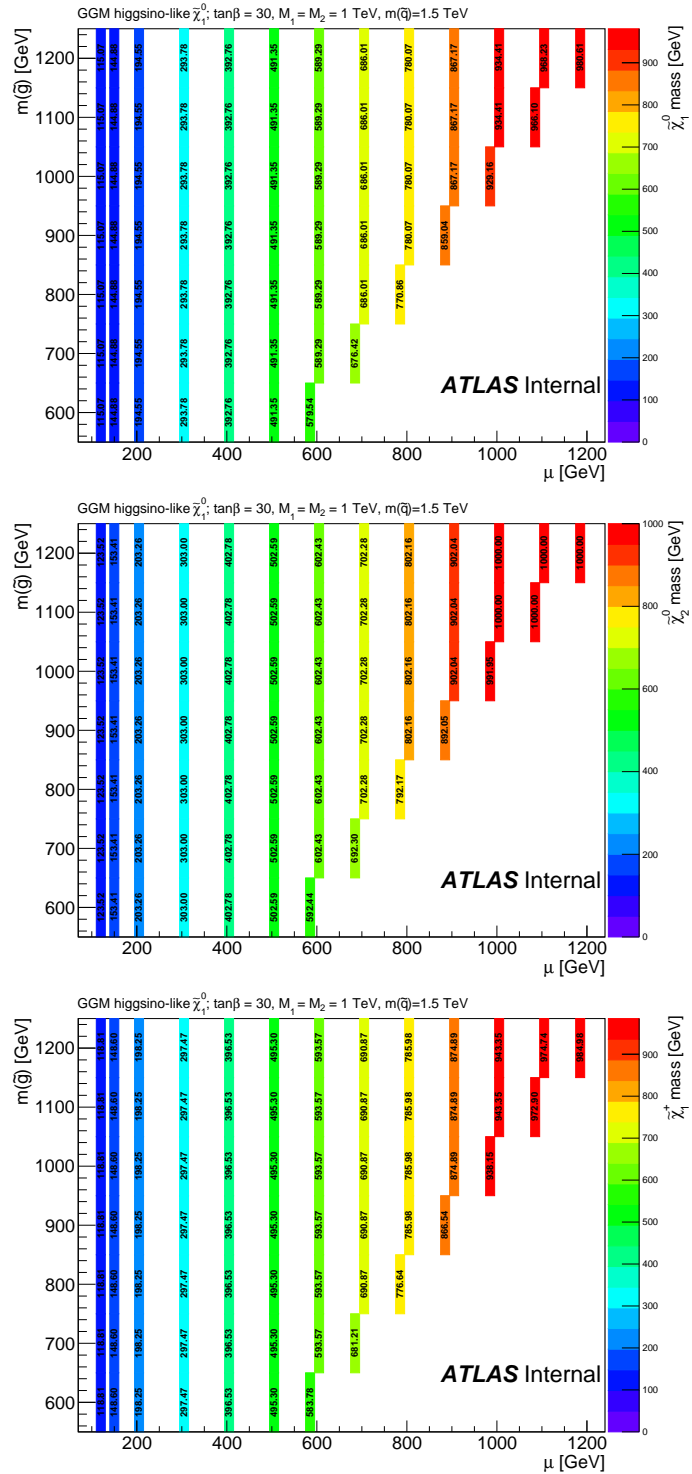


Figure 4.13: Masses of  $\tilde{\chi}_1^0$  (top),  $\tilde{\chi}_2^0$  (middle) and  $\tilde{\chi}_1^+$  (bottom) for the GGM model with  $\tan\beta = 30$ .

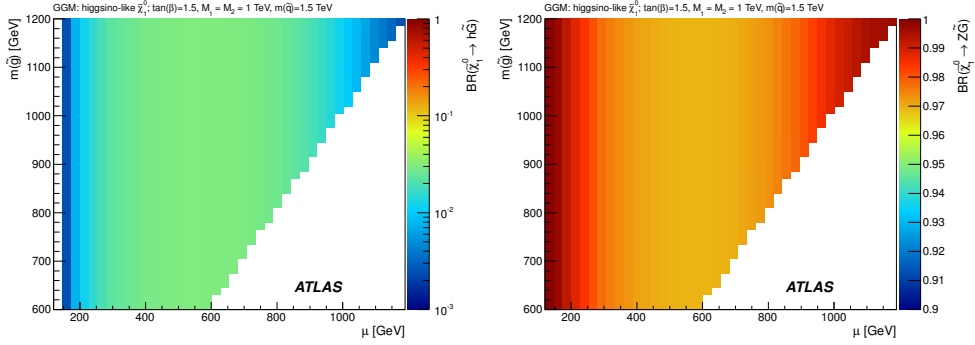


Figure 4.14: Branching ratio for  $\tilde{\chi}_1^0 \rightarrow h\tilde{G}$  (left) and  $\tilde{\chi}_1^0 \rightarrow Z\tilde{G}$  (right) for the GGM model with  $\tan\beta = 1.5$ .

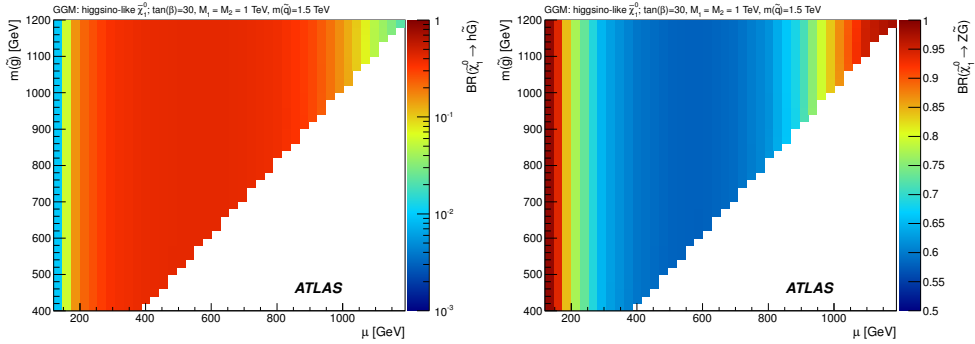


Figure 4.15: Branching ratio for  $\tilde{\chi}_1^0 \rightarrow h\tilde{G}$  (left) and  $\tilde{\chi}_1^0 \rightarrow Z\tilde{G}$  (right) for the GGM model with  $\tan\beta = 30$ .

## 4.4 Physics object identification and selection

In this section, all objects used in the analysis are introduced: electrons, muons and jets as well as the missing transverse energy. In the first three cases preselection cuts are applied, before performing the overlap removal between objects, which are then tightened in the event selection.

Before going into details it will be useful to list three general definitions that will be used in this section:

- The primary vertex is defined as the reconstructed vertex with the highest  $\sum p_T^2$ , where the summation includes all particle tracks with  $p_T > 400$  MeV associated with a given reconstructed vertex.
- The distance of closest approach between a particle object and the primary vertex in the longitudinal (transverse) plane is denoted by  $z_0$  ( $d_0$ ).
- The sum of the transverse momenta of all charged-particle tracks (associated with the primary vertex, excluding the track of the object under consideration) within a cone of radius  $\Delta R$  surrounding the object under consideration is defined as:  $p_T^{\text{cone}(\Delta R \times 100)}$ .

### 4.4.1 Electrons

Electron candidates are reconstructed using an algorithm that identifies energy deposits in the electromagnetic calorimeter and associates (*matches*) these clusters of energy with reconstructed tracks in the Inner Detector. The identification criteria for these electron candidates are implemented based on sequential cuts on calorimeter, tracking and combined track-cluster variables. These requirements are optimized in order to provide good separation between isolated electrons and background from mainly three sources: hadrons misidentified as electrons, non-isolated electrons (e.g. from semileptonic decays of heavy-flavour particles), and electrons from photon conversions. Three sets of reference selection criteria, labelled *loose*, *medium* and *tight*, are defined for use in ATLAS analyses. These criteria are designed in a hierarchical way so as to provide increasing background-rejection power at some cost to the identification efficiency. The increased background-rejection power is obtained both by adding discriminating variables at each step and by tightening the requirements on the original variables. The loose, medium and tight selections used for electron identification are detailed in Table 1 of Ref. [110].

Electrons used in this analysis are assigned either *baseline* or *signal* status. The definitions of these two status are summarised in Table 4.4 and described in detail in the next lines. Baseline electrons are required to have a transverse momentum  $p_T > 10$  GeV, satisfy the medium criteria and reside within  $|\eta| < 2.47$  and not in the range  $1.37 < |\eta| < 1.52$ . Signal electrons are further required to be consistent with the primary vertex and isolated with respect to the other objects in the event, with a  $p_T$ -dependent isolation requirement. Furthermore, if their  $p_T$  is  $p_T \geq 25$  GeV they must additionally satisfy the more stringent shower shape, track quality and matching requirements of the tight selection criteria. In addition to this, for signal electrons with  $p_T < 25$  GeV ( $\geq 25$  GeV), the sum of the transverse momenta of all charged-particle tracks with  $p_T > 400$  MeV associated with the primary vertex, excluding the electron track, within  $\Delta R = 0.3$  (0.2) surrounding the electron must be less than 16% (10%) of the electron  $p_T$ . That is,  $p_T^{\text{cone30}}/p_T < 0.16$  ( $p_T^{\text{cone20}}/p_T < 0.10$ ). Electrons with  $p_T < 25$  GeV must reside within a distance  $|z_0 \sin \theta| < 0.4$  mm of the primary vertex along the direction of the beamline. The significance of the transverse-plane distance of closest approach of the electron to the primary vertex must be  $|d_0/\sigma_{d_0}| < 5$ . For electrons with  $p_T \geq 25$  GeV,  $|z_0|$  is required to be  $< 2$  mm and  $d_0 < 1$  mm.

Electron definition	
Baseline Electron	
$p_T > 10 \text{ GeV},  \eta  < 2.47$ and $1.37 \leq  \eta  \leq 1.52$	
Medium quality (Ref. [110])	
Overlap Removal (see Sec. 4.4.4)	
Signal Electron	
Baseline Electron Selection +:	
$p_T < 25 \text{ GeV}$	$p_T \geq 25 \text{ GeV}$
Medium quality	Tight quality
Isolation: $p_T^{\text{cone30}}/p_T < 0.16$	Isolation: $p_T^{\text{cone20}}/p_T < 0.10$
$ z_0 \sin\theta  < 0.4 \text{ mm}$	$ z_0  < 2 \text{ mm}$
$ d_0/\sigma_{d_0}  < 5$	$ d_0  < 1 \text{ mm}$

Table 4.4: Summary of the electron selection criteria. The signal selection requirements are applied on top of the baseline requirements.

#### 4.4.2 Muons

Baseline muons are reconstructed from either ID tracks matched to a muon segment in the muon spectrometer or combined tracks formed both from the ID and muon spectrometer [111]. They are required to be of good quality, as described in Ref. [59], and to satisfy  $p_T > 10 \text{ GeV}$  and  $|\eta| < 2.4$ . Signal muons are further required to be isolated, with the scalar sum of the  $p_T$  of charged particle tracks associated with the primary vertex, excluding the muon track, within a cone of size  $\Delta R < 0.3$  surrounding the muon being less than 12% of the muon  $p_T$  for muons with  $p_T < 25 \text{ GeV}$ . For muons with  $p_T \geq 25 \text{ GeV}$ , the scalar sum of the  $p_T$  of the charged-particle tracks associated with the primary vertex excluding the muon track, within  $\Delta R < 0.2$  surrounding the muon must be less than 1.8 GeV. Signal muons with  $p_T < 25 \text{ GeV}$  must also have  $|z_0 \sin\theta| \leq 1 \text{ mm}$  and  $|d_0/\sigma_{d_0}| < 3$ . These definitions are outlined in Table 4.5.

Muon definition	
Baseline muon	
$p_T > 10 \text{ GeV},  \eta  < 2.4$ Loose quality (Ref. [59]) Overlap Removal (see Sec. 4.4.4)	
Signal muon	
Baseline Muon Selection +:	
$p_T < 25 \text{ GeV}$	$p_T \geq 25 \text{ GeV}$
Isolation: $p_T^{\text{cone30}}/p_T < 0.12$	Isolation: $p_T^{\text{cone20}} < 1.8 \text{ GeV}$
$ z_0 \sin\theta  < 1 \text{ mm}$	
$ d_0/\sigma_{d_0}  < 3$	

Table 4.5: Summary of the electron selection criteria. The signal selection requirements are applied on top of the baseline requirements.

### 4.4.3 Jets

Jets are reconstructed from topological clusters<sup>1</sup> in the calorimeter using the anti- $k_t$  algorithm [60] with a distance parameter of 0.4. Each cluster is categorised as being electromagnetic or hadronic in origin according to its shape [112] so as to account for the differing calorimeter response for electrons/photons and hadrons. A cluster-level correction is then applied to electromagnetic and hadronic energy deposits using correction factors derived from both MC simulation and data. Jets are corrected for expected pileup contributions [113] and further calibrated to account for the calorimeter response with respect to the true jet energy [62, 114]. A small residual correction is applied to the jets in data to account for differences between response in data and MC simulation. Baseline jets are selected with  $p_T > 20 \text{ GeV}$ . Events in which these jets do not pass specific jet quality requirements are rejected so as to remove events affected by detector noise and non-collision backgrounds [115]. Signal jets are required to satisfy  $p_T > 35 \text{ GeV}$  and  $|\eta| < 2.5$ . To reduce the impact of jets from pileup to a negligible level, jets with  $p_T < 50 \text{ GeV}$  within  $|\eta| < 2.4$  are further required to have a jet vertex fraction  $\text{JVF} > 0.25$ . Here the JVF is the  $p_T$ -weighted fraction of tracks matched to the jet that are associated with the primary vertex [116], with jets without any associated tracks being assigned  $\text{JVF} = -1$ . A schematic view of these requirements can be found in Table 4.6.

<sup>1</sup>Topological clusters, or topoclusters, are groups of calorimeter cells clustered into three-dimensional energy deposits exploiting the longitudinal and transverse calorimeter segmentation.

Jet definition
Baseline jet
$p_T > 20$ GeV Very loose quality (Ref. [115]) Overlap Removal (see Sec. 4.4.4)
Signal jet
Baseline Jet Selection +: $p_T > 35$ GeV , $ \eta  < 2.5$ if jet has ( $p_T < 50$ GeV and $ \eta  < 2.4$ ) $\rightarrow  \text{JVF}  > 0.25$

Table 4.6: Summary of the jet selection criteria. The signal selection requirements are applied on top of the baseline requirements.

#### 4.4.4 Overlap removal

The overlap removal takes care of two aspects of the object selection that are similar in their implementation but performed for different reasons. One of the reasons to apply the overlap removal is to ensure that each physics object is counted only once. It can happen that a single, broad object is reconstructed as two objects by the reconstruction algorithms; that would lead to a double counting. In this case only one of the two objects is an actual object while the other is an artefact of the reconstruction mechanism. This is the case of an electron that is erroneously reconstructed twice. In order to reject the second electron, if any two baseline electrons reside within  $\Delta R(e, e) = 0.05$  of one another, the electron with lower  $E_T$  is discarded. Following this, it can also happen that an electron and a jet are both reconstructed as jets by the jet algorithms, therefore any baseline jets within  $\Delta R(e, \text{jet}) = 0.2$  of a baseline electron are removed.

The other reason to apply the overlap removal deals with the spatial separation of two objects. Leptons can arise from the semileptonic decay of  $b$  or  $c$  quarks inside a jet, so after the requirements of the previous paragraph, any baseline electron or muon residing within  $\Delta R(\text{lep}, \text{jet}) = 0.4$  of a remaining baseline jet is discarded. Finally, muons and electrons are also seen to overlap in the detector when an muon emits bremsstrahlung and the resulting photon is misidentified as an electron. Any baseline electron within  $\Delta R(e, \mu) = 0.01$  of any remaining baseline muon is removed from the event. This is all summarized in Table 4.7.

Overlap Removal	
If	Remove
$\Delta R(e, e) \leq 0.05$	electron with lower $E_T$
$\Delta R(e, \text{jet}) \leq 0.2$	jet
$\Delta R(\text{lep}, \text{jet}) \leq 0.04$	lepton
$\Delta R(e, \mu) \leq 0.01$	electron

Table 4.7: Summary of the overlap removal (OR) requirements.

#### 4.4.5 Missing transverse energy

The  $E_T^{\text{miss}}$  is defined as the magnitude of the vector sum of the transverse momenta of all photons, electrons, muons, baseline jets and an additional “soft term” [117]. The soft term includes clusters of energy in the calorimeter not associated with any calibrated object, which are corrected for material effects and the non-compensating nature of the calorimeter. Reconstructed photons used in the  $E_T^{\text{miss}}$  calculation are required to satisfy the “tight” requirements of Ref. [118].

### 4.5 Event selection.

After applying data-quality requirements (related to the beam and detector conditions) and event cleaning cuts following the ATLAS SUSY Working Group prescriptions, a general pre-selection is applied to the events. Some cuts in this pre-selection are common to various SUSY analyses (see Ref. [119]), whilst the last cuts on the pre-selection were chosen taking into account the specific details of this analysis’ target models.

Following this general pre-selection a Signal Region (SR) optimization is performed in order to obtain the best combination of cuts for a high sensitivity to GGM signal models. Some of these cuts are used for all the regions in the analysis, whereas some others are signal region specific.

The particular details of the pre-selection and the different regions used in the analysis will be discussed in this section. Moreover, a schematic view of all these cuts can be seen in Tables 4.8 and 4.9.

#### 4.5.1 Event pre-selection

Events selected for this analysis must have at least five tracks with  $p_T > 400$  MeV associated with the primary vertex. Any event containing a baseline muon with  $|z_0 \sin \theta| > 0.2$  mm and  $|d_0| > 1$  mm is rejected in order to remove cosmic-ray events. To reject events with fake  $E_T^{\text{miss}}$ , those containing poorly measured muon candidates, characterised by large uncertainties on the measured momentum, are also removed.

<b>Event preselection</b>	
<b>Common to other analyses (Ref. [119])</b>	
Data-quality and event cleaning cuts	following ATLAS general prescriptions
$e$ - $e$ OR	if $\Delta R(e_1, e_2) < 0.05 \rightarrow$ remove electron with lower $E_{\text{T}}$
$e$ - $j$ OR	if $\Delta R(e, j) < 0.2 \rightarrow$ remove jet
$j$ - $e$ OR	if $\Delta R(j, e) < 0.4 \rightarrow$ remove electron
$j$ - $\mu$ OR	if $\Delta R(j, \mu) < 0.4 \rightarrow$ remove muon
$e$ - $\mu$ OR	if $\Delta R(e, \mu) < 0.01 \rightarrow$ remove electron
Primary vertex	$> 4$ tracks with $p_{\text{T}} > 400$ MeV
Cosmic muon veto	remove events containing a $\mu$ with $ z_0 \sin \theta  > 0.2$ mm and $ d_0  > 1$ mm
Bad muon veto	remove events containing a muon with $\sigma(q/p)/ q/p  > 0.2$
<b>Analysis Specific Event preselection</b>	
$\geq 2$ signal leptons	if $> 2 \rightarrow$ the 2 with largest $p_{\text{T}}$ are selected
Trigger matching	as specified in the text
Opposite charge	of the 2 leading leptons
Leading lepton $p_{\text{T}}$	$> 25$ GeV
Subleading lepton $p_{\text{T}}$	$> 10$ or $14$ GeV
Drell-Yan veto	remove events with $m_{\ell\ell} < 15$ GeV
$\geq 2$ signal jets	with $p_{\text{T}} > 35$ GeV and $ \eta  < 2.5$

Table 4.8: Pre-selection cuts common to all the regions used in this analysis. The upper part of the table shows cuts which are common to several SUSY analyses, whereas the bottom part shows the cuts which are designed for this analysis only.



GGM scenarios are the target of this search, where the  $\tilde{G}$  from  $\tilde{\chi}_1^0 \rightarrow (Z/h) + \tilde{G}$  decays is expected to result in  $E_T^{\text{miss}}$ . Due to the low branching ratio of  $Z$  to leptons, the four lepton final state has a low acceptance times branching ratio. Therefore, the final state that includes at least one  $Z$  boson which decays to a pair of electrons or muons is considered here. This is why events are required to contain at least two signal leptons (electrons or muons). If more than two signal leptons are present, the two with the largest values of  $p_T$  are selected. These leptons must pass one of the leptonic triggers [97], with the two leading leptons being matched, within  $\Delta R < 0.15$ , to the online trigger objects that triggered the event in the case of the dilepton triggers. For events selected by a single-lepton trigger, one of the two leading leptons must be matched to the online trigger object in the same way. The leading lepton in the event must have  $p_T > 25$  GeV and the sub-leading lepton is required to have  $p_T > 10$ – $14$  GeV, depending on the  $p_T$  threshold of the trigger selecting the event. The two leading leptons must be oppositely charged. If the invariant mass of the two leading leptons in the event is less than 15 GeV the event is vetoed to suppress low-mass particle decays and Drell–Yan production. Since  $b$ -jets are often, but not always, expected in GGM decay chains, no requirement is placed on  $b$ -tagged jet multiplicity.

### 4.5.2 Analysis regions

Three types of regions are used in the analysis. Control regions are used to constrain the SM backgrounds. These backgrounds, estimated in the CRs, are first extrapolated to the validation regions as a cross check and then to the signal regions, where an excess over the expected background is searched for.

#### SR

The SR corresponds to a reoptimized version of the SRs already developed in the previous analysis round [94]. On top of the cuts described in Sec. 4.5.1, the two leptons must be in the  $Z$  boson mass window, which in this search is  $81 < m_{\ell\ell} < 101$  GeV, and be same-flavour (SF) lepton pairs. Data-to-MC comparison plots of all relevant distributions after the preselection,  $Z$ -mass window and SF lepton cuts are shown in Figures 4.16 to 4.23.

#### Optimization

After requiring the selection criteria specified previously, in order to obtain a high sensitivity to GGM signals, a global scan in several discriminating variables is performed to identify the best cut scenario for selected points in a given signal grid.

The measure for optimization is given by the significance  $Z_n$ , defined as:

$$Z_n = \sqrt{2} * \text{TMath} :: \text{ErfInverse}(1 - 2p * 2),$$

$$p = \text{RooStats} :: \text{NumberCountingUtils} :: \text{BinomialExpP}(s, b, \alpha)$$

where  $s$  and  $b$  are the number of expected signal and background events and  $\alpha$  is the fractional background uncertainty, taken to be 35% during this study. The variables involved in the global scan over signal points are the following:

- jet multiplicity
- transverse momentum of leading jet
- transverse momentum of subleading jet
- $E_{\text{T}}^{\text{miss}}$
- $H_{\text{T}}$ , i.e. the scalar sum of the  $p_{\text{T}}$  of all signal jets and the two leading leptons:  $H_{\text{T}} \equiv \sum_i p_{\text{T}}^{\text{jet},i} + \sum_{i=1,2} p_{\text{T}}^{\text{lepton},i}$

Moreover, for each combination of cuts the statistical error related to signal and background is required to be less than 30 percent.

The values for the contemplated variables, found in the optimization procedure, are described next. All events are required to contain at least two signal jets of  $p_{\text{T}} > 35$  GeV. SR events must have  $E_{\text{T}}^{\text{miss}} > 225$  GeV and  $H_{\text{T}} > 600$  GeV.

A further requirement on the azimuthal opening angle between each of the leading two jets and the  $E_{\text{T}}^{\text{miss}}$  ( $\Delta\phi(\text{jet}_{1,2}, E_{\text{T}}^{\text{miss}}) > 0.4$ ) is introduced to reject events with jet mismeasurements contributing to large fake  $E_{\text{T}}^{\text{miss}}$ .

Signal Region	
Preselection	Table 4.8
$Z$ mass window	$81 < m_{\ell\ell} < 101$ GeV
SF lepton pairs	$ee$ or $\mu\mu$
$E_{\text{T}}^{\text{miss}}$	$> 225$ GeV
$H_{\text{T}}$	$> 600$ GeV
$\Delta\phi(\text{jet}_{1,2}, E_{\text{T}}^{\text{miss}})$	$> 0.4$

Table 4.9: Cuts defining the signal region.

### CRs

The CRs are defined in order to estimate the contribution of various SM backgrounds to the SR. These regions are constructed with selection criteria similar to those of the SR, differing either

in  $m_{\ell\ell}$  or  $E_T^{\text{miss}}$  ranges, or in lepton flavour requirements (the different-flavour (DF) channel is exploited to estimate certain backgrounds, such as that due to  $t\bar{t}$  production). A comprehensive discussion of the various methods used to perform these estimates follows in Sect. 4.6.

As mentioned before, additional VRs are defined at lower  $E_T^{\text{miss}}$  and  $H_T$  to cross-check the SM background estimation methods.

A schematic view of the selection conditions common to all the regions in this analysis can be seen in Table 4.8, including the pre-selection discussed in the previous section; whilst the cuts defining the SR are shown in Table 4.9. In addition, the main features of each of the regions used in the analysis are summarised in Table 4.1.

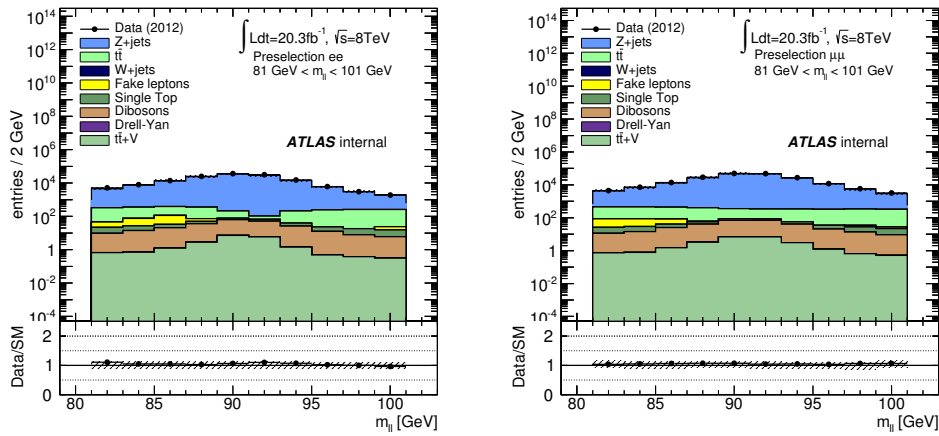


Figure 4.16: Invariant mass distribution for events containing opposite sign electrons (left) and muons (right) after preselection and  $81 \text{ GeV} < m_{\ell\ell} < 101 \text{ GeV}$  cut. The plot labelled “Data/SM” shows the ratio of the distribution from data to that of the total SM background. Only experimental uncertainties are shown.

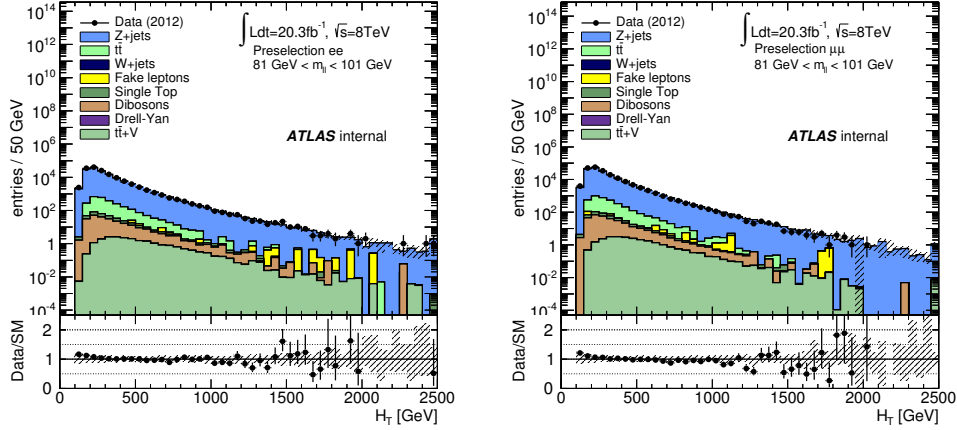


Figure 4.17:  $H_T$  distribution for events containing opposite sign electrons (left) and muons (right) after preselection and  $81 \text{ GeV} < m_{\ell\ell} < 101 \text{ GeV}$  cut. The plot labelled “Data/SM” shows the ratio of the distribution from data to that of the total SM background. Only experimental uncertainties are shown.

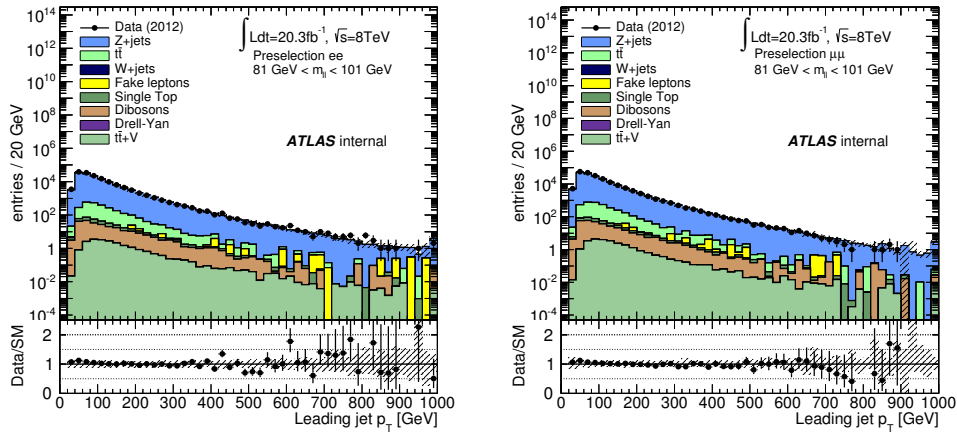


Figure 4.18: Leading jet  $p_T$  distribution for events containing opposite sign electrons (left) and muons (right) after preselection and  $81 \text{ GeV} < m_{\ell\ell} < 101 \text{ GeV}$  cut. The plot labelled “Data/SM” shows the ratio of the distribution from data to that of the total SM background. Only experimental uncertainties are shown.

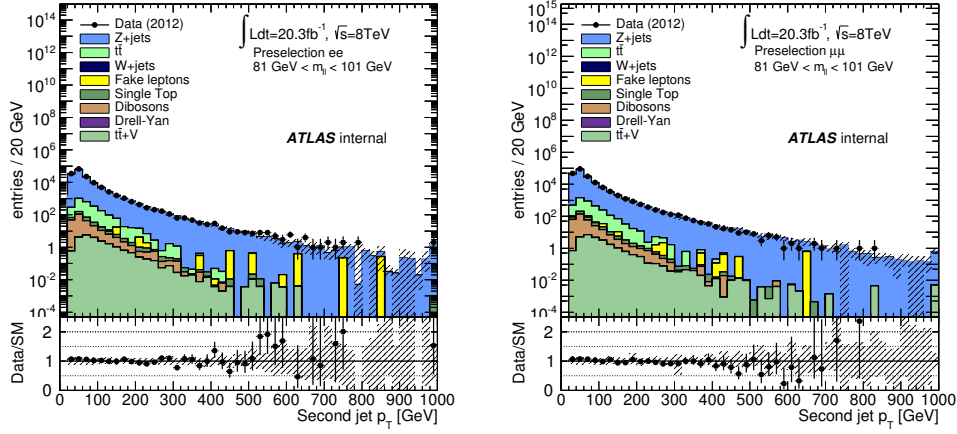


Figure 4.19: Subleading jet  $p_T$  distribution for events containing opposite sign electrons (left) and muons (right) after preselection and  $81 \text{ GeV} < m_{\ell\ell} < 101 \text{ GeV}$  cut. The plot labelled “Data/SM” shows the ratio of the distribution from data to that of the total SM background. Only experimental uncertainties are shown.

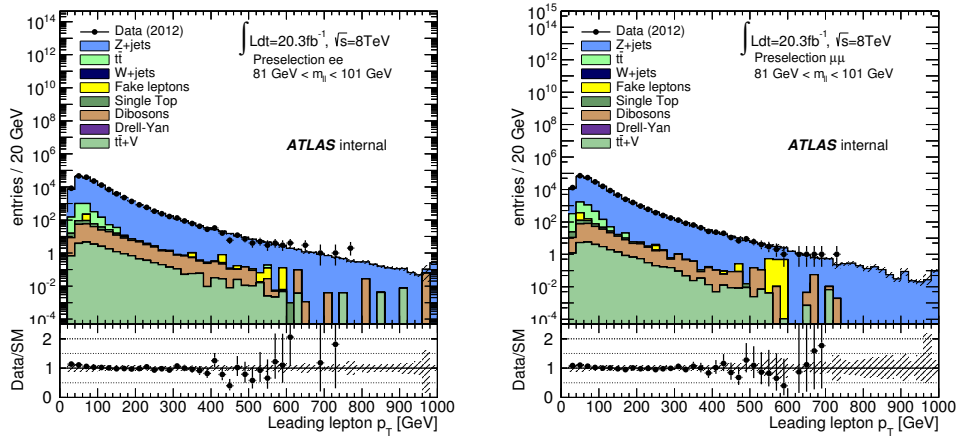


Figure 4.20: Leading lepton  $p_T$  distribution for events containing opposite sign electrons (left) and muons (right) after preselection and  $81 \text{ GeV} < m_{\ell\ell} < 101 \text{ GeV}$  cut. The plot labelled “Data/SM” shows the ratio of the distribution from data to that of the total SM background. Only experimental uncertainties are shown.

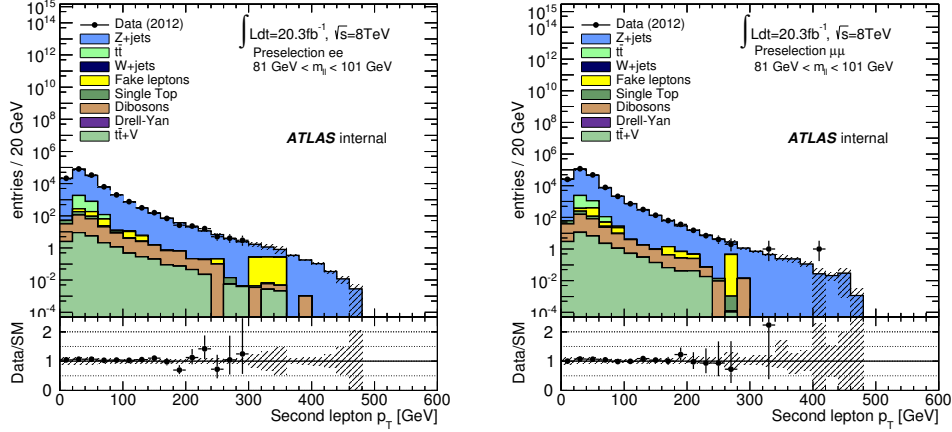


Figure 4.21: Subleading lepton  $p_T$  distribution for events containing opposite sign electrons (left) and muons (right) after preselection and  $81 \text{ GeV} < m_{\ell\ell} < 101 \text{ GeV}$  cut. The plot labelled “Data/SM” shows the ratio of the distribution from data to that of the total SM background. Only experimental uncertainties are shown.

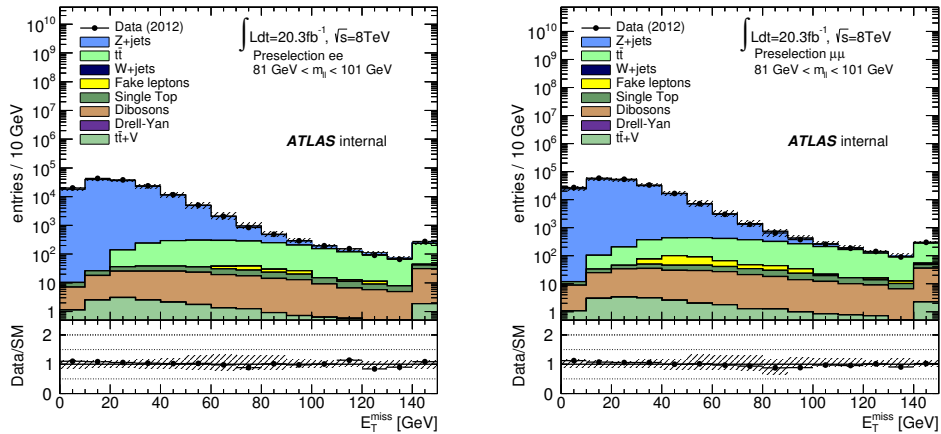


Figure 4.22:  $E_T^{\text{miss}}$  distribution for events containing opposite sign electrons (left) and muons (right) after preselection and  $81 \text{ GeV} < m_{\ell\ell} < 101 \text{ GeV}$  cut. The plot labelled “Data/SM” shows the ratio of the distribution from data to that of the total SM background. Only experimental uncertainties are shown.

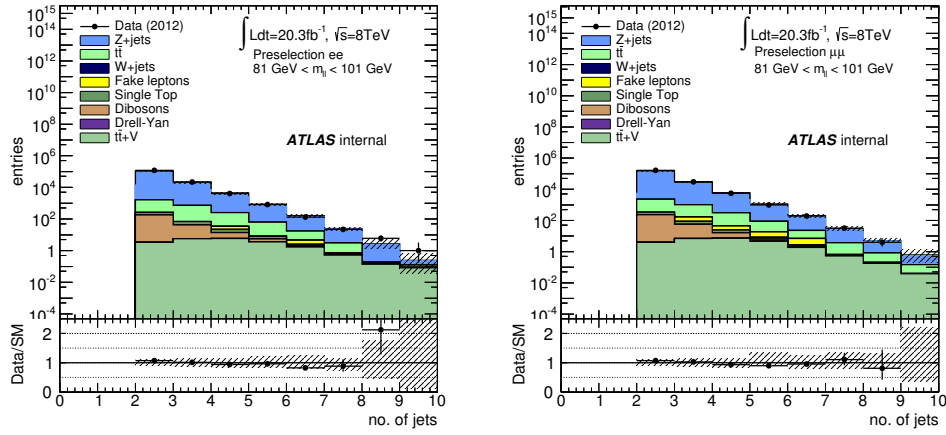


Figure 4.23: Jet multiplicity distribution for events containing opposite sign electrons (left) and muons (right) after preselection and  $81\text{ GeV} < m_{\ell\bar{\ell}} < 101\text{ GeV}$  cut. The plot labelled “Data/SM” shows the ratio of the distribution from data to that of the total SM background. Only experimental uncertainties are shown.

## 4.6 Background estimation

This section discusses the details of the background estimation and the methods used to assess them. Table 4.10 contains a summary of the main backgrounds with the methods used to estimate each of them.

Background	Description	Nominal Estimation Method
$Z(ee, \mu\mu) + \text{jets}$	Real $Z$ , fake $E_{\text{T}}^{\text{miss}}$	Jet smearing
$Z \rightarrow \tau\tau$ di-leptonic	Real $Z$ , real $E_{\text{T}}^{\text{miss}}$	Flavour symmetry
$t\bar{t}$ di-leptonic	Two leptons, no $Z$ , real $E_{\text{T}}^{\text{miss}}$	Flavour symmetry
$WW$ di-leptonic	Two leptons, no $Z$ , real $E_{\text{T}}^{\text{miss}}$	Flavour symmetry
$Wt$ (single top) di-leptonic	Two leptons, no $Z$ , real $E_{\text{T}}^{\text{miss}}$	Flavour symmetry
$WZ$	Real $Z$ , real $E_{\text{T}}^{\text{miss}}$	MC
$ZZ$	Real $Z$ , real $E_{\text{T}}^{\text{miss}}$ from $Z$ decays to $\nu s$	MC
$t\bar{t}V$	Two leptons, real $E_{\text{T}}^{\text{miss}}$ , no $Z$	MC
$tZ$ (single top)	Real $Z$ , real $E_{\text{T}}^{\text{miss}}$	MC
Drell-Yan	Real $Z$ , fake $E_{\text{T}}^{\text{miss}}$	MC
$W + \text{jets}$	Fake lepton/s, no $Z$ , real $E_{\text{T}}^{\text{miss}}$	Matrix method
$t\bar{t}$ semileptonic and hadronic	Fake lepton/s, no $Z$ , real $E_{\text{T}}^{\text{miss}}$	Matrix method
single top ( $s, t$ channels)	Fake lepton/s, no $Z$ , real $E_{\text{T}}^{\text{miss}}$	Matrix method
Multijet	Two fake leptons, no $Z$ , fake $E_{\text{T}}^{\text{miss}}$	Matrix method

Table 4.10: Main background descriptions and their nominal estimation methods. The  $Z + \text{jets}$  and Drell-Yan backgrounds differ only in the invariant mass of the leptons, where the former considers only  $m_{\ell\ell} > 40$  GeV while for the later  $m_{\ell\ell} < 40$  GeV.



### 4.6.1 $Z/\gamma^* + \text{jets}$ background estimation

With the SR defined at large  $E_T^{\text{miss}}$ , any contribution from  $Z/\gamma^* + \text{jets}$  will be a consequence of artificially high  $E_T^{\text{miss}}$  in the event. The  $Z/\gamma^* + \text{jets}$  events that populate the signal region result from mismeasurements of physics objects where, for example, one of the final-state jets has its energy underestimated, resulting in an overestimate of the total  $E_T^{\text{miss}}$  in the event.

Despite its contribution predicted to be negligible in the SR, this background must be carefully estimated since the peaking  $Z/\gamma^* + \text{jets}$  background can mimic the signal. Due to the difficulties of modelling instrumental  $E_T^{\text{miss}}$  in simulation, MC events are not relied upon alone for the estimation of this background. A data-driven technique is used as the nominal method for estimating it. This technique confirms the expectation from MC simulation that the  $Z + \text{jets}$  background is negligible in the SR.

The primary method used to model this background in the SR is the so-called “jet smearing” method, which is described in detail in Ref. [120]. This method involves defining a region with  $Z/\gamma^* + \text{jets}$  events containing well-measured jets (at low  $E_T^{\text{miss}}$ ), known as the “seed” region (SeedR). The jets in these events are then smeared using functions that describe the detector’s jet  $p_T$  response and  $\phi$  resolution as a function of jet  $p_T$ , creating a set of pseudo-data events. The jet-smearing method provides an estimate for the contribution from events containing both fake  $E_T^{\text{miss}}$ , from object mismeasurements, and real  $E_T^{\text{miss}}$ , from neutrinos in heavy-flavour quark decays, by using different response functions for light-flavour and  $b$ -tagged jets. The response function is measured by comparing generator-level jet  $p_T$  to reconstructed jet  $p_T$  in PYTHIA8 dijet MC events, generated using the CT10 NLO PDF set. This function is then tuned to data, based on a dijet balance analysis in which the  $p_T$  asymmetry is used to constrain the width of the Gaussian core. The non-Gaussian tails of the response function are corrected based on  $\geq 3$ -jet events in data, selected such that the  $E_T^{\text{miss}}$  in each event points either towards, or in the opposite direction to one of the jets. This ensures that one of the jets is clearly associated with the  $E_T^{\text{miss}}$ , and the jet response can then be described in terms of the  $E_T^{\text{miss}}$  and reconstructed jet  $p_T$ . This procedure results in a good estimate of the overall jet response.

In order to calculate the  $E_T^{\text{miss}}$  distribution of the pseudo-data, the  $E_T^{\text{miss}}$  is recalculated using the new (smeared) jet  $p_T$  and  $\phi$ . The distribution of pseudo-data events is then normalised to data in the low- $E_T^{\text{miss}}$  region ( $10 < E_T^{\text{miss}} < 50$  GeV) of a validation region, denoted VRZ, after the requirement of  $\Delta\phi(\text{jet}_{1,2}, E_T^{\text{miss}}) > 0.4$ . This region is defined in Table 4.1 and is designed to be representative of the signal region but at lower  $E_T^{\text{miss}}$ , where the contamination for relevant GGM signal models is expected to be less than 1%.

The seed region must contain events with topologies similar to those expected in the signal region. To ensure that this is the case, the  $H_T$  and jet multiplicity requirements applied to the seed region remain the same as in the signal region, while the  $E_T^{\text{miss}}$  threshold of 225 GeV is removed, as shown in Table 4.1. Although the seed events should have little to no  $E_T^{\text{miss}}$ , enforcing

a direct upper limit on  $E_T^{\text{miss}}$  can introduce a bias in the jet  $p_T$  distribution in the seed region compared with the signal region. To avoid this, a requirement on the  $E_T^{\text{miss}}$  significance, defined as:

$$E_T^{\text{miss}} \text{ sig.} = \frac{E_T^{\text{miss}}}{\sqrt{\sum E_T^{\text{jet}} + \sum E_T^{\text{soft}}}}, \quad (4.1)$$

is used in the seed region. Here  $\sum E_T^{\text{jet}}$  and  $\sum E_T^{\text{soft}}$  are the summed  $E_T$  from the baseline jets and the low-energy calorimeter deposits not associated with final-state physics objects, respectively. Placing a requirement on this variable does not produce a shape difference between jet  $p_T$  distributions in the seed and signal regions, while effectively selecting well-balanced  $Z/\gamma^* + \text{jets}$  events in the seed region. This requirement is also found to result in no event overlap between the seed region and SR.

In the seed region an additional requirement is placed on the soft term fraction,  $f_{\text{ST}}$ , defined as the fraction of the total  $E_T^{\text{miss}}$  in an event originating from calorimeter energy deposits not associated with a calibrated lepton or jet ( $f_{\text{ST}} = \sum E_T^{\text{miss, Soft}} / E_T^{\text{miss}}$ ), to select events with small  $f_{\text{ST}}$ . This is useful because it is events with low soft term fractions ( $f_{\text{ST}} < 0.6$ ) that tend to lead to large values of fake  $E_T^{\text{miss}}$ .

The requirements on the  $E_T^{\text{miss}}$  significance and  $f_{\text{ST}}$  are initially optimised by applying the jet smearing method to  $Z/\gamma^* + \text{jets}$  MC events and testing the agreement in the  $E_T^{\text{miss}}$  spectrum between direct and smeared MC events in the VRZ. This closure test is performed using the response function derived from MC simulation.

The  $Z/\gamma^* + \text{jets}$  background predominantly comes from events where a single jet is grossly mismeasured, since the mismeasurement of additional jets is unlikely, and can lead to smearing that reduces the total  $E_T^{\text{miss}}$ . The requirement on the opening angle in  $\phi$  between either of the leading two jets and the  $E_T^{\text{miss}}$ ,  $\Delta\phi(\text{jet}_{1,2}, E_T^{\text{miss}}) > 0.4$ , strongly suppresses this background. The estimate of the  $Z/\gamma^* + \text{jets}$  background is performed both with and without this requirement as it can be seen in Section 4.8.1. The optimisation of the  $E_T^{\text{miss}}$  significance and  $f_{\text{ST}}$  requirements are performed separately with and without the requirement, although the optimal values are not found to differ significantly.

The jet smearing method using the data-corrected jet response function is validated in VRZ, comparing smeared pseudo-data to data. The resulting  $E_T^{\text{miss}}$  distributions show agreement within uncertainties assessed based on varying the response function and the  $E_T^{\text{miss}}$  significance requirement in the seed region. The  $E_T^{\text{miss}}$  distribution in VRZ, with the additional requirement  $\Delta\phi(\text{jet}_{1,2}, E_T^{\text{miss}}) > 0.4$ , is shown in Fig. 4.24. Here the  $E_T^{\text{miss}}$  range extends only up to 100 GeV, since  $t\bar{t}$  events begin to dominate at higher  $E_T^{\text{miss}}$  values. The pseudo-data to data agreement in VRZ motivates the final determination of the  $E_T^{\text{miss}}$  significance requirement used for the seed region ( $E_T^{\text{miss}} \text{ sig.} < 0.9$ ). Backgrounds containing real  $E_T^{\text{miss}}$ , including  $t\bar{t}$  and diboson production, are

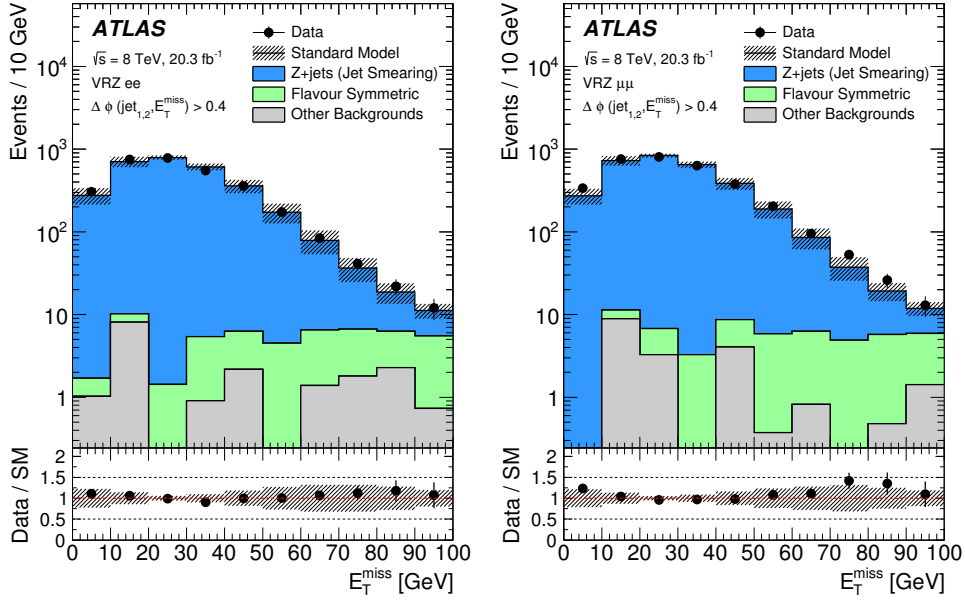


Figure 4.24: Distribution of  $E_T^{\text{miss}}$  in the electron (left) and muon (right) channel in VRZ following the requirement of  $\Delta\phi(\text{jet}_{1,2}, E_T^{\text{miss}}) > 0.4$ . Here the  $Z/\gamma^* + \text{jets}$  background (solid blue) is modelled using  $p_T$ - and  $\phi$ -smeared pseudo-data events. The hatched uncertainty band includes the statistical uncertainty on the simulated event samples and the systematic uncertainty on the jet-smearing estimate due to the jet response function and the seed selection. The backgrounds due to  $WZ$ ,  $ZZ$  or rare top processes, as well as from lepton fakes, are included under “Other Backgrounds”.

taken from MC simulation for this check. The chosen values are detailed in Table 4.1 with a summary of the kinematic requirements imposed on the seed and  $Z$  validation region. Extrapolating the jet smearing estimate to the signal regions yields the results detailed in Table 4.11. The data-driven estimate is compatible with the MC expectation that the  $Z + \text{jets}$  background contributes significantly less than one event in the SR.

Signal region	Jet-smearing	$Z + \text{jets}$ MC
SR $ee$	$0.05 \pm 0.04$	$0.05 \pm 0.03$
SR $\mu\mu$	$0.02^{+0.03}_{-0.02}$	$0.09 \pm 0.05$

Table 4.11: Number of  $Z/\gamma^* + \text{jets}$  background events estimated in the signal region (SR) using the jet smearing method. This is compared with the prediction from the SHERPA MC simulation. The quoted uncertainties include those due to statistical and systematic effects (see Sect. 4.7).

Given the possibility of this background mimicking the SUSY signal, many

more tests have been performed to validate the jet smearing results. All these tests are carefully described in the ATLAS internal note in Ref. [97]

#### 4.6.2 Lepton flavour-symmetric background estimation: $t\bar{t}$ , $WW$ , $Wt$ , $Z \rightarrow \tau\tau$

Since the dileptonic branching fractions to  $ee$ ,  $\mu\mu$  and  $e\mu$  from  $t\bar{t}$ ,  $WW$ ,  $Wt$  and  $Z \rightarrow \tau\tau$  decays follow a 1:1:2 ratio, opposite-flavour ( $e\mu$ ) events are used to estimate the background in the same-flavour ( $ee$  and  $\mu\mu$ ) channels from these processes in the SR. The number of  $e\mu$  data events,  $N_{e\mu}^{\text{data}}$ , observed in the corresponding control region  $\text{CRe}\mu$ , defined as being identical to the SR but in the opposite-flavour channel (see Table 4.1), is taken to perform an estimation following the relations:

$$\begin{aligned} N_{ee}^{\text{est}} &= \frac{1}{2} N_{e\mu}^{\text{data,corr}} k_{ee} \alpha, \\ N_{\mu\mu}^{\text{est}} &= \frac{1}{2} N_{e\mu}^{\text{data,corr}} k_{\mu\mu} \alpha, \end{aligned} \quad (4.2)$$

with  $N_{e\mu}^{\text{data,corr}} = N_{e\mu}^{\text{data}} - N_{e\mu}^{\text{sub}}$  being the number of data events in  $\text{CRe}\mu$  corrected by subtracting the flavour non-symmetric backgrounds  $N_{e\mu}^{\text{sub}}$  in the same region (estimated either from MC or with the matrix method). The  $k_{ee}$  and  $k_{\mu\mu}$  factors account for differences between the electron and muon reconstruction efficiencies and  $\alpha$  accounts for the differing trigger efficiencies of the same and opposite flavour dilepton triggers. These three factors are defined as follows:

$$k_{ee} = \sqrt{\frac{N_{ee}^{\text{data}}(\text{VRZ})}{N_{\mu\mu}^{\text{data}}(\text{VRZ})}}, \quad k_{\mu\mu} = \sqrt{\frac{N_{\mu\mu}^{\text{data}}(\text{VRZ})}{N_{ee}^{\text{data}}(\text{VRZ})}}, \quad \alpha = \frac{\sqrt{\epsilon_{\text{trig}}^{ee} \epsilon_{\text{trig}}^{\mu\mu}}}{\epsilon_{\text{trig}}^{e\mu}}. \quad (4.3)$$

##### 4.6.2.1 Estimation of $N_{e\mu}^{\text{data,corr}}$

The number of  $e\mu$  data events, observed in the opposite-flavour control region,  $\text{CRe}\mu$ , is denoted by  $N_{e\mu}^{\text{data}}$ . To represent the number of events attributed to background processes expected to follow this 1:1:2 ratio for  $ee:\mu\mu:e\mu$  final states, the number of flavour non-symmetric backgrounds,  $N_{e\mu}^{\text{sub}}$ , must be subtracted from  $N_{e\mu}^{\text{data}}$ . These flavour non-symmetric backgrounds are taken from MC when they contain two real leptons ( $WZ$ ,  $ZZ$ ,  $t\bar{t}V$ ,  $Z(\rightarrow ee, \mu\mu) + \text{jets}$ , single top ( $tZ$ ), Drell-Yan) and estimated using the matrix method (see Section 4.6.4) when they contain fake leptons (semileptonic- and hadronic- $t\bar{t}$ ,  $W + \text{jets}$ , single top ( $s$ ,  $t$  channels), multijets). Table 4.12 summarizes the contribution of these processes. For MC estimates, only the experimental uncertainties, summarized in Table 4.30, are shown.

Bkg	$CR_{e\mu}$
$WZ, ZZ$	$0.03 \pm 0.01 \pm_{0.01}^{0.02}$
$t\bar{t}V$	$0.07 \pm 0.02 \pm_{0.02}^{0.01}$
$Z(\rightarrow ee, \mu\mu) + \text{jets}$	$0.00 \pm 0.00 \pm 0.00$
Drell-Yan	$0.00 \pm 0.00 \pm 0.00$
$tZ$	$0.00 \pm 0.00 \pm 0.00$
Total $N_{e\mu}^{\text{sub,MC}}$	$0.10 \pm 0.02 \pm 0.02$
Fake leptons	$0.66 \pm 0.57 \pm 0.25$
$N_{e\mu}^{\text{data}}$	6
$N_{e\mu}^{\text{sub}}$	$0.76 \pm 0.57 \pm 0.25$
$N_{e\mu}^{\text{data,corr}}$	<b><math>5.24 \pm 2.51 \pm 0.17</math></b>

Table 4.12: Contribution of the subtracted flavour non-symmetric processes in  $CR_{e\mu}$  estimated from MC or with the matrix method. The lower part of the table shows the number of data events, the total sum of the flavour non-symmetric processes and the result of subtracting these two numbers,  $N_{e\mu}^{\text{data,corr}}$ , in  $CR_{e\mu}$ . The first error gives the statistical uncertainty. The second one corresponds to the experimental systematic uncertainties (theoretical uncertainties are not included).

	$\epsilon_{\text{barrel,barrel}}$	$\epsilon_{\text{barrel,endcap}}$	$\epsilon_{\text{endcap,endcap}}$
$ee$	0.96	0.94	0.91
$\mu\mu$	0.88	0.90	0.92
$e\mu$	0.80	0.81	0.82
$\alpha$	1.15	1.14	1.12

Table 4.13: Trigger efficiency factors.

#### 4.6.2.2 $\alpha$ factor

Differing efficiencies for dielectron, dimuon and  $e\mu$  triggers are accounted for by  $\alpha$ , defined in Eq. 4.3. Since trigger efficiencies vary depending on whether leptons fall in the endcap or barrel regions of the detector, three trigger efficiency regions are defined as follows:

- barrel-barrel, where both leptons are in the barrel;
- barrel-endcap, where one lepton is in the barrel and the other in one endcap;
- endcap-endcap, where both leptons are in the endcaps.

The trigger efficiencies for these three regions are shown in Table 4.13, following the trigger efficiency study in [121], and a 5% uncertainty has been assigned to each of these efficiencies. The corresponding correction factor  $\alpha$  is also shown in Table 4.13.

#### 4.6.2.3 $k_{ee}$ and $k_{\mu\mu}$ factors

The scaling factors  $k_{ee}$  and  $k_{\mu\mu}$  are calculated in a low  $E_T^{\text{miss}}$  validation region, VRZ (as defined in Table 4.1). This region is enriched with  $Z$ +jets events, ensuring a sample of well measured leptons. Table 4.14 summarizes the composition of backgrounds in VRZ, taken from direct MC. Note that in Table 4.14 and the tables that follow in this section, the first uncertainty corresponds to statistical uncertainty while the second accounts for experimental systematic uncertainties<sup>2</sup>. These factors take into account the differences between the electron and muon reconstruction efficiencies as well as the different efficiencies for the dielectron and dimuon triggers applied.

The dependency of these  $k_{ee}$  and  $k_{\mu\mu}$  factors on  $E_T^{\text{miss}}$  was studied by calculating these factors in various  $E_T^{\text{miss}}$  windows in VRZ. The results are given in Table 4.15. The difference between the highest and the lowest values for  $k_{ee}$  and  $k_{\mu\mu}$  among the  $E_T^{\text{miss}}$  bins is taken as a systematic uncertainty on the  $k$  factors. This uncertainty is propagated to the calculation of  $N_{ee}^{\text{est}}$  and  $N_{\mu\mu}^{\text{est}}$ .

Given that different  $\alpha$  factors are applied to different detector areas (barrel-barrel, barrel-endcap, endcap-endcap), the  $k_{ee}$  and  $k_{\mu\mu}$  factors are also calculated separately in these three zones. The estimated event yields in the  $ee$  and  $\mu\mu$  channels,  $N_{ee}^{\text{est}}$  and  $N_{\mu\mu}^{\text{est}}$  are therefore calculated separately for each of these regions, with the total estimate being given by the sum of the calculated contributions in each region.

Table 4.16 summarises the values of the  $N_{ee}^{\text{data}}$ ,  $N_{\mu\mu}^{\text{data}}$ ,  $k_{ee}$  and  $k_{\mu\mu}$  in VRZ, determined from data and compared with numbers derived from MC only. Contributions from fake leptons in VRZ are subtracted from  $N_{ee}^{\text{data}}$ ,

<sup>2</sup>This includes JES, JER, systematics on  $E_T^{\text{miss}}$ , pileup and lepton scale factors, as explained in detail in Section 4.7.

VRZ	$N_{ee}^{MC}$	$N_{\mu\mu}^{MC}$	$N_{e\mu}^{MC}$
$Z(ee, \mu\mu) + jets$	$4520.89 \pm 19.23 \pm_{155.42}^{163.10}$	$5190.06 \pm 20.48 \pm_{137.50}^{184.78}$	$0.28 \pm 0.08 \pm_{0.03}^{0.02}$
$st(s, t)$	$2.12 \pm 0.11 \pm_{0.07}^{0.09}$	$2.48 \pm 0.12 \pm_{0.14}^{0.14}$	$0.01 \pm 0.00 \pm_{0.00}^{0.01}$
$WZ + ZZ$	$11.83 \pm 0.87 \pm_{1.78}^{0.81}$	$9.13 \pm 0.67 \pm_{0.44}^{0.62}$	$0.63 \pm 0.17 \pm_{0.09}^{0.05}$
$t\bar{t}V$	$4.97 \pm 0.15 \pm_{0.21}^{0.21}$	$5.10 \pm 0.16 \pm_{0.29}^{0.24}$	$0.51 \pm 0.05 \pm_{0.03}^{0.06}$
Total non-sym. bkgs	$4539.82 \pm 19.25 \pm_{155.43}^{163.10}$	$5206.78 \pm 20.49 \pm_{137.50}^{184.78}$	$1.42 \pm 0.20 \pm_{0.10}^{0.08}$
$t\bar{t}$	$67.73 \pm 2.06 \pm_{4.34}^{4.10}$	$73.25 \pm 2.09 \pm_{43.06}^{4.39}$	$132.29 \pm 2.83 \pm_{34.28}^{7.58}$
$Z(\tau\tau) + jets$	$0.14 \pm 0.10 \pm_{0.05}^{0.07}$	$0.05 \pm 0.04 \pm_{0.00}^{0.00}$	$1.33 \pm 0.77 \pm_{0.13}^{0.13}$
$st(Wt)$	$2.29 \pm 0.13 \pm_{0.14}^{0.15}$	$2.62 \pm 0.14 \pm_{0.12}^{0.17}$	$4.40 \pm 0.18 \pm_{0.21}^{0.20}$
$WW$	$0.90 \pm 0.24 \pm_{0.25}^{0.09}$	$0.64 \pm 0.19 \pm_{0.13}^{0.14}$	$1.63 \pm 0.31 \pm_{0.19}^{0.04}$
Total sym. bkgs	$71.07 \pm 2.08 \pm_{4.35}^{4.11}$	$76.57 \pm 2.10 \pm_{43.06}^{4.39}$	$139.64 \pm 2.96 \pm_{34.28}^{7.58}$
Total bkgs	$4610.89 \pm 19.36 \pm_{155.50}^{163.16}$	$5283.35 \pm 20.59 \pm_{144.09}^{184.83}$	$141.06 \pm 2.97 \pm_{34.28}^{7.58}$

Table 4.14: Background composition in VRZ estimated from MC directly. The first error corresponds to statistical uncertainties. The second one gives the experimental uncertainties.

$E_T^{miss}$ [ GeV]	$N_{ee}^{data}$	$N_{\mu\mu}^{data}$	$k_{ee}$	$k_{\mu\mu}$
0-150	4452	4960	$0.947 \pm 0.010$	$1.056 \pm 0.011$
0-20	1398	1468	$0.976 \pm 0.018$	$1.025 \pm 0.019$
20-30	1057	1139	$0.963 \pm 0.021$	$1.038 \pm 0.022$
30-45	1128	1263	$0.945 \pm 0.019$	$1.058 \pm 0.022$
45-150	869	1090	$0.893 \pm 0.020$	$1.120 \pm 0.026$

Table 4.15: Number of  $ee$  and  $\mu\mu$  events and the values of  $k_{ee}$  and  $k_{\mu\mu}$  estimated from data in the validation region VRZ for several cuts on  $E_T^{miss}$ .

$N_{\mu\mu}^{data}$  before the  $k$  factors are calculated. The data-estimated values for  $k_{ee}$  and  $k_{\mu\mu}$  are in good agreement with the values estimated from MC. Global  $k_{ee}$  and  $k_{\mu\mu}$  factors (estimated without discriminating in barrel/endcap zones) are also shown for completeness. They are consistent, within uncertainties, with those estimated by summing the contributions in the three different zones.

VRZ	$N_{ee}^{\text{data}}$	$N_{\mu\mu}^{\text{data}}$	$k_{ee}$	$k_{\mu\mu}$
barrel-barrel	2399	1995	$1.099 \pm 0.017 \pm 0.08$	$0.910 \pm 0.014 \pm 0.1$
barrel-endcap	1215	1667	$0.853 \pm 0.016 \pm 0.08$	$1.173 \pm 0.022 \pm 0.1$
endcap-endcap	838	1298	$0.805 \pm 0.018 \pm 0.08$	$1.242 \pm 0.028 \pm 0.1$
Global	4452	4960	$0.947 \pm 0.010 \pm 0.08$	$1.056 \pm 0.011 \pm 0.1$
VRZ	$N_{ee}^{\text{MC}}$	$N_{\mu\mu}^{\text{MC}}$	$k_{ee}^{\text{MC}}$	$k_{\mu\mu}^{\text{MC}}$
barrel-barrel	$2438.6 \pm 13.1 \pm_{119.0}^{128.0}$	$2110.4 \pm 11.5 \pm_{89.8}^{117.3}$	$1.075 \pm 0.004 \pm_{0.035}^{0.041}$	$0.930 \pm 0.004 \pm_{0.030}^{0.036}$
barrel-endcap	$1310.2 \pm 11.2 \pm_{84.8}^{85.2}$	$1777.1 \pm 13.1 \pm_{92.5}^{113.4}$	$0.859 \pm 0.005 \pm_{0.036}^{0.039}$	$1.165 \pm 0.007 \pm_{0.048}^{0.053}$
endcap-endcap	$862.1 \pm 8.8 \pm_{53.1}^{54.6}$	$1395.9 \pm 10.9 \pm_{64.4}^{86.9}$	$0.786 \pm 0.005 \pm_{0.030}^{0.035}$	$1.272 \pm 0.008 \pm_{0.049}^{0.056}$
Global	$4610.9 \pm 19.4 \pm_{155.5}^{163.2}$	$5283.3 \pm 20.6 \pm_{144.1}^{184.8}$	$0.934 \pm 0.003 \pm_{0.020}^{0.023}$	$1.070 \pm 0.003 \pm_{0.023}^{0.027}$

Table 4.16: Number of  $ee$ ,  $\mu\mu$  events and the values of  $k_{ee}$ ,  $k_{\mu\mu}$  and their statistical error estimated from data and MC in validation region VRZ. Values for three different zones of the detector (barrel-barrel, barrel-endcap, endcap-endcap) are given. The Global  $k_{ee}$ ,  $k_{\mu\mu}$  values are calculated without discriminating in barrel/endcap zones. For the MC estimates, the first uncertainty shown corresponds to the statistical error, the second one to the experimental systematic uncertainties. For the data estimates the second uncertainty is due to the  $E_T^{\text{miss}}$  dependence of the  $k$  factors.

#### 4.6.2.4 Results from flavour-symmetry method

The final results for the data-driven estimation for the dileptonic  $t\bar{t}$ ,  $WW$ ,  $Wt$ ,  $Z \rightarrow \tau\tau$  backgrounds in the signal region are shown in Table 4.17. As explained above, the final estimates for flavour-symmetric backgrounds have been calculated separately for barrel-barrel, barrel-endcap and endcap-endcap regions due to the different trigger factors  $\alpha$  to be applied in different detector regions. The final estimate is calculated by summing up the contributions from these three regions, with the associated uncertainties being propagated appropriately. The uncertainties associated with the estimate are calculated using the formulae below:

$$\begin{aligned}
(\sigma_{N_{ee}^{\text{est}}})^2 &= (\sigma_{N_{ee}^{\text{est}}})_{\text{stat}}^2 + (\sigma_{N_{ee}^{\text{est}}})_{\text{sys}}^2 + (\sigma_{N_{ee}^{\text{est}}})_{\text{met}}^2 \\
(\sigma_{N_{ee}^{\text{est}}})_{\text{stat}} &= (\alpha/2) \sqrt{\left( \sigma_{N_{e\mu}^{\text{data,corr}}} \right)_{\text{stat}}^2 k_{ee}^2 + (\sigma_{k_{ee}})_{\text{stat}}^2 \left( N_{e\mu}^{\text{data,corr}} \right)^2} \\
(\sigma_{N_{ee}^{\text{est}}})_{\text{sys}} &= (\alpha/2) k_{ee} \sqrt{\left( \sigma_{N_{e\mu}^{\text{data,corr}}} \right)_{\text{sys}}^2 + \frac{3}{2} (0.05)^2 \left( N_{e\mu}^{\text{data,corr}} \right)^2} \\
(\sigma_{N_{ee}^{\text{est}}})_{\text{met}} &= (\alpha/2) N_{e\mu}^{\text{data,corr}} (\sigma_{k_{ee}})_{\text{met}}
\end{aligned}$$

where  $(\sigma_{k_{ee}})_{\text{met}}$  is the  $k_{ee}$  uncertainty due to the dependence on  $E_T^{\text{miss}}$ , and the



factor 0.05 is the uncertainty assigned to the trigger efficiencies (as explained in 4.6.2.2). For the  $\mu\mu$  channel the formulae are analogous.

SR	$N_{e\mu}^{data}$	$N_{e\mu}^{data,corr}$	$N_{ee}^{est}$	$N_{\mu\mu}^{est}$
barrel-barrel	2	$1.39 \pm 1.48 \pm_{0.13}^{0.13}$	$0.88 \pm 0.93 \pm_{0.10}^{0.10} \pm 0.07$	$0.73 \pm 0.77 \pm_{0.09}^{0.09} \pm 0.08$
barrel-endcap	4	$4.19 \pm 2.00 \pm_{0.10}^{0.11}$	$2.02 \pm 0.97 \pm_{0.15}^{0.15} \pm 0.20$	$2.78 \pm 1.33 \pm_{0.21}^{0.21} \pm 0.23$
endcap-endcap	0	$-0.35 \pm 0.34 \pm_{0.02}^{0.02}$	$-0.16 \pm 0.15 \pm_{0.01}^{0.01} \mp 0.02$	$-0.24 \pm 0.24 \pm_{0.02}^{0.02} \mp 0.02$
SUM	6	$5.24 \pm 2.51 \pm_{0.17}^{0.17}$	<b><math>2.75 \pm 1.35 \pm_{0.18}^{0.18} \pm 0.21</math></b>	<b><math>3.27 \pm 1.56 \pm_{0.23}^{0.23} \pm 0.24</math></b>
Global k			$2.82 \pm 1.36 \pm_{0.19}^{0.19}$	$3.15 \pm 1.51 \pm_{0.21}^{0.21}$

Table 4.17: Summary of data-driven estimation of dileptonic  $t\bar{t}$ , WW, Wt and  $Z \rightarrow \tau\tau$  backgrounds in SR. The first uncertainty shown corresponds to the statistical error, the second one to the experimental systematic uncertainties. The third number corresponds to the uncertainty due to the dependency of  $k_{ee}$ ,  $k_{\mu\mu}$  on  $E_T^{miss}$ .

The final estimate in the muon channel is slightly enhanced with respect to the electron channel. This method is highly sensitive to statistical fluctuations, which is reflected by the statistical error. Some of the MC predictions, as well as the fake lepton estimation, are also affected by low statistics. Of course, there are differences in lepton isolation requirements, trigger efficiencies, and reconstruction efficiencies that can lead to differences between the electron and muon channels. This leads to a non-symmetric global estimate for the electron and muon channels, as will be seen in Section 4.8.

### 4.6.3 Cross-checks on the flavour-symmetry method

In order to cross-check different aspects of the flavour-symmetry method a variety of tests has been performed. A detailed description of these cross-checks can be found in the next subsections, Appendix B.1 and Ref. [97], and they are summarized in the following list:

- *MC closure*: apply the flavour-symmetry method to MC samples to obtain  $N_{ee}^{est,MC}$  and  $N_{\mu\mu}^{est,MC}$  in order to compare these results with the direct MC estimates. (Section 4.6.3.1)
- *Cross-check using the side-band fit*: perform a fit to normalize the  $t\bar{t}$  background to data in CRT (analogous to SR but in the  $Z$  mass side-band) and extrapolate the normalization factor to the SR. (Section 4.6.3.2)
  - *Test on the stability of the  $m_{\ell\ell}$  extrapolation*: validate the extrapolation over  $m_{\ell\ell}$  using specific validation regions. (Section 4.6.3.2.1)
- *Closure test of the analysis in validation regions*: estimate the background prediction in CRT and six validation regions (using the nominal methods of the analysis) and compare them to the number of data events in those regions. (Section 4.6.3.3)

- *Further checks:*
  - *Testing the  $N_{ee}^{MC}:N_{\mu\mu}^{MC}:N_{e\mu}^{MC}$  ratio in VRZ but in the  $Z$  side-band:* Validate the assumption that the mentioned ratio of  $ee : \mu\mu : e\mu$  events is 1:1:2. (Appendix B.1.1)
  - *Comparison of the side-band fit results with different  $t\bar{t}$  MC generators.* (Section 7.3.2.2 of Ref. [97])
  - *Testing  $m_{\ell\ell}$  distributions:*  $m_{\ell\ell}$  plots in different regions and with different  $t\bar{t}$  generators. (Appendix B.1.2 and Appendix B.2.2 of Ref. [97])
  - *$t\bar{t}$  reweighting:* a cross-section based  $t\bar{t}$ -reweighting technique has been tested and did not have any impact on background predictions in the SR. It was decided not to apply  $t\bar{t}$ -reweighting. (Appendix B.2.3 of Ref. [97])

#### 4.6.3.1 MC closure

As previously mentioned, a closure test has been performed in order to cross-check the flavour-symmetry method. All the steps of the method have been applied to MC samples using the  $k_{ee}^{MC}$ ,  $k_{\mu\mu}^{MC}$  factors, derived from MC, in Table 4.16 and the number of MC  $e\mu$  events in  $\text{CRE}\mu$ . The result of this test is shown in the top part of Table 4.18. It is known that the  $t\bar{t}$  background is overestimated in MC [122, 123], making it unsurprising that the closure test results are not directly comparable to those from data unless a normalization factor is applied to  $t\bar{t}$ . Even so, the results of the MC closure test are encouraging, since the MC estimates for the  $t\bar{t}$ ,  $WW$ ,  $Wt$  and  $Z \rightarrow \tau\tau$  backgrounds using the flavour-symmetry method are compatible, within statistical and systematic errors, with the direct MC estimate of such backgrounds. This can be seen in Table 4.18 (the numbers to be compared are shown in bold).

SR	$N_{e\mu}^{MC}$	$N_{e\mu}^{MC,corr}$	$N_{ee}^{est,MC}$	$N_{\mu\mu}^{est,MC}$
barrel-barrel	$10.39 \pm 0.78 \pm_{3.11}^{1.49}$	$10.34 \pm 0.78 \pm_{3.11}^{1.49}$	$6.38 \pm 0.48 \pm_{1.98}^{1.05} \pm 0.49$	$5.53 \pm 0.42 \pm_{1.72}^{0.91} \pm 0.56$
barrel-endcap	$6.31 \pm 0.60 \pm_{2.37}^{0.50}$	$6.27 \pm 0.60 \pm_{2.37}^{0.50}$	$3.05 \pm 0.29 \pm_{1.18}^{0.35} \pm 0.29$	$4.13 \pm 0.39 \pm_{1.60}^{0.48} \pm 0.34$
endcap-endcap	$0.73 \pm 0.21 \pm_{0.20}^{0.15}$	$0.73 \pm 0.21 \pm_{0.20}^{0.15}$	$0.32 \pm 0.09 \pm_{0.09}^{0.07} \pm 0.03$	$0.52 \pm 0.15 \pm_{0.15}^{0.12} \pm 0.04$
<b>SUM (MC Closure)</b>	$17.44 \pm 1.00 \pm_{3.91}^{1.58}$	$17.34 \pm 1.00 \pm_{3.91}^{1.58}$	<b><math>9.75 \pm 0.57 \pm_{2.31}^{1.11} \pm 0.58</math></b>	<b><math>10.18 \pm 0.59 \pm_{2.35}^{1.04} \pm 0.66</math></b>
Global			$9.50 \pm 0.55 \pm_{2.21}^{1.01}$	$10.31 \pm 0.60 \pm_{2.39}^{1.10}$
SR			$N_{ee}^{direct,MC}$	$N_{\mu\mu}^{direct,MC}$
<b>Direct MC estimation</b>			<b><math>8.66 \pm 0.72 \pm_{0.84}^{0.70}</math></b>	<b><math>9.30 \pm 0.72 \pm_{4.60}^{0.65}</math></b>

Table 4.18: Summary of closure test for the estimation of dileptonic- $t\bar{t}$ ,  $WW$ ,  $Wt$  and  $Z \rightarrow \tau\tau$  backgrounds in SR. The first uncertainty shown corresponds to the statistical error, the second one to the experimental systematic uncertainties. The third number corresponds to the uncertainty due to the dependency of  $k_{ee}$ ,  $k_{\mu\mu}$  on  $E_T^{\text{miss}}$ , as detailed in Section 4.6.2.3. The bottom part of the table shows the summary of direct MC estimation of dileptonic- $t\bar{t}$ ,  $WW$ ,  $Wt$  and  $Z \rightarrow \tau\tau$  backgrounds in SR.

### 4.6.3.2 Cross-check using the side-band fit

As another cross-check for the data-driven estimation of flavour-symmetric backgrounds in the signal region, a fit in the  $m_{\ell\ell}$  side-bands (which are the regions outside the  $Z$  mass peak) has been performed. This involves normalizing the  $t\bar{t}$  background in control region CRT, defined to this end as shown in Table 4.1. CRT is essentially the same as the signal region with a selection of the  $m_{\ell\ell}$  side-bands rather than the  $Z$  mass peak. The procedure of extrapolation in  $m_{\ell\ell}$  is checked in validation regions, as discussed in 4.6.3.2.1. All these regions are dominated by  $t\bar{t}$  background and have low signal contamination. Note that the general approach and configuration of the fit using HistFitter is described in detail in [124, 125]. Here only the details specific to this analysis are considered.

Since the goal of this fit is to obtain a cross-check for the estimate given by the flavour-symmetry method, the flavour non-symmetric backgrounds are considered the same way as in the nominal analysis whenever possible. Therefore, the  $Z/\gamma^* + \text{jets}$  background contribution in the  $Z$  mass regions is taken from the jet smearing method results (see Section 4.6.1). However, since the jet smearing method cannot be applied to CRT, where the  $Z$  mass side-band is selected, the  $Z/\gamma^* + \text{jets}$  background is taken from MC in CRT. The rest of flavour non-symmetric dileptonic backgrounds is taken from MC both in SR and in CRT and the matrix method is used to estimate the contribution from events with fake leptons.

The normalization of the  $t\bar{t}$  background is left free in the fit, and since the fit has one single-bin control region, all backgrounds other than  $t\bar{t}$  are left unconstrained. Detector systematics as well as theory uncertainties on the MC samples considered are taken into account as nuisance parameters. The results of the fits for electron channel, muon channel and their combination (SF channel) can be found in Tables 4.19, 4.20, 4.21 for SR and CRT<sup>3</sup>.

After the fit,  $t\bar{t}$  normalization factors of  $\mu_{Top} = 0.53 \pm 0.14$ ,  $0.51 \pm 0.15$  and  $0.52 \pm 0.12$  are obtained for the  $ee$ ,  $\mu\mu$  and SF channels, respectively. This result is compatible with observations from other ATLAS analyses, which indicate that MC simulation tends to overestimate data in regions dominated by  $t\bar{t}$  events accompanied by high jet activity [126, 127]. MC simulation has also been seen to overestimate contributions from  $t\bar{t}$  processes in regions with high  $E_T^{\text{miss}}$  [81].

The contribution of flavour-symmetric backgrounds ( $t\bar{t}$ ,  $tW$ ,  $WW$ ,  $Z \rightarrow \tau\tau$ ) in the signal region estimated by the fit are compared to the data-driven estimation by the flavour-symmetry method in Table 4.22. The side-band fit yields a prediction slightly higher than, but consistent within  $1\sigma$  with, the

---

<sup>3</sup>Three different  $Z/\gamma^* + \text{jets}$  MC samples are mentioned in the tables. They were defined in order to increase the low statistics of the  $Z/\gamma^* + \text{jets}$  background. The particular details of these samples go beyond the scope of this Thesis. Nevertheless, the necessity of three samples is mentioned here to emphasise the difficulty of modelling this background using MC simulation.

flavour-symmetry estimate<sup>4</sup>.

channel	SRee	CRTEE
Observed events	-	50
Fitted bkg events	$6.38 \pm 1.45$	$49.97 \pm 7.13$
Fitted PowhegPythiaTTbar events	$4.14 \pm 1.41$	$31.97 \pm 8.54$
Fitted SherpaZMassiveBC events	$0.00 \pm 0.00$	$4.13 \pm 1.79$
Fitted SherpaZMassiveBC_extStats events	$0.00 \pm 0.00$	$0.01 \pm 0.01$
Fitted SherpaZMassiveBC_HTFilter events	$0.00 \pm 0.00$	$0.00 \pm 0.00$
Fitted JetSmearing events	$0.05 \pm 0.04$	$0.00 \pm 0.00$
Fitted SingleTopDiLept events	$0.50 \pm 0.32$	$6.32 \pm 3.00$
Fitted PowhegDibosons events	$1.42 \pm 0.38$	$4.51 \pm 0.89$
Fitted ttbarV events	$0.17 \pm 0.08$	$0.49 \pm 0.18$
data-driven fake lepton events	$0.10^{+0.38}_{-0.10}$	$2.54 \pm 1.95$
MC exp. SM events	10.10	78.72
MC exp. PowhegPythiaTTbar events	7.86	60.74
MC exp. SherpaZMassiveBC events	0.00	4.12
MC exp. SherpaZMassiveBC_extStats events	0.00	0.01
MC exp. SherpaZMassiveBC_HTFilter events	0.00	0.00
MC exp. JetSmearing events	0.05	0.00
MC exp. SingleTopDiLept events	0.50	6.32
MC exp. PowhegDibosons events	1.42	4.51
MC exp. ttbarV events	0.17	0.49
data-driven exp. fake lepton events	0.10	2.53

Table 4.19: Background fit results in the electron channel for an integrated luminosity of  $20.3 \text{ fb}^{-1}$ . Nominal MC and data-driven expectations are given for comparison. The uncertainties shown are statistical + systematic.

#### 4.6.3.2.1 Test on the stability of $m_{\ell\ell}$ extrapolation

Due to the fact that the control and signal regions are statistically limited and that the extrapolation in the fit takes place over the invariant mass ( $m_{\ell\ell}$ ), it is not trivial to define a good validation region to test the side-band fit. Hence a method slightly different from the usual “validation region” procedure has been developed in order to test the stability of the  $m_{\ell\ell}$  extrapolation.

<sup>4</sup>The flavour-symmetry background estimate was chosen as the nominal method prior to examining the data yields in the signal region, since it relies less heavily on simulation and provides the most precise estimate.

<b>channel</b>	<b>SRmm</b>	<b>CRTmm</b>
Observed events	-	45
Fitted bkg events	$8.41 \pm 2.08$	$45.01 \pm 6.76$
Fitted PowhegPythiaTTbar events	$4.15 \pm 1.62$	$27.51 \pm 8.07$
Fitted SherpaZMassiveBC events	$0.00 \pm 0.00$	$4.09 \pm 1.82$
Fitted SherpaZMassiveBC_extStats events	$0.00 \pm 0.00$	$0.69 \pm 0.40$
Fitted SherpaZMassiveBC_HTFilter events	$0.00 \pm 0.00$	$0.16 \pm 0.12$
Fitted JetSmearing events	$0.02^{+0.03}_{-0.02}$	$0.00 \pm 0.00$
Fitted SingleTopDiLept events	$0.58 \pm 0.36$	$5.78 \pm 2.75$
Fitted PowhegDibosons events	$2.30 \pm 0.66$	$5.63 \pm 1.09$
Fitted ttbarV events	$0.13 \pm 0.06$	$0.53 \pm 0.19$
data-driven fake lepton events	$1.22^{+1.25}_{-1.22}$	$0.61^{+1.28}_{-0.61}$
MC exp. SM events	12.39	71.38
MC exp. PowhegPythiaTTbar events	8.14	53.90
MC exp. SherpaZMassiveBC events	0.00	4.07
MC exp. SherpaZMassiveBC_extStats events	0.00	0.69
MC exp. SherpaZMassiveBC_HTFilter events	0.00	0.16
MC exp. JetSmearing events	0.02	0.00
MC exp. SingleTopDiLept events	0.58	5.79
MC exp. PowhegDibosons events	2.30	5.62
MC exp. ttbarV events	0.13	0.53
data-driven exp. fake lepton events	1.22	0.61

Table 4.20: Background fit results in the muon channel for an integrated luminosity of  $20.3 \text{ fb}^{-1}$ . Nominal MC and data-driven expectations are given for comparison. The uncertainties shown are statistical + systematic.

The method and the motivations to choose the regions involved are described through this section.

As already mentioned, the extrapolation from CR to SR is performed over  $m_{\ell\ell}$ . Consequently, by normalizing  $t\bar{t}$  in VRT\_highHT and transferring the normalization factor to VRTZ\_highHT, the extrapolation in  $m_{\ell\ell}$  can be tested in a region with slightly lower  $E_T^{\text{miss}}$  than the SR. The definition of all these regions can be seen in Table 4.1. However, VRTZ\_highHT has also very low statistics, therefore it is necessary to define a new set of regions loosening some cuts in order to gain statistics. For this purpose VRT and VRTZ are defined by lowering the  $H_T$  cut to 500 GeV. A schematic view of these regions can be seen in Fig. 4.25. Sketches describing all the regions can be found in Figs. B.1 and B.2 in Appendix B.1.

In this test,  $t\bar{t}$  is normalized in VRT (i.e. this is used as control region) and

<b>channel</b>	<b>SRSF</b>	<b>CRTSF</b>
Observed events	-	95
Fitted bkg events	$14.80 \pm 2.89$	$95.15 \pm 9.95$
Fitted PowhegPythiaTTbar events	$8.32 \pm 2.52$	$59.63 \pm 13.59$
Fitted SherpaZMassiveBC events	$0.00 \pm 0.00$	$8.22 \pm 3.61$
Fitted SherpaZMassiveBC_extStats events	$0.00 \pm 0.00$	$0.70 \pm 0.35$
Fitted SherpaZMassiveBC_HTFilter events	$0.00 \pm 0.00$	$0.16 \pm 0.09$
Fitted JetSmearing events	$0.07 \pm 0.05$	$0.00 \pm 0.00$
Fitted SingleTopDiLept events	$1.07 \pm 0.68$	$12.01 \pm 5.76$
Fitted PowhegDibosons events	$3.71 \pm 0.99$	$10.12 \pm 1.98$
Fitted ttbarV events	$0.30 \pm 0.13$	$1.03 \pm 0.37$
data-driven fake lepton events	$1.32^{+1.51}_{-1.32}$	$3.24^{+3.38}_{-3.24}$
MC exp. SM events	22.49	150.10
MC exp. PowhegPythiaTTbar events	16.00	114.63
MC exp. SherpaZMassiveBC events	0.00	8.19
MC exp. SherpaZMassiveBC_extStats events	0.00	0.70
MC exp. SherpaZMassiveBC_HTFilter events	0.00	0.16
MC exp. JetSmearing events	0.07	0.00
MC exp. SingleTopDiLept events	1.08	12.12
MC exp. PowhegDibosons events	3.72	10.13
MC exp. ttbarV events	0.30	1.03
data-driven exp. fake lepton events	1.32	3.15

Table 4.21: Background fit results in the SF channel (ee and  $\mu\mu$  combined) for an integrated luminosity of  $20.3 \text{ fb}^{-1}$ . Nominal MC and data-driven expectations are given for comparison. The uncertainties shown are statistical + systematic.

	$N_{ee}$	$N_{\mu\mu}$	$N_{SF}$
<b>Side-band fit</b>			
$t\bar{t}$	$4.14 \pm 1.41$	$4.15 \pm 1.62$	$8.32 \pm 2.52$
tW	$0.49 \pm 0.28$	$0.54 \pm 0.32$	$1.02 \pm 0.61$
WW	$0.24 \pm 0.10$	$0.62 \pm 0.48$	$0.86 \pm 0.67$
Total flavour-symmetric bkg	<b><math>4.87 \pm 1.43</math></b>	<b><math>5.31 \pm 1.72</math></b>	<b><math>10.18 \pm 2.67</math></b>
<b>Flavour-symmetry method</b>			
Total flavour-symmetric bkg	<b><math>2.75 \pm 1.38</math></b>	<b><math>3.27 \pm 1.60</math></b>	<b><math>6.02 \pm 2.56</math></b>

Table 4.22: Final estimates for flavour-symmetric backgrounds from the flavour-symmetry method compared to the estimates from the side-band fit. The contribution of  $Z \rightarrow \tau\tau$  to the fit is negligible. All sources of uncertainty are considered in the shown errors.

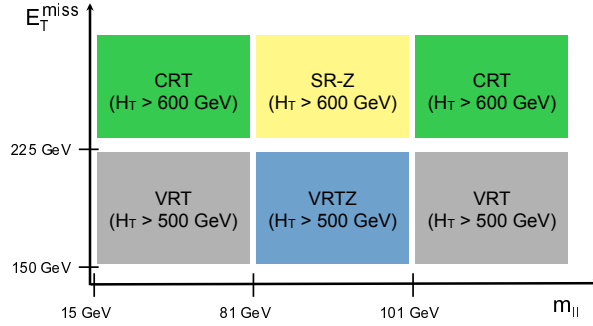


Figure 4.25: Diagram indicating the position in the  $E_T^{\text{miss}}$  versus dilepton invariant mass plane of the SR, the control region CRT, and the two validation regions (VRT and VRTZ) used to validate the side-band fit. VRT and VRTZ have lower  $H_T$  thresholds than CRT and SR.

the normalization factor is transferred to VRTZ (used as validation region). The results of this method for the  $ee$ ,  $\mu\mu$  and SF channels are shown in Table 4.23. Good agreement is found between the observed and fitted number of events in VRTZ in the  $ee$  and same-flavour channels. In the  $\mu\mu$  channel agreement within approximately one sigma is observed, although the fitted number of events is below data.

It should be noticed that these regions are very statistically limited. If the  $\Delta\phi$  cut is dropped in order to gain some statistics, a perfect agreement is found in this test for all three channels,  $ee$ ,  $\mu\mu$  and SF, as it can be seen in Table B.19. Hence the larger difference between expected and observed events in the VRTZ  $\mu\mu$  channel on Table 4.23, compared to the  $ee$  and SF channels, is attributed to a statistical fluctuation in data in this channel. The good agreement between the observed and fitted number of events in VRTZ

supports the assumption that extrapolation in  $m_{\ell\ell}$  (as done for the CRT to SR extrapolation) is reliable. The  $t\bar{t}$  normalization factors obtained when using VRT as control region are  $\mu_{Top}^{\text{VRT}} = 0.75 \pm 0.12$ ,  $0.67 \pm 0.12$  and  $0.71 \pm 0.11$  for  $ee$ ,  $\mu\mu$  and SF channel, respectively. For completeness, Table 4.24 shows the normalization factors found in all the studied regions.

It can be seen that  $\mu_{Top}$  factors in CRT are lower than  $\mu_{Top}^{\text{VRT}}$ . The reason why these two sets of factors show a disagreement becomes evident when looking at Fig. 4.26: the agreement between data and MC, especially in the electron channel, is better in the lower  $E_T^{\text{miss}}$  region where VRT is located, resulting in higher  $t\bar{t}$  normalization factors in low  $E_T^{\text{miss}}$  regions.

While trying to use VRTZ\_highHT as a validation region to test the normalization factor obtained in CRT<sup>5</sup> ( $\mu_{Top}$ ), a cross-section based  $t\bar{t}$ -reweighting technique was tested to correct the MC shape to data. Although this resulted in a higher  $\mu_{Top}$  factor, the final estimates in the SR were completely consistent (within a few percent) with the ones obtained before reweighting. Hence it was decided not to apply the  $t\bar{t}$ -reweighting. Thus the  $\mu_{Top}$  obtained from VRTZ\_highHT is known to be invalid in the SR at higher  $E_T^{\text{miss}}$ .

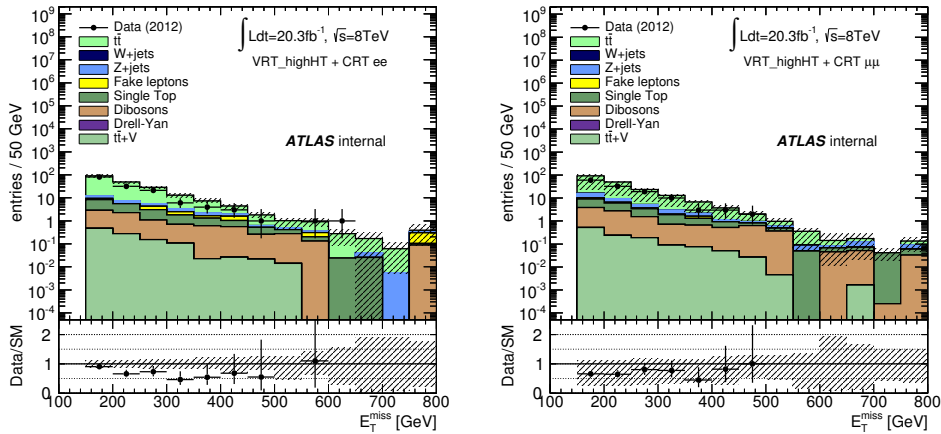


Figure 4.26:  $E_T^{\text{miss}}$  distribution in VRT\_highHT ( $E_T^{\text{miss}} < 225$  GeV) and CRT ( $E_T^{\text{miss}} > 225$  GeV) for the electron (left) and muon (right) channels. The agreement between data and MC is better for lower  $E_T^{\text{miss}}$  values, corresponding to VRT\_highHT.

<sup>5</sup>This would mean having a usual “validation region” procedure, where the VR is used to directly test the normalization factor obtained in the CR, as the majority of the analyses do.



	SRee	VRTee	VRTZee
Observed events	-	166	23
Fitted bkg events	$8.12 \pm 1.23$	$165.97 \pm 13.00$	$26.31 \pm 3.09$
Fitted PowhegPythiaTTbar events	$5.88 \pm 1.10$	$132.08 \pm 15.90$	$19.21 \pm 2.91$
MC exp. SM events	10.10	210.37	32.77
MC exp. PowhegPythiaTTbar events	7.86	176.48	25.67
	SRmm	VRTmm	VRTZmm
Observed events	-	162	30
Fitted bkg events	$9.73 \pm 2.41$	$161.93 \pm 12.85$	$22.31 \pm 4.25$
Fitted PowhegPythiaTTbar events	$5.47 \pm 1.98$	$123.17 \pm 17.12$	$16.95 \pm 4.29$
MC exp. SM events	12.39	221.76	30.53
MC exp. PowhegPythiaTTbar events	8.14	183.00	25.18
	SRSF	VRTSF	VRTZSF
Observed events	-	328	53
Fitted bkg events	$17.87 \pm 2.59$	$327.83 \pm 18.41$	$48.43 \pm 5.35$
Fitted PowhegPythiaTTbar events	$11.37 \pm 1.95$	$255.30 \pm 27.02$	$36.07 \pm 5.14$
MC exp. SM events	22.49	432.13	63.20
MC exp. PowhegPythiaTTbar events	16.00	359.48	50.84

Table 4.23: Background fit results from VRT in the the SR, VRT and VRTZ for an integrated luminosity of  $20.3 \text{ fb}^{-1}$ . The uncertainties shown are statistical + systematic. VRT has been used as control region to normalize  $t\bar{t}$ , while VRTZ is used as validation region.

	$ee$ channel	$\mu\mu$ channel	SF channel
$\mu_{Top}$ (CRT)	$0.53 \pm 0.14$	$0.51 \pm 0.15$	$0.52 \pm 0.12$
$\mu_{Top}^{VRT\_highHT}$	$0.83 \pm 0.11$	$0.63 \pm 0.11$	$0.73 \pm 0.08$
$\mu_{Top}^{VRT}$	$0.75 \pm 0.12$	$0.67 \pm 0.12$	$0.71 \pm 0.11$

Table 4.24: Summary of the  $t\bar{t}$  normalization factors ( $\mu_{Top}$ ) found in three different Control Region selections.

### 4.6.3.3 Closure test of the analysis in validation regions

In this section, the whole flavour-symmetry method is tested in CRT as well as in six different validation regions defined as close to SR/CRT as possible by lowering the  $E_{\text{T}}^{\text{miss}}$  and/or  $H_{\text{T}}$  cuts. Three of these regions lie within the  $Z$  mass-window (VRTZ, VRTZ\_highHT, VRTZ\_highMET, as defined in Table 4.1) while the other four are in the  $Z$ -side-band (CRT, VRT, VRT\_highHT, VRT\_highMET, also defined in Table 4.1).

The test is conceived to be as similar to the nominal analysis as possible, so all backgrounds are estimated in the same way as in SR whenever possible:

- Flavour-symmetric backgrounds are estimated with the flavour-symmetry method.
- $Z(\rightarrow ee, \mu\mu)+\text{jets}$  is estimated using the jet-smearing method in the  $Z$ -window regions (except for VRTZ\_highMET with too low statistics to apply jet-smearing) in the  $ee$  and  $\mu\mu$  channels and from direct MC in the  $Z$ -side-band regions and in the  $e\mu$  channel.
- Fake leptons are estimated with the matrix method.
- Other background sources are taken from direct MC.

The final SM background estimate in each of these regions is compared with the number of observed data events. These results are shown in Table 4.25 for the  $Z$ -window regions and in Table 4.26 for the  $Z$ -side-band regions. Note that the Flavour-symmetry method takes  $N_{e\mu}$  from data and subtracts the flavour-non-symmetric backgrounds from MC. Therefore, the total background number for  $N_{e\mu}$  perfectly agrees with the number of data by construction. Only statistical errors are shown in these tables.

An overview of the final background estimates compared to data in all regions is shown in Fig. 4.27. In all cases the data are consistent with the prediction. These results show the robustness of the background estimation methods used and the consistency of the analysis.

Region	background type	$N_{ee}^{est}$	$N_{\mu\mu}^{est}$	$N_{e\mu}$
VRTZ	Flavour-sym method	$22.24 \pm 3.99$	$23.21 \pm 4.22$	$39.51 \pm 6.41$
	$Z(\rightarrow ee, \mu\mu)+jets$ (jet-smearing)	$0.46 \pm 0.11$	$0.64 \pm 0.14$	$0.00 \pm 0.00$
	tZ, WZ, ZZ, $t\bar{t}V$	$2.73 \pm 0.38$	$2.53 \pm 0.33$	$0.33 \pm 0.08$
	Fakes	$1.55 \pm 1.08$	$-0.10 \pm 1.13$	$0.16 \pm 1.34$
	<b>TOTAL bkg</b>	<b><math>26.98 \pm 4.15</math></b>	<b><math>26.28 \pm 4.38</math></b>	$40.00 \pm 6.55$
	<b>DATA</b>	<b>23</b>	<b>30</b>	40
VRTZ_highHT	Flavour-sym method	$11.70 \pm 2.73$	$12.41 \pm 2.92$	$20.96 \pm 4.62$
	$Z(\rightarrow ee, \mu\mu)+jets$ (jet-smearing)	$0.35 \pm 0.09$	$0.50 \pm 0.12$	$0.00 \pm 0.00$
	tZ, WZ, ZZ, $t\bar{t}V$	$1.60 \pm 0.30$	$1.44 \pm 0.25$	$0.21 \pm 0.08$
	Fakes	$1.10 \pm 0.82$	$0.30 \pm 0.83$	$-0.16 \pm 0.68$
	<b>TOTAL bkg</b>	<b><math>14.75 \pm 2.87</math></b>	<b><math>14.65 \pm 3.05</math></b>	$21.00 \pm 4.67$
	<b>DATA</b>	<b>17</b>	<b>12</b>	21
VRTZ_highMET	Flavour-sym method	$4.77 \pm 1.82$	$5.43 \pm 2.11$	$8.87 \pm 3.34$
	$Z(\rightarrow ee, \mu\mu)+jets$ (MC)	$0.00 \pm 0.00$	$0.00 \pm 0.00$	$0.00 \pm 0.00$
	tZ, WZ, ZZ, $t\bar{t}V$	$2.38 \pm 0.36$	$2.53 \pm 0.33$	$0.09 \pm 0.03$
	Fakes	$-0.04 \pm 0.45$	$0.83 \pm 0.99$	$1.04 \pm 1.16$
	<b>TOTAL bkg</b>	<b><math>7.11 \pm 1.91</math></b>	<b><math>8.79 \pm 2.36</math></b>	$10.00 \pm 3.54$
	<b>DATA</b>	<b>11</b>	<b>12</b>	10

Table 4.25: Estimated number of events for the  $ee$  and  $\mu\mu$  channels in the  $Z$ -window regions compared to the number of observed data.  $N_{e\mu}$  is taken from data and shown only for completeness. Only statistical errors are shown.

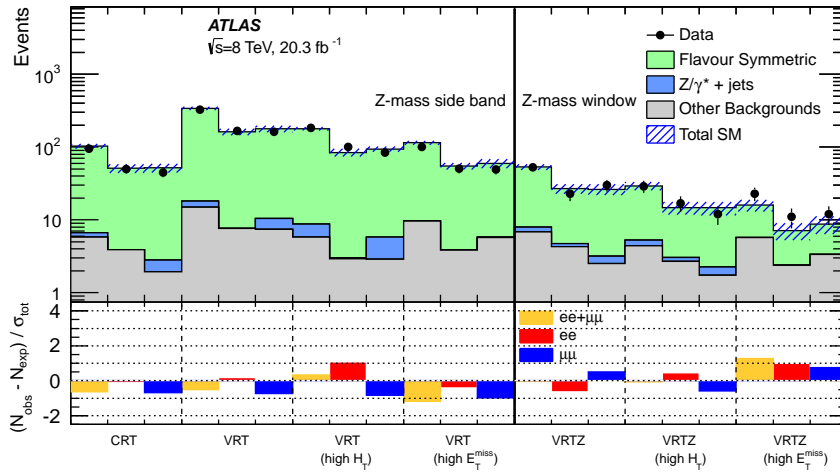


Figure 4.27: The observed and expected yields in CRT and the VRs in the  $Z$  boson mass side-bands (*left*) and the  $Z$  boson mass window (*right*) regions. The *bottom* plot shows the difference in standard deviations between the observed and expected yields. The backgrounds due to  $WZ$ ,  $ZZ$  or rare top processes, as well as from lepton fakes, are included under “Other Backgrounds”.

Region	background type	$N_{ee}^{\text{est}}$	$N_{\mu\mu}^{\text{est}}$	$N_{e\mu}$
CRT	Flavour-sym method	$47.32 \pm 6.77$	$49.06 \pm 7.08$	$83.77 \pm 9.98$
	$Z(\rightarrow ee, \mu\mu)+\text{jets}$ (MC)	$0.01 \pm 0.01$	$0.84 \pm 0.08$	$0.28 \pm 0.05$
	$tZ, WZ, ZZ, t\bar{t}V$	$1.35 \pm 0.22$	$1.34 \pm 0.18$	$2.19 \pm 0.26$
	Fakes	$2.53 \pm 1.96$	$0.61 \pm 1.97$	$4.76 \pm 3.67$
	<b>TOTAL bkg</b>	<b><math>51.21 \pm 7.05</math></b>	<b><math>51.85 \pm 7.35</math></b>	$91.0 \pm 10.17$
	<b>DATA</b>	<b>50</b>	<b>45</b>	91
VRT	Flavour-sym method	$154.41 \pm 15.54$	$167.98 \pm 16.81$	$280.41 \pm 18.89$
	$Z(\rightarrow ee, \mu\mu)+\text{jets}$ (MC)	$0.06 \pm 0.01$	$3.10 \pm 0.25$	$0.30 \pm 0.05$
	$tZ, WZ, ZZ, t\bar{t}V$	$1.93 \pm 0.23$	$2.00 \pm 0.20$	$3.73 \pm 0.32$
	Fakes	$5.68 \pm 5.57$	$5.41 \pm 8.15$	$11.56 \pm 11.51$
	<b>TOTAL bkg</b>	<b><math>162.08 \pm 16.51</math></b>	<b><math>179.49 \pm 18.68</math></b>	$296.0 \pm 22.12$
	<b>DATA</b>	<b>166</b>	<b>162</b>	296
VRT_highHT	Flavour-sym method	$81.50 \pm 9.73$	$88.36 \pm 7.01$	$147.73 \pm 13.60$
	$Z(\rightarrow ee, \mu\mu)+\text{jets}$ (MC)	$0.06 \pm 0.01$	$2.93 \pm 0.23$	$0.22 \pm 0.04$
	$tZ, WZ, ZZ, t\bar{t}V$	$1.23 \pm 0.18$	$1.13 \pm 0.14$	$2.21 \pm 0.24$
	Fakes	$1.70 \pm 3.21$	$1.74 \pm 3.61$	$8.84 \pm 7.20$
	<b>TOTAL bkg</b>	<b><math>84.49 \pm 10.25</math></b>	<b><math>94.16 \pm 7.89</math></b>	$159.00 \pm 15.39$
	<b>DATA</b>	<b>100</b>	<b>84</b>	159
VRT_highMET	Flavour-sym method	$50.99 \pm 5.4$	$53.87 \pm 7.51$	$91.16 \pm 10.43$
	$Z(\rightarrow ee, \mu\mu)+\text{jets}$ (MC)	$0.00 \pm 0.00$	$0.12 \pm 0.10$	$0.09 \pm 0.02$
	$tZ, WZ, ZZ, t\bar{t}V$	$0.97 \pm 0.18$	$1.30 \pm 0.20$	$1.64 \pm 0.26$
	Fakes	$2.89 \pm 2.05$	$4.42 \pm 3.62$	$5.12 \pm 4.50$
	<b>TOTAL bkg</b>	<b><math>54.85 \pm 5.78</math></b>	<b><math>59.59 \pm 8.34</math></b>	$98.00 \pm 11.36$
	<b>DATA</b>	<b>51</b>	<b>49</b>	98

Table 4.26: Estimated number of events for the  $ee$  and  $\mu\mu$  channels in the  $Z$ -sideband regions compared to the number of observed data.  $N_{e\mu}$  is taken from data and shown only for completeness. Only statistical errors are shown.

#### 4.6.4 Fake-lepton background estimation

Events from  $W \rightarrow \ell\nu + \text{jets}$ , semileptonic and hadronic  $t\bar{t}$ , single top ( $s$ - and  $t$ -channel) and multi-jets (or QCD) contribute to the background in the dilepton channels due to “fake” leptons. Fakes can arise from  $b$ -hadron decays, misidentified hadrons or converted photons. In the case of photon conversions and  $b$ -hadron decays, an actual electron is present in the final state. These electrons are still considered fake in the sense that they are not produced in isolation as part of the prompt decay of a particle of interest. Therefore, the term “real” lepton is reserved for prompt leptons produced in isolation (e.g. from the decays of  $Z$  bosons).

The fake leptons contribution is estimated using a data-driven Matrix Method (MM) which is described in detail in Ref. [128] and is summarized in the next paragraphs. For the sake of clarity, the matrix method for a single lepton selection will be explained first and after that, the method will

be expanded to the case, used in this analysis, of a dilepton selection<sup>6</sup>.

### The Matrix Method

The MM involves creating a control sample using baseline leptons, thereby loosening the lepton isolation and identification requirements (as described in Section 4.4) and increasing the probability of selecting a fake lepton. For each analysis region (control, validation or signal), the relevant cuts are applied to this control sample and the next steps are followed:

- count the number of events with leptons that pass the baseline (*loose*) selection but fail the signal lepton (*tight*) selection,  $N^L$ .<sup>7</sup>
- count the number of events with leptons that pass the signal lepton (*tight*) selection,  $N^T$ .
- These numbers can be expressed as linear combinations of the number of events with a real or a fake lepton:

$$N^L = N_{\text{Real}}^L + N_{\text{Fake}}^L, \quad (4.4)$$

$$N^T = \frac{r}{1-r} N_{\text{Real}}^L + \frac{f}{1-f} N_{\text{Fake}}^L, \quad (4.5)$$

- where  $r = N_{\text{Real}}^T / (N_{\text{Real}}^L + N_{\text{Real}}^T)$  is the fraction of real leptons passing the loose selection that also pass the tight selection and
- $f = N_{\text{Fake}}^T / (N_{\text{Fake}}^L + N_{\text{Fake}}^T)$  is the fraction of fake leptons passing the loose selection that also pass the tight selection.
- If  $r$  and  $f$  are known, the number of events with fake leptons can be calculated from Equation 4.4 as:

$$N_{\text{Fake}}^T = \frac{N^L - (1/r - 1)N^T}{1/f - 1/r}, \quad (4.6)$$

given a measured  $N^L$  and  $N^T$ .

This method is expanded to a dilepton sample using a four-by-four matrix to account for the various possible real-fake combinations for the two leading leptons in the events. This matrix relates the number of tight-tight (TT), tight-loose (TL), loose-tight (LT) and loose-loose (LL) leptons in the event to the number of real-real

<sup>6</sup>Although the MM for a single lepton selection has been explained in the previous chapter, it will also be described here, for the sake of clarity and, to define a more appropriate notation for the case where two fake leptons can be selected.

<sup>7</sup>To conserve the original MM notation, baseline leptons will be denoted as “loose” and signal leptons as “tight” in this section.

(RR), real-fake (RF), fake-real (FR) and fake-fake (FF) leptons in the event:

$$\begin{pmatrix} N^{\text{TT}} \\ N^{\text{TL}} \\ N^{\text{LT}} \\ N^{\text{LL}} \end{pmatrix} = \begin{bmatrix} rr & rf & fr & ff \\ r(1-r) & r(1-f) & f(1-r) & f(1-f) \\ (1-r)r & (1-r)f & (1-f)r & (1-f)f \\ (1-r)(1-r) & (1-r)(1-f) & (1-f)(1-r) & (1-f)(1-f) \end{bmatrix} \cdot \begin{pmatrix} N_{\text{RR}} \\ N_{\text{RF}} \\ N_{\text{FR}} \\ N_{\text{FF}} \end{pmatrix}$$

This matrix can then be inverted to take the measured quantities ( $N^{\text{TT}}$ ,  $N^{\text{TL}}$ ,  $N^{\text{LT}}$ ,  $N^{\text{LL}}$ ) and extract the quantities we want to know ( $N_{\text{RR}}$ ,  $N_{\text{RF}}$ ,  $N_{\text{FR}}$ ,  $N_{\text{FF}}$ ).

It is important to note that the weights associated with the MM for TT and LL events are negative. This allows for the possibility for the MM to give an accurate prediction in regions where there are no fake leptons, since the event weights can sum to zero. However, this assumption is driven by the statistical composition ( $N^{\text{TT}}$ ,  $N^{\text{TL}}$ ,  $N^{\text{LT}}$ ,  $N^{\text{LL}}$ ) and the separation between the real and fake efficiency. There are cases where an overall negative prediction can occur, however within the statistical and systematic errors the prediction should be consistent with zero.

The efficiency for fake leptons,  $f$ , is estimated in control regions enriched with multi-jet events. The background due to processes containing prompt leptons, estimated from MC samples, is subtracted from the total data contribution in this region. From the resulting data sample the fraction of events in which the baseline leptons pass the signal lepton requirements give the fake efficiency. The real lepton efficiency,  $r$ , is estimated using  $Z \rightarrow \ell^+ \ell^-$  events in a data sample enriched with leptonically decaying  $Z$  bosons.

The calculations of the fake and real lepton efficiencies used in this analysis were performed centrally by the ATLAS group dedicated to the “*Search for strongly produced supersymmetric particles in decays with leptons*” and are documented in Appendix G of the internal note in Ref [129].

#### 4.6.4.1 Fake leptons background validation

In order to investigate the validity of the estimate of the fake lepton background a new validation region has been defined. The fake lepton enriched region used to perform the validation is defined as follows:

- at least two signal leptons
- two leading leptons are same sign
- Leading lepton  $p_T > 25$  GeV, second lepton  $p_T > 10$  GeV
- $E_T^{\text{miss}} < 100$  GeV
- veto the lowest range of the invariant mass of two leading leptons  $m_{\ell\ell} > 15$  GeV

	$E_T^{\text{miss}}[\text{GeV}]$	$n_{\text{jets}}$	$m_{\ell\ell}[\text{GeV}]$	charge sign
VRQCD	$< 100$	$\geq 2$	$m_{\ell\ell} > 15$ AND ( $m_{\ell\ell} < 40$ OR $m_{\ell\ell} > 140$ )	SS

Table 4.27: Definition of the fake lepton enriched validation region. The dilepton pair electric charge sign is denoted as SS for same sign. More details about the selection are given in the text

- invariant mass of two leading leptons in the  $Z$  boson mass side-band  $m_{\ell\ell} < 40$  OR  $m_{\ell\ell} > 140$
- two or more jets with  $p_T > 35$  GeV (and  $|JVF| > 0.25$  if  $p_T < 50$ ,  $|\eta| < 2.4$ )
- trigger matching as specified in Section 4.5.1

An overview of this validation region can be seen in Table 4.27. Comparisons between the background estimation and data distributions in both  $H_T$  and  $E_T^{\text{miss}}$  in the VRQCD are shown in Figures 4.28 and 4.29, respectively. The indicated error lines (denoted as “Fake unc. up and down”) contain only the statistical and systematic uncertainties on the fake lepton background as no detector-related uncertainties have been considered for this study. To avoid double counting fake lepton events, all MC estimations have been done requiring both leptons to be prompt by selecting only events where both leptons originate from either a tau lepton, a top quark, or a  $W/Z$  boson. There is an exception to this in the electron channel, where leptons originating from photon conversions are also allowed in order to account for trident events<sup>8</sup>. This is done because for electrons in a same-sign selection there is non-negligible overlap between fakes and charge-flip from trident processes, and disentangling these effects is beyond the scope of this study.

An apparent dip in data with respect to the background estimation is observed in the  $\mu\mu$  channel (Fig. 4.29 right) and has been subject to scrutiny. Checks on the distributions of events falling in this dip have not turned up anything suspicious. It’s also worth pointing out that these plots do not include all the uncertainties in the error band. This apparent lack of data events is therefore attributed to a statistical fluctuation of the data. Consequently, it can be concluded that these plots show in general good agreement within the errors.

<sup>8</sup>Trident event: A process of an electron emitting a bremsstrahlung photon where the photon later converts into an  $e^+e^-$  pair. In the end, three tracks coming from the electron, forming a trident pattern, are detected. In the hard bremsstrahlung case, for instance,

$$e_{\text{hard}}^- \rightarrow e_{\text{soft}}^- + \gamma_{\text{hard}} \rightarrow e_{\text{soft}}^- + e_{\text{soft}}^- + e_{\text{hard}}^+,$$

the reconstructed positron contains most of the energy of the electron from the  $Z$  decay but with opposite charge, therefore it produces same-sign events in the  $Z$  mass region.

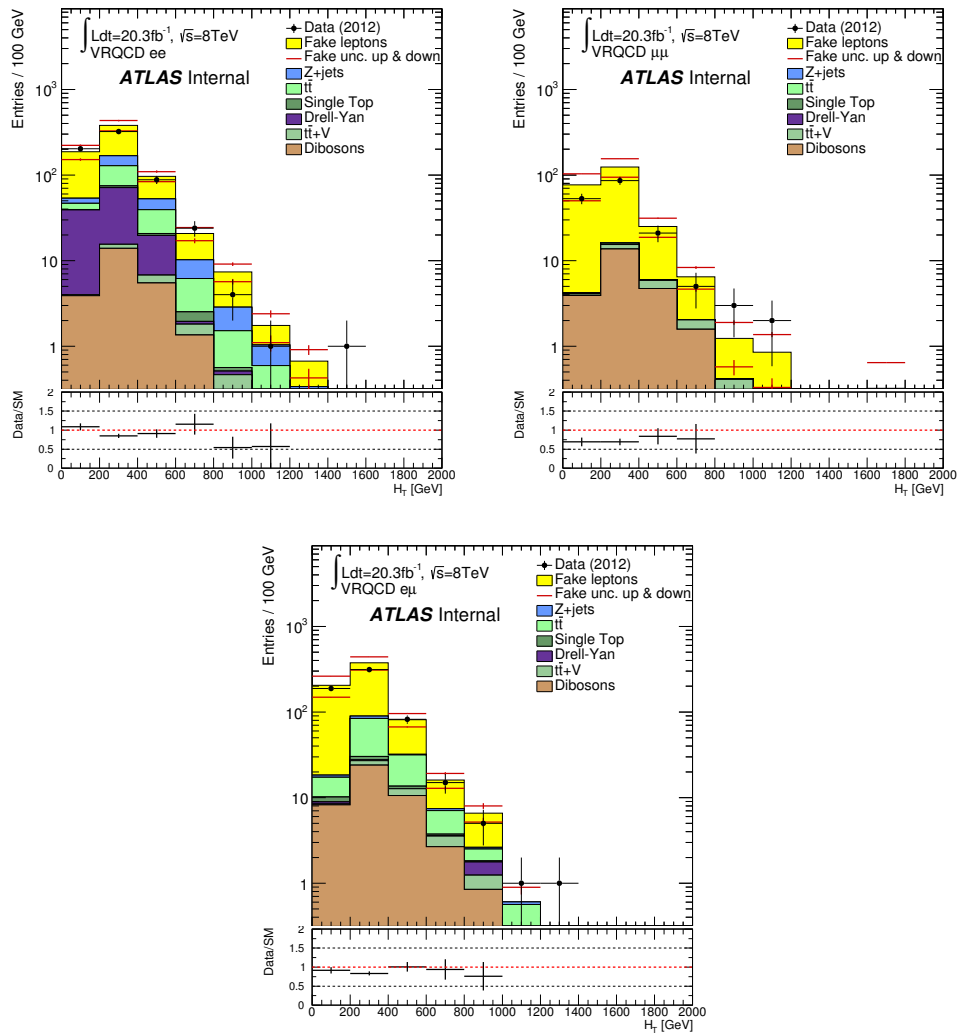


Figure 4.28:  $H_T$  distribution in VRQCD for  $ee$  channel (left),  $\mu\mu$  channel (right) and  $e\mu$  channel (bottom). Only fake leptons statistical and systematic errors and data statistical errors are shown. No detector related uncertainties are considered here.



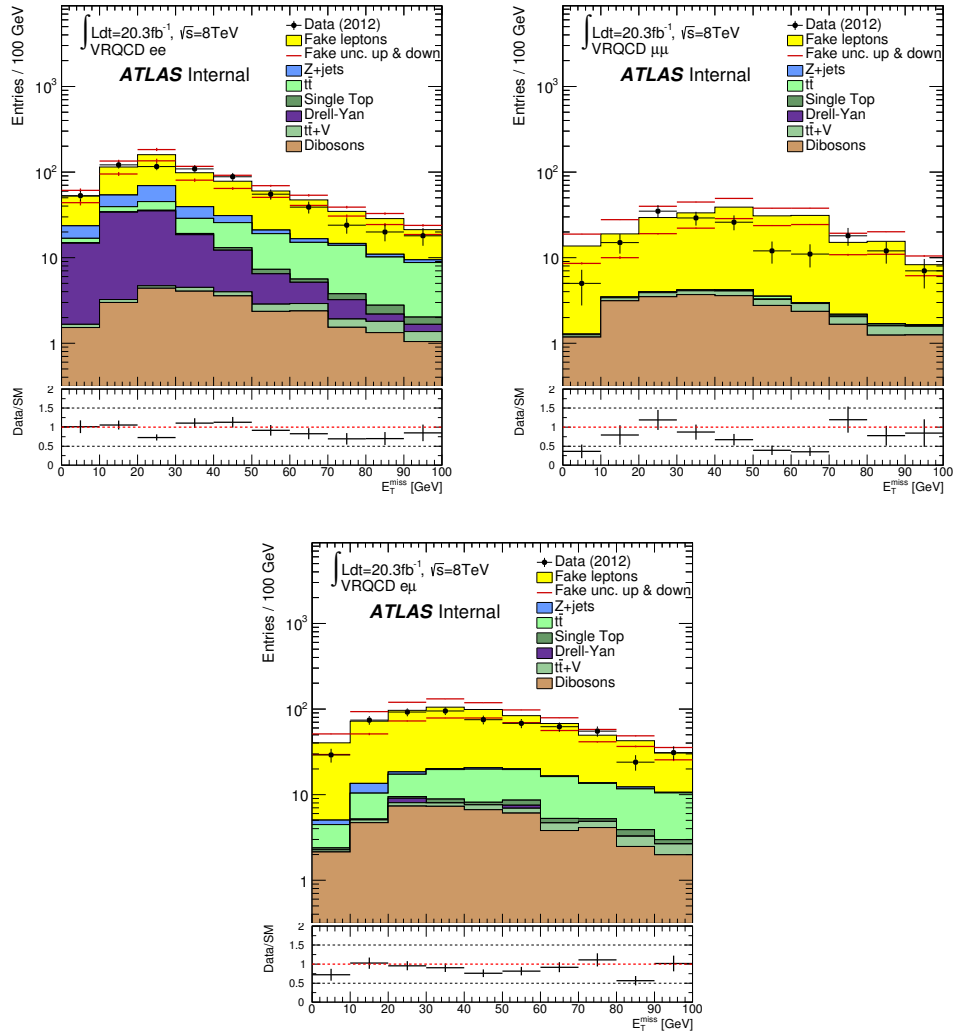


Figure 4.29:  $E_T^{\text{miss}}$  distribution in VRQCD for  $ee$  channel (left),  $\mu\mu$  channel (right) and  $e\mu$  channel (bottom). Only fake leptons statistical and systematic errors and data statistical errors are shown. No detector related uncertainties are considered here.

#### 4.6.4.2 Results of the Fake Leptons estimation

The estimates for this background are small ( $< 10\%$  of the total background) in all regions, and are summarized in Table 4.28. For comparisons with the total background estimates in each region, one needs to go back to Tables 4.14, 4.19, 4.20 and 4.21. The definitions of all regions can be found in Table 4.1.

The background yields are shown for the  $ee$  and  $\mu\mu$  channel separately (except for  $\text{CRe}\mu$  which has only a single opposite-flavour channel) as well as for the combination of both (SF channel). This facilitates the integration of these estimations into other parts of the analysis. Note that for the previously mentioned background methods (see Sections 4.6.1 and 4.6.2) these estimations of the number of fake lepton events in each region have been used.

channel	SRee	SRmm	SRSF
Fake lepton events	$0.10 \pm_{0.10}^{0.66}$	$1.22 \pm_{1.22}^{1.30}$	$1.32 \pm_{1.32}^{1.70}$
channel	$\text{CRe}\mu$		
Fake lepton events	$0.66 \pm 0.62$		
channel	CRTee	CRTmm	CRTSF
Fake lepton events	$2.53 \pm 1.96$	$0.61 \pm_{0.61}^{1.97}$	$3.15 \pm_{3.15}^{3.64}$
channel	VRTee	VRTmm	VRTSF
Fake lepton events	$5.67 \pm 5.57$	$5.41 \pm_{5.41}^{8.15}$	$11.08 \pm_{11.08}^{13.39}$
channel	VRTZee	VRTZmm	VRTZSF
Fake lepton events	$1.55 \pm 1.08$	$0.00 \pm_{0.00}^{1.13}$	$1.45 \pm_{1.45}^{1.95}$

Table 4.28: Number of fake lepton events in SR,  $\text{CRe}\mu$ , CRT, VRT and VRTZ estimated with the Matrix Method. The uncertainties shown are statistical and systematic added quadratically.

#### 4.6.5 Estimation of other backgrounds

The remaining background processes, including diboson events with a  $Z$  boson decaying to leptons and the  $t\bar{t} + W(W)/Z$  and  $t + Z$  backgrounds, are estimated from MC simulation. In these cases the most accurate theoretical cross sections available are used. Care is taken to ensure that the flavour-symmetric component of these backgrounds (for events where the two leptons do not originate from the same  $Z$  decay) is not double-counted.

## 4.7 Systematic uncertainties

Systematic uncertainties affecting the predicted background rate and SUSY signal yields in the signal regions have been evaluated and will be summarized in this section. Table 4.30 summarizes the systematic uncertainties applied to the background estimations and points which ones are used for the flavour-symmetry method and the side-band fit.

### 4.7.1 Experimental uncertainties

All experimental uncertainties are listed in this section.

- **Jet energy scale (JES)** The JES uncertainty is estimated based on Monte Carlo studies and in-situ measurements and provided by the ATLAS Jet/Etmiss group in bins of  $p_T$  and  $\eta$  of the jets. This analysis uses a reduced set of JES nuisance parameters. For the fit used to constrain the backgrounds in this analysis, a further reduction to this set of nuisance parameters is made. Any uncertainties contributing less than 2% of the total background systematic in all control, signal, and validation regions are not included in the nominal fit setup. More details can be found in Refs. [62, 114].
- **Trigger efficiency** A 5% uncertainty is applied to account for the uncertainty on the trigger efficiency, as in [121].
- **Jet energy resolution (JER)** This uncertainty is estimated using an ATLAS centrally produced software package [130]. It provides the current estimate of the jet energy resolution and its uncertainty for jets reconstructed with the anti- $k_t$ 4 jet algorithm as described in Ref. [131].
- **Jet vertex fraction (JVF)** The uncertainty on the JVF is assessed by varying the JVF threshold from the nominal 0.25 down to 0.21 and up to 0.28.
- **Lepton scale, resolution and efficiency** The measurements of the lepton identification efficiencies and the corresponding correction factors are also influenced by systematic uncertainties [132]. The related uncertainties are provided by the ATLAS Egamma [133] and MCP groups [134]. In the analysis the efficiency scale factors are varied up and down within the uncertainties as specified in the corresponding packages.
- **Pileup uncertainty** An uncertainty on the pileup weight is assessed by varying the scaling factor as recommended by the SUSY WG.
- **Missing energy uncertainties** Two parameters are associated with the  $E_T^{\text{miss}}$  soft terms uncertainty. One considers variations in the Cell Out energy scale and the other variations in the Cell Out energy resolution.

#### 4.7.1.1 Uncertainties for the data-driven background estimates

The  $Z/\gamma^* + \text{jets}$  background estimate has an uncertainty to account for differences between pseudo-data and MC events, the choice of seed region definition, the statistical precision of the seed region, and the jet response functions used to create the pseudo-data.

The additional sources of systematic uncertainties for the background estimation via the flavour-symmetry method are summarized in the following:

- MC systematic uncertainties due to subtraction of non flavour-symmetric backgrounds ( $ZZ$ ,  $WZ$ , single top ( $tZ$ ) and  $t\bar{t}V$ ) from data in the  $\text{CRe}\mu$ .
- A detailed study of the relevant trigger efficiencies has been performed in [121]. A flat 5% uncertainty is assigned to account for the small differences observed between data and MC.
- $E_T^{\text{miss}}$  dependence of  $k_{ee}$  and  $k_{\mu\mu}$  scale factors, as detailed in section 4.6.2.3

MC estimates based on the flavour-symmetry method and direct MC estimation are compatible within errors, as has been shown in Section 4.6.3.1. Therefore, no additional non-closure uncertainty is applied.

An uncertainty derived from the difference in real-lepton efficiency observed in  $t\bar{t}$  and  $Z \rightarrow \ell^+\ell^-$  events is assigned to the fake-background prediction. An additional uncertainty due to the number of events in the control samples used to derive the real efficiencies and fake rates is assigned to this background, as well as a 20% uncertainty on the MC background subtraction in the control samples.

### 4.7.2 Signal contamination in control and validation regions

Another possible source of uncertainty is the signal contamination in the control and validation regions. The presence of signal events in all the relevant regions has been checked and its magnitude is summarized in Table 4.29. In the GGM model, the maximal signal contamination is typically obtained for low mass scales and it decreases both with  $m(\tilde{g})$  and with  $\mu$ . In the lower mass scale region a signal-to-background ratio of  $S/B < 0.15$  has been found along the exclusion line already set by the  $5.8 \text{ fb}^{-1}$  analysis (see Ref. [94]) in the studied regions (CRe $\mu$ , VRZ, CRT, VRT). For higher mass scales the table shows the maximum signal contamination in these regions along the observed and expected exclusion lines in the current analysis. As it can be read from the table, a maximum value of  $S/B < 0.04$  is seen for the interesting signal parameter space region and thus a possible signal contamination in control and validation regions can be regarded as negligible.

Region	GGM	Max. S/B along exclusion line	
	$\tan \beta$	observed	expected
CRe $\mu$	30	0.02	0.01
	1.5	0.03	0.01
VRZ	30	0.01	0.01
	1.5	0.01	0.01
CRT	30	0.04	0.02
	1.5	0.03	0.01
VRT	30	0.03	0.01
	1.5	0.03	0.01

Table 4.29: Maximum signal contamination in control and validation regions.

### 4.7.3 Theoretical uncertainties

For all backgrounds estimated from MC simulation, the following theoretical uncertainties are considered. The uncertainties due to the choice of factorisation and renormalisation scales are calculated by varying the nominal values by a factor of two. Uncertainties on the PDFs are evaluated following the prescription recommended by PDF4LHC [135]. Total cross-section uncertainties of 22% [136] and 50% are applied to  $t\bar{t} + W/Z$  and  $t\bar{t} + WW$  sub-processes, respectively. For the  $t\bar{t} + W$  and  $t\bar{t} + Z$  sub-processes, an additional uncertainty is evaluated by comparing samples generated with different numbers of partons, to account for the impact of the finite number of partons generated in the nominal samples. For the  $WZ$  and  $ZZ$  diboson samples, a parton shower uncertainty is estimated by comparing samples showered with PYTHIA and HERWIG+JIMMY [137, 138] and cross-section uncertainties of 5% and 7%

are applied, respectively. These cross-section uncertainties are estimated from variations of the value of the strong coupling constant, the PDF and the generator scales. For the small contribution from  $t + Z$ , a 50% uncertainty is assigned. Finally, a statistical uncertainty derived from the finite size of the MC samples used in the background estimation process is included.

Signal cross sections are calculated to next-to-leading order in the strong coupling constant, adding the resummation of soft gluon emission at NLO+NLL accuracy [103–107]. The nominal cross section and the uncertainty are taken from an envelope of cross-section predictions using different PDF sets and factorisation and renormalisation scales, as described in Section 4.3.2.

Type	Uncertainty	Used in:	
		Nominal Method	Side-band Fit
<b>Experimental uncertainties</b>			
JES	Jet Energy Scale	✓	✓
JVF	Jet Vertex Fraction	✓	✓
$E_T^{\text{miss}}$	$E_T^{\text{miss}}$ soft-terms (SCALEST)	✓	✓
JER	Jet Energy Resolution	✓	✓
Trigger	Trigger Efficiency	✓	✓
Event weight	Pile-up weight	✓	✓
	Lepton reconstruction efficiencies (LE)	✓	✓
<b>Flavour-symmetry method specific uncertainties</b>			
	Experimental uncertainties in subtracted MC expectations	✓	
	$k_{ee}, k_{\mu\mu}$ dependency on $E_T^{\text{miss}}$	✓	
	Trigger efficiencies	✓	
<b>Jet-smearing specific uncertainties</b>			
	Statistical uncertainty due to limited number of seed events	✓	✓
	Response function	✓	✓
	$\max(E_T^{\text{miss}}$ significance cut, MC non-closure)	✓	✓
<b>Theory uncertainties</b>			
Dibosons ( $WZ, ZZ$ )	Cross-section	✓	✓
	Parton density function	✓	✓
	Combined MC generator and parton shower	✓	✓
	Factorisation scale variations	✓	✓
	Renormalisation scale variations	✓	✓
$t\bar{t}+V$	Cross-section	✓	✓
	Parton density function	✓	✓
	Envelope (Finite number of partons, parton shower, scale variations)	✓	✓
$t\bar{t}$	MC generator		✓
	Parton shower		✓
	Parton density function		✓
	Envelope (ISR/FSR, factorisation/renormalisation scale variations)		✓
Z+jets	Factorisation scale		✓
	Renormalisation scale		✓
	Parton density function		✓
	Jet-smearing non-closure		✓
Single top	Cross-section		✓
	Parton density function		✓
	Envelope (ISR/FSR, interference, parton shower, MC generator)		✓
Dibosons ( $WW$ )	Cross-section		✓
	Parton density function		✓
	MC generator		✓
	Parton Shower		✓
	Factorisation scale variations		✓
	Renormalisation scale variations		✓

Table 4.30: Summary of uncertainties.

#### 4.7.4 Dominant uncertainties on the background estimates

The dominant uncertainties in the SR, along with their values relative to the total background expectation, are summarised in Table 4.31. The largest uncertainty is that associated with the flavour-symmetric background, whose statistical uncertainty due to the finite data yields in the  $\text{CR}e\mu$  is 24%. The combined MC generator and parton shower modelling uncertainty on the  $WZ$  background (7%), as well as the uncertainty due to the fake-lepton background (14%), are also important.

Source	Relative systematic uncertainty [%] in SR SF
Total systematic uncertainty	29
Flavour-symmetry statistical	24
Flavour-symmetry systematic	4
Fake lepton	14
$WZ$ MC + parton shower	7

Table 4.31: Overview of the dominant sources of systematic uncertainty on the background estimate in the signal region for the SF channel. Their relative values with respect to the total background expectation are shown in %.

## 4.8 Results

The resulting background estimates in the SR, along with the observed event yields, are displayed in Table 4.32. The dominant backgrounds are those due to flavour-symmetric and  $WZ$  and  $ZZ$  diboson processes. The group of flavour-symmetric backgrounds is dominated by  $t\bar{t}$  and makes up  $\sim 60\%$  of the predicted background. Dibosons with real  $Z$  boson production contribute up to 25%, whilst other processes, including those that might be present due to mis-reconstructed jets entering as leptons, can contribute up to 10%. Both the matrix method for fake leptons as well as the flavour-symmetry method can be affected by statistical fluctuations in data. This can be observed, for instance, in the difference of the fakes estimate between the  $ee$  and the  $\mu\mu$  channel and also shows up in the large statistical errors on these estimates. This difference is, therefore, largely attributed to statistical fluctuations, though other sources have been explored in Ref. [97] Appendices F and G.

Table 4.33 shows a comparison of the final results from the flavour-symmetry method with those from the side-band fit. Note that the uncertainties on the flavour symmetry background estimate and those from the sideband fit estimate are uncorrelated (the uncertainty on the flavour symmetry estimate is dominated by the data statistics in  $\text{CR}e\mu$ ). The final estimates from these two methods agree within uncertainties for all regions, though the fit gives a slightly higher nominal estimate. For the interpretations in the next section,



Channel	SR $ee$	SR $\mu\mu$	SRSF
Observed events	16	13	29
Expected background events	$4.2 \pm 1.6$	$6.4 \pm 2.2$	$10.6 \pm 3.2$
Flavour-symmetric backgrounds	$2.8 \pm 1.4$	$3.3 \pm 1.6$	$6.0 \pm 2.6$
$Z/\gamma^* + \text{jets}$ (jet-smearing)	$0.05 \pm 0.04$	$0.02^{+0.03}_{-0.02}$	$0.07 \pm 0.05$
Rare top	$0.18 \pm 0.06$	$0.17 \pm 0.06$	$0.35 \pm 0.12$
$WZ/ZZ$ diboson	$1.2 \pm 0.5$	$1.7 \pm 0.6$	$2.9 \pm 1.0$
Fake leptons	$0.1^{+0.7}_{-0.1}$	$1.2^{+1.3}_{-1.2}$	$1.3^{+1.7}_{-1.3}$

Table 4.32: Final background estimation in SRs after applying a  $\Delta\phi(\text{jet}_{1,2}, E_T^{\text{miss}}) > 0.4$  cut, using the flavour-symmetry method. All sources of uncertainties are considered in the shown errors.

the results from the flavour-symmetry method are taken as the background estimate.

In both the  $ee$  and  $\mu\mu$  channel some excess of data over the estimated background is observed. For each channel, a local probability for the background estimate to produce a fluctuation greater than or equal to the excess observed in the data is calculated using pseudo-experiments. When expressed in terms of the number of standard deviations, this value is referred to as the local significance, or simply the significance. These significances are quantified in the last column of Table 4.34 and correspond to a  $1.7\sigma$  deviation in the muon channel and a  $3.0\sigma$  deviation in the electron channel, with the combined significance, calculated from the sum of the background predictions and observed yields in the muon and electron channels, being  $3.0\sigma$ . The uncertainties on the background predictions in the  $ee$  and  $\mu\mu$  channels are correlated as they are dominated by the statistical uncertainty of the  $e\mu$  data sample that is used to derive the flavour-symmetric background in both channels. Since this sample is common to both channels, the relative statistical error on the flavour-symmetric background estimation does not decrease when combining the  $ee$  and  $\mu\mu$  channels.

Various cross-checks and studies were performed to understand the origin of this excess. They are described in Ref. [97] Appendices A to M.

A summary plot analogous to that in Figure 4.27 but including the SR is shown in Figure 4.30. The plot shows the good agreement between data and prediction in all analysis regions except for the SR.

Signal Region	Flavour-symmetry method	Side-band Fit	Observed events	Significance ( $Z$ ) Flavour-sym	Significance ( $Z$ ) Side-band Fit
SRee	$4.2 \pm 1.6$	$6.4 \pm 1.4$	16	3.0	2.7
SR $\mu\mu$	$6.4 \pm 2.2$	$8.4 \pm 2.1$	13	1.7	1.2
SRSF (ee + $\mu\mu$ )	$10.6 \pm 3.2$	$14.8 \pm 2.9$	29	3.0	2.5

Table 4.33: Background estimates from the flavour-symmetry method and the side-band fit with corresponding uncertainties; final observed number of events and the corresponding Gaussian significance,  $Z$ , in SRs given for the flavour-symmetry method results and for the side-band fit results.

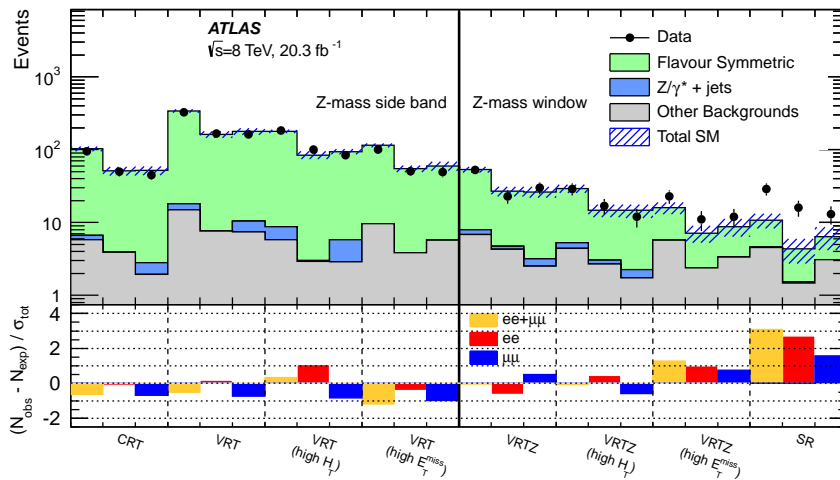


Figure 4.30: Summary of the agreement between data and prediction in all the analysis regions: CRT, VRT( $Z$ ), VRT( $Z$ ) with an additional requirement of  $H_T > 600$  GeV (VRT( $Z$ )-highHT), VRT( $Z$ ) with a higher  $E_T^{\text{miss}} > 225$  GeV requirement and  $400 < H_T < 600$  GeV (VRT( $Z$ )-highMET), and the signal region (SR).

#### 4.8.1 Comparison of data and MC in unblinded SR before and after the $\Delta\phi$ cut

The most relevant kinematic distributions of data and MC are outlined in this subsection. In all plots the background has been taken from MC as it is not straightforward to derive shapes for the various distributions from the nominal background estimation techniques used in this analysis (flavour-symmetry and jet smearing method). Still, these plots are useful to discover obvious problems or features in the unblinded data. The  $t\bar{t}$  background has been scaled by a factor of 0.49 for the case without  $\Delta\phi$  cut and by a factor of 0.52 when the  $\Delta\phi$  cut is applied for both channels as retrieved from the side band fit (see Section 4.6.3.2).

Three GGM signal samples with  $\tan\beta = 1.5$  and  $(m(\tilde{g}) = 700 \text{ GeV}, \mu =$

200 GeV), ( $m(\tilde{g}) = 900$  GeV,  $\mu = 500$  GeV) and ( $m(\tilde{g}) = 1000$  GeV,  $\mu = 700$  GeV) are shown for comparison. These plots can also be used to find other useful variables to distinguish between background and signal in future analysis rounds.

$\Delta\phi(\text{jet}_{1,2}, E_T^{\text{miss}})$  distributions are shown in Fig. 4.31 in the SRs before the cut. Results for the distributions of  $E_T^{\text{miss}}$ ,  $H_T$ ,  $m_{\ell\ell}$  and number of jets in the SRs are shown in Figs. 4.32 to 4.35 respectively.

These comparison plots demonstrate approximately flat ratios between data and MC in many of the SR distributions. There are exceptions, including the  $m_{\ell\ell}$ -distribution, which suggests a  $Z$ -like excess, particularly in the  $ee$  channel. The signal models show a stronger peak in the  $m_{\ell\ell}$ -distribution in the  $ee$  channel as well. The excess appears to be located towards lower values of  $H_T$  in both channels, and at low jet multiplicities in the  $ee$  channel in particular. More quantitative conclusions in the SRs are difficult due to the low statistics.

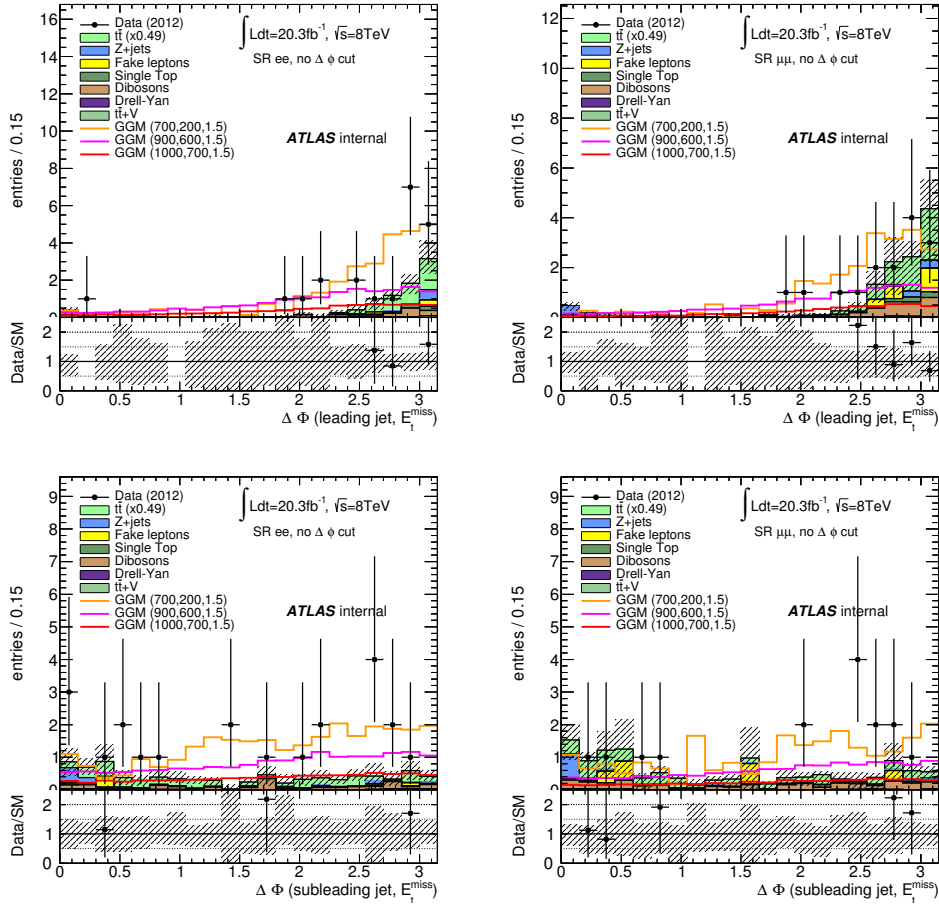


Figure 4.31:  $\Delta\phi$  between leading jet and  $E_T^{\text{miss}}$  (top) and between the subleading jet and  $E_T^{\text{miss}}$  (bottom) in the SRs before the  $\Delta\phi(E_T^{\text{miss}}, \text{jet}) > 0.4$  cut is applied, for electron (left) and muon (right) channel. All detector-related uncertainties are included. Normalization of  $t\bar{t}$  by 0.49 is indicated.

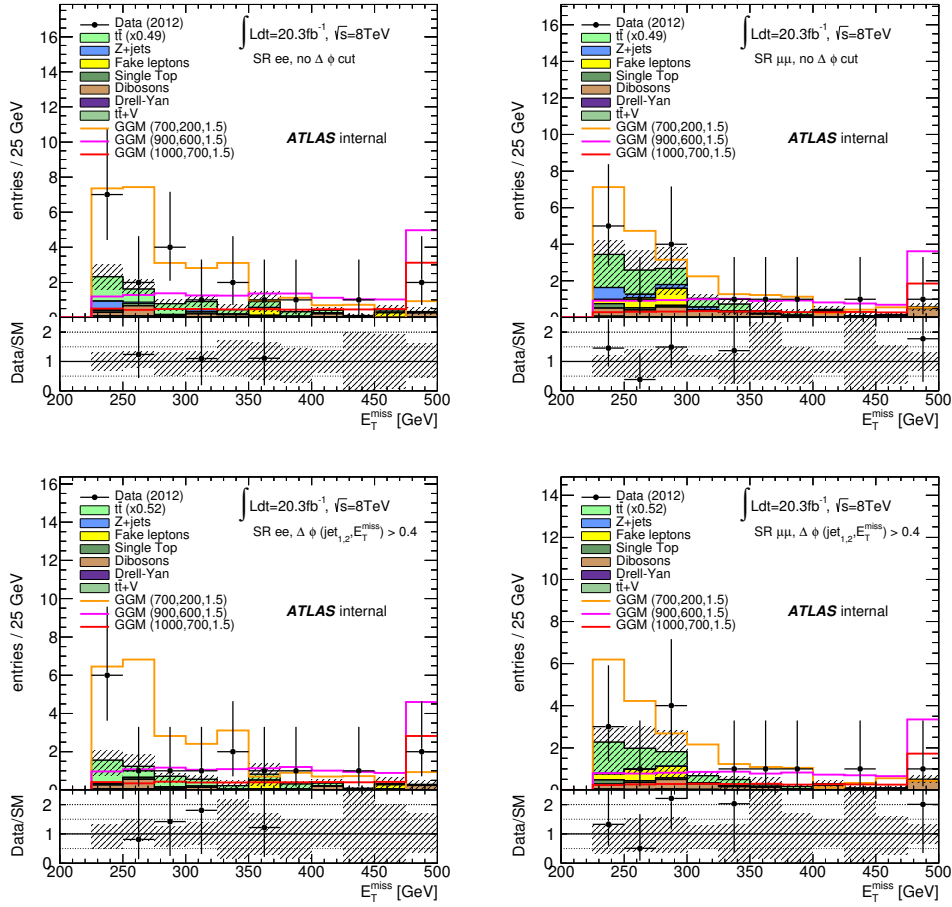


Figure 4.32:  $E_T^{\text{miss}}$  distribution after unblinding in the SRs before (top) and after (bottom) the  $\Delta\phi(E_T^{\text{miss}}, \text{jet}) > 0.4$  cut is applied, for electron (left) and muon (right) channel. All detector-related uncertainties are included. Normalization of  $t\bar{t}$  by 0.49 or 0.52 respectively is indicated.

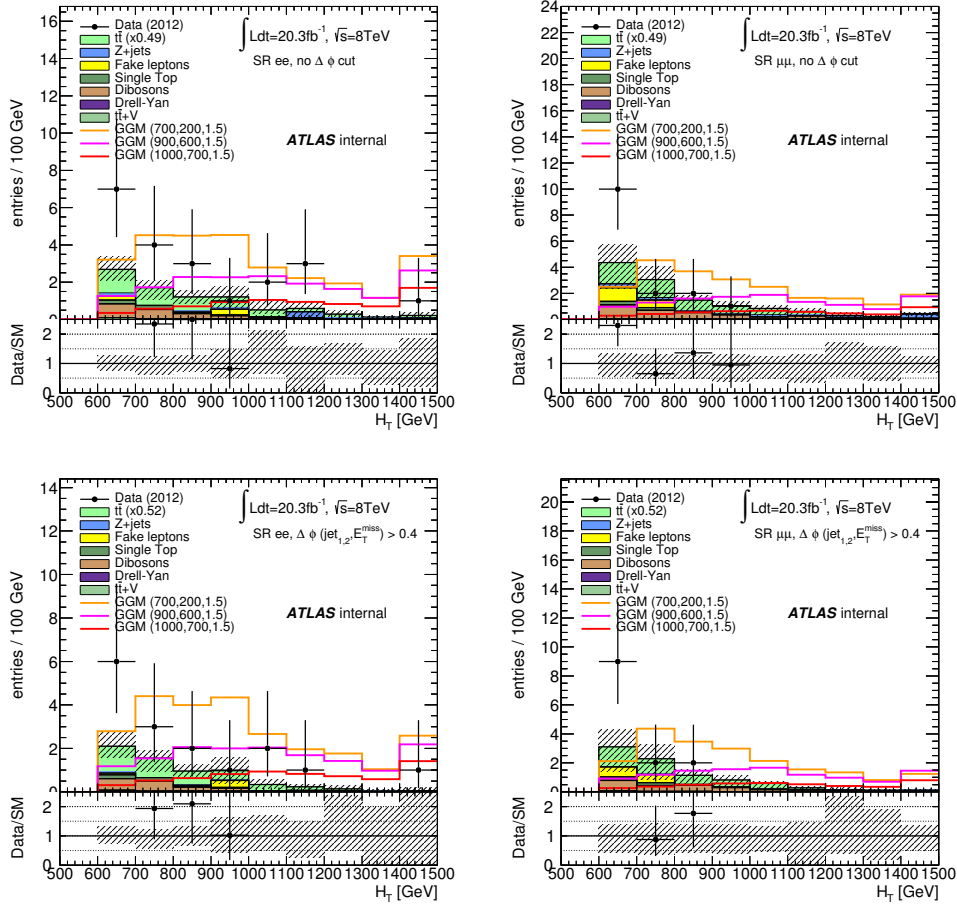


Figure 4.33:  $H_T$  distribution after unblinding in the SRs before (top) and after (bottom) the  $\Delta\phi(E_T^{\text{miss}}, \text{jet}) > 0.4$  cut is applied, for electron (left) and muon (right) channel. All detector-related uncertainties are included. Normalization of  $t\bar{t}$  by 0.49 or 0.52 respectively is indicated.

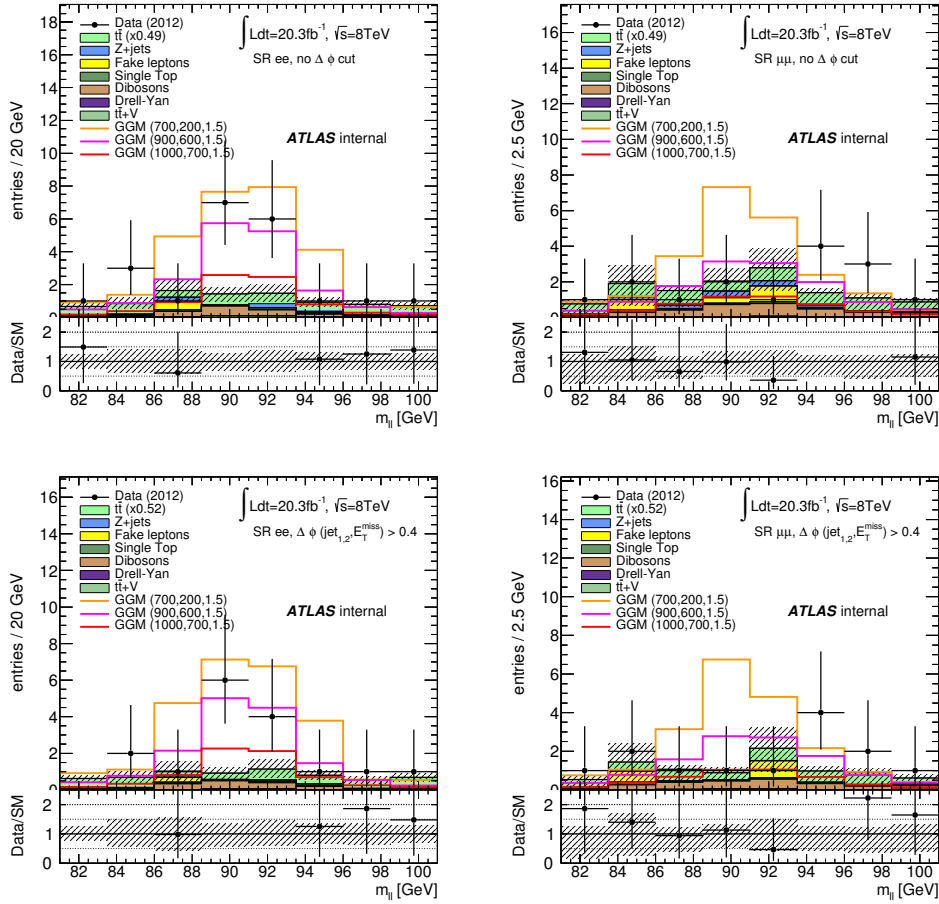


Figure 4.34: Invariant mass distribution after unblinding in the SRs before (top) and after (bottom) the  $\Delta\phi(E_T^{\text{miss}}, \text{jet}) > 0.4$  cut is applied, for electron (left) and muon (right) channel. All detector-related uncertainties are included. Normalization of  $t\bar{t}$  by 0.49 or 0.52 respectively is indicated.

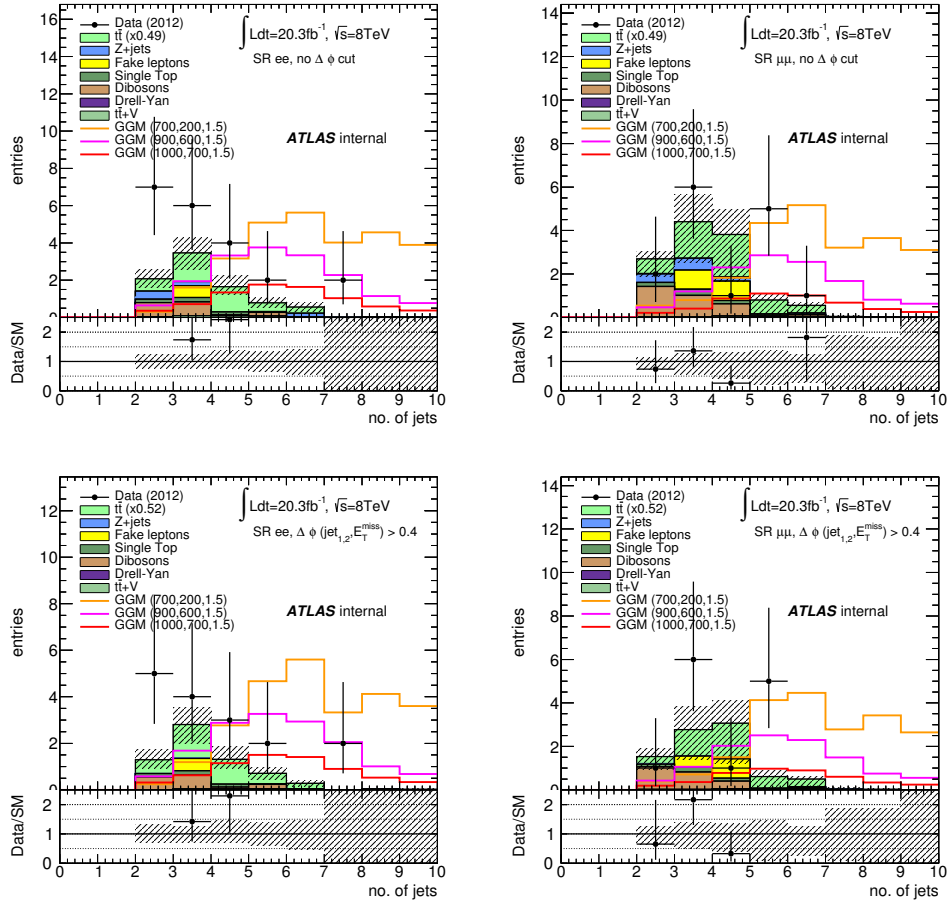


Figure 4.35: Jet multiplicity distribution after unblinding in the SRs before (top) and after (bottom) the  $\Delta\phi(E_T^{\text{miss}}, \text{jet}) > 0.4$  cut is applied, for electron (left) and muon (right) channel. All detector-related uncertainties are included. Normalization of  $t\bar{t}$  by 0.49 or 0.52 respectively is indicated.



## 4.9 Interpretation

In this section, exclusion limits are shown for the SUSY models described in Sect. 4.3. The asymptotic  $CL_s$  prescription [139], implemented in the HistFitter program [140], is used to determine upper limits at 95% confidence level (CL). (Descriptions of all these statistical concepts can be found in Appendix A.) All signal and background uncertainties are taken into account using a Gaussian model of nuisance parameter integration. All uncertainties except that on the signal cross section are included in the limit-setting configuration. The impact of varying the signal cross sections by their uncertainties is indicated separately. Numbers quoted in the text are evaluated from the observed exclusion limit based on the nominal signal cross section minus its  $1\sigma$  theoretical uncertainty.

The data exceeds the background expectations in the  $ee$  ( $\mu\mu$ ) channel with a significance of 3.0 (1.7) standard deviations. Exclusion limits in specific models illustrate which regions of the model parameter space are affected by the observed excess, by comparing the expected and observed limits. The results in  $SRee$  and  $SR\mu\mu$  (Table 4.32) are considered simultaneously. The signal contamination in  $CR\epsilon\mu$  is found to be at the  $\sim 1\%$  level, and is therefore neglected in this procedure. The expected and observed exclusion contours, in the plane of  $\mu$  versus  $m(\tilde{g})$  for the GGM model, are shown in Fig. 4.36. The  $\pm 1\sigma_{\text{exp}}$  and  $\pm 2\sigma_{\text{exp}}$  experimental uncertainty bands indicate the impact on the expected limit of all uncertainties considered on the background processes. The  $\pm 1\sigma_{\text{theory}}^{\text{SUSY}}$  uncertainty lines around the observed limit illustrate the change in the observed limit as the nominal signal cross section is scaled up and down by the theoretical cross-section uncertainty. Given the observed excess of events with respect to the SM prediction, the observed limits are weaker than expected. In the case of the  $\tan\beta = 1.5$  exclusion contour, the analysis is able to exclude gluino masses up to 850 GeV for  $\mu > 450$  GeV, whereas gluino masses of up to 820 GeV are excluded for the  $\tan\beta = 30$  model for  $\mu > 600$  GeV. The lower exclusion reach for the  $\tan\beta = 30$  models is due to the fact that the branching fraction for  $\tilde{\chi}_1^0 \rightarrow Z\tilde{G}$  is significantly smaller at  $\tan\beta = 30$  than at  $\tan\beta = 1.5$ .

The triangular area at the bottom right of each plot indicates the region where the NLSP is the gluino, which is not considered in this analysis.

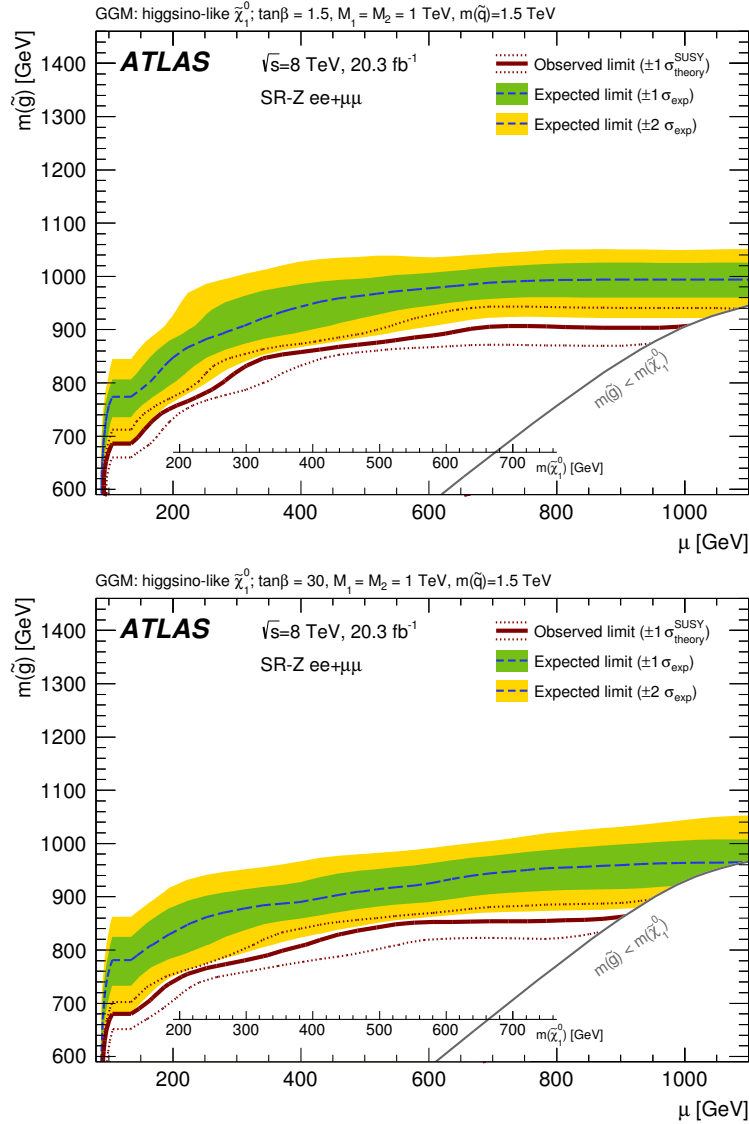


Figure 4.36: The 95% CL exclusion limit from the combined same-flavour channels in the  $\mu$  versus  $m(\tilde{g})$  plane in the GGM model with  $\tan\beta = 1.5$  (top) and  $\tan\beta = 30$  (bottom). The dark blue dashed line indicates the expected limits at 95% CL and the green (yellow) bands show the  $\pm 1\sigma$  ( $\pm 2\sigma$ ) variation on the expected limit as a consequence of the experimental and theoretical uncertainties on the background prediction. The observed limits are shown by the solid red lines, with the dotted red lines indicating the limit obtained upon varying the signal cross section by  $\pm 1\sigma$ . The region below the grey line has the gluino mass less than the lightest neutralino mass and is hence not considered. The value of the lightest neutralino mass is indicated by the  $x$ -axis inset.

Signal Region	$\langle\epsilon\sigma\rangle_{\text{obs}}^{95}$ [fb]	$S_{\text{obs}}^{95}$	$S_{\text{exp}}^{95}$	$CL_B$	$p(s=0)$	Gaussian significance
SR $ee$	1.00	20.2	$8_{-2}^{+4}$	0.998	0.0013	3.0
SR $\mu\mu$	0.72	14.7	$9_{-2}^{+4}$	0.951	0.0430	1.7
SRSF ( $ee + \mu\mu$ )	1.46	29.6	$12_{-2}^{+5}$	0.998	0.0013	3.0

Table 4.34: From left to right: 95% CL upper limits on the visible cross section ( $\langle\epsilon\sigma\rangle_{\text{obs}}^{95}$ ) and on the number of signal events ( $S_{\text{obs}}^{95}$ ); the expected 95% CL upper limit on the number of signal events is denoted by  $S_{\text{exp}}^{95}$  and is derived from the expected number of background events (and the  $\pm 1\sigma$  uncertainty on the expectation); two-sided  $CL_B$  value, which is the confidence level observed for the background-only hypothesis; the discovery  $p$ -value for 0 signal strength  $s$  ( $p(s=0)$ ), and the Gaussian significance for the on- $Z$  search.

Signal Region	$\langle\epsilon\sigma\rangle_{\text{obs}}^{95}$ [fb]	$S_{\text{obs}}^{95}$	$S_{\text{exp}}^{95}$	$CL_B$	$p_0$ -value	Gaussian Significance
SR $ee$	0.89	18.1	$8.4_{-1.9}^{+3.2}$	0.99343	0.00433	2.651
SR $\mu\mu$	0.64	13.0	$9.6_{-2.7}^{+2.9}$	0.87735	0.11767	1.187
SRSF	1.25	25.4	$12.6_{-3.0}^{+4.6}$	0.99216	0.00567	2.532

Table 4.35: 95% confidence level expected and observed upper limits on the contribution of BSM physics events to the signal regions,  $CL_B$  values, the  $p_0$ -value for the observed result, and the corresponding Gaussian significance based on the combined fit background estimation. The expected upper limit on number of events is shown with the  $1\sigma$  uncertainties.

### 4.9.1 Model independent upper limits

The signal regions are also used to place upper limits on the allowed number of BSM events ( $N_{\text{BSM}}$ ) in each region. The observed ( $S_{\text{obs}}^{95}$ ) and expected ( $S_{\text{exp}}^{95}$ ) 95% CL upper limits are also derived using the  $CL_S$  procedure. These upper limits on  $N_{\text{BSM}}$  can be interpreted as upper limits on the visible BSM cross section ( $\langle\epsilon\sigma\rangle_{\text{obs}}^{95}$ ) by normalising  $N_{\text{BSM}}$  by the total integrated luminosity. Here  $\langle\epsilon\sigma\rangle_{\text{obs}}^{95}$  is defined as the product of the signal production cross section, acceptance and reconstruction efficiency. The results are obtained using pseudo-experiments. These numbers are presented in Table 4.34.

These tables also present the confidence level observed for the background-only hypothesis  $CL_B$ , and the one-sided discovery  $p$ -value,  $p(s=0)$ , which is the probability that the event yield obtained in a single hypothetical background-only experiment (signal,  $s=0$ ) is greater than that observed in this dataset. The  $p(s=0)$  value is truncated at 0.5.

For comparison, the same results are shown in Table 4.35 using the combined fit for the background estimation. As expected from the somewhat higher background expectations, the  $p_0$ -values are somewhat higher and the significances are somewhat lower. These are reflected in upper limits that are slightly closer to the expectation.

In generating these results, the statistical uncertainty on both the jet-

smearing and flavour-symmetry backgrounds were treated using Poisson constraint terms, as both come from the limited statistics in the seed or control regions. An alternative configuration using a Gaussian constraint term yields significances higher by 0.1-0.2, as expected from the somewhat smaller high-end tail in a Gaussian distribution compared to a Poisson. The upper limits are generally within about half an event and do not show a strong consistent trend towards being tighter or looser.

## 4.10 Conclusions and outlook

This chapter presents the results of a search for supersymmetric particles in events with a leptonically-decaying  $Z$  boson, jets, and  $E_{\text{T}}^{\text{miss}}$ , using  $20.3 \text{ fb}^{-1}$  of 8 TeV  $pp$  collisions recorded by the ATLAS detector at the LHC. In this search  $6.4 \pm 2.2$  ( $4.2 \pm 1.6$ ) events from SM processes are expected in the  $\mu\mu$  ( $ee$ ) SR, as predicted using almost exclusively data-driven methods. The background estimates for the major and most difficult-to-model backgrounds are cross-checked using MC simulation normalised in data control regions, providing further confidence in the SR prediction. Following this assessment of the expected background contribution to the SR the number of events in data is higher than anticipated, with 13 observed in  $\text{SR}_{\mu\mu}$  and 16 in  $\text{SR}_{ee}$ . The corresponding significances are 1.7 standard deviations in the muon channel and 3.0 standard deviations in the electron channel. These results are interpreted in a supersymmetric model of general gauge mediation, and probe gluino masses up to 900 GeV.

The excitement generated by this result is reflected in the substantial number of theoretical papers, trying to interpret the data excess, that have appeared on the arXiv posterior to the publication of these ATLAS results in Ref. [141] (which has more than 70 citations). For instance, the one in Ref. [142], in which the author has participated.

Despite all the excitement, a search with selection criteria almost identical to that presented in this chapter<sup>9</sup> has been performed, with  $\sqrt{s} = 13 \text{ TeV}$  data, not being able to corroborate the excess. This search used the  $14.7 \text{ fb}^{-1}$  of  $pp$  collision data recorded in 2015 and 2016 by the ATLAS detector. A total of 60 events are observed in data with a predicted background of  $53.5 \pm 9.3$  events, corresponding to a significance of 0.47 standard deviations. More details can be found in Ref. [144]. CMS has also performed searches, in similar kinematic regions, with  $\sqrt{s} = 8 \text{ TeV}$  and  $\sqrt{s} = 13 \text{ TeV}$  finding the observed results consistent with the SM expectations [145, 146].

---

<sup>9</sup>Differing only in the details of the analysis object definitions and missing transverse momentum.

## Chapter 5

# Conclusions

The Standard Model of Particle Physics (SM) provides the current most accurate description of the Elementary Particle Physics phenomenology. It has been experimentally tested up to the TeV scale with remarkably successful results. Nevertheless, there are pieces of evidence pointing to some New Physics beyond the SM such as the existence of Dark Matter, the matter-antimatter asymmetry of the Universe, the neutrino masses, or the hierarchy problem. Thus, the SM needs to be extended or included in a more complete theory. Several theories have been developed in this direction among which Supersymmetry (SUSY) is one of the most favoured.

This Thesis is devoted to search for Supersymmetry in two different scenarios. In order to do this, the data produced by the LHC and recorded by the ATLAS detector have been used. The theoretical and experimental frameworks and the key statistical concepts needed to understand the motivations and basic procedures to perform these searches have been summarized in Chapter 1, Chapter 2 and Appendix A, respectively.

In many SUSY models lepton and baryon-number violating interactions are forbidden by the requirement of  $R$ -parity conservation in order to prevent rapid proton decay. However, proton decay can also be prevented by forbidding only one of the two mentioned violations, in which case some  $R$ -parity-violating interactions (bilinear lepton-number violating interactions in the case of bRPV) are allowed. Introducing RPV into supersymmetric models can significantly weaken mass and cross-section limits from collider experiments and also provide a rich phenomenology. Most relevant is the fact that the LSP is unstable and decays to SM particles rather than escaping unseen as predicted by models that conserve  $R$ -parity.

In Chapter 3, a search for bRPV-mSUGRA SUSY in ATLAS with  $4.7 \text{ fb}^{-1}$  of  $\sqrt{s} = 7 \text{ TeV}$  LHC data, is presented. This search is a counting experiment based on the selection of final states involving one lepton (electron or muon), seven or more jets and  $E_{\text{T}}^{\text{miss}}$ . In this context, a SR is defined in which bRPV is expected to dominate over the Standard Model background. This SR is characterised by the following requirements: exactly one isolated lepton with  $p_{\text{T}} > 25 \text{ GeV}$ ; at least seven jets, with leading jet  $p_{\text{T}} > 80 \text{ GeV}$  and subleading

jets  $p_T > 25$  GeV;  $E_T^{\text{miss}} > 180$  GeV; transverse mass  $m_T > 120$  GeV; and effective mass  $m_{\text{eff}} > 750$  GeV. In order to make sure that the behaviour of the SM background is properly understood and accounted for, a set of control and validation regions, orthogonal to the SR, are also defined.

The main background processes in the SR are top quark production (mostly semi- and fully-leptonic  $t\bar{t}$  pairs, but also single top to a lesser extent) and the production of  $W$  and  $Z$  bosons in association with jets (where the  $W/Z$  boson decays leptonically,  $W \rightarrow \ell\nu$  or  $Z \rightarrow \ell\ell$ ). In addition, an estimate on the QCD jet production is required in the SR, since large uncertainties affect both the theory and the lepton fake rates.

A global likelihood simultaneous fit in all CRs is performed, finding  $4.3 \pm 1.2$  ( $2.2 \pm 1.1$ ) fitted background events in the SR for the electron (muon) channel. The observed number of data events is 7 (7). After considering all sources of systematic uncertainties, the significance can be calculated to be 1.1 (2.1) standard deviations. Therefore, one can conclude that no significant discrepancy is seen between the expected number of SM events in the SRs and the observed data.

This agreement between data and SM is interpreted in terms of bRPV-mSUGRA. The mSUGRA model is defined by five parameters: the common boson and fermion masses at the GUT scale  $m_0$  and  $m_{1/2}$ , the ratio of the Higgs vacuum expectation values  $\tan\beta$ , the common GUT scale trilinear coupling  $A_0$  and the sign of the Higgs potential parameter  $\mu$ . In the bRPV-mSUGRA models probed in this Thesis, these parameters take the following values:  $\tan\beta = 10$ ,  $A_0 = 0$  GeV and  $\text{sign}(\mu) = +1$ , while  $m_0$  and  $m_{1/2}$  are kept as free parameters in the range:  $100 < m_0 < 1400$  GeV and  $260 < m_{1/2} < 1000$  GeV. The statistically independent electron and muon channels are combined to set limits in this bRPV-mSUGRA model using the CLs prescription. These limits greatly extend previous results [59] from ATLAS.

A full description of this search, together with other interpretations, can be found in Ref. [46]. This analysis is an extension to higher jet multiplicity of the 3- and 4-jet channels described in Ref. [47]. Searches for new phenomena in channels with high jet multiplicity and  $E_T^{\text{miss}}$  (vetoing on leptons) have also been reported by the ATLAS Collaboration in Refs. [48] and [49].

Beyond the scope of this Thesis, several analyses have continued to probe bRPV mSUGRA/CMSSM models with  $\sqrt{s} = 8$  TeV data with an integrated luminosity of  $20 \text{ fb}^{-1}$  [79–82]. These searches at 8 TeV extend the parameter space probed and the exclusion limits. Other analyses, including one that considers electroweak production, are currently being developed in order to keep exploring the bRPV mSUGRA/CMSSM parameter space.

The other scenario presented in this Thesis is a search for Supersymmetry in final states containing a leptonically-decaying  $Z$  boson, jets and large  $E_T^{\text{miss}}$ . The proton-proton collision data used in this search were collected during 2012 at a center-of-mass energy  $\sqrt{s} = 8$  TeV and correspond to an integrated luminosity of  $20.3 \text{ fb}^{-1}$ .

Events are required to contain at least two same-flavoured leptons (elec-

trons or muons) with opposite electric charge. If more than two leptons are present, the two with the largest values of  $p_T$  are selected. The leading (highest  $p_T$ ) lepton must have a  $p_T > 25$  GeV, whereas the subleading lepton  $p_T$  can be as low as 10 GeV. Their invariant mass must fall within the  $Z$  boson mass window, here considered as  $81 < m_{\ell\ell} < 101$  GeV. In addition, all events are required to contain at least two jets of  $p_T > 35$  GeV and  $|\eta| < 2.5$  (signal jets) and to have  $E_T^{\text{miss}} > 225$  GeV and  $H_T > 600$  GeV, where  $H_T$  is the scalar sum of the  $p_T$  of all signal jets and the two leading leptons. Furthermore, the azimuthal angle between each of the two leading jets and the  $E_T^{\text{miss}}$  is required to be  $\Delta\phi > 0.4$ .

A great effort has been made to accurately estimate the number of SM events that survive the previous selection. The dominant background processes and those that are expected to be most difficult to model using MC simulation are estimated using data-driven or semi-data-driven techniques. A brief description of the considered backgrounds and their estimation methods is given below.

The dominant backgrounds come from so-called *flavour-symmetric* processes. Here the branching fractions to  $ee$ ,  $\mu\mu$  and  $e\mu$  have a 1:1:2 ratio such that the same-flavour contributions can be estimated with data using information from the different-flavour contribution. This group of backgrounds is dominated by  $t\bar{t}$  and also includes  $WW$ , single top ( $Wt$ ) and  $Z \rightarrow \tau\tau$ , and makes up  $\sim 60\%$  of the predicted SM background.

Diboson backgrounds with real  $Z$  boson production contribute up to 25% of the total background. These are estimated using MC simulation, as are *Rare Top* backgrounds, which include  $t\bar{t} + W$ ,  $t\bar{t} + Z$  and single top ( $tZ$ ) processes. The Rare Top contribution is less than 5%.

Processes with “fake leptons”, i.e. jets mis-reconstructed as leptons, are estimated using the Matrix Method, which is a data-driven method widely used in most of ATLAS analyses.

Finally, there is the special case of the  $Z/\gamma^* + \text{jets}$  background. Since only  $Z \rightarrow ee$  and  $Z \rightarrow \mu\mu$  (and not  $Z \rightarrow \tau\tau$ ) decays are selected, no real  $E_T^{\text{miss}}$  can be produced in these events. Consequently, high  $E_T^{\text{miss}}$  in events from this background (usually called instrumental or fake  $E_T^{\text{miss}}$ ) is due to jet mismeasurements. Given that the  $Z/\gamma^* + \text{jets}$  background could mimic a possible signal, particular care has been taken to suppress it as much as possible (the  $\Delta\phi$  cut mentioned before reduces this background to negligible levels) and to estimate its remaining, although negligible, contribution as precisely as possible. To perform this estimation, given the difficulties of modelling instrumental  $E_T^{\text{miss}}$  in MC simulation, the data-driven *jet smearing* method is applied. This method provides an estimate for the contribution from events containing both fake  $E_T^{\text{miss}}$ , from object mismeasurements, and real  $E_T^{\text{miss}}$ , from neutrinos in heavy flavour quark decays.

The resulting background estimates are  $4.2 \pm 1.6$ ,  $6.4 \pm 2.2$  and  $10.6 \pm 3.2$  for the  $ee$ ,  $\mu\mu$  and  $(ee + \mu\mu)$  channels, respectively. While the observed event yields are 16, 13 and 29, showing that the data exceeds the background expectations

with a significance of 3.0, 1.7 and 3.0 standard deviations in the electron, muon and combined channels respectively.

The results are interpreted in a GGM model where the gravitino is the LSP and a higgsino-like neutralino is the NLSP. The higgsino mass ( $\mu$ ) and the gluino mass are free parameters. The  $U(1)$  and  $SU(2)$  gaugino mass parameters,  $M_1$  and  $M_2$ , are fixed to be 1 TeV, and the masses of all other sparticles are set at 1.5 TeV. In addition,  $\mu$  is set to be positive. Two different possibilities for the ratio, between the vacuum expectation values of the two Higgs doublets,  $\tan\beta$  have been selected: 1.5 and 30. Exclusion limits are set in this model resulting in the observed limits being weaker than the expected ones due to the data excess.

The excitement generated by this result is reflected in the substantial number of theoretical papers, trying to interpret the data excess, that have appeared on the arXiv posterior to the publication of these ATLAS results in Ref. [141]. For instance, the one in Ref. [142], in which the author has participated.

Despite all the excitement, an almost identical search to that presented in this Thesis has been performed, with  $\sqrt{s} = 13$  TeV data, not corroborating the excess. This search used the  $14.7 \text{ fb}^{-1}$  of  $pp$  collision data recorded in 2015 and 2016 by the ATLAS detector. A total of 60 events are observed in data with a predicted background of  $53.5 \pm 9.3$  events, corresponding to a significance of 0.47 standard deviations. More details can be found in Ref. [144]. CMS has also performed searches, in similar kinematic regions, with  $\sqrt{s} = 8$  TeV and  $\sqrt{s} = 13$  TeV finding the observed results consistent with the SM expectations [145, 146].

A new perspective for searches involving the  $Z$  boson is currently being developed by Theorists: The reconstruction of the different terms of the angular distribution in the  $Z$  boson decay, one by one through appropriate asymmetries, determines the 8 multipolar parameters (3 polarizations and 5 alignments, since it is a spin 1 boson). The values of these parameters are shown to be radically different depending on the production mechanism of the  $Z$  boson, allowing a clear distinction between the SM and any form of New Physics. The use of these parameters (called New Physics messengers) offers the possibility of a whole new methodology for NP searches beyond the hunt of excesses in the number of events.

There are still several years of the LHC Run 2 ahead in which the chances of finding Supersymmetry if it exists are truly great. For all we know, Supersymmetry might be just around the corner. In any case, one must remember that science is based in hypothesis testing and that:

“There are two possible outcomes: if the result confirms the hypothesis, then you’ve made a discovery. If the result is contrary to the hypothesis, then you’ve made a discovery.” Enrico Fermi



## Capítulo 6

# Resumen en español

La Física de Partículas, o Física de Altas Energías, es la rama de la ciencia que estudia los componentes elementales del Universo y sus interacciones fundamentales. En las décadas de 1960 y 1970, se estableció la teoría de las partículas fundamentales y sus interacciones, conocida como el Modelo Estándar (SM, sus siglas en inglés). Ésta describe tres de las cuatro fuerzas fundamentales de la Naturaleza, y establece a los quarks y los leptones como sus constituyentes fundamentales. El Modelo Estándar proporciona la descripción más precisa, hasta la fecha, de la fenomenología de la Física de Partículas Elementales. Se ha demostrado su validez hasta escalas de energía del orden de TeV. Uno de los grandes logros del SM fue la predicción y el posterior descubrimiento de los bosones masivos  $W^\pm$  y  $Z$  de la interacción débil en el CERN en 1983 y del quark top, el quark más masivo del SM, en 1995 en el acelerador Tevatron.

A pesar de sus grandes triunfos, el SM no se considera la teoría fundamental definitiva de la Física de Partículas ya que existen evidencias que advierten de Nueva Física, más allá del SM, como la existencia de Materia Oscura, la asimetría entre materia y antimateria del Universo, las masas de los neutrinos o el problema de la jerarquía. Por lo tanto el SM necesita, o bien una extensión, o bien ser incluido en una teoría más completa.

Varias teorías se han desarrollado en esta dirección, entre las que destaca la Supersimetría (SUSY). Se ha demostrado que SUSY es la única extensión posible de las simetrías espacio-temporales conocidas en las interacciones de partículas. Durante los primeros años de su desarrollo, en la década de 1970, ésta era una teoría puramente intelectual, sin aplicaciones físicas, hasta que los físicos empezaron a percatarse de que SUSY podía, de hecho, resolver muchos de los problemas del SM. Supersimetría es, sin duda, una de las ideas más elegantes en la Física reciente.

La característica clave de la fenomenología de SUSY es la predicción de *spartículas* (partículas supersimétricas). Cada partícula del SM tiene una compañera supersimétrica de la que difiere en spin en  $1/2$ . De momento, ningún experimento ha observado estas supercompañeras, lo cual indica que SUSY tiene que ser una simetría rota, por lo que las spartículas (si existen) deben de ser más masivas que sus compañeras del SM. Puesto que se sabe muy poco

sobre el mecanismo de ruptura y del espectro de masa de las nuevas partículas, las posibles señales de SUSY pueden ser muy diversas dependiendo del modelo particular que se considere.

Para producir partículas muy pesadas se necesitan colisiones a altísimas energías. Para ello se utilizan aceleradores que pueden incrementar la energía de dos haces de partículas y hacerlos colisionar. El Gran Colisionador Hadrónico (LHC), operado por el Laboratorio Europeo de Física de Partículas (CERN) en la frontera franco-suiza, es uno de estos aceleradores en el que se producen colisiones entre protones. Con su energía en el centro de masas,  $\sqrt{s}$ , y su luminosidad,  $\mathcal{L}$ , sin precedentes, ofrece unas condiciones excelentes para la búsqueda de nuevas partículas con masas del orden de TeV y también para descubrir insólitos procesos de producción. Varios detectores de grandísimas dimensiones observan y registran los resultados de estas colisiones.

El experimento ATLAS, los datos del cual se han utilizado en esta Tesis, es uno de los cuatro detectores de más envergadura del LHC. Es un experimento diseñado para explorar el SM y la Física que pueda haber más allá de éste. Para esto hay unos 2500 físicos repartidos por todo el mundo trabajando en él. La propuesta formal de ATLAS se presentó en 1994 y 10 años después empezó la instalación del detector, finalizando en 2008.

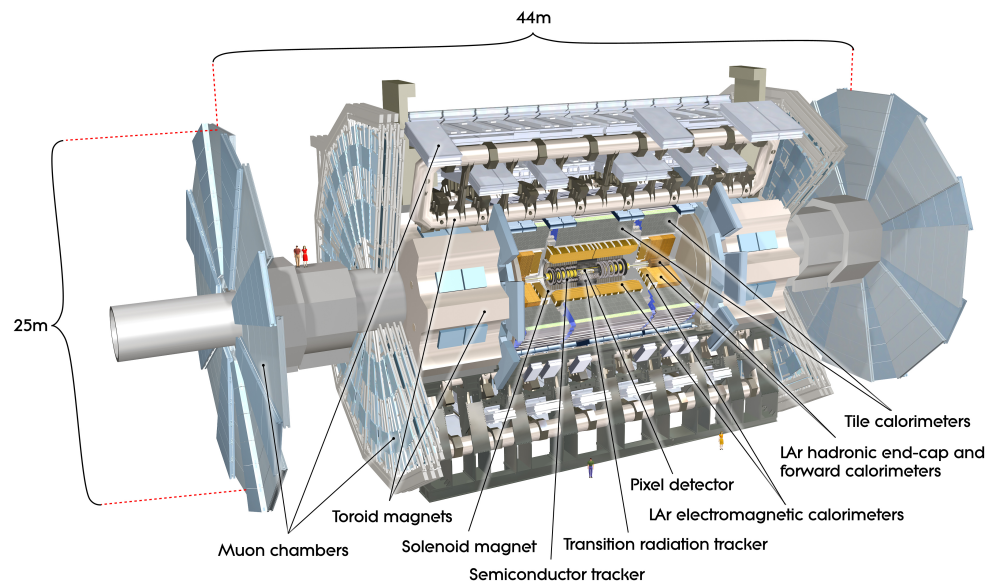


Figura 6.1: Diseño gráfico del detector ATLAS.

ATLAS (Figura 6.1) es un detector cilíndrico nominalmente simétrico, con capas de subdetectores. Mide 44 m de largo y 25 m de alto. El subdetector más interno es un detector de trazas, el Inner Detector (ID). Éste está sumergido en un campo magnético de 2 T (generado por un solenoide superconductor que rodea al ID) y consiste en sensores de silicio y tubos de deriva. Sus principales

propósitos son la identificación y medida de la carga y el momento de las partículas que lo atraviesan, además de la reconstrucción con gran precisión de los vértices primarios y secundarios. Fuera del solenoide se encuentran los calorímetros. El primero, el calorímetro electromagnético, utiliza Argón líquido como medio ionizante, con los absorbentes dispuestos en una geometría con forma de acordeón. Permite la identificación y medida de electrones y fotones. Rodeándolo se encuentra el calorímetro hadrónico, que usa una tecnología de baldosas centelleadoras que permiten medir jets<sup>1</sup> hadrónicos y que ayudan a determinar la energía faltante ( $E_T^{\text{miss}}$ ). A continuación de los calorímetros, ATLAS cuenta con un espectrómetro de muones que realiza medidas del momento de los muones. Éste se encuentra dentro de un campo magnético toroidal que está generado por tres toroides superconductores gigantes y huecos. Esto permite una capacidad de curvatura de trazas extraordinaria en un volumen considerable, lo cual tiene la ventaja de mantener una estructura ligera y abierta, minimizando por lo tanto los efectos de interacción múltiple y consiguiendo así una excelente resolución en el momento de los muones. El espectrómetro de muones define las dimensiones totales de ATLAS siendo su subdetector más externo.

Esta Tesis presenta dos búsquedas distintas de SUSY utilizando datos de ATLAS. El procedimiento general de búsquedas de Nueva Física empieza con la definición de Regiones de Señal (SRs), las cuales son conjuntos de criterios de selección (*cortes*) que favorecen la señal con respecto al fondo<sup>2</sup>. Sin embargo, no es posible eliminar todos los fondos de la SR únicamente aplicando cortes. Para estimar con precisión estos fondos que sobreviven en la SR se definen Regiones de Control (CRs) en las que la señal es prácticamente nula. Mediante simulaciones Monte Carlo (MC) u otros métodos que utilizan los datos directamente (*data-driven*) se estiman los fondos en las CRs donde, a su vez, son comparados con los datos para cerciorarse de que la estimación es correcta. Esta estimación en las CRs se extrapola a las SRs. La validez del método de extrapolación se comprueba en Regiones de Validación (VR). Finalmente, en la SR se compara la estimación del fondo con los datos reales observados para determinar si existe alguna discrepancia significativa. Entonces se utiliza el método CLs para establecer límites de exclusión o declarar un descubrimiento.

La Supersimetría se puede manifestar de muchas formas distintas dependiendo de las masas de las nuevas partículas y de sus interacciones. Para no perderse en el grandísimo océano de posibilidades de la Supersimetría se necesita dibujar mapas y diseñar rutas para buscar la tierra supersimétrica. Con este propósito las búsquedas de SUSY están organizadas en análisis que buscan diferentes estados finales y que son interpretados en el contexto de diferentes modelos y escenarios supersimétricos. Las búsquedas de SUSY en ATLAS se clasifican en tres grupos principales dependiendo del mecanismo

<sup>1</sup>Un jet es un estrecho cono de partículas que provienen de la hadronización de un quark o gluon.

<sup>2</sup>En las búsquedas de Nueva Física el fondo son los procesos del Modelo Estándar.

de producción de las spartículas: producción fuerte, electrodébil o de tercera generación. Después de esta clasificación principal las búsquedas se subdividen por las características de sus estados finales. Los análisis que se presentan en esta Tesis pertenecen a la categoría de producción fuerte. Son búsquedas inclusivas de gluinos y quarks de primera y segunda generación.

El primer análisis que se presenta en esta Tesis consiste en una búsqueda de Supersimetría, con violación bilineal de paridad  $R$  (bRPV), en ATLAS con  $4.7 \text{ fb}^{-1}$  de datos del LHC a  $\sqrt{s} = 7 \text{ TeV}$ .

En muchos modelos de SUSY se prohíben las interacciones con violación de número bariónico y leptónico mediante la imposición de conservación de la paridad  $R$ , con el propósito de prevenir la rápida desintegración del protón. Sin embargo, la descomposición del protón se puede prevenir también si se prohíbe sólo una de las dos violaciones anteriores, en cuyo caso algunas interacciones que violen paridad  $R$  (RPV) están permitidas (interacciones que violan el número leptónico mediante términos bilineales en el caso de bRPV). El hecho de introducir RPV en modelos supersimétricos puede disminuir significativamente los límites de masas y secciones eficaces de los experimentos en colisionadores, además de proporcionar una rica fenomenología. La característica más relevante de estos modelos es que la partícula supersimétrica más ligera (LSP) es inestable y se desintegra en partículas del SM en vez de escapar sin ser vista como predicen los modelos de conservación de paridad  $R$ .

Este primer análisis consiste en la selección de estados finales con un leptón (electrón o muon), siete o más jets y  $E_T^{\text{miss}}$ . En este contexto se define una SR en la que se predice que bRPV domina sobre el fondo de SM. Esta SR se caracteriza por los siguientes requisitos:

- exactamente un leptón aislado con  $p_T > 25 \text{ GeV}$ ;
- por lo menos siete jets donde el jet con mayor  $p_T$  tiene que cumplir  $p_T > 80 \text{ GeV}$  y el resto de jets  $p_T > 25 \text{ GeV}$ ;
- $E_T^{\text{miss}} > 180 \text{ GeV}$ ;
- masa transversa (definida en la Ref. [46])  $m_T > 120 \text{ GeV}$  y
- masa efectiva (definida en la Ref. [46])  $m_{\text{eff}} > 750 \text{ GeV}$ .

Para asegurar que el comportamiento de los fondos del SM se entienden correctamente se definen también un conjunto de regiones de control y validación ortogonales a la SR.

Los principales procesos de fondo en la SR son la producción de quarks top (mayoritariamente pares  $t\bar{t}$  leptónicos y semileptónicos y, aunque en menor medida, single top) y la producción de bosones  $W$  y  $Z$  junto con jets (donde el bosón  $W/Z$  se desintegra leptónicamente,  $W \rightarrow \ell\nu$  o  $Z \rightarrow \ell\ell$ ). Además, también es importante la estimación de la producción de jets de QCD en la SR.

La estimación del fondo en la SR es  $4,3 \pm 1,2$  ( $2,2 \pm 1,1$ ) sucesos en el canal del electrón (muon) y el número de sucesos observados en los datos es

7 (7). Con esto se puede calcular cuán significativa es la discrepancia entre datos y predicción obteniendo un valor de 1.1 (2.1) desviaciones estándar. Por lo tanto se puede concluir que no hay discrepancias significativas entre el número esperado de sucesos del SM en las SRs y los datos observados.

Este acuerdo entre los datos y el SM se interpreta en términos de bRPV-mSUGRA. El modelo mSUGRA se define con cinco parámetros: las masas de los fermiones y bosones ( $m_0$  y  $m_{1/2}$ ) a la escala de la Gran Unificación (GUT), la fracción entre los valores esperados de los dobletes de Higgs ( $\tan \beta$ ), el acoplo trilineal a la escala de GUT ( $A_0$ ), y el signo del parámetro del potencial del Higgs ( $\mu$ ). Para los modelos de bRPV-mSUGRA que se sondan en esta Tesis, los parámetros anteriores toman los siguientes valores:  $\tan \beta = 10$ ,  $A_0 = 0$  GeV y  $\mu > 0$ , mientras que  $m_0$  y  $m_{1/2}$  toman distintos valores cumpliendo  $100 < m_0 < 1400$  GeV y  $260 < m_{1/2} < 1000$  GeV. Los canales del electrón y el muon se combinan para establecer límites de exclusión en el espacio de parámetros de bRPV-mSUGRA descrito, utilizando el método CLs. Estos límites están representados en la Figura 6.2 y extienden de manera importante los resultados de búsquedas anteriores en ATLAS [59].

Fuera del marco de esta Tesis, varios análisis han seguido investigando modelos de bRPV-mSUGRA utilizando datos con  $\sqrt{s} = 8$  TeV [79–82]. Estas búsquedas a 8 TeV extienden el espacio de parámetros investigado y los límites de exclusión.

El otro escenario que presenta esta Tesis es una búsqueda de Supersimetría con estados finales que contienen un bosón  $Z$  que se desintegra leptónicamente, jets y gran cantidad de  $E_T^{\text{miss}}$ . Los datos de colisiones protón-protón que se han utilizado en esta búsqueda se recopilaron durante 2012 a una energía en el centro de masas de  $\sqrt{s} = 8$  TeV y corresponden a una luminosidad integrada de  $20.3 \text{ fb}^{-1}$ .

Aquí se requiere que los sucesos contengan, por lo menos, dos leptones del mismo sabor (electrones o muones) con carga eléctrica opuesta. Si hay presentes más de dos leptones, los dos con los valores más altos de  $p_T$  son los que se seleccionan. Los requisitos adicionales son los siguientes:

- el primer leptón (el de  $p_T$  más alto) debe tener un  $p_T > 25$  GeV;
- un segundo leptón con  $p_T > 10$  GeV;
- la masa invariante de estos dos debe de ser compatible con la del bosón  $Z$ :  $81 < m_{\ell\ell} < 101$  GeV;
- por lo menos dos jets con  $p_T > 35$  GeV y  $|\eta| < 2,5$  (jets de señal);
- $E_T^{\text{miss}} > 225$  GeV;
- $H_T > 600$  GeV, donde  $H_T$  es la suma escalar del  $p_T$  de todos los jets de señal y de los dos primeros leptones y
- $\Delta\phi > 0,4$ .

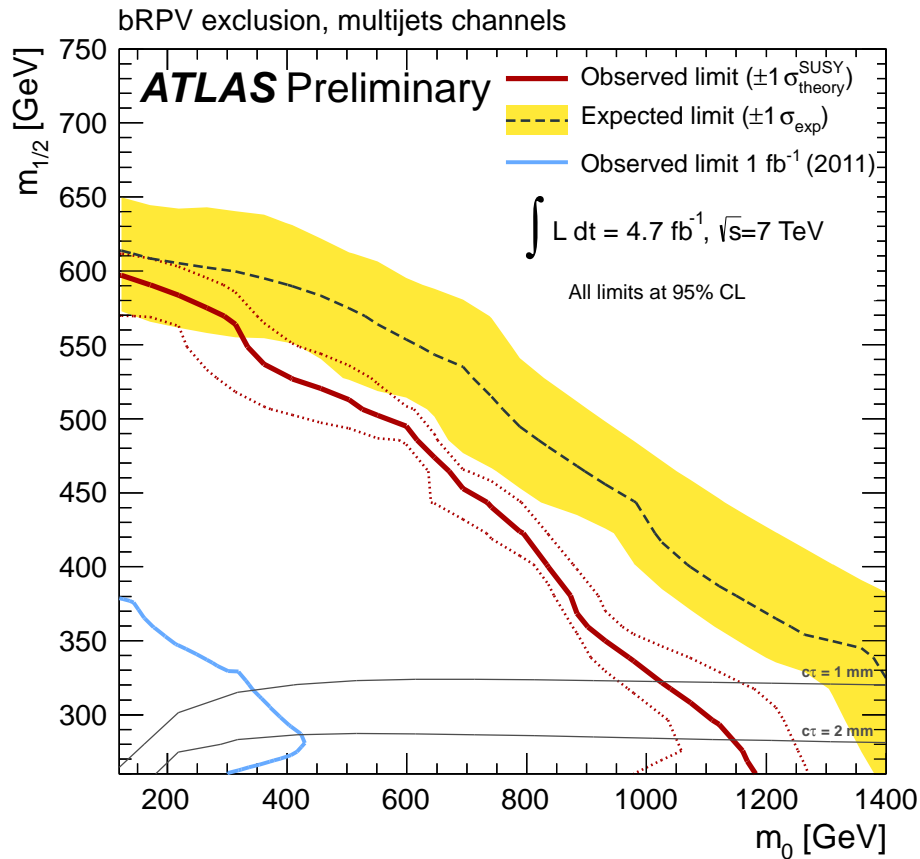


Figura 6.2: Límites de exclusión a 95% CL, esperados y observados en el modelo con bRPV. Los resultados se obtienen al combinar los canales de electrón y muon. La banda amarilla alrededor del límite esperado representa las variaciones de  $\pm 1\sigma$  en los límites esperados cuando se incluyen todas las incertidumbres excepto las teóricas de la señal. Las líneas de puntos alrededor del límite observado indican la sensibilidad al variar las incertidumbres teóricas en  $\pm 1\sigma$ . Las líneas negras sólidas presentan la vida media de la LSP. El resultado de las búsquedas anteriores en ATLAS [59] se muestran en azul.

Los fondos del SM que sobreviven a la selección previa se han estimado con gran meticulosidad. Los fondos dominantes y aquellos que se espera que sean más difíciles de simular con MC, se han estimado utilizando métodos data-driven o semi-data-driven. A continuación se expone una breve descripción de los fondos considerados y de sus métodos de estimación.

Los fondos dominantes provienen de los llamados *procesos simétricos en sabor*. En éstos, las probabilidades de desintegrarse a  $ee$ ,  $\mu\mu$  y  $e\mu$  cumplen la proporción 1:1:2. Debido a esto se puede estimar la contribución de los fondos de mismo sabor utilizando el número de sucesos de distinto sabor observados en los datos. Este grupo de fondos está dominado por  $t\bar{t}$  e incluye además  $WW$ , single top ( $Wt$ ) y  $Z \rightarrow \tau\tau$ , y contribuye en un 60% a la estimación total del fondo del SM.

El fondo debido a dibosones con producción real de bosones  $Z$  contribuye en un 25% al total del fondo. Éste se estima mediante simulaciones MC, al igual que los procesos de *Top Raros* que incluyen  $t\bar{t} + W$ ,  $t\bar{t} + Z$  y single top ( $tZ$ ) y constituyen un 5% del total del fondo.

Los procesos con *leptones falsos*, es decir jets que se han reconstruido erróneamente como leptones, se estiman usando el *Método de la Matriz*, que es un método data-driven utilizado en la mayoría de análisis de ATLAS.

Finalmente, está el caso especial del fondo de  $Z/\gamma^* + \text{jets}$ . Puesto que únicamente las desintegraciones  $Z \rightarrow ee$  y  $Z \rightarrow \mu\mu$  se seleccionan (y no  $Z \rightarrow \tau\tau$ ) no se puede haber producido  $E_T^{\text{miss}}$  en estos sucesos. Consecuentemente, una  $E_T^{\text{miss}}$  alta en sucesos de este fondo sólo puede deberse a jets medidos erróneamente (generalmente se le llama  $E_T^{\text{miss}}$  instrumental). Dado que el fondo  $Z/\gamma^* + \text{jets}$  podría imitar una posible señal, se ha prestado particular atención a suprimirlo todo lo posible y a estimar su restante, aunque despreciable, contribución de la forma más precisa posible. Para realizar esta estimación, dadas las dificultades para reproducir la  $E_T^{\text{miss}}$  instrumental con simulación MC, se ha utilizado el método data-driven *jet smearing*. Este método proporciona una estimación de sucesos con  $E_T^{\text{miss}}$  instrumental y de sucesos con  $E_T^{\text{miss}}$  real que proviene de neutrinos en las desintegraciones de quarks de sabores pesados.

Los resultados para la estimación total de los fondos son  $4,2 \pm 1,6$ ,  $6,4 \pm 2,2$  y  $10,6 \pm 3,2$  para los canales  $ee$ ,  $\mu\mu$  y  $(ee + \mu\mu)$  respectivamente, mientras que el total de sucesos observados en los datos es 16, 13 y 29, lo cual indica que los datos exceden las predicciones con una significancia de 3.0, 1.7 y 3.0 desviaciones estándar en los canales de electrón, muon y combinación respectivamente. En la Figura 6.3 se puede ver el número de sucesos observados comparado con el número estimado de sucesos de fondo para todas las regiones consideradas en este análisis. Esta gráfica es especialmente interesante ya que demuestra que el exceso en los datos no proviene de una estimación incorrecta de algún fondo. Como se puede ver, el número predicho y observado de sucesos en todas las regiones, excepto en la SR, están en perfecto acuerdo. Así que este exceso puede interpretarse como un indicio de Nueva Física o como una fluctuación estadística, necesitándose los datos del Run 2 del LHC para discernir entre ambas posibilidades, sin embargo no puede ser el fruto de una estimación

errónea de los fondos.

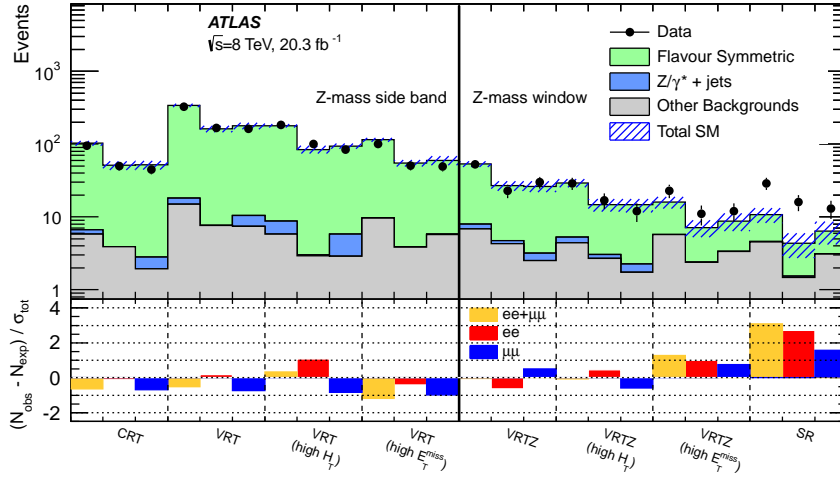


Figura 6.3: Resumen del acuerdo entre datos y predicción en todas las regiones del análisis.

Estos resultados se han interpretado en un modelo de Supersimetría Generalizado de Mediación de Gauge (GGM) donde el gravitino es la LSP y un neutralino de tipo higgsino es la segunda partícula supersimétrica más ligera (Next to LSP, NLSP). La masa del higgsino ( $\mu$ ) y la masa del gluino son parámetros libres. Los parámetros de las masas de los gauginos  $U(1)$  y  $SU(2)$ ,  $M_1$  y  $M_2$ , son fijos e igual a 1 TeV, y las masas de todas las otras partículas se toman como 1.5 TeV. Además,  $\mu$  se toma positivo y se considera dos posibles valores para la fracción entre los valores esperados en el vacío de los dos dobletes de Higgs ( $\tan \beta$ ): 1.5 y 30. Los límites de exclusión calculados para estos modelos se pueden observar en la Figura 6.4, resultando que los límites observados son menos restrictivos que los predichos debido al exceso de sucesos en los datos.

El entusiasmo generado por este resultado queda reflejado en la enorme cantidad de artículos teóricos, que intentan interpretar este exceso, que han aparecido en el arXiv después de la publicación de estos resultados de ATLAS en la Ref. [141] (la cual ha sido citada en más de 70 artículos). Como ejemplo, uno de estos artículos, en el que la autora de estas líneas ha participado, se puede encontrar en la Ref. [142].

A pesar de todo este entusiasmo, una búsqueda prácticamente idéntica a la presentada en esta Tesis se ha llevado a cabo con datos tomados a  $\sqrt{s} = 13$  TeV y no se ha podido corroborar el exceso. Dicha búsqueda ha utilizado  $14.7 \text{ fb}^{-1}$  de los datos de colisiones  $pp$  recopilados por el detector ATLAS en 2015 y 2016. Se ha observado un total de 60 sucesos para una predicción de  $53,5 \pm 9,3$ , lo cual corresponde a una significancia de 0.47 desviaciones estándar. Se puede encontrar más detalles en la Ref. [144]. CMS, otro de los experimentos del



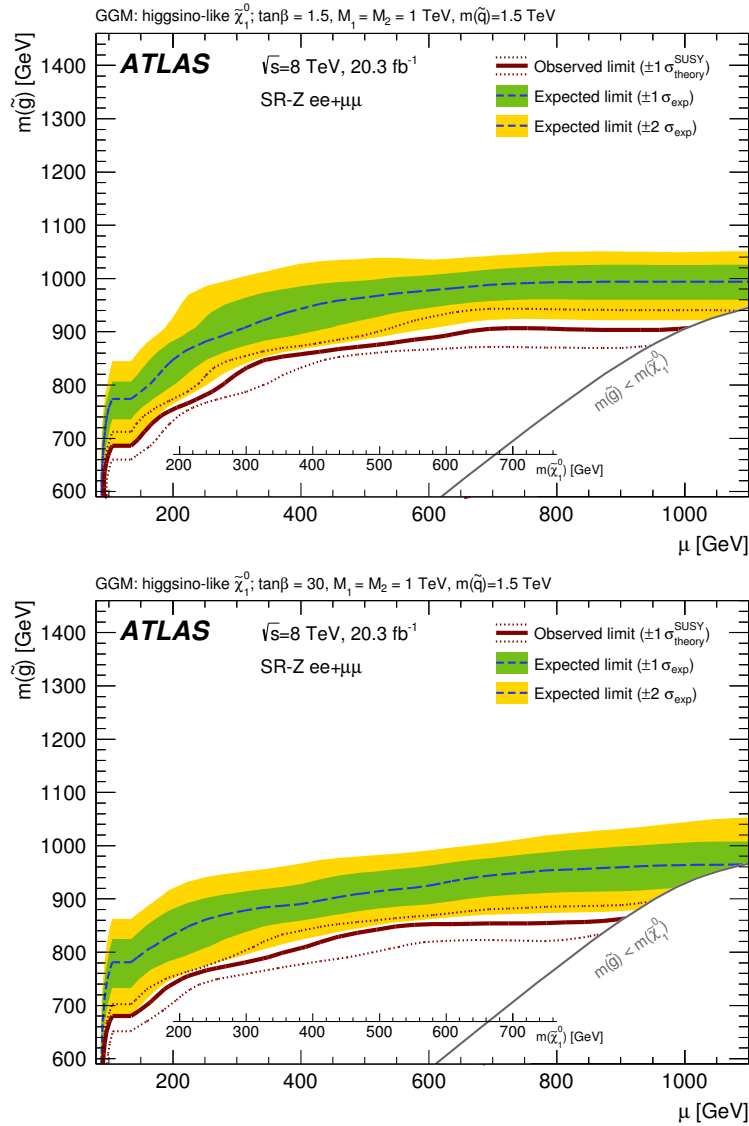


Figura 6.4: Límites de exclusión a 95% CL para  $(ee + \mu\mu)$  para los modelos GGM con  $\tan\beta = 1,5$  (arriba) y  $\tan\beta = 30$  (abajo). La línea azul de puntos indica los límites esperados, la banda verde (amarilla) muestra la variación a  $\pm 1\sigma$  ( $\pm 2\sigma$ ) del límite esperado como consecuencia de las incertidumbres teóricas y experimentales en la predicción del fondo. Los límites observados se presentan mediante las líneas sólidas rojas, siendo las líneas rojas de puntos los límites obtenidos al variar la sección eficaz de la señal en  $\pm 1\sigma$ . La región por debajo de la línea gris no se considera en este análisis. El valor de la masa del neutralino más ligero está indicada en el eje  $x$  adicional.

LHC, también ha realizado búsquedas, en regiones cinemáticas muy similares, a  $\sqrt{s} = 8$  TeV y  $\sqrt{s} = 13$  TeV obteniendo resultados compatibles con las predicciones del SM [145, 146].

Todavía quedan por delante varios años del Run 2 del LHC durante los cuales las probabilidades de encontrar Supersimetría, si es que ésta existe, son realmente altas. Por lo que sabemos de momento, SUSY podría perfectamente estar a la vuelta de la esquina. En cualquier caso, debemos recordar que la ciencia se basa en la comprobación de hipótesis y que:

“Sólo hay dos soluciones posibles: si los resultados confirman la hipótesis, entonces se ha hecho un descubrimiento. Si los resultados son contrarios a la hipótesis, entonces se ha hecho un descubrimiento.” Enrico Fermi.

# Appendices



# Appendix A

## Statistics

### Introduction

The basic problem an experimentalist faces is how to summarise his data efficiently. Usually this will consist either of using the data to determine a parameter of a model (*parameter estimation*) or in checking whether the data are consistent with a given hypothesis (*hypothesis testing*). In real life situations there is a degree of overlap between the two: a parameter determination may well involve the assumption that a specific theory is correct, while a particular theory may predict the value of a parameter.

This Thesis deals with SUSY searches and consequently performs several hypothesis tests, that is why it has been considered interesting to include this appendix where the basics to understand such tests are given. It is not the purpose of this text to give rigorous mathematical proofs and explanations. Concepts and formulas have been simplified as much as possible with the main goal of giving a guide to understand the complex plots presented in ATLAS and CMS searches. For more details References [72, 73, 147–150] can be consulted.

In *probability theory* one generally starts with a well defined problem and calculates the possible outcomes of a specific experiment. Therefore, one proceeds from the theory to the data. In *statistics*, however, the inverse problem is the one that has to be solved, i.e. the data is used to deduce what are the rules or laws relevant for the specific experiment. The actual problem of analysing experimental data is thus more related to statistics, however statistics depend on the results of probability theory, and that is why some considerations of probability are to be found here.

### A.1 Basic concepts

In order to understand hypothesis testing and parameter estimation one needs to be familiar with the concepts of probability density functions, the likelihood function and auxiliary measurements. In this section an overview of these three concepts is given.

### A.1.1 Probability density functions

In many situations one deals with experiments in which the essential circumstances are kept constant, and yet repetitions of the experiment produce different results. As a consequence the result of an individual measurement or trial will be unpredictable, but the possible results of a series of such measurements may have a well-defined distribution. These distributions are usually called *probability density functions* (pdf) and they have the important property of being normalised to unity.

A pdf  $f(x)$  will describe how often a value of the variable  $x$  occurs in a defined sample. In order to provide some sort of description of such a distribution one needs the  $x$  value at which the distribution is centred, and how wide the distribution is. The mean  $\mu$  and the variance  $\sigma^2$  are suitable magnitudes for this (it is customary to quote  $\sigma$  as the accuracy or error of a measurement). For a set of  $N$  separate measurements they are defined as

$$\bar{x} = \sum_i^N \frac{x_i}{N} \quad (\text{A.1})$$

and

$$s^2 = \sum_i^N \frac{(x_i - \mu)^2}{N}. \quad (\text{A.2})$$

The true mean and variance are denoted by  $\mu$  and  $\sigma^2$ , while the measured mean and variance of a sample are  $\bar{x}$  and  $s^2$ . In general, the true mean  $\mu$  is not known, and so Eq. A.2 cannot in fact be used to estimate the variance. Instead it is replaced by<sup>1</sup>

$$s^2 = \frac{1}{N-1} \sum_i^N (x_i - \bar{x})^2. \quad (\text{A.3})$$

It is important to realise that  $s$  is the measure of how spread out the distribution is, and is not the accuracy to which the mean  $\bar{x}$  is determined. Thus by taking more and more observations of  $x$ , the variance  $s^2$  will not change (apart from fluctuations) since the numerator and denominator of Eq. A.3 grow more or less proportionally; this is sensible since  $s^2$  is supposed to be an estimate of the variance of the overall population, which is clearly independent on the sample size  $N$ . On the other hand, the variance of the mean ( $s^2/N$ , i. e. the accuracy to which the mean  $\bar{x}$  is determined) decreases with increasing  $N$ ; more data help locate the mean to higher accuracy.

#### The error of the mean:

The obtaining of the variance of the mean, that has been quoted in the previous paragraph, is shown here.

<sup>1</sup>Note that the factor  $1/(N-1)$  in Eq. A.3 is required in order to make  $s^2$  an *unbiased* estimate of the population's variance  $\sigma^2$ , i.e., for a large sample  $s^2$  will tend to  $\sigma^2$ .

The average  $\bar{x}$  of  $N$  measurements  $x_i$  each of accuracy  $\delta(x_i) = s$  is given by Eq. A.1, therefore, using the well known error propagation formula:

$$\sigma_a^2 = \sigma_b^2 + \sigma_c^2,$$

where  $a$  is a linear combination of  $b$  and  $c$ , one can see that:

$$\delta^2(\bar{x}) = \sum_i (\delta(x_i/N))^2 = \sum_i (s/N)^2 = \frac{1}{N^2} \sum_i s^2 = \frac{1}{N^2} N s^2 = \frac{s^2}{N}$$

↓

$$\delta(\bar{x}) = \frac{s}{\sqrt{N}}$$

Thus, the error of the mean is known more accurately than the variance of the distribution by a factor  $\sqrt{N}$ .

The form of the distribution depends on the nature of the experiment. Below, the Poisson and Gaussian distributions will be considered as examples of pdfs and their most important properties will be discussed as they are two of the most common pdfs used in physics.

### Poisson

A discrete random variable  $x$  has a Poisson distribution with parameter  $\mu > 0$  if, for  $x = k$ , where  $k = 0, 1, 2, \dots$ , the pdf of  $x$  is given by:

$$f(k|\mu) = \text{Probability}(x = k|\mu) = \frac{\mu^k e^{-\mu}}{k!}$$

This is the probability of observing  $k$  independent successes when the expected number of successes is  $\mu$  (when the number of trials tends to infinity). The shape of a Poisson distribution can be seen in Fig. A.1. The mean (or expected) value and the variance of  $x$  for a variable with a Poisson distribution is  $\mu$ . This is the basis (for reasons that will become clear in Sec. A.2) of the well known

$$x \pm \sqrt{x} \tag{A.4}$$

formula that applies to statistical errors in many situations involving the counting of independent events during a fixed interval.

As  $\mu \rightarrow \infty$ , the Poisson distribution tends to a Gaussian (which will be discussed below); for this approximation to be reasonably valid, it turns out that five or more is usually a good enough approximation to infinity for  $\mu$ . This is very useful since many statistical calculations are much simpler to perform if the errors are Gaussian distributed.

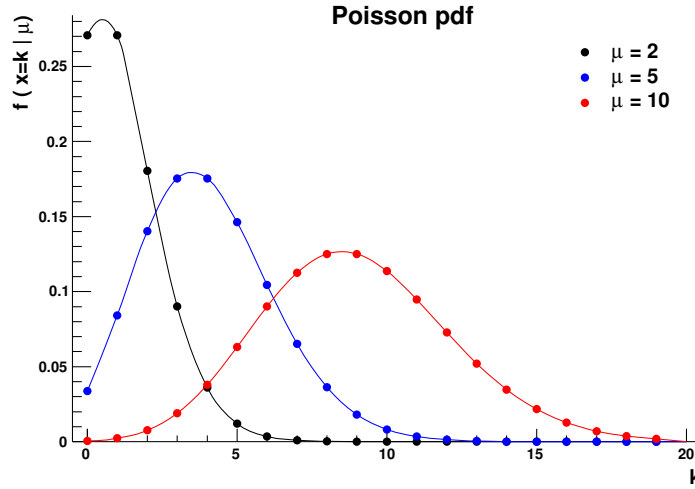


Figure A.1: The plot shows the probability of obtaining  $x = k$  occurrences when the expected value is  $\mu = 2$  (black), 5 (blue) and 10 (red). The function is defined only at integer values of  $k$ . The connecting lines are only guides for the eye.

## Gaussian

The general form of the Gaussian distribution in one variable  $x$  is:

$$y \equiv f(x|\mu, \sigma) = \frac{1}{\sqrt{(2\pi)}\sigma} e^{-(x-\mu)^2/(2\sigma^2)}. \quad (\text{A.5})$$

The curve of  $y$  as a function of  $x$  is symmetric about the value  $x = \mu$ , at which point  $y$  has its maximum value. The parameter  $\sigma$  characterises the width of the distribution. These properties can be seen in Fig. A.2. The factor  $(\sqrt{(2\pi)}\sigma)^{-1}$  ensures that  $\int_{-\infty}^{+\infty} y \, dx = 1$ .

The parameter  $\mu$  is the mean of the distribution, while  $\sigma$  has the following properties:

- The mean square deviation (variance) of the distribution from its mean is  $\sigma^2$ .
- The height of the curve at  $x = \mu \pm \sigma$  is  $1/\sqrt{e}$  of the maximum value.
- The fractional area underneath the curve and with  $\mu - \sigma \leq x \leq \mu + \sigma$  is 0.68.
- By a suitable change of variable to  $x' = (x - \mu)/\sigma$ , any normal distribution can be transformed into a standardised form:

$$y = \frac{1}{\sqrt{(2\pi)}} e^{-x'^2/2}, \quad (\text{A.6})$$



with mean zero and unit variance.

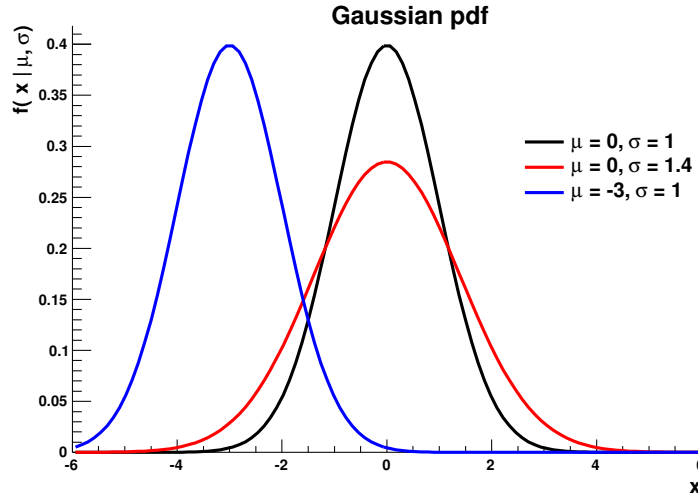


Figure A.2: The plot shows the gaussian pdf curves for different values of the mean,  $\mu$ , and standard deviation,  $\sigma$ .

#### A.1.1.1 Probability models

Often one considers a parametric family of pdfs

$$f(x|\omega),$$

read “ $f$  of  $x$  given  $\omega$ ” and referred to as a *probability model* or just *model*. The parameters of the model ( $\omega$ ) typically represent parameters of a physical theory or an unknown property of the detector’s response. As parameters are not frequentist in nature they will be written in Greek letters to be clearly distinguished from observables (random variables) which will be written in Roman letters <sup>2</sup>. From the full set of parameters, one is typically only interested in a few: the *parameters of interest* ( $\omega_{poi}$  or  $\mu$ )<sup>3</sup>. The rest of the

<sup>2</sup>The frequentist notion of probability of an event is defined as the limit of its relative frequency in a large number of trials. The large number of trials is referred to as an ensemble. In Particle Physics the ensemble is formed conceptually by repeating the experiment many times. The true values of the parameters, on the other hand, are states of nature, not the outcome of an experiment. The true mass of the  $Z$  boson has no frequentist probability distribution. The existence or non-existence of the Higgs boson has no frequentist probability associated with it.

<sup>3</sup>Although in the previous section the symbol  $\mu$  has been used to describe the mean of a distribution, in this section and the following  $\mu$  will be used to denote the parameter of interest (POI), which is not necessarily the mean of the distribution, unless it is explicitly stated.

parameters are referred to as *nuisance parameters* ( $\omega_{nuis}$  or  $\theta$ ), as they must be accounted for even though one is not interested in them directly.

While  $f(x)$  describes the probability density for the observable  $x$  for a single event, one also needs to describe the probability density for a dataset with many events,  $\mathcal{D} = \{x_1, \dots, x_n\}$ . If the events are independently drawn from the same underlying distribution, then clearly the probability density is just a product of densities for each event. However, if one has a prediction of the total number of events expected, call it  $\nu$ , then the overall Poisson probability for observing  $n$  events given  $\nu$  expected should be included. Thus, one arrives at what statisticians call a marked Poisson model,

$$\mathfrak{f}(\mathcal{D}|\nu, \omega) = Pois(n|\nu) \prod_{e=1}^n f(x_e|\omega), \quad (\text{A.7})$$

where a bold  $\mathfrak{f}$  is used to distinguish it from the individual event probability density  $f(x)$ . In practice, the expectation is often parametrized as well and some parameters simultaneously modify the expected rate and shape, thus one can write  $\nu \rightarrow \nu(\omega)$ .

### A.1.2 The likelihood function

The *likelihood function*  $L(\omega)$  is numerically equivalent to  $f(x|\omega)$  with  $x$  fixed – or  $\mathfrak{f}(\mathcal{D}|\nu, \omega)$  with  $\mathcal{D}$  fixed. The likelihood function should NOT be interpreted as a probability density for  $\omega$ . In particular, the likelihood function does NOT have the property that it normalizes to unity. It is common to work with the log-likelihood (or negative log-likelihood) function.

To reiterate the terminology:

- *probability density function* refers to the value of  $f$  as a function of  $x$  given a fixed value of  $\omega$ ,
- *likelihood function* refers to the value of  $f$  as a function of  $\omega$  given a fixed value of  $x$  and
- *model* refers to the full structure of  $f(x|\omega)$ .

### Generalization to various channels

In the context of high-energy physics experiments, usually searches are composed of several “channels” or regions indexed by  $c$ . Here a channel is defined by its associated event selection criteria ( e.g. all events with four electrons with energy greater than 10 GeV), not by an underlying physical process. In addition to the number of selected events,  $n_c$ , each channel may make use of some other measured quantity,  $x_c$  which is usually called discriminating variable <sup>4</sup>.

---

<sup>4</sup>Discriminating variable: a property of the events that can be measured and helps discriminate the signal from background, e.g. the invariant mass of the candidate Higgs boson.

Probability models can be constructed to simultaneously describe several channels, that is several disjoint regions of the data defined by their associated selection criteria. In this context, the data is a collection of smaller datasets:

$$\begin{aligned} \mathcal{D}_{simult} &= \{\mathcal{D}_1, \dots, \mathcal{D}_{c_{max}}\} \\ &= \{\{x_{c=1,e=1} \dots x_{c=1,e=n_c}\}, \dots, \{x_{c_{max},e=1} \dots x_{c_{max},e=n_{c_{max}}}\}\}, \end{aligned}$$

where the number of events in the  $c^{th}$  channel is  $n_c$  and the value of the  $e^{th}$  event in the  $c^{th}$  channel is  $x_{ce}$ . The key point here is that there are now multiple Poisson terms. Thus one can write the combined (or simultaneous) model

$$f(\mathcal{D}|\omega) = \prod_{c \in channels} \left[ Pois(n_c|\nu(\omega)) \prod_{e=1}^{n_c} f(x_{ce}|\omega) \right], \quad (\text{A.8})$$

remembering that the symbol product over channels has implications for the structure of the dataset.

### A.1.3 Auxiliary measurements

Auxiliary measurements (or, in Physics notation, control regions) can be used to estimate or reduce the effect of systematic uncertainties. The signal region and control region are not fundamentally different. In the language used here, they are just two different channels.

A common example is a simple counting experiment with an uncertain background. The true, unknown, background in the signal region is a nuisance parameter,  $\nu_B$ . Calling the true, unknown, signal rate  $\nu_S$  and the number of events in the signal region  $n_{SR}$  one can write the model  $Pois(n_{SR}|\nu_S + \nu_B)$ . As long as  $\nu_B$  is a free parameter, there is no ability to make any useful inference about  $\nu_S$ . Often one has some estimate for the background, which may have come from some control sample with  $n_{CR}$  events. If the control sample has no signal contamination and is populated by the same background processes as the signal region, then one can write  $Pois(n_{CR}|\tau\nu_B)$ , where  $\tau$  is a factor used to extrapolate the background from the signal region to the control region. Thus the total probability model can be written  $f_{sim}(n_{SR}, n_{CR}|\nu_S, \nu_B) = Pois(n_{SR}|\nu_S + \nu_B) \cdot Pois(n_{CR}|\tau\nu_B)$ . This is a special case of Eq. A.8 and is often referred to as the ‘‘on/off’’ problem.

Based on the control region alone, one would estimate (or ‘measure’)  $\nu_B = n_{CR}/\tau$ . Intuitively the estimate comes with an ‘uncertainty’ of  $\sqrt{n_{CR}}/\tau$ . The important lesson here is that one can use auxiliary measurements (i.e.  $n_{CR}$ ) to describe the uncertainty on the nuisance parameter  $\nu_B$  statistically. It is common to say that auxiliary measurements ‘constrain’ the nuisance parameters. Therefore one can use auxiliary measurements to constrain parameters of the model. To do so, one must relate the effect of some common parameter  $\omega_p$  in multiple channels. This is implicit in Eq. A.8.

Often a detailed probability model for an auxiliary measurement is not available and therefore cannot be included directly in the model. The more

common situation for background and systematic uncertainties only has an estimate, “central value”, or best guess for a parameter  $\omega_p$  and some notion of uncertainty on this estimate. In this case one typically resorts to including idealized terms into the likelihood function, here referred to as “constraint terms”, as surrogates for a more detailed model of the auxiliary measurement. This estimate for the parameters will be denoted as  $a_p$ . In this case there is a single measurement of  $a_p$  per experiment, thus it is referred to as a “global observable”. There is no general receipt for the treatment of constraint terms, therefore the way each experiment deals with these terms is somewhat *ad hoc*.

The constraint terms can be written in the form  $f(a_p|\omega_p)$  to include them in our probability model. Often this constraint terms are approximated to Gaussian or Poisson distributions. Denoting the set of parameters with constraint terms as  $\mathbb{S}$  and the global observables  $\mathcal{G} = \{\omega_p\}$  with  $p \in \mathbb{S}$  and including the constraint terms explicitly (instead of implicitly as an additional channel) we arrive at the total probability model, which we will not need to generalize any further:

$$f_{\text{tot}}(\mathcal{D}_{\text{sim}}, \mathcal{G}|\omega) = \prod_{c \in \text{channels}} \left[ \text{Pois}(n_c|\nu_c(\omega)) \prod_{e=1}^{n_c} f_c(x_{ce}|\omega) \right] \cdot \prod_{p \in \mathbb{S}} f_p(a_p|\omega_p). \quad (\text{A.9})$$

In conclusion, auxiliary measurements are a way to have some control over the parameters that we are not interested in but need to be estimated to a certain degree.

## A.2 Measurement as parameter estimation

One of the most common tasks of the working physicist is to estimate some model parameter. We do it so often, that we often don’t realize it. For instance, the sample mean  $\bar{x} = \sum_{e=1}^n x_e/n$  is an estimate for the mean,  $\mu$ , of a Gaussian probability density  $f(x|\mu, \sigma) = \text{Gauss}(x|\mu, \sigma)$ . More generally, an *estimator*  $\hat{\omega}(\mathcal{D})$  is some function of the data, and its value is used to estimate the true value of some parameter  $\omega$ . The most widely used estimator in Physics is the *maximum likelihood estimator* (MLE). It is defined as the value of  $\omega$  which maximizes the likelihood function  $L(\omega)$ . Equivalently this value,  $\hat{\omega}$ , maximizes  $\log L(\omega)$  and minimizes  $-\log L(\omega)$ . The jargon is that one *fits* the function and the maximum likelihood estimate is the *best fit value*.

When one has a multi-parameter likelihood function  $L(\omega)$ , then the situation is slightly more complicated. The maximum likelihood estimate for the full parameter list,  $\hat{\omega}$ , is clearly defined. The various components  $\hat{\omega}_p$  are referred to as the *unconditional maximum likelihood estimates*. In the physics jargon, one says that the parameters are ‘floating’. One can also ask about the maximum likelihood estimate of  $\omega_p$  with some other parameters  $\omega_0$  fixed; this is called the *conditional maximum likelihood estimate* (CMLE) and is denoted  $\hat{\omega}_p(\omega_0)$ .

Using the Physics notation, the maximum likelihood estimates (MLEs)  $\hat{\mu}$  and  $\hat{\theta}$  are the values of the parameters that maximize the likelihood function  $L(\mu, \theta)$ . The dependence of the likelihood function on the data propagates to the values of the MLEs, so when needed, the MLEs will be given subscripts to indicate the data set used. For instance,  $\hat{\theta}_{\text{obs}}$  is the MLE of  $\theta$  derived from the observed data and global observables [148].

The conditional maximum likelihood estimate (CMLEs)  $\hat{\theta}(\mu)$  is the value of  $\theta$  that maximizes the likelihood function with  $\mu$  fixed; it can be seen as a multidimensional function of the single variable  $\mu$ . Again, the dependence on  $\mathcal{D}_{\text{sim}}$  and  $\mathcal{G}$  is implicit. This procedure for choosing specific values of the nuisance parameters for a given value of  $\mu$ ,  $\mathcal{D}_{\text{sim}}$  and  $\mathcal{G}$  is often referred to as *profiling*. Similarly,  $\hat{\theta}(\mu)$  is often called *the profiled value of  $\theta$* .

Given these definitions, one can construct the profile likelihood ratio

$$\lambda(\mu) = \frac{L(\mu, \hat{\theta}(\mu))}{L(\hat{\mu}, \hat{\theta})}, \quad (\text{A.10})$$

which depends explicitly on the parameter of interest  $\mu$ , implicitly on the data  $\mathcal{D}_{\text{sim}}$  and global observables  $\mathcal{G}$ , and is independent of the nuisance parameters  $\theta$  (which have been eliminated via *profiling*).

The profile likelihood ratio is an important quantity in hypothesis testing as will be shown later. The concept of variance of the estimates is also generalized to the covariance matrix, whose diagonal elements are the same as the variance for the individual parameters.

In the case of a Poisson model  $Pois(n|\nu)$  the maximum likelihood estimate of  $\nu$  is simply  $\hat{\nu} = n$ . Thus, it follows that the variance of the estimator is  $\sigma^2 = \text{var}[\hat{\nu}] = \text{var}[n] = \nu$ . Thus if the true rate is  $\nu$  one expects to find estimates  $\hat{\nu}$  with a characteristic spread around  $\nu$ ; it is in this sense that the measurement (the estimate of the parameter) has some uncertainty or ‘error’ of  $\sqrt{n}$ .

## A.3 Hypothesis tests

The goal of a hypothesis test is to make a statement about how well the observed data agrees with given predicted probabilities, i.e. a *hypothesis*. The hypothesis under consideration is traditionally called the *null hypothesis*,  $H_0$ , which could specify, for example, a probability density  $f(x)$  of a random variable. If the hypothesis determines  $f(x)$  uniquely it is said to be simple; if the form of the pdf is defined but not the values of at least one free parameter  $\omega$ , the  $f(x|\omega)$  is called a composite hypothesis.

### A.3.1 Null vs alternate hypotheses

A statement about the validity of  $H_0$  often involves a comparison with some alternative hypotheses,  $H_1, H_2, \dots$ . Suppose one has the measured data  $\mathcal{D}$  and

a set of hypotheses,  $H_0, H_1, \dots$ , each of which specifies a given joint pdf,  $f(\mathcal{D}|H_0), f(\mathcal{D}|H_1), \dots$ . In order to investigate the degree of agreement between the observed data and a given hypothesis, one can construct a function of the measured variables called a *test statistic*  $T(\mathcal{D})$ . A test statistic is a function that maps the data to a single real number:  $T(\mathcal{D}) \rightarrow \mathbb{R}$ , examples of test statistics can be<sup>5</sup>:

- the difference between the observed and expected number of events:  $T(\mathcal{D}) = n - \nu$ ,
- the likelihood ratio:  $T(\mathcal{D}) = f(\mathcal{D}|H_1)/f(\mathcal{D}|H_0)$ , used in the case of two simple hypotheses (probability models without any free parameters),
- the profile likelihood ratio,  $T(\mathcal{D}) = \lambda(\mu) = \frac{L(\mu, \hat{\boldsymbol{\theta}}(\mu))}{L(\hat{\mu}, \hat{\boldsymbol{\theta}})}$ , where  $\hat{\boldsymbol{\theta}}(\mu)$  is the CMLE and  $\hat{\mu}$  and  $\hat{\boldsymbol{\theta}}$  are the (unconditional) MLEs.

Each of the hypotheses will imply a given pdf for the test statistic  $T$ , i.e.  $g(T|H_0), g(T|H_1), \dots$ . Let us suppose for the moment that we have chosen a scalar function  $T(\mathcal{D})$ , which has the pdf  $g(T|H_0)$  if  $H_0$  is true, and  $g(T|H_1)$  if  $H_1$  is true, as shown in Fig A.3.

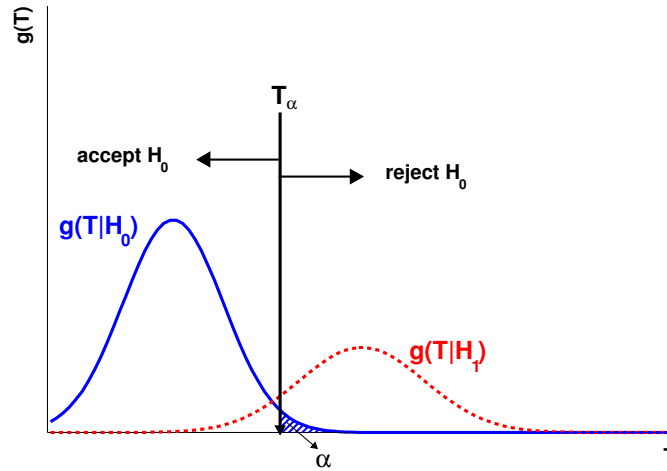


Figure A.3: Illustration of a simple hypothesis test.

Often one formulates the statement about the compatibility between the data and the various hypotheses in terms of a decision to accept or reject a given null hypothesis  $H_0$ . This is done by:

<sup>5</sup>For an informal but pedagogical discussion about the choice of the test statistic see “Section 3.2 and 5” of [148], and for more complete discussion on construction of test statistics see “Chapter 4” of [151].

- defining a critical region for  $T$ , such that if the value of  $T$  actually observed is in the critical region, one rejects the hypothesis  $H_0$ ; otherwise,  $H_0$  is accepted.<sup>6</sup>

- The critical region is chosen such that the probability for  $T$  to be observed there, under assumption of the hypothesis  $H_0$ , is some value  $\alpha$ , called the *significance level* or the *size* of the test.

For example, the critical region could consist of values of  $T$  greater than a certain value  $T_\alpha$ , called the cut or decision boundary, as shown in Fig A.3. The significance level is then

$$\alpha = \int_{T_\alpha}^{\infty} g(T|H_0)dT = P(T(\mathcal{D}) \geq T_\alpha|H_0). \quad (\text{A.11})$$

One would then accept (or, strictly speaking, not reject) the hypothesis  $H_0$  if  $T_{obs} < T_\alpha$ , where  $T_{obs}$  is the value of the test statistic for the observed data.

- There is thus a probability of  $\alpha$  to reject  $H_0$  if  $H_0$  is true. This is called a *Type I error*.
- A *Type II error* takes place if the hypothesis  $H_0$  is accepted (i.e.  $T$  observed is less than  $T_\alpha$ ) but the true hypothesis was not  $H_0$  but rather some alternative hypothesis  $H_1$ . The probability for this is

$$\beta = \int_{-\infty}^{T_\alpha} g(T|H_1)dT = P(T(\mathcal{D}) \leq T_\alpha|H_1). \quad (\text{A.12})$$

- $1 - \beta$  is called the *power of the test* to discriminate against the alternative hypothesis  $H_1$ .

### A.3.2 P-value

Another way of quantifying the compatibility of  $H_0$  with the observed data is to state the so-called *p-value*:

$$p = \int_{T_{obs}}^{\infty} g(T|H_0)dT = P(T(\mathcal{D}) \geq T_{obs}|H_0). \quad (\text{A.13})$$

i.e. the probability, under assumption of  $H_0$ , of obtaining a result as compatible or less with  $H_0$  than the one actually observed. The *p-value* is also called the *observed significance level*. Here the *p-value* is a random variable, in contrast to the previous situation, where the significance level  $\alpha$  was a constant specified before carrying out the test. This kind of test is often carried out to judge whether a discrepancy between data and expectation is sufficiently significant to merit a claim for a new discovery.

<sup>6</sup>The complement of the critical region is called the acceptance region.

Note the  $p$ -value is NOT to be interpreted as the probability of the null hypothesis given the data, instead, the  $p$ -value is a statement about the probability to have obtained data with a certain property assuming the null hypothesis. One must remember that  $P(H_0|\mathcal{D}) \neq P(\mathcal{D}|H_0)$ . It sometimes helps clarifying the difference between  $P(A|B) \neq P(B|A)$  by remembering that the probability of being pregnant given the fact that you are a female is considerably smaller than the probability of being a female given the fact that you are pregnant.

**Example: Discovery as a hypothesis test**

Typically, new physics searches are looking for a signal that is additive on top of the background. Discovery is formulated in terms of a hypothesis test where the *background-only hypothesis* plays the role of the null hypothesis and the *signal-plus-background hypothesis* plays the roll of the alternative. Roughly speaking, the claim of a discovery is a statement that the data are incompatible with the background-only hypothesis. Consider the simplest scenario where one is counting events in the signal region,  $n_{SR}$ , and expects  $\nu_B$  events from background and  $\nu_S$  events from the considered signal. Then, one has the following hypotheses:

symbol	statistical name	physics name	probability model
$H_0$	null hypothesis	background-only	$Pois(n_{SR} \nu_B)$
$H_1$	alternate hypothesis	signal-plus-background	$Pois(n_{SR} \nu_S + \nu_B)$

In this simple example, evidence for a signal shows up as an excess of events, therefore a reasonable way to quantify the compatibility of the observed data,  $n_{SR}^{obs}$ , and the null hypothesis is to calculate the probability that the background-only would produce at least this many events, i.e. the  $p$ -value, in this example defined as:

$$p = \sum_{n=n_{SR}^{obs}}^{\infty} Pois(n|\nu_B). \quad (\text{A.14})$$

If this  $p$ -value is very small, then one might choose to reject the null hypothesis.

The  $p$ -value calculated in the previous example corresponds to the background-only hypothesis, this is usually called  $p_0$  or  $p_b$  to distinguish it from the  $p$ -value corresponding to the signal-plus-background hypothesis,  $p_{s+b}$  or  $p_\mu$ .

It is customary to convert the background-only  $p$ -value into the *sigma* of a unit Gaussian. This conversion is purely conventional and makes no



assumption that the test statistic  $T$  is Gaussian distributed. The conversion is defined as:

$$Z = \Phi^{-1}(1 - p_0) \quad (\text{A.15})$$

where  $\Phi^{-1}$  is the inverse of the cumulative distribution for a unit Gaussian. One says the significance of the result is  $Z\sigma$  and the standard discovery convention is  $5\sigma$ , corresponding to a  $p_0 = 2.87 \cdot 10^{-7}$ .

The use of Gaussian distributions in this context relies on the following assumptions:

- The value of the quantity of interest has been correctly calculated (e.g. there are no important systematic biases).
- The magnitude of the error has been correctly calculated. This is particularly important, in that an incorrect estimate of the accuracy of the experiment could have a very large effect on the calculated significance of the result and hence on the conclusions. E.g. an underestimate of the experimental errors by a factor of two could change a two standard deviation effect (which occurs at the 5% level) into a four standard deviation one (whose probability is only  $10^{-5}$ , i.e. such an effect ‘cannot’ happen if the theory is correct).
- The form of the experimental resolution is such that the Gaussian approximation is reasonable. This is almost always untrue, in that the probability of obtaining large deviations ( $\gtrsim 3\sigma$ ) from the correct value is often larger than given by the Gaussian distribution. This effect is also likely to result in an artificial enhancement of the estimation of the significance of observed deviations.

Assuming the above complications are absent, a simple example, extracted from Ref. [147], will be considered to illustrate the usage of the Gaussian distributions to assess a significance to experimental results.

#### **Example: Lifetime of the neutron**

The lifetime of the neutron has been measured in an experiment to be  $950 \pm 20$  s. A certain theory predicts that the lifetime is 910 s. To what extent are these numbers in agreement? For this, a graph or table showing the fractional area under the tails of a Gaussian curve (error function) with  $|t| > r$  is necessary, where

$$t = \frac{x - \mu}{\sigma} \quad (\text{A.16})$$

What these kind of graphs, Fig. A.4, show is, in other words, the area under the tails of the Gaussian beyond any value  $r$  of the parameter  $t$ . In the example of the neutron lifetime,  $t = \frac{950-910}{20} = 2$  and the corresponding probability is 4.6%. Thus if 1000 experiments of the same precision as this one were performed to measure

the neutron lifetime, if the theory is correct and the experiments are bias-free, then about 46 of them would be expected to differ from the predicted value by at least as much as this one. The question of whether the theory and the experiment are considered compatible or not still remains, but at least with this method there is a number on which to base such a judgement.

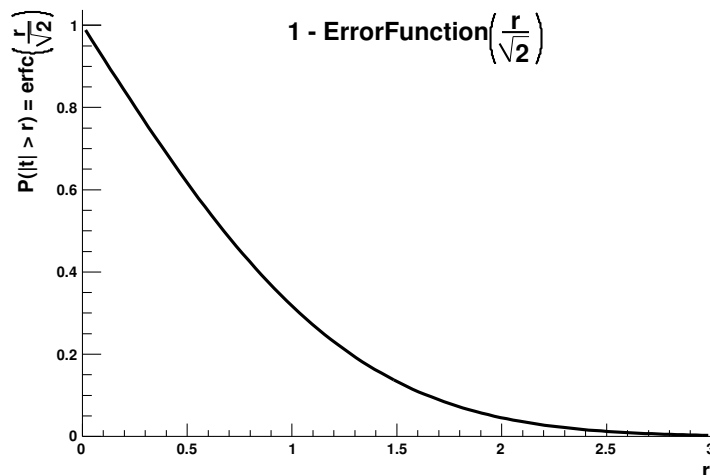


Figure A.4: The plot shows

It is important to realise that  $\sigma$  in Eq. A.16 is supposed to be the true value of the experimental resolution. In some cases, this will simply be estimated from the observed spread of a repeated set of measurements. Then fluctuations in the denominator of  $t$  are expected to widen its distribution as compared with a Gaussian; the expected distribution is Student's  $t$ , and depends on the number of observations  $N$  used to estimate  $\sigma$ . Since such information about other people's experiments is often unobtainable, most physicists would use a Gaussian distribution to estimate the significance of  $t$ . The difference between these distributions can be important for small  $N$ . Thus the probability of obtaining  $|t| > 3$  is 0.3% for a Gaussian distribution, but is 3% for Student's  $t$  with  $N = 6$ , and 20% for  $N = 2$ .

In most cases, the theoretical estimate  $x_{\text{th}}$  will have an uncertainty  $\sigma_{\text{th}}$  associated with it; theory, after all, is based on experiment, and hence predictions in general are calculated from other experimental numbers which of course have their own experimental errors. In that case, the above procedure can be repeated with the parameter  $t$  redefined as:

$$t = \frac{x_{\text{obs}} - x_{\text{th}}}{\sqrt{(\sigma^2 + \sigma_{\text{th}}^2)}},$$

where the measured value is  $x_{\text{obs}} \pm \sigma$  and it has been assumed that the errors on  $x_{\text{obs}}$  and  $x_{\text{th}}$  are uncorrelated.

### Generalization to models with many free parameters

How can one extend the previous concepts to the case of the more general model in Eq. A.9 with many free parameters? First one must still define the null and the alternate hypotheses. Typically this is done by saying some parameters – the parameters of interest  $\omega_{\text{poi}}$  – take on a particular value for the signal-plus-background hypothesis and a different value for the background-only hypothesis. For instance, the signal production cross-section might be singled out as the *parameter of interest* and it would take on the value of zero for the background-only and some reference value for the signal-plus-background. The remaining parameters are called the *nuisance parameters*  $\omega_{\text{nuis}}$ .

In this case the profile likelihood ratio is used as the test statistic. Remembering that the test statistic  $T$  is a real-valued function of the data, then any particular probability model  $f_{\text{tot}}(\mathcal{D}|\omega)$  implies a distribution for the test statistic  $f(T|\omega)$ .<sup>7</sup> Note the distribution for the test statistic depends on the value of  $\omega$ . Once one has the distribution, then one can calculate the  $p$ -value:

$$p(\omega) = \int_{T_{\text{obs}}}^{\infty} f(T|\omega) dT = P(T \geq T_{\text{obs}}|\omega), \quad (\text{A.17})$$

where  $T_{\text{obs}}$  is the value of the test statistic based on the observed data.

Given that the  $p$ -value depends on  $\omega$ , how does one decide to accept or reject the null hypothesis? Remembering that  $\omega_{\text{poi}}$  takes on a specific value for the null hypothesis, one should be worried about how the  $p$ -value changes as a function of the nuisance parameters. It is natural to say that one should not reject the null hypothesis if the  $p$ -value is larger than the size of the test for *any value of the nuisance parameters*. Thus, one should either present the  $p$ -value explicitly as a function of  $\omega_{\text{nuis}}$  or take its maximal (or supremum) value

$$p_{\text{sup}}(\omega_{\text{poi}}) = \sup_{\omega_{\text{nuis}}} p(\omega_{\text{nuis}}) \quad (\text{A.18})$$

As a final note it is worth mentioning that the size of the test, which serves as the threshold for rejecting the null hypothesis, is purely conventional. In most sciences conventional choices of the size are 10%, 5%, or 1%. In Particle Physics, the conventional threshold for discovery is the  $5\sigma$  criterion – which is a conventional way to refer to  $\alpha = 2.87 \cdot 10^{-7}$ . This is an incredibly small

<sup>7</sup>How one constructs this distribution is a different problem beyond the scope of this Thesis. For more on this topic see [148] and [151]

rate of Type-I error, reflecting that claiming a discovery of new physics would be a monumental statement. The origin of the  $5\sigma$  criterion has its roots in: the fact that traditionally scientists lacked the tools to properly incorporate systematics, the fear that there are systematics that may not be fully under control, and the fact that many searches for new physics are performed thus there are many chances to reject the background-only hypothesis.

### A.3.3 Confidence intervals: excluded and allowed regions

Often one considers a new physics model that is parametrized by theoretical parameters. For instance, the mass or coupling of a new particle. In that case one typically wants to ask what values of these theoretical parameters are allowed or excluded given available data. The allowed regions of the parameters space are called *confidence intervals* or *confidence regions*, and the parameter points outside them are considered excluded. Associated with a confidence interval there is a confidence level, usually 95% or 68%. If one repeats the experiments and obtains different data, then the confidence intervals will change. It is useful to think of the confidence intervals as being random in the same way the data are random. The defining property of a 95% confidence interval is that it *covers* the true value 95% of the time.

How can one possibly construct a confidence interval that has the desired property, that it *covers* the true value with a specified probability, given that we don't know the true value? The procedure for building a confidence interval is based on "inverting" a series of hypothesis tests. In particular, for each value of  $\omega$  in the parameter space one performs a hypothesis test based on some test statistic where the null hypothesis is  $\omega$ . Note that *in this context the null hypothesis is changing for each test and generally is not the background-only*. If one wants a 95% confidence interval, then one constructs a series of hypothesis test with a size of 5%. The confidence interval  $I(\mathcal{D})$  is constructed by taking the set of parameter points where the null hypothesis is accepted:

$$I(\mathcal{D}) = \{\omega \mid [P(T(\mathcal{D}) > T_\alpha \mid \omega) < \alpha]\}. \quad (\text{A.19})$$

Since a hypothesis test with a size of 5% should accept the null hypothesis 95% of the time if it is true, confidence intervals constructed in this way satisfy the defining property. This same property is usually formulated in terms of *coverage*. Coverage is the probability that the interval will contain (cover) the parameter  $\omega$  when it is true,

$$\text{coverage}(\omega) = P(\omega \in I \mid \omega). \quad (\text{A.20})$$

The equation above can easily be mis-interpreted as the probability the parameter is in a fixed interval  $I$ ; but one must remember that in evaluating the probability above the data  $\mathcal{D}$ , and thus the corresponding intervals produced by the procedure  $I(\mathcal{D})$ , are random quantities. Note that coverage is a property that can be quantified for any procedure that produces the confidence intervals  $I$ . Intervals produced using the procedure explained above are said to

“cover by construction”; however, one can consider alternative procedures that may either under-cover or over-cover. Undercoverage means that  $P(\omega \in I|\omega)$  is smaller than desired and over-coverage means that is larger than desired. Note that in general coverage depends on the assumed true value  $\omega$ .

### A.3.4 Example: the discovery of a Higgs boson

Remember that the (formula of the) likelihood function is numerically equivalent to the pdf of our model but with the data and global constraint terms fixed and with the parameters of interest and nuisance parameters left as free parameters.

$$L(\mu, \theta|\mathcal{D}, \mathcal{G}) \tag{A.21}$$

By maximizing the likelihood function, one obtains the (unconditional) maximum likelihood estimates for the model. Those estimates are called the best fit values  $(\hat{\mu}, \hat{\theta})$ .

#### Signal strength

In the case of searches for the standard model Higgs boson, the only free parameter in the Lagrangian is  $m_H$ . Once  $m_H$  is specified, the expected number of events and the cross sections are predicted by the theory. The results are often presented as a scan over  $m_H$ , therefore for each value of  $m_H$  one could perform a simple hypothesis test between background-only and signal-plus-background. However, usually one chooses to construct a parametrized model that does not directly correspond to any theory. In this case the parameter of interest is the *signal strength*, a scaling of the expected number of events with respect to the standard model prediction that can be seen as  $\nu_{\text{total}} = \mu \times \nu_s + \nu_b$ , where  $\mu = 0$  corresponds to the background-only hypothesis and  $\mu = 1$  corresponds to the SM Higgs boson hypothesis (which, in this case, is just one of the possible signal-plus-background hypothesis).

One can then fit the likelihood function, with the data and global constraint terms fixed, and obtain the signal strength best fit value,  $\hat{\mu}$ , for each value of  $m_H$ . This is what is shown in the bottom plot of Fig. A.5. This plot can be interpreted as how much signal is needed to make the models compatible with the measured data.

#### Discovery of a signal

If one now wants to test the background-only hypothesis (here the SM without Higgs) the needed procedure is a bit more complex. In this case, the test statistic used is based on the profile likelihood ratio with  $\mu = 0$ , which will be called  $q_0$  for simplicity. In order not to forget that the test statistic is a function of the data, the dependence will be written explicitly<sup>8</sup>:

$$q_0(\mathcal{D}) = -2 \ln \lambda(\mu = 0|\mathcal{D}) = -2 \ln \frac{L(\mu = 0|\mathcal{D})}{L(\hat{\mu}|\mathcal{D})} \tag{A.22}$$

<sup>8</sup>If also depends on the global constraint terms, but these will be omitted here to simplify the notation

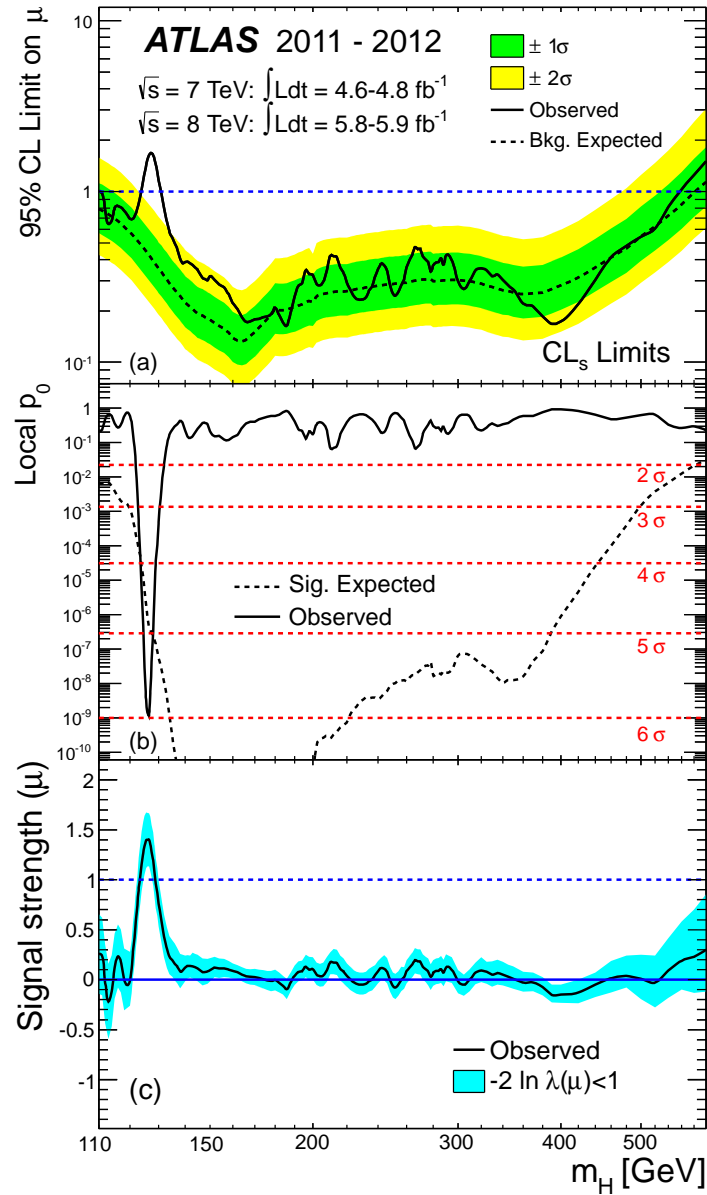


Figure A.5: (a) The observed (solid) 95% CL upper limit on the signal strength as a function of  $m_H$  and the expectation (dashed) under the background-only hypothesis. The dark and light shaded bands show the plus/minus one sigma and plus/minus two sigma uncertainties on the background-only expectation. (b) The observed (solid) local  $p_0$  as a function of  $m_H$  and the expectation (dashed) for a SM Higgs boson signal hypothesis ( $\mu = 1$ ) at the given mass. (c) The best-fit signal strength  $\hat{\mu}$  as a function of  $m_H$ . The band indicates the approximate 68% CL interval around the fitted value. [152]

One can obtain the value of  $q_0$  given the measured (observed) data. This real number will be called here  $q_0^{\text{obs}} = q_0(\mathcal{D}_{\text{obs}}) = -2 \ln \lambda(0|\mathcal{D}_{\text{obs}})$ . If instead of using the real data, one simulates experiments with MC (toy experiments), one can obtain a distribution of values for  $q_0$ :

$$q_0(\mathcal{D}_{MC}) = -2 \ln \lambda(\mu = 0|\mathcal{D}_{MC}) = -2 \ln \frac{L(\mu = 0|\mathcal{D}_{MC})}{L(\hat{\mu}_{MC}|\mathcal{D}_{MC})}, \quad (\text{A.23})$$

where  $\mathcal{D}_{MC}$  means datasets simulated with MC. As it has been mentioned before, the test statistic  $q_0$  will have different distributions for the background-only hypothesis:  $b = f(q_0|\mu = 0)$ ; and signal-plus-background hypothesis:  $s+b = f(q_0|\mu)$ . These distributions will look similar to the ones shown in Fig. A.6. Drawing  $q_0^{\text{obs}}$  in the same histogram one gets a graphical idea of the  $p$ -value for the background-only hypothesis ( $p_0$ ).  $p_0$  is the probability, assuming that the background-only hypothesis is true, of obtaining  $q_0 \geq q_0^{\text{obs}}$ :

$$p_0 = \int_{q_0^{\text{obs}}}^{\infty} f(q_0|0) dq_0. \quad (\text{A.24})$$

Therefore, the smaller the  $p$ -value, the less compatible the data are with the background-only hypothesis. The middle plot in Fig. A.5 shows the  $p_0$  for each value of  $m_H$ .

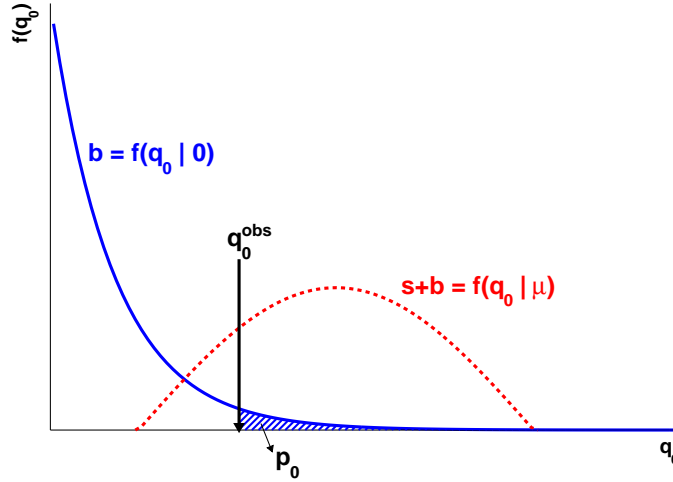


Figure A.6: Illustration of the background-only  $p$ -value ( $p_0$ ) definition.

### Setting upper limits

Finally, the top plot on Fig. A.5 shows the 95% confidence level (CL) limit on  $\mu$  for each  $m_H$ . For purposes of establishing an upper limit on the strength parameter  $\mu$ , one may define  $q_\mu = -2 \ln \lambda(\mu)$ , where  $\lambda(\mu)$  is the profile likelihood ratio as defined in Eq. A.10. As with the case of discovery,

one quantifies the level of agreement between the data and the hypothesised  $\mu$  with the  $p$ -value (in this case  $p_\mu$ ). For an observed value of  $q_\mu^{\text{obs}}$  (see Figure A.7, one has:

$$p_\mu = \int_{q_\mu^{\text{obs}}}^{\infty} f(q_\mu|\mu) dq_\mu. \quad (\text{A.25})$$

In this notation the subscript of  $q$  refers to the hypothesis being tested and the second argument in  $f(q_\mu|\mu)$  gives the value assumed in the distribution of data. A standard 95% confidence level upper limit is obtained by solving  $p_{\mu_{up}} = 5\% = 0.05$ , where  $\mu_{up}$  is the upper limit<sup>9</sup>.

In other words and looking at Fig. A.5, taking a given value of  $m_H$ , one can test all the possible values of  $\mu$  calculating its  $p$ -values (i.e. perform several hypothesis test where the null hypothesis is not the background-only, here the null hypothesis is the corresponding value of  $\mu$  in each test). The value of  $\mu$  that gives a  $p$ -value = 0.05 is the 95% confidence level limit on  $\mu$ . Values of  $\mu$  that yield  $p$ -values lower than 0.05 will be excluded (their compatibility with the data is very small), while values of  $\mu$  with  $p$ -values higher than 0.05 have not been proven incompatible with the data, therefore they cannot be excluded.

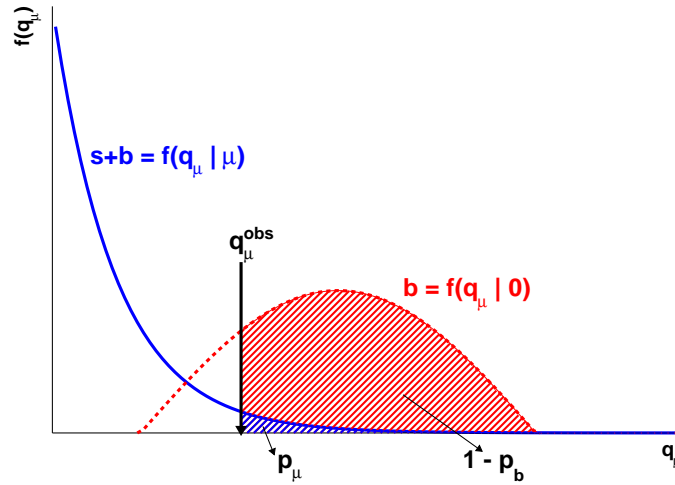


Figure A.7: Illustration of the signal-plus-background  $p$ -value ( $p_\mu$ ) and the  $1 - p_b$  definitions.

Looking at the mentioned plot, one can conclude that all values of  $\mu$  above the solid black line are excluded. Remembering that  $\mu = 1$  corresponds to the SM Higgs hypothesis, all values of  $m_H$  that have  $\mu = 1$  above the solid black line are excluded, leaving only a mass range of  $m_H$  125 GeV compatible with the observed data.

<sup>9</sup>Usually the CLs value is used instead of  $p_\mu$ . The CLs method will be explained in the next section.



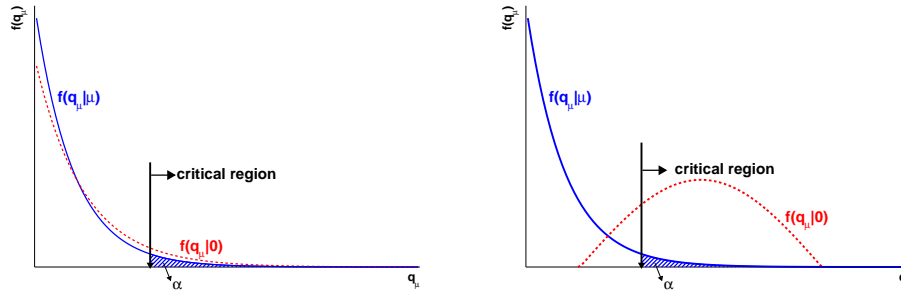


Figure A.8: Illustration of statistical tests of parameter values  $\mu$  for the cases of: (left) little sensitivity and (right) substantial sensitivity.

The dashed black line still remains to be explained. What this line is showing is the limits that one would obtain if the background-only hypothesis (SM without Higgs) were true. One can see that this also indicates the sensitivity of the experiment, given that the  $\mu = 1$  line is above the expected limit for all the mass range, which means that if the background-only hypothesis were true one could exclude the SM Higgs hypothesis for the shown mass range.

### A.3.5 The sensitivity problem: the $CL_s$ method.

When testing a hypothesized strength parameter  $\mu$ , it can happen that the magnitude of the signal implied by  $\mu$  is extremely small – so small, that the probabilities for the data are very close to what they would be in the absence of the signal process, i.e.,  $\mu = 0$ . In such a case one has little or no sensitivity to the given value of  $\mu$ .

For example, Fig. A.8 (left) illustrates a situation where there is only a very small level of sensitivity to a given strength parameter  $\mu$ . The plot shows the pdfs of the test statistic  $q_\mu$  under the assumption of strength parameter  $\mu$ , and also assuming  $\mu = 0$ , i.e.,  $f(q_\mu|\mu)$  and  $f(q_\mu|0)$ . If the observed value of the test statistic is found in the critical region corresponding to the top 5% of  $f(q_\mu|\mu)$ , then the hypothesized  $\mu$  is rejected. But as the two pdfs almost coincide, the probability to reject  $\mu$  if the true strength parameter is zero is also close to  $\alpha = 0.05$ . Fig. A.8 (right) shows the same distributions as (left) but for a different value of  $\mu$ . The size of the test is, as in (left), equal to  $\alpha$ . Here, however, the distribution of  $q_\mu$  under the assumption of  $\mu = 0$  leads to a substantially greater probability to reject  $\mu$ , i.e., to find  $q_\mu$  in the critical region.

In the context of a search for a new phenomenon, this means that with probability not less than  $\alpha$  one will exclude hypotheses to which one has little or no sensitivity. This corresponds to the case where the expected number of signal events is much less than that of background. If, for example, the expected numbers of signal and background events are  $\nu_s$  and  $\nu_b$ , respectively, and one has  $\nu_s \ll \nu_b$ , then if the observed number of events has a sufficient

downward fluctuation relative to  $\nu_s + \nu_b$  (which is approximately equal to  $\nu_b$ ), then this value of  $\nu_s$  will be excluded. In the limit where  $\nu_s \ll \nu_b$ , one might want intuitively this exclusion probability to go to zero, but in fact it approaches  $\alpha = 5\%$ . Given that Particle Physics experiments often carry out many searches covering a broad parameter range for many signal models, it is not desirable that one out of twenty searches where one has no sensitivity should result in exclusion.

To protect against excluding models to which one has little or no sensitivity, in the  $\text{CL}_s$  procedure a signal model is regarded as excluded if one finds

$$\text{CL}_s \equiv \frac{p_{s+b}}{1 - p_b} < \alpha. \quad (\text{A.26})$$

That is, the  $p$ -value is effectively penalized by dividing by  $1 - p_b$ . Here  $p_{s+b} = p_\mu$  according to the previous section notation, and  $p_b$  is defined as:

$$p_b = \int_{-\infty}^{q_\mu^{\text{obs}}} f(q_\mu|0) dq_\mu. \quad (\text{A.27})$$

If the two distributions  $f(q_\mu|\mu)$  and  $f(q_\mu|0)$  are widely separated, then  $1 - p_b$  is only slightly less than unity, the penalty is slight, and thus exclusion based in  $\text{CL}_s$  is similar to that obtained from the usual  $p$ -value  $p_{s+b}$ . If, however, one has little sensitivity to the signal model, then the two distributions are close together,  $1 - p_b$  becomes small, and thus the  $p$ -value of s+b is penalized (increased) more. In this way one is prevented from excluding signal models in cases of low sensitivity. As previously, one takes the upper limit to be the largest value of the parameter (e.g., the signal rate  $\nu_s$ ) not excluded.

From the definition A.26, one can see that  $\text{CL}_s$  is always greater than the  $p$ -value  $p_{s+b}$ . Thus the models excluded by requiring  $\text{CL}_s < \alpha$  are a subset of those excluded by the usual criterion  $p_{s+b} < \alpha$ , and the upper limit from  $\text{CL}_s$  is therefore higher (weaker). In this sense the  $\text{CL}_s$  procedure is conservative, but also avoids the undesirable property that of two experiments with the same (small) expected signal rate but different backgrounds, the experiment with the larger background may have a better expected performance.

## Appendix B

# Further studies on the $Z +$ jets $+ E_T^{\text{miss}}$ analysis

### B.1 Further details on flavour-symmetric backgrounds estimation

This section documents validations and cross-checks performed on the flavour symmetric background estimation beyond those already discussed in Section 4.6.3.

For clarification purposes, sketches describing all the regions used as control and validation regions are shown here. See Figures B.1 and B.2.

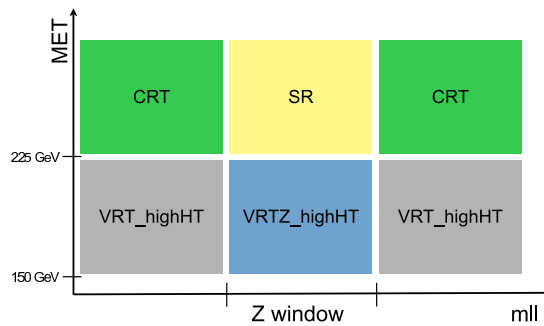


Figure B.1: Sketch showing the relative situation of regions SR, CRT, VRT\_highHT, VRTZ\_highHT. Extrapolation from CRT to VRT\_highHT is done in  $E_T^{\text{miss}}$  while extrapolation from CRT to SR is done in  $m_{\ell\ell}$ .

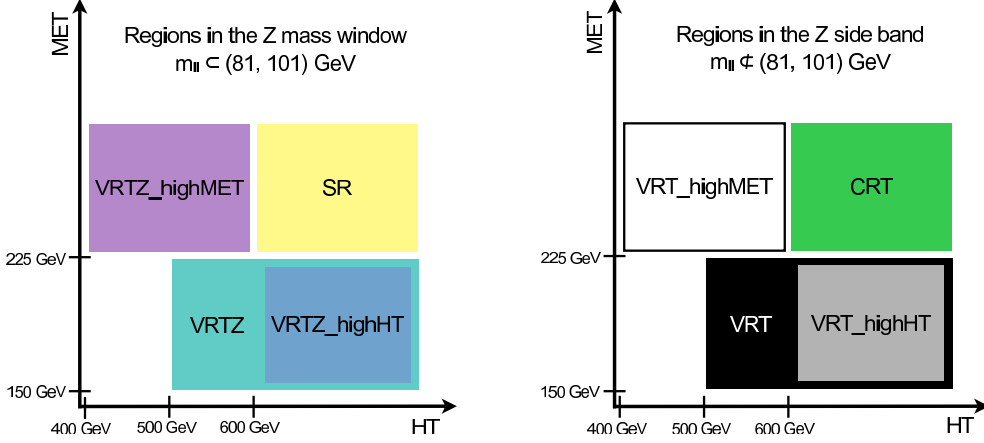


Figure B.2: Sketch showing the relative situation of regions SR, VRTZ, VRTZ\_highMET, VRTZ\_highHT in the  $Z$ -mass window and the analogous regions in the  $Z$ -mass side band.

### B.1.1 Testing the $N_{ee}^{MC}:N_{\mu\mu}^{MC}:N_{e\mu}^{MC}$ ratio in VRZ\_Zsideband

In order to test that the  $N_{ee}^{MC}:N_{\mu\mu}^{MC}:N_{e\mu}^{MC} = 1:1:2$  ratio holds, especially after applying the trigger and reconstruction correction factors defined in Equation 4.3, validation region VRZ\_Zsideband (rich in dileptonic- $t\bar{t}$  events) is defined with the same requirements as VRZ (see Table 4.1) but in the invariant mass side band:

- Presel\_Zsideband = 2 OS leptons, lep1Pt > 25 GeV, lep2Pt > 10 GeV,  $m_{ll} > 15$  GeV,  $m_{ll} < 81$  GeV OR  $m_{ll} > 101$  GeV
- VRZ\_Zsideband = Presel\_Zsideband + Njets  $\geq$  2,  $H_T > 600$  GeV,  $E_T^{\text{miss}} < 150$  GeV

The actual ratio of  $ee:\mu\mu:e\mu$  is determined in VRZ\_Zsideband and can be seen in Table B.1 together with the number of dileptonic- $t\bar{t}$  events before applying any correction factors.

After applying the corresponding trigger efficiency factor  $\alpha$  and the  $k_{ee}$  factor ( $k_{ee}$  taken from the original VRZ) the ratio between number of events in the electron-electron, muon-muon and electron-muon channels is closer to 1:1:2, as expected from theory and shown in Table B.2. Only statistical errors are shown in the following tables.

VRZ_Zsideband	$N_{ee}^{MC}$	$N_{\mu\mu}^{MC}$	$N_{e\mu}^{MC}$	$N_{ee}^{MC}:N_{\mu\mu}^{MC}:N_{e\mu}^{MC}$
barrel-barrel	$360.11 \pm 4.74$	$296.58 \pm 4.21$	$581.64 \pm 3.83$	$1 \pm 0.02$ : <b>0.82</b> $\pm$ 0.02: <b>1.62</b> $\pm$ 0.02
barrel-endcap	$233.23 \pm 3.83$	$277.00 \pm 4.05$	$495.49 \pm 3.53$	$1 \pm 0.02$ : <b>1.19</b> $\pm$ 0.03: <b>2.12</b> $\pm$ 0.04
endcap-endcap	$35.92 \pm 1.51$	$65.95 \pm 1.99$	$92.36 \pm 1.58$	$1 \pm 0.06$ : <b>1.84</b> $\pm$ 0.10: <b>2.57</b> $\pm$ 0.12
TOTAL:	$629.27 \pm 6.27$	$639.52 \pm 6.17$	$1169.48 \pm 5.44$	$1 \pm 0.01$ : <b>1.02</b> $\pm$ 0.01: <b>1.86</b> $\pm$ 0.02

Table B.1: Number of dileptonic- $t\bar{t}$  events in VRZ\_Zsideband per barrel-endcap region **before applying any correction factor**. Uncertainties are statistical only.

VRZ_Zsideband	$N_{ee}^{MC}$	$N_{\mu\mu}^{MC} \times k_{ee}^2$	$N_{e\mu}^{MC} \times k_{ee} \times \alpha$	$N_{ee}^{MC}:N_{\mu\mu}^{MC}:N_{e\mu}^{MC}$
barrel-barrel	$360.11 \pm 4.74$	$358.21 \pm 7.52$	$734.41 \pm 12.34$	$1 \pm 0.02$ : <b>0.99</b> $\pm$ 0.02: <b>2.04</b> $\pm$ 0.04
barrel-endcap	$233.23 \pm 3.83$	$201.55 \pm 4.79$	$478.55 \pm 9.60$	$1 \pm 0.02$ : <b>0.86</b> $\pm$ 0.02: <b>2.05</b> $\pm$ 0.05
endcap-endcap	$35.92 \pm 1.51$	$42.73 \pm 1.61$	$82.96 \pm 2.33$	$1 \pm 0.06$ : <b>1.19</b> $\pm$ 0.07: <b>2.31</b> $\pm$ 0.12
TOTAL:	$629.27 \pm 6.27$	$602.49 \pm 9.06$	$1295.92 \pm 15.81$	$1 \pm 0.01$ : <b>0.96</b> $\pm$ 0.02: <b>2.06</b> $\pm$ 0.03

Table B.2: Number of dileptonic- $t\bar{t}$  events in VRZ\_Zsideband per barrel-endcap region **after correcting  $N_{\mu\mu}, N_{e\mu}$  with  $k_{ee}$  and  $\alpha$**  ( $N_{ee}^{MC}$  is taken as reference). Uncertainties are statistical only.

### B.1.2 Testing $m_{\ell\ell}$ distributions: data/MC ratios in the $Z$ -window / $Z$ -side band.

In the side-band fit, CRT is used to normalize  $t\bar{t}$  to data and the obtained normalization factor is transferred to SR. Since the extrapolation from CRT to SR is done in  $m_{\ell\ell}$ , the stability of this distribution was tested in a high statistics region, close to SR+CRT: VRTZ+VRT, defined as SR+CRT but with a lowered  $E_T^{\text{miss}}$  cut of  $150 < E_T^{\text{miss}} < 225$  GeV and a lowered  $H_T$  cut of  $H_T > 500$  GeV (see Section 4.6.3.2.1 for details on the fit). In these regions it was found that the ratio data/MC was stable over the full  $m_{\ell\ell}$  distribution, as can be seen in Figure B.3, where a constant ratio of  $\sim 0.7$  is found for the three  $m_{\ell\ell}$  regions defined:  $m_{\ell\ell} < 81$  GeV,  $81 < m_{\ell\ell} < 101$  GeV and  $m_{\ell\ell} > 101$  GeV and for the three flavour channels:  $ee$ ,  $\mu\mu$  and  $e\mu$ . It should be noticed the  $t\bar{t}$  has not been normalized in these plots.

After unblinding, the same test was done for SR+CRT, where it is seen from Figure B.4 that the data/MC ratio is consistent within uncertainties among the low and high  $m_{\ell\ell}$  sidebands (first and third bins in each of the plots) while the excess is only observable in the  $81 < m_{\ell\ell} < 101$  GeV range (second bin), corresponding to SR, mainly in the  $ee$  channel. In these plots, a normalization factor of 0.52 is applied to  $t\bar{t}$  as given by the side-band fit results (section 4.6.3.2).

If one lowers only the  $E_T^{\text{miss}}$  cut while keeping the  $H_T$  cut as in SR+CRT, the data/MC ratio is compatible among the three bins, as seen in Figure B.5 for (VRTZ+VRT)\_highHT, defined in Table 4.1. On the other hand, if the  $H_T$  cut is brought down to  $400 < H_T < 600$  GeV while  $E_T^{\text{miss}}$  is kept at  $E_T^{\text{miss}} > 225$  GeV, the excess in the  $81 < m_{\ell\ell} < 101$  GeV range starts to be visible, as seen in Figure B.6 for (VRTZ+VRT)\_highMET.

The detailed data/MC ratios for all these regions can be found in Table B.3.

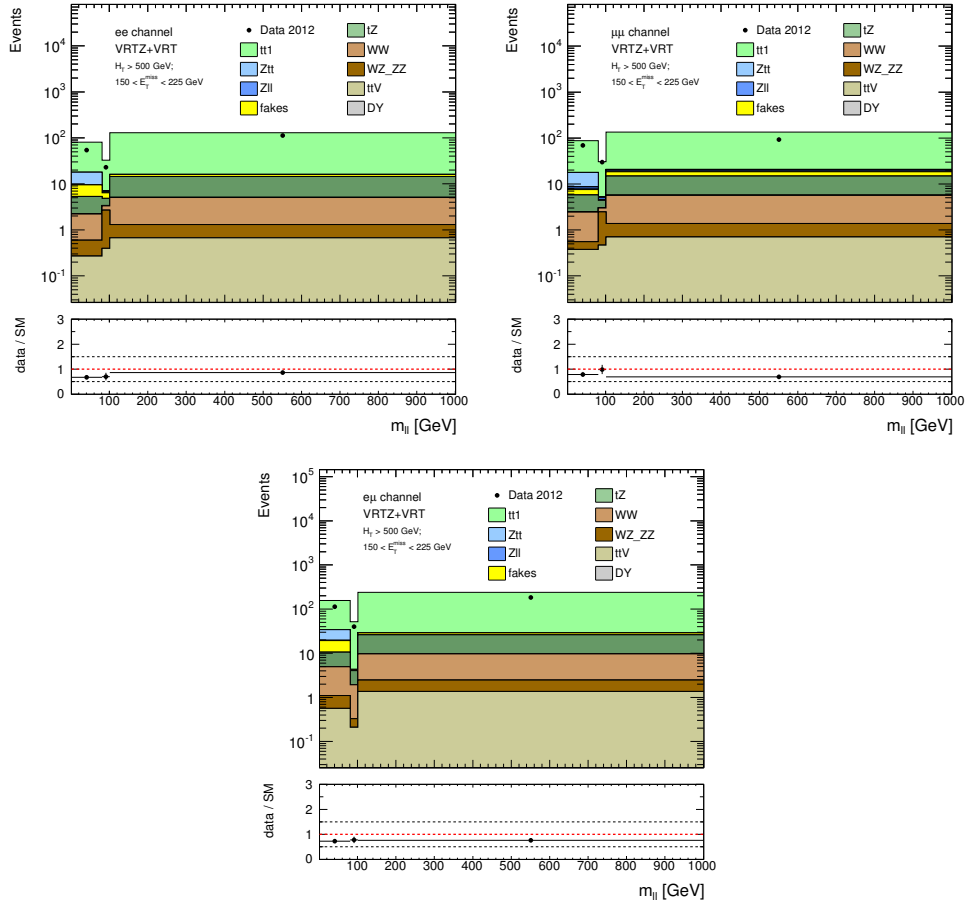


Figure B.3: Data-MC comparison in the  $m_{\ell\ell}$  distribution for VRTZ+VRT. No normalization factor has been applied to  $t\bar{t}$ . Only statistical errors are shown.

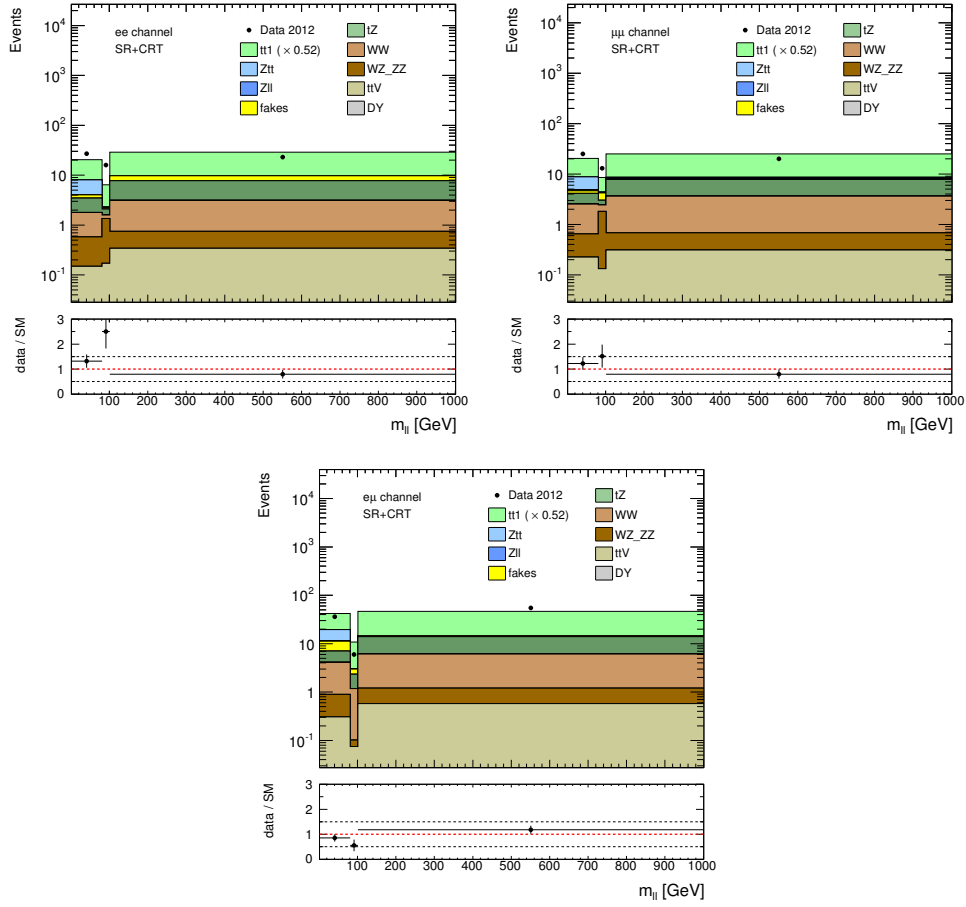


Figure B.4: Data-MC comparison in the  $m_{\ell\ell}$  distribution for SR+CRT. For  $t\bar{t}$ , a normalization factor of 0.52 has been applied as suggested by the side-band fit. Only statistical errors are shown.

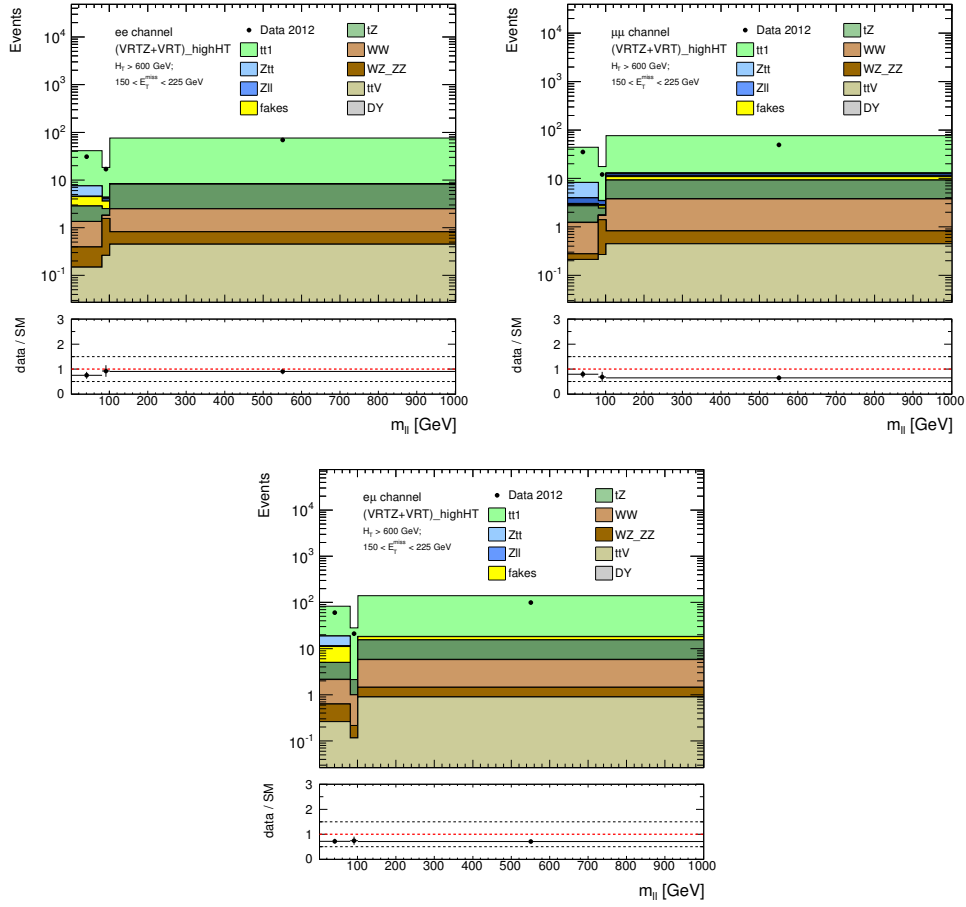


Figure B.5: Data-MC comparison in the  $m_{\ell\ell}$  distribution for (VRTZ+VRT)\_highHT. No normalization factor has been applied to  $t\bar{t}$ . Only statistical errors are shown.



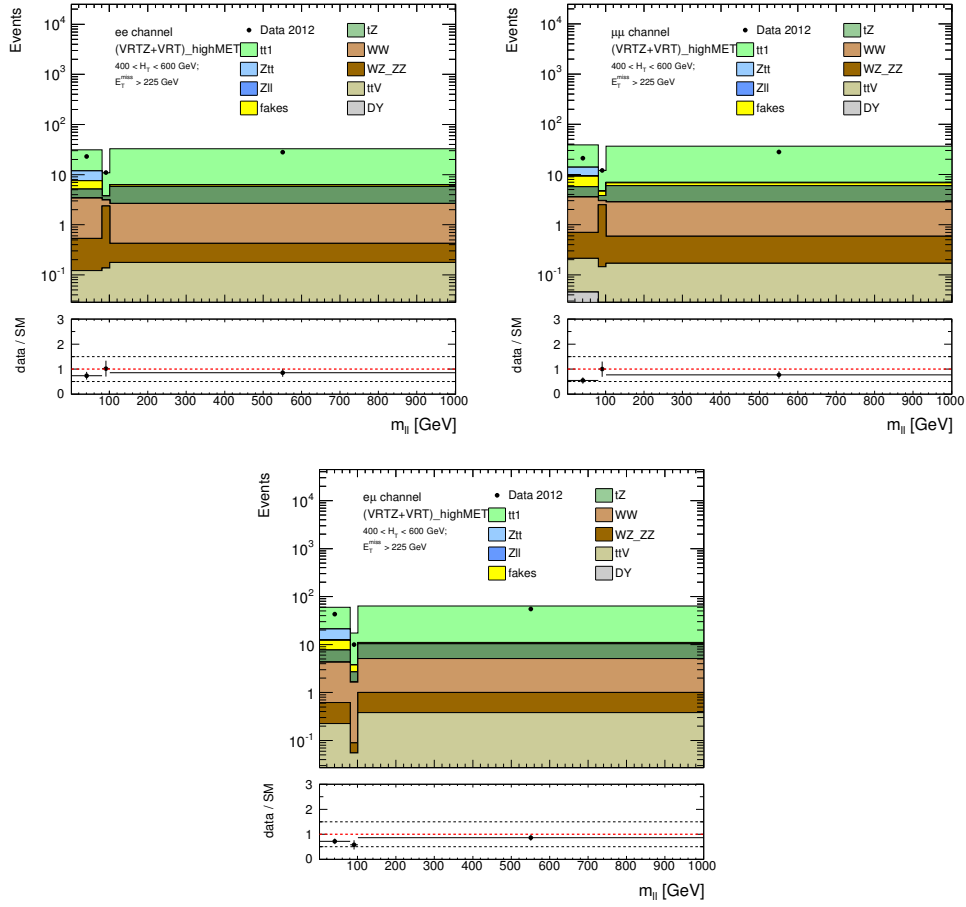


Figure B.6: Data-MC comparison in the  $m_{\ell\ell}$  distribution for (VRTZ+VRT)<sub>highMET</sub>. No normalization factor has been applied to  $t\bar{t}$ . Only statistical errors are shown.

Region	channel	$m_{\ell\ell} < 81$ GeV	$81 < m_{\ell\ell} < 101$ GeV	$m_{\ell\ell} > 101$ GeV
SR+CRT ( $t\bar{t}$ _Norm = 0.52)	$ee$	$1.32 \pm 0.26$	$2.50 \pm 0.68$	$0.79 \pm 0.17$
	$\mu\mu$	$1.23 \pm 0.25$	$1.52 \pm 0.46$	$0.80 \pm 0.18$
	$e\mu$	$0.85 \pm 0.15$	$0.55 \pm 0.23$	$1.18 \pm 0.16$
VRTZ+VRT ( $t\bar{t}$ _Norm = 1)	$ee$	$0.67 \pm 0.09$	$0.70 \pm 0.15$	$0.86 \pm 0.08$
	$\mu\mu$	$0.79 \pm 0.10$	$0.99 \pm 0.19$	$0.69 \pm 0.07$
	$e\mu$	$0.72 \pm 0.07$	$0.78 \pm 0.13$	$0.76 \pm 0.06$
(VRTZ+VRT)_highHT ( $t\bar{t}$ _Norm = 1)	$ee$	$0.75 \pm 0.14$	$0.92 \pm 0.23$	$0.91 \pm 0.11$
	$\mu\mu$	$0.79 \pm 0.14$	$0.68 \pm 0.20$	$0.64 \pm 0.09$
	$e\mu$	$0.72 \pm 0.10$	$0.74 \pm 0.17$	$0.71 \pm 0.07$
(VRTZ+VRT)_highMET ( $t\bar{t}$ _Norm = 1)	$ee$	$0.73 \pm 0.16$	$1.01 \pm 0.32$	$0.85 \pm 0.17$
	$\mu\mu$	$0.54 \pm 0.12$	$1.00 \pm 0.30$	$0.76 \pm 0.15$
	$e\mu$	$0.71 \pm 0.11$	$0.58 \pm 0.19$	$0.86 \pm 0.12$

Table B.3: Data/MC ratios for different regions in the low  $m_{\ell\ell}$ -sideband,  $m_{\ell\ell} < 81$  GeV; the  $m_{\ell\ell}$ -window,  $81 < m_{\ell\ell} < 101$  GeV; and the high  $m_{\ell\ell}$ -sideband,  $m_{\ell\ell} > 101$  GeV. In each of the regions, the normalization factor applied to  $t\bar{t}$ ,  $t\bar{t}$ \_Norm, is also given. Only statistical errors are shown.

## B.2 Study on the impact of a $\Delta\phi(\text{jet}, E_T^{\text{miss}})$ cut on SR.

Hard jets mis-measurement can lead to high fake  $E_T^{\text{miss}}$  pointing to the mis-measured jet direction. A cut on the angle between the  $E_T^{\text{miss}}$  and the leading jets direction,  $\Delta\phi(\text{jet}, E_T^{\text{miss}})$ , can be used to avoid events containing such sources of fake  $E_T^{\text{miss}}$ . The original signal region defined for this analysis, which was approved by the SUSY group for unblinding in April 2014, did not include any requirements on this angle. After unblinding, a cut on this variable was proposed and its impact on the background estimation methods and in the analysis sensitivity was studied. A summary of the checks carried out for this study, for which the signal region was re-blinded, is presented in this appendix.

Taking into account that only high- $p_T$  jets can lead to large fake  $E_T^{\text{miss}}$  and given the tight  $E_T^{\text{miss}}$  requirement applied in this analysis, only the leading and subleading jets are considered in this study. Therefore, when a  $\Delta\phi > x$  cut is applied, the angles between  $E_T^{\text{miss}}$  and the leading jet and between  $E_T^{\text{miss}}$  and the subleading jet are required to be larger than  $x$ .

### B.2.1 Applying a $\Delta\phi$ cut on the flavour-symmetry method

The whole flavour-symmetry method has been applied to the original SR with five different  $\Delta\phi$  cut values. The expected number of events in the  $ee$  and  $\mu\mu$  channels are shown in Table B.4. Results in this table have been calculated separating the three detector regions as usual, although for simplicity only the final number is shown. The number of data events in the  $e\mu$  channel is reduced by 33% for the  $\Delta\phi > 0.4$  cut. This causes a similar reduction in the final  $N_{ee}^{\text{est}}$  and  $N_{\mu\mu}^{\text{est}}$  estimates and makes their relative statistical error increase to 50%.

$\Delta\phi$ cut	$N_{e\mu}^{\text{data}}$	$N_{e\mu}^{\text{data,corr}}$	$N_{ee}^{\text{est}}$	$N_{\mu\mu}^{\text{est}}$
no cut	9	$7.85 \pm 3.07 \pm_{0.29}^{0.29}$	$4.00 \pm 1.60 \pm_{0.28}^{0.28} \pm 0.34$	$5.00 \pm 1.95 \pm_{0.37}^{0.37} \pm 0.39$
> 0.1	8	$7.07 \pm 2.90 \pm_{0.23}^{0.23}$	$3.63 \pm 1.52 \pm_{0.25}^{0.25} \pm 0.29$	$4.49 \pm 1.83 \pm_{0.32}^{0.32} \pm 0.33$
> 0.2	7	$6.27 \pm 2.71 \pm_{0.18}^{0.18}$	$3.25 \pm 1.44 \pm_{0.21}^{0.21} \pm 0.25$	$3.96 \pm 1.69 \pm_{0.27}^{0.27} \pm 0.29$
> 0.3	7	$6.27 \pm 2.71 \pm_{0.18}^{0.18}$	$3.25 \pm 1.44 \pm_{0.21}^{0.21} \pm 0.25$	$3.96 \pm 1.69 \pm_{0.27}^{0.27} \pm 0.29$
> 0.4	6	$5.24 \pm 2.51 \pm_{0.17}^{0.17}$	$2.75 \pm 1.35 \pm_{0.18}^{0.18} \pm 0.21$	$3.27 \pm 1.56 \pm_{0.23}^{0.23} \pm 0.24$
> 0.5	5	$4.18 \pm 2.31 \pm_{0.16}^{0.16}$	$2.24 \pm 1.26 \pm_{0.15}^{0.15} \pm 0.16$	$2.57 \pm 1.41 \pm_{0.18}^{0.18} \pm 0.19$

Table B.4: Summary of data-driven estimation of  $t\bar{t}$ , WW, Wt and  $Z(\tau\tau) + j$  backgrounds in SR for several cut values on  $\Delta\phi(\text{jet}, E_T^{\text{miss}})$ . The first uncertainty shown corresponds to the statistical error. The second one, to the detector systematic uncertainties. The third number corresponds to the uncertainty due to the dependency of  $k_{ee}$ ,  $k_{\mu\mu}$  on  $E_T^{\text{miss}}$ .

### B.2.2 Applying a $\Delta\phi$ cut on the jet-smearing method

When a  $\Delta\phi$  cut was initially applied to the jet-smearing method, it was found that the agreement between data and the jet-smearred distributions in  $E_T^{\text{miss}}$  got deteriorated. To solve this mismodelling of  $\Delta\phi(\text{jet}, E_T^{\text{miss}})$  by the smeared data, a phi smearing has been introduced in the method resulting in an improved description of  $\Delta\phi$  which leads to a good agreement between data and jet smeared  $E_T^{\text{miss}}$  also when a cut on  $\Delta\phi$  is applied. This can be seen in Fig. B.7. The upper plots in this figure show the jet-smearred  $E_T^{\text{miss}}$  distribution, including phi smearing, in the original SR before any cut on  $\Delta\phi$  applied, together with all other background sources for the  $ee$  (left) and  $\mu\mu$  (right) channels. On the bottom plots, the distributions are presented in SR with  $\Delta\phi > 0.4$ , showing a good agreement between data and the distribution given by the improved jet-smearing method. The smeared  $\Delta\phi$  distribution has been analysed in slices of  $E_T^{\text{miss}}$  giving a reasonable agreement with data for all  $E_T^{\text{miss}}$  slices as shown in Sec.??.

After the application of the  $\Delta\phi > 0.4$  cut, most of the Z+jets background is eliminated, leading to very small predictions for the Z+jets background by the jet-smearing method. These predictions have been found to be in good agreement with direct MC predictions, as shown in Table B.5 both in the original SR and in SR with the  $\Delta\phi > 0.4$  cut applied.

Region	channel	jet-smearing	direct MC
SR1, no $\Delta\phi$ cut	$ee$	$1.73 \pm 0.90$	$0.96 \pm 0.57$
	$\mu\mu$	$1.19 \pm 0.34$	$1.34 \pm 0.67$
SR1, $\Delta\phi > 0.4$	$ee$	$0.048 \pm 0.037$	$0.05 \pm 0.03$
	$\mu\mu$	$0.024 \pm 0.031$	$0.09 \pm 0.05$

Table B.5: Z+jets estimation from the jet smearing method and from direct MC in SR before and after applying the  $\Delta\phi > 0.4$  cut.

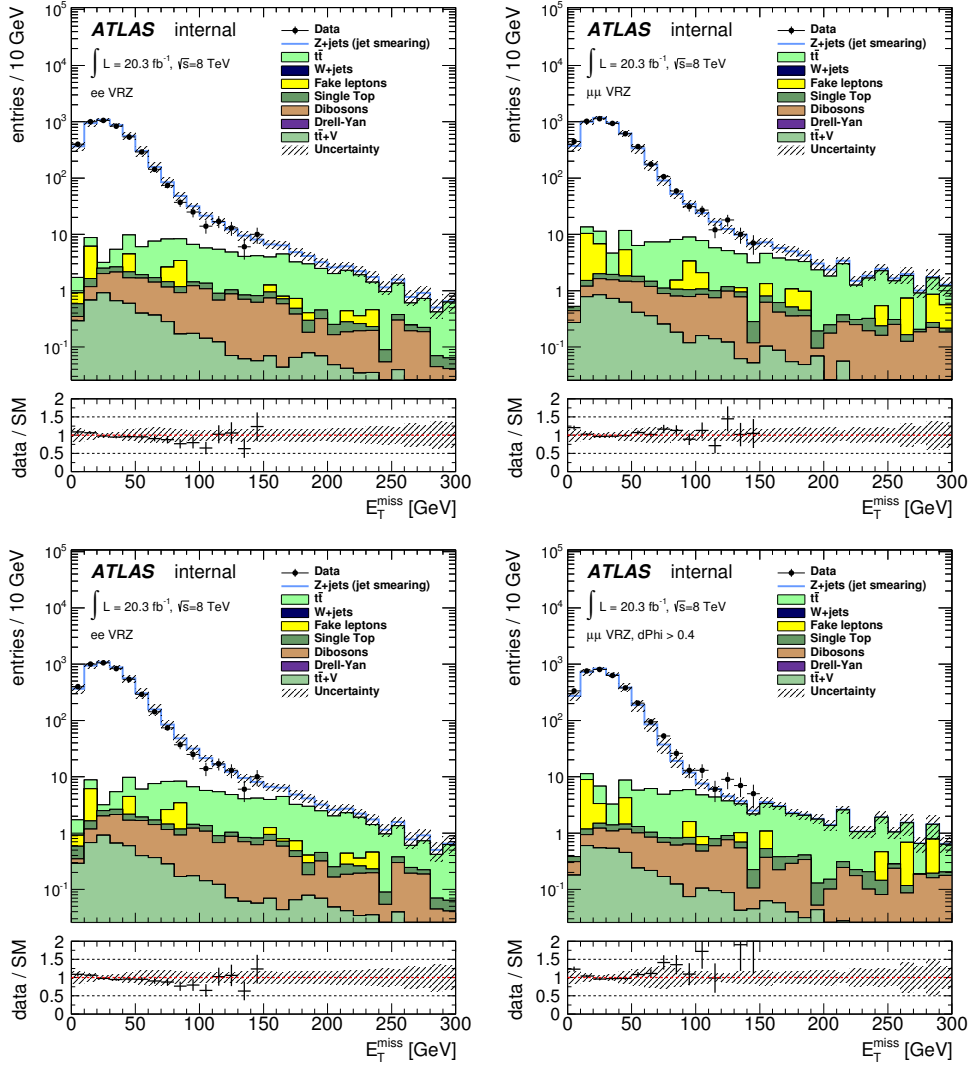


Figure B.7:  $E_T^{\text{miss}}$  distributions in SR without  $\Delta\phi$  cuts (top) and SR with  $\Delta\phi > 0.4$  (bottom). Z+jet has been estimated with the jet-smearing method. All other sources of background are taken from MC. Left:  $ee$  channel. Right:  $\mu\mu$  channel.

### B.2.3 Applying a $\Delta\phi$ cut on MC-estimated backgrounds and on fake leptons estimation

The effect of the application of the  $\Delta\phi$  cut to the flavour non-symmetric backgrounds is a reduction of approximately 50% of their contribution. The expected number of events for the different cuts studied is shown in Table B.6 for the  $ee$  channel and in Table B.7 for the  $\mu\mu$  channel.

Bkg type	no $\Delta\phi$ cut	$\Delta\phi > 0.1$	$\Delta\phi > 0.2$	$\Delta\phi > 0.3$	$\Delta\phi > 0.4$	$\Delta\phi > 0.5$
Total non-sym. bkgs:	$2.76 \pm 0.54$	$2.32 \pm 0.48$	$1.73 \pm 0.46$	$1.46 \pm 0.33$	$1.41 \pm 0.33$	$1.36 \pm 0.33$
$Z(ee, \mu\mu) + jets(MC)$	$0.96 \pm 0.40$	$0.64 \pm 0.32$	$0.25 \pm 0.31$	$0.07 \pm 0.02$	$0.05 \pm 0.02$	$0.05 \pm 0.02$
$st(s, t)$	$0.01 \pm 0.00$	$0.01 \pm 0.00$	$0.01 \pm 0.00$	$0.01 \pm 0.00$	$0.01 \pm 0.00$	$0.01 \pm 0.00$
$WZ + ZZ$	$1.51 \pm 0.36$	$1.42 \pm 0.36$	$1.24 \pm 0.34$	$1.19 \pm 0.33$	$1.18 \pm 0.33$	$1.15 \pm 0.33$
$t\bar{t}V$	$0.27 \pm 0.05$	$0.25 \pm 0.04$	$0.23 \pm 0.04$	$0.19 \pm 0.04$	$0.17 \pm 0.04$	$0.15 \pm 0.04$
Fakes	$0.07 \pm 0.77$	$-0.14 \pm 0.69$	$0.07 \pm 0.67$	$0.07 \pm 0.67$	$0.10 \pm 0.66$	$-0.21 \pm 0.52$

Table B.6: MC-estimated backgrounds and fake leptons estimation in SR<sub>ee</sub> for different  $\Delta\phi$  cuts. Only statistical and detector systematic uncertainties are included in this table.

Bkg type	no $\Delta\phi$ cut	$\Delta\phi > 0.1$	$\Delta\phi > 0.2$	$\Delta\phi > 0.3$	$\Delta\phi > 0.4$	$\Delta\phi > 0.5$
Total non-sym. bkgs	$4.07 \pm 0.64$	$2.76 \pm 0.39$	$2.43 \pm 0.38$	$2.10 \pm 0.33$	$1.94 \pm 0.32$	$1.75 \pm 0.31$
$Z(ee, \mu\mu) + jets(MC)$	$1.34 \pm 0.49$	$0.34 \pm 0.08$	$0.19 \pm 0.06$	$0.11 \pm 0.04$	$0.09 \pm 0.04$	$0.08 \pm 0.04$
$st(s, t)$	$0.05 \pm 0.02$	$0.05 \pm 0.02$	$0.05 \pm 0.02$	$0.05 \pm 0.01$	$0.04 \pm 0.01$	$0.03 \pm 0.01$
$WZ + ZZ$	$2.47 \pm 0.41$	$2.17 \pm 0.38$	$2.03 \pm 0.37$	$1.81 \pm 0.33$	$1.68 \pm 0.32$	$1.52 \pm 0.31$
$t\bar{t}V$	$0.21 \pm 0.04$	$0.20 \pm 0.04$	$0.16 \pm 0.04$	$0.13 \pm 0.03$	$0.13 \pm 0.03$	$0.12 \pm 0.03$
Fakes	$1.55 \pm 1.39$	$1.55 \pm 1.39$	$1.58 \pm 1.38$	$1.58 \pm 1.38$	$1.22 \pm 1.29$	$1.22 \pm 1.29$

Table B.7: MC-estimated backgrounds and fake leptons estimation in SR<sub>μμ</sub> for different  $\Delta\phi$  cuts. Only statistical and detector systematic uncertainties are included in this table.

### B.2.4 Applying a $\Delta\phi$ cut on GGM signal

The application of a  $\Delta\phi$  cut does not have strong effects on the expected number of GGM events in SR. On average, the number of events in SR gets reduced in 10, 12, 15% for a  $\Delta\phi$  cut of 0.3, 0.4, 0.5 respectively except for some points at low  $\mu$ , high  $m_{\tilde{g}}$  values where the reduction is more pronounced. These signal points are not covered by the expected exclusion limits even for the original SR before the  $\Delta\phi$  cut so no loss of sensitivity is expected to be caused by the  $\Delta\phi$  cut. An example of the reduction in GGM when applying the cut is shown in Fig. B.8. The plot shows the difference in the number of expected events when applying a  $\Delta\phi$  cut of 0.4 with respect to the original SR values, in percentage, for GGM with  $\tan\beta = 1.5$  in the  $ee$  channel. A similar plot is obtained for the  $\mu\mu$  channel and for the GGM with  $\tan\beta = 30$  grid.

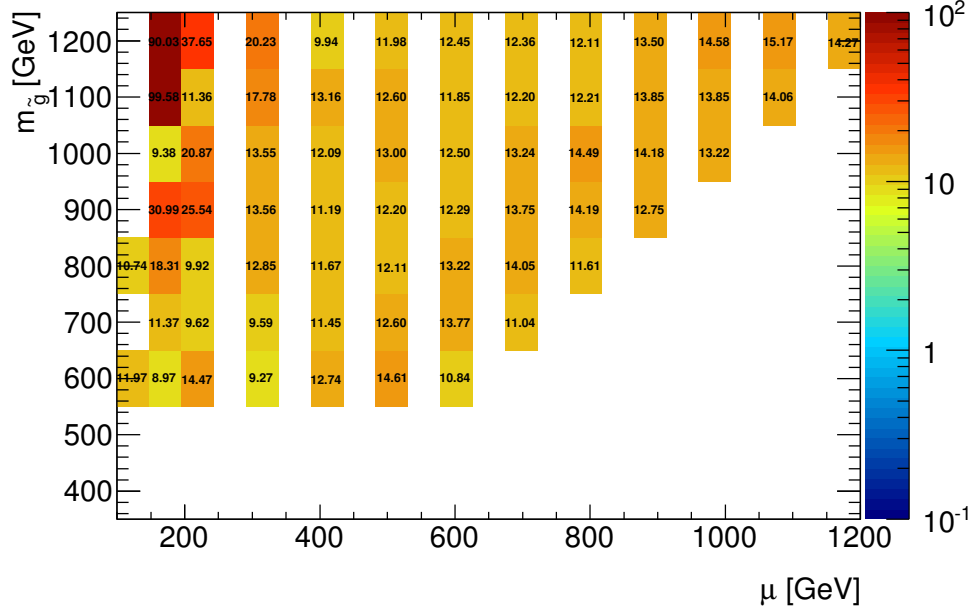


Figure B.8: Reduction (in percentage) on the number of expected events in GGM ( $\tan\beta = 1.5$ ) signal when applying a  $\Delta\phi > 0.4$  in SR with respect to the nominal SR expectation, in the  $ee$  channel.

SRee	no $\Delta\phi$ cut	$\Delta\phi > 0.1$	$\Delta\phi > 0.2$	$\Delta\phi > 0.3$	$\Delta\phi > 0.4$	$\Delta\phi > 0.5$
Fitted bkg events	$6.82 \pm 1.91$	$5.81 \pm 1.78$	$5.05 \pm 1.63$	$4.78 \pm 1.65$	$4.26 \pm 1.56$	$3.39 \pm 1.41$
MC exp. GGM_600_120_0 events	14.98	14.57	14.57	13.19	13.19	12.33
MC exp. GGM_700_200_0 events	28.14	27.08	26.27	25.82	25.44	25.05
MC exp. GGM_900_600_0 events	17.05	16.50	15.98	15.43	14.94	14.40
MC exp. GGM_1000_700_0 events	7.73	7.46	7.21	15.43	6.70	6.48
Exp. sig. GGM_600_120_0 events	3.21	3.26	3.41	3.13	3.21	3.19
Exp. sig. GGM_700_200_0 events	5.26	5.26	5.34	5.22	5.26	5.37
Exp. sig. GGM_900_600_0 events	3.57	3.61	3.42	3.55	3.55	3.59
Exp. sig. GGM_1000_700_0 events	1.79	1.82	1.86	1.80	1.79	1.85

Table B.8: Final background estimation in SRee and signal MC expectations and expected significance for different  $\Delta\phi$  cut values. The signal expected significance is also shown.

SRmm	no $\Delta\phi$ cut	$\Delta\phi > 0.1$	$\Delta\phi > 0.2$	$\Delta\phi > 0.3$	$\Delta\phi > 0.4$	$\Delta\phi > 0.5$
Fitted bkg events	$10.62 \pm 2.54$	$8.80 \pm 2.42$	$7.97 \pm 2.25$	$7.64 \pm 2.24$	$6.43 \pm 2.08$	$5.54 \pm 1.95$
MC exp. GGM_600_120_0 events	5.19	4.69	4.69	4.69	4.68	4.68
MC exp. GGM_700_200_0 events	22.63	21.74	21.35	20.65	20.04	19.49
MC exp. GGM_900_600_0 events	12.51	12.12	11.83	11.48	11.12	10.76
MC exp. GGM_1000_700_0 events	4.93	4.78	4.64	4.51	4.38	4.25
Exp. sig. GGM_600_120_0 events	0.98	0.92	0.97	0.97	1.03	1.08
Exp. sig. GGM_700_200_0 events	3.86	3.83	3.93	3.83	3.87	3.90
Exp. sig. GGM_900_600_0 events	2.32	2.34	2.40	2.34	2.38	2.40
Exp. sig. GGM_1000_700_0 events	0.92	0.94	0.96	0.93	0.96	0.97

Table B.9: Final background estimation in SRmm and signal MC expectations and expected significance for different  $\Delta\phi$  cut values. The signal expected significance is also shown.

Tables B.8 and B.9 show the final background estimates for the different  $\Delta\phi$  cuts studied in the  $ee$  and  $\mu\mu$  channels respectively, together with the expectations for four signal points and the effect of the  $\Delta\phi$  cut on their expected significances. In both channels and for all the detailed signal points, the expected significance is relatively stable through the  $\Delta\phi$  cuts studied. The  $\Delta\phi > 0.4$ , also used in other analyses [153], is selected for the rest of the study.

### B.2.5 Full background estimation using the flavour-symmetry method

The final background estimation in SR before applying the  $\Delta\phi$  cut is shown in Table B.10. These results can be compared with the ones obtained after the  $\Delta\phi$  cut, in Table B.11. MC expectations for four signal points are also shown in the table.

The final background expectation is reduced by 40% after applying the  $\Delta\phi > 0.4$  cut, with the relative errors increasing from approximately 25% before the cut to approximately 35% after the cut. The signal expectation is reduced in 10 – 15% in the studied points.

The impact of this cut on the expected GGM exclusion limits is negligible, as it can be seen in Fig. B.9, showing the expected limits before (dashed blue line with yellow uncertainty band) and after (green dashed line with green dotted uncertainty lines) the application of this cut, in the  $ee$  (left) and  $\mu\mu$  (right) channels, for both GGM grids.



	SR <sub>ee</sub>	SR <sub>mm</sub>	SRSF
Observed events	21	15	36
Total Background	$7.60 \pm 2.01$	$10.46 \pm 2.62$	$18.07 \pm 3.95$
Flavour-Symmetry method events	$4.00 \pm 1.66$	$5.00 \pm 2.03$	$9.00 \pm 3.14$
$Z/\gamma^*$ + jets (jet-smearing) events	$1.73 \pm 0.89$	$1.19 \pm 0.34$	$2.92 \pm 0.98$
MC exp. SingleTopDiLept events	$0.01 \pm 0.01$	$0.05 \pm 0.03$	$0.06 \pm 0.03$
MC exp. PowhegDibosons events	$1.51 \pm 0.51$	$2.47 \pm 0.81$	$3.98 \pm 1.22$
MC exp. ttbarV events	$0.27 \pm 0.13$	$0.21 \pm 0.10$	$0.48 \pm 0.23$
Data-driven exp. fake lepton events	$0.07^{+0.42}_{-0.07}$	$1.55 \pm 1.39$	$1.62^{+1.76}_{-1.62}$
MC exp. GGM_600_120_0 events	$14.98 \pm 2.67$	$5.19 \pm 1.07$	$20.17 \pm 2.77$
MC exp. GGM_700_200_0 events	$28.14 \pm 1.83$	$22.63 \pm 1.56$	$50.77 \pm 1.42$
MC exp. GGM_900_600_0 events	$17.05 \pm 0.48$	$12.51 \pm 0.35$	$29.56 \pm 0.83$
MC exp. GGM_1000_700_0 events	$7.73 \pm 0.22$	$4.93 \pm 0.42$	$12.66 \pm 0.35$

Table B.10: Final background estimation in SR with no  $\Delta\phi$  cut using the flavour-symmetry method. All sources of uncertainties are considered in the shown errors.

$\Delta\phi > 0.4$	SR <sub>ee</sub>	SR <sub><math>\mu\mu</math></sub>	SRSF
Observed events	16	13	29
Total Background	$4.25 \pm 1.49$	$6.36 \pm 2.12$	$10.62 \pm 3.12$
Flavour-Symmetry method events	$2.75 \pm 1.38$	$3.27 \pm 1.60$	$6.02 \pm 2.56$
$Z/\gamma^*$ + jets (jet-smearing) events	$0.05 \pm 0.04$	$0.02^{+0.03}_{-0.02}$	$0.07 \pm 0.05$
Fitted SingleTopDiLept events	$0.01 \pm 0.00$	$0.04 \pm 0.03$	$0.05 \pm 0.03$
MC exp. PowhegDibosons events	$1.18 \pm 0.41$	$1.68 \pm 0.55$	$2.86 \pm 0.89$
MC exp. ttbarV events	$0.17 \pm 0.09$	$0.13 \pm 0.07$	$0.30 \pm 0.15$
Data-driven exp. fake lepton events	$0.10^{+0.38}_{-0.10}$	$1.22^{+1.25}_{-1.22}$	$1.32^{+1.51}_{-1.32}$
MC exp. GGM_600_120_0 events	$13.19 \pm 2.56$	$4.68 \pm 1.12$	$17.87 \pm 2.73$
MC exp. GGM_700_200_0 events	$25.44 \pm 1.74$	$20.04 \pm 1.42$	$45.48 \pm 1.27$
MC exp. GGM_900_600_0 events	$14.95 \pm 0.42$	$11.12 \pm 0.31$	$26.07 \pm 0.73$
MC exp. GGM_1000_700_0 events	$6.71 \pm 0.19$	$4.38 \pm 0.26$	$11.09 \pm 0.31$

Table B.11: Final background estimation in SR after applying a  $\Delta\phi(\text{jet}_{1,2}, E_T^{\text{miss}}) > 0.4$  cut, using the flavour-symmetry method. All sources of uncertainties are considered in the shown errors.

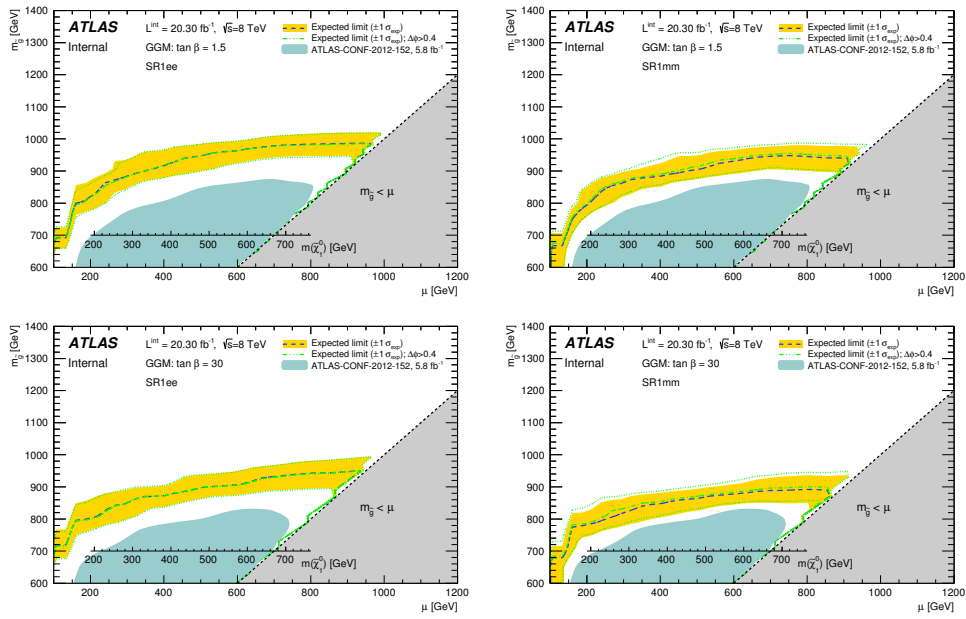


Figure B.9: Expected exclusion limits in SR before applying the  $\Delta\phi(\text{jet}_{1,2}, E_T^{\text{miss}})$  cut (dashed blue line with yellow uncertainty band) compared to expected exclusion in SR with  $\Delta\phi > 0.4$  (green dashed line with green dotted uncertainty lines). Upper plots: GGM with  $\tan\beta = 1.5$ ; Bottom plots: GGM with  $\tan\beta = 30$ ; Left: ee channel; Right:  $\mu\mu$  channel.

### B.2.6 Full background estimation using the side-band fit

As a cross-check of the result in the previous section, a side-band fit has been used to estimate the  $t\bar{t}$  background. To be as close as possible to the SR, the same  $\Delta\phi$  requirement is applied to CRT and SR in the fit. This way the extrapolation from CRT to SR is done only in  $m_{ll}$  as it was designed for the original SR. See a summary of the estimates given by the side-band fit in SR before (Table B.12) and after (Table B.13) the  $\Delta\phi > 0.4$  cut.

channel	SRee	SRmm	SRSF
Observed events	21	15	36
Fitted bkg events	$9.11 \pm 1.80$	$12.23 \pm 2.47$	$21.32 \pm 3.52$
Fitted PowhegPythiaTTbar events	$4.59 \pm 1.51$	$5.46 \pm 1.94$	$10.03 \pm 2.96$
data-driven JetSmearing events	$1.73 \pm 0.89$	$1.19 \pm 0.34$	$2.92 \pm 0.98$
Fitted SingelTopDiLept events	$0.64 \pm 0.40$	$0.73 \pm 0.46$	$1.37 \pm 0.86$
Fitted PowhegDiboson events	$1.81 \pm 0.49$	$3.09 \pm 0.88$	$4.90 \pm 1.29$
Fitted ttbarV events	$0.27 \pm 0.12$	$0.21 \pm 0.09$	$0.48 \pm 0.21$
data-driven fake lepton events	$0.07^{+0.42}_{-0.07}$	$1.55 \pm 1.39$	$1.62^{+1.76}_{-1.62}$
$\mu_{\text{Top}}$	$0.48 \pm 0.12$	$0.50 \pm 0.14$	$0.49 \pm 0.11$

Table B.12: Final background estimation in SR according to the side-band fit method. All sources of uncertainties are considered in the shown shown errors.

$\Delta\phi > 0.4$	SRee	SRmm	SRSF
Observed events	16	13	29
Fitted bkg events	$6.38 \pm 1.45$	$8.41 \pm 2.08$	$14.80 \pm 2.89$
Fitted PowhegPythiaTTbar events	$4.14 \pm 1.41$	$4.15 \pm 1.62$	$8.30 \pm 2.51$
data-driven JetSmearing events	$0.05 \pm 0.04$	$0.02^{+0.03}_{-0.02}$	$0.07 \pm 0.05$
Fitted SingleTopDiLept events	$0.50 \pm 0.32$	$0.58 \pm 0.36$	$1.07 \pm 0.68$
Fitted PowhegDiboson events	$1.42 \pm 0.38$	$2.30 \pm 0.66$	$3.71 \pm 0.99$
Fitted ttbarV events	$0.17 \pm 0.08$	$0.13 \pm 0.06$	$0.30 \pm 0.13$
data-driven fake lepton events	$0.10^{+0.38}_{-0.10}$	$1.22^{+1.25}_{-1.22}$	$1.32^{+1.51}_{-1.32}$
$\mu_{\text{Top}}$	$0.53 \pm 0.14$	$0.51 \pm 0.15$	$0.52 \pm 0.12$

Table B.13: Final background estimation in SR with  $\Delta\phi > 0.4$  according to the side-band fit method. All sources of uncertainties are considered in the shown errors.

### B.2.7 Comparison of flavour-symmetric bkg estimation in the previous sections.

Table B.14 shows a comparison of the estimates for the flavour-symmetric backgrounds as given by the flavour-symmetry method and by the side-band fit. The first two columns correspond to the results in the SR without any requirement on  $\Delta\phi$ . The third and fourth columns show the results in SR after applying the  $\Delta\phi > 0.4$  cut (same results as in Table 4.22). As in SR without  $\Delta\phi$ , the side-band fit gives larger estimates than the flavour-symmetry method for both  $ee$  and  $\mu\mu$  channels when the  $\Delta\phi > 0.4$  cut is applied. Nevertheless, the results are compatible between the two methods within uncertainties.

SR	no $\Delta\phi$ cut		$\Delta\phi > 0.4$	
	$N_{ee}$	$N_{\mu\mu}$	$N_{ee}$	$N_{\mu\mu}$
Flavour-symmetry method				
Total flavour-symmetric bkg	<b>4.00 ± 1.66</b>	<b>5.00 ± 2.03</b>	<b>2.75 ± 1.38</b>	<b>3.27 ± 1.60</b>
Side-Band fit				
$t\bar{t}$	4.59 ± 1.51	5.46 ± 1.94	4.14 ± 1.41	4.15 ± 1.62
tW	0.63 ± 0.36	0.68 ± 0.41	0.49 ± 0.28	0.54 ± 0.32
WW	0.30 ± 0.15	0.62 ± 0.54	0.24 ± 0.10	0.62 ± 0.48
Total flavour-symmetric bkg	<b>5.53 ± 1.68</b>	<b>6.76 ± 2.15</b>	<b>4.87 ± 1.43</b>	<b>5.31 ± 1.72</b>

Table B.14: Final estimates for flavour-symmetric backgrounds from the flavour-symmetry method compared to the estimates from the side-band fit. The contribution of  $Z \rightarrow \tau\tau$  to the fit is negligible. All sources of uncertainty are considered in the shown errors.

### B.2.8 Checks in the original SR, before the $\Delta\phi$ cut

Looking at the results obtained in this appendix, the decision was made to apply a  $\Delta\phi(\text{jet}, E_T^{\text{miss}}) > 0.4$  cut to SR. Most of the checks initially performed in SR without the cut have been remade including the cut and they have been documented in the main part of this note. In this subsection, the analogous results of these tests done in SR before the cut are collected.

- MC closure test for the flavour-symmetry method. Table B.15, analogous to Table 4.18.
- Results from the Side band fit. Tables B.16 to B.18, analogous to Tables 4.19 to 4.21.
- Tests on  $m_{ll}$  extrapolation. Table B.19, analogous to Table 4.23 respectively.
- Testing the  $t\bar{t}$  normalization with different MC generators (Ref. [97]).

SR	$N_{e\mu}^{MC}$	$N_{e\mu}^{MC,corr}$	$N_{ee}^{est,MC}$	$N_{\mu\mu}^{est,MC}$
barrel-barrel	$13.11 \pm 0.87 \pm_{3.90}^{1.52}$	$13.04 \pm 0.87 \pm_{3.90}^{1.52}$	$8.05 \pm 0.54 \pm_{2.49}^{1.14} \pm 0.62$	$6.97 \pm 0.47 \pm_{2.15}^{0.98} \pm 0.71$
barrel-endcap	$7.85 \pm 0.67 \pm_{2.66}^{0.90}$	$7.78 \pm 0.67 \pm_{2.66}^{0.90}$	$3.78 \pm 0.32 \pm_{1.33}^{0.40} \pm 0.37$	$5.13 \pm 0.44 \pm_{1.81}^{0.54} \pm 0.42$
endcap-endcap	$0.89 \pm 0.22 \pm_{0.31}^{0.14}$	$0.88 \pm 0.22 \pm_{0.31}^{0.14}$	$0.39 \pm 0.10 \pm_{0.14}^{0.07} \pm 0.04$	$0.63 \pm 0.16 \pm_{0.23}^{0.11} \pm 0.05$
<b>SUM (MC Closure)</b>	$21.84 \pm 1.12 \pm_{4.73}^{1.60}$	$21.70 \pm 1.12 \pm_{4.73}^{1.60}$	<b><math>12.22 \pm 0.64 \pm_{2.82}^{1.21} \pm 0.72</math></b>	<b><math>12.72 \pm 0.66 \pm_{2.82}^{1.13} \pm 0.83</math></b>
Global			$11.57 \pm 0.60 \pm_{2.60}^{1.05}$	$13.26 \pm 0.68 \pm_{2.98}^{1.21}$
SR			$N_{ee}^{direct,MC}$	$N_{\mu\mu}^{direct,MC}$
<b>Direct MC estimation</b>			<b><math>10.55 \pm 0.79 \pm_{0.77}^{0.72}</math></b>	<b><math>12.37 \pm 0.84 \pm_{1.02}^{0.89}</math></b>

Table B.15: Summary of closure test for the estimation of  $t\bar{t}^{2l}$ , WW, Wt and  $Z \rightarrow \tau\tau$  backgrounds in SR. The first uncertainty shown corresponds to the statistical error, the second one to the experimental systematic uncertainties. The third number corresponds to the uncertainty due to the dependency of  $k_{ee}$ ,  $k_{\mu\mu}$  on  $E_T^{\text{miss}}$ , as detailed in Section 4.6.2.3. The bottom part of the table shows the summary of direct MC estimation of  $t\bar{t}^{2l}$ , WW, Wt and  $Z \rightarrow \tau\tau$  backgrounds in SR.

- Comparison of  $t\bar{t}$  normalization factor obtained in different control regions. Table B.20, analogous to Table 4.24.
- Comparison of final estimates using the nominal analysis (with the flavour-symmetry method) to the side band fit. Table B.21, analogous to Table 4.33.
- Model-independent upper limits on production of new physics, p-values, and Gaussian significance. Table B.22, analogous to Table 4.34.
- Testing the full analysis in seven validation regions. Tables B.23 and B.24, analogous to tables 4.25 and 4.26.

All conclusions obtained after these tests are the same as those obtained in SR with the  $\Delta\phi$  cut.

<b>channel</b>	<b>SRee</b>	<b>CRTEE</b>
Observed events	21	57
Fitted bkg events	$9.11 \pm 1.80$	$57.00 \pm 7.63$
Fitted PowhegPythiaTTbar events	$4.59 \pm 1.51$	$36.57 \pm 9.37$
Fitted SherpaZMassiveBC events	$0.00 \pm 0.00$	$4.37 \pm 1.91$
Fitted SherpaZMassiveBC_extStats events	$0.00 \pm 0.00$	$0.09 \pm 0.05$
Fitted SherpaZMassiveBC_HTFilter events	$0.00 \pm 0.00$	$0.18 \pm 0.17$
data-driven JetSmearing events	$1.73 \pm 0.89$	$0.00 \pm 0.00$
Fitted SingleTopDiLept events	$0.64 \pm 0.40$	$7.22 \pm 3.44$
Fitted PowhegDibosons events	$1.81 \pm 0.49$	$4.92 \pm 1.00$
Fitted ttbarV events	$0.27 \pm 0.12$	$0.57 \pm 0.21$
Fitted fake lepton events	$0.07^{+0.42}_{-0.07}$	$3.09 \pm 2.29$
MC exp. SM events	14.09	96.66
MC exp. PowhegPythiaTTbar events	9.56	76.23
MC exp. SherpaZMassiveBC events	0.00	4.35
MC exp. SherpaZMassiveBC_extStats events	0.00	0.09
MC exp. SherpaZMassiveBC_HTFilter events	0.00	0.18
data-driven JetSmearing events	1.73	0.00
MC exp. SingleTopDiLept events	0.64	7.24
MC exp. PowhegDibosons events	1.81	4.92
MC exp. ttbarV events	0.27	0.57
data-driven exp. fake lepton events	0.07	3.09

Table B.16: Background fit results in the electron channel, obtained with the discovery fit configuration for an integrated luminosity of  $20.3 \text{ fb}^{-1}$ . The uncertainties shown are statistical + systematic.

channel	SRmm	CRTmm
Observed events	15	57
Fitted bkg events	$12.23 \pm 2.47$	$56.90 \pm 7.63$
Fitted PowhegPythiaTTbar events	$5.47 \pm 1.95$	$33.43 \pm 9.46$
Fitted SherpaZMassiveBC events	$0.00 \pm 0.00$	$4.64 \pm 2.05$
Fitted SherpaZMassiveBC_extStats events	$0.00 \pm 0.00$	$3.77 \pm 1.55$
Fitted SherpaZMassiveBC_HTFilter events	$0.00 \pm 0.00$	$0.65 \pm 0.29$
data-driven JetSmearing events	$1.19 \pm 0.34$	$0.00 \pm 0.00$
Fitted SingleTopDiLept events	$0.73 \pm 0.46$	$6.89 \pm 3.27$
Fitted PowhegDibosons events	$3.08 \pm 0.88$	$6.32 \pm 1.23$
Fitted ttbarV events	$0.21 \pm 0.09$	$0.65 \pm 0.24$
Fitted fake lepton events	$1.55 \pm 1.39$	$0.14^{+1.20}_{-0.14}$
MC exp. SM events	17.82	91.22
MC exp. PowhegPythiaTTbar events	11.06	67.61
MC exp. SherpaZMassiveBC events	0.00	4.64
MC exp. SherpaZMassiveBC_extStats events	0.00	3.77
MC exp. SherpaZMassiveBC_HTFilter events	0.00	0.65
data-driven JetSmearing events	1.19	0.00
MC exp. SingleTopDiLept events	0.73	6.89
MC exp. PowhegDibosons events	3.09	6.33
MC exp. ttbarV events	0.21	0.65
data-driven exp. fake lepton events	1.55	0.16

Table B.17: Background fit results in the electron channel, obtained with the discovery fit configuration for an integrated luminosity of  $20.3 \text{ fb}^{-1}$ . The uncertainties shown are statistical + systematic.

channel	SRSF	CRTSF
Observed events	36	114
Fitted bkg events	$21.32 \pm 3.52$	$113.93 \pm 10.95$
Fitted PowhegPythiaTTbar events	$10.04 \pm 2.97$	$70.01 \pm 15.58$
Fitted SherpaZMassiveBC events	$0.00 \pm 0.00$	$9.01 \pm 3.94$
Fitted SherpaZMassiveBC_extStats events	$0.00 \pm 0.00$	$3.85 \pm 1.66$
Fitted SherpaZMassiveBC_HTFilter events	$0.00 \pm 0.00$	$0.83 \pm 0.47$
data-driven JetSmearing events	$2.92 \pm 0.98$	$0.00 \pm 0.00$
Fitted SingleTopDiLept events	$1.37 \pm 0.86$	$14.07 \pm 6.73$
Fitted PowhegDibosons events	$4.91 \pm 1.29$	$11.28 \pm 2.22$
Fitted ttbarV events	$0.48 \pm 0.21$	$1.22 \pm 0.44$
Fitted fake lepton events	$1.62^{+1.76}_{-1.62}$	$3.31^{+3.77}_{-3.31}$
MC exp. SM events	31.91	187.87
MC exp. PowhegPythiaTTbar events	20.62	143.84
MC exp. SherpaZMassiveBC events	0.00	8.99
MC exp. SherpaZMassiveBC_extStats events	0.00	3.85
MC exp. SherpaZMassiveBC_HTFilter events	0.00	0.83
data-driven JetSmearing events	2.92	0.00
MC exp. SingleTopDiLept events	1.37	14.13
MC exp. PowhegDibosons events	4.90	11.25
MC exp. ttbarV events	0.48	1.22
data-driven exp. fake lepton events	1.62	3.25

Table B.18: Background fit results in the electron channel, obtained with the discovery fit configuration for an integrated luminosity of  $20.3 \text{ fb}^{-1}$ . The uncertainties shown are statistical + systematic.



	SR <sub>ee</sub>	VRT <sub>ee</sub>	VRTZ <sub>ee</sub>
Observed events	-	199	36
Fitted bkg events	$11.28 \pm 1.64$	$198.83 \pm 14.24$	$37.24 \pm 5.30$
Fitted PowhegPythiaTTbar events	$6.75 \pm 1.22$	$157.79 \pm 18.05$	$22.83 \pm 3.27$
MC exp. SM events	14.09	264.19	46.70
MC exp. PowhegPythiaTTbar events	9.56	223.23	32.29
	SR <sub>mm</sub>	VRT <sub>mm</sub>	VRTZ <sub>mm</sub>
Observed events	-	203	36
Fitted bkg events	$13.89 \pm 2.44$	$202.88 \pm 14.41$	$35.90 \pm 5.30$
Fitted PowhegPythiaTTbar events	$7.12 \pm 1.85$	$149.51 \pm 19.93$	$20.48 \pm 4.24$
MC exp. SM events	17.82	285.50	47.21
MC exp. PowhegPythiaTTbar events	11.06	232.16	31.80
	SRSF	VRTSF	VRTZSF
Observed events	-	402	72
Fitted bkg events	$25.26 \pm 3.04$	$402.23 \pm 20.62$	$73.10 \pm 9.24$
Fitted PowhegPythiaTTbar events	$13.97 \pm 2.21$	$308.46 \pm 32.41$	$43.38 \pm 5.98$
MC exp. SM events	31.91	549.70	93.90
MC exp. PowhegPythiaTTbar events	20.62	455.39	64.09

Table B.19: Background fit results, obtained with the discovery fit configuration for an integrated luminosity of  $20.3 \text{ fb}^{-1}$ . The uncertainties shown are statistical + systematic. VRT has been used as control region to normalize  $t\bar{t}$ . VRTZ\_highHT is used as validation region.

Region used as CR	$ee$ channel	$\mu\mu$ channel	SF channel
CRT	$0.48 \pm 0.13$	$0.49 \pm 0.14$	$0.49 \pm 0.11$
VRT_highHT	$0.72 \pm 0.10$	$0.58 \pm 0.11$	$0.65 \pm 0.09$
VRT	$0.71 \pm 0.11$	$0.65 \pm 0.11$	$0.68 \pm 0.10$

Table B.20: Summary of the  $t\bar{t}$  normalization factors ( $\mu_{Top}$ ) found in three different selections of the Control Region.

Signal Region	Flavour-symmetry method	Combined Fit	Observed events	Significance ( $Z$ ) Flavour-sym	Significance ( $Z$ ) Side-Band Fit
SRee	$7.60 \pm 2.01$	$9.11 \pm 1.80$	21	2.78	2.64
SR1 $\mu\mu$	$10.46 \pm 2.62$	$12.23 \pm 2.47$	15	0.82	0.47
SRSF ( $ee + \mu\mu$ )	$18.07 \pm 3.95$	$21.32 \pm 3.52$	36	2.41	2.12

Table B.21: Background estimates from the flavour-symmetry method and the side-band fit with corresponding uncertainties; final observed number of events and the corresponding significance,  $Z$  value (calculated as  $Z = \text{RooStats}::\text{NumberCountingUtils}::\text{BinomialObsZ}(\text{obs}, \text{exp}, \text{RelUnc})$ ), in SRs given for the flavour-symmetry method results and for the side-band fit results.

Signal Region	$\langle\epsilon\sigma\rangle_{\text{obs}}^{95}$ [fb]	$S_{\text{obs}}^{95}$	$S_{\text{exp}}^{95}$	$CL_B$	$p_0$ -value	Gaussian Significance
SRee	1.14	23.1	$9.9_{-2.5}^{+3.7}$	0.99870	0.00067	3.207
SR $\mu\mu$	0.67	13.5	$10.0_{-2.5}^{+3.1}$	0.85734	0.14733	1.048
SRSF	1.50	30.4	$14.4_{-4.2}^{+6.2}$	0.99510	0.00500	2.576

Table B.22: 95 % confidence level expected and observed upper limits on the contribution of BSM physics events to the signal regions, the  $p_0$ -value for the observed result, and the corresponding Gaussian significance. The expected upper limit on number of events is shown with the  $1\sigma$  uncertainties. No cut on the opening angle between jets and the  $E_T^{\text{miss}}$  is applied.

Region	background type	$N_{ee}^{\text{est}}$	$N_{\mu\mu}^{\text{est}}$	$N_{e\mu}$
VRTZ	Flavour-sym method	$26.89 \pm 3.89$	$29.22 \pm 4.24$	$48.83 \pm 7.02$
	$Z(\rightarrow ee, \mu\mu)+\text{jets}$ (jet-smearing)	$8.06 \pm 1.60$	$6.97 \pm 1.62$	$0 \pm 0$
	$tZ, WZ, ZZ, t\bar{t}V$	$3.88 \pm 0.45$	$3.50 \pm 0.41$	$0.43 \pm 0.03$
	Fakes	$1.20 \pm 1.16$	$0.94 \pm 1.50$	$-0.25 \pm 0.94$
	<b>TOTAL bkg</b>	<b><math>40.03 \pm 4.39</math></b>	<b><math>40.63 \pm 4.80</math></b>	<b><math>49.01 \pm 7.08</math></b>
	<b>DATA</b>	<b>36</b>	<b>36</b>	49
VRTZ_highHT	Flavour-sym method	$15.22 \pm 2.94$	$16.04 \pm 3.11$	$27.19 \pm 5.21$
	$Z(\rightarrow ee, \mu\mu)+\text{jets}$ (jet-smearing)	$6.88 \pm 1.26$	$5.87 \pm 1.24$	$0 \pm 0$
	$tZ, WZ, ZZ, t\bar{t}V$	$2.51 \pm 0.38$	$2.12 \pm 0.30$	$0.27 \pm 0.02$
	Fakes	$0.96 \pm 0.89$	$1.42 \pm 1.37$	$-0.5 \pm 0.5$
	<b>TOTAL bkg</b>	<b><math>25.57 \pm 3.34</math></b>	<b><math>25.45 \pm 3.63</math></b>	<b><math>26.96 \pm 5.23</math></b>
	<b>DATA</b>	<b>26</b>	<b>16</b>	27
VRTZ_highMET	Flavour-sym method	$5.03 \pm 1.76$	$6.34 \pm 2.23$	$9.88 \pm 3.44$
	$Z(\rightarrow ee, \mu\mu)+\text{jets}$ (MC)	$0.10 \pm 0.10$	$0.82 \pm 0.44$	$0 \pm 0$
	$tZ, WZ, ZZ, t\bar{t}V$	$2.83 \pm 0.40$	$2.97 \pm 0.36$	$0.11 \pm 0.02$
	Fakes	$-0.12 \pm 0.42$	$0.59 \pm 0.93$	$1.00 \pm 0.47$
	<b>TOTAL bkg</b>	<b><math>7.84 \pm 1.86</math></b>	<b><math>10.72 \pm 2.48</math></b>	<b><math>10.99 \pm 3.47</math></b>
	<b>DATA</b>	<b>13</b>	<b>13</b>	11

Table B.23: Estimated number of events for the  $ee$  and  $\mu\mu$  channels in the  $Z$ -window regions compared to the number of observed data.  $N_{e\mu}$  is taken from data and shown only for completeness. Only statistical errors are shown.

Region	background type	$N_{ee}^{est}$	$N_{\mu\mu}^{est}$	$N_{e\mu}$
CRT	Flavour-sym method	$60.4 \pm 6.2$	$63.8 \pm 6.5$	$107.9 \pm 10.8$
	$Z(\rightarrow ee, \mu\mu)$ +jets (MC)	$0.5 \pm 0.3$	$5.5 \pm 0.6$	$0.2 \pm 0.1$
	$tZ, WZ, ZZ, t\bar{t}V$	$1.7 \pm 0.3$	$2.1 \pm 0.5$	$2.6 \pm 0.2$
	Fakes	$3.1 \pm 2.3$	$0.1 \pm 1.2$	$5.3 \pm 2.9$
	<b>TOTAL bkg</b>	<b><math>65.7 \pm 6.6</math></b>	<b><math>71.5 \pm 6.7</math></b>	$116.0 \pm 11.2$
	<b>DATA</b>	<b>57</b>	<b>57</b>	116
VRT	Flavour-sym method	$187.4 \pm 10.6$	$211.7 \pm 11.9$	$347.4 \pm 19.2$
	$Z(\rightarrow ee, \mu\mu)$ +jets (MC)	$1.0 \pm 0.3$	$14.6 \pm 2.1$	$0.5 \pm 0.2$
	$tZ, WZ, ZZ, t\bar{t}V$	$3.0 \pm 0.6$	$3.0 \pm 0.6$	$4.4 \pm 0.2$
	Fakes	$7.3 \pm 4.8$	$6.9 \pm 6.4$	$11.7 \pm 8.9$
	<b>TOTAL bkg</b>	<b><math>198.7 \pm 11.7</math></b>	<b><math>236.2 \pm 13.7</math></b>	$364.0 \pm 21.2$
	<b>DATA</b>	<b>199</b>	<b>203</b>	364
VRT_highHT	Flavour-sym method	$104.2 \pm 8.0$	$113.2 \pm 8.7$	$189.2 \pm 14.3$
	$Z(\rightarrow ee, \mu\mu)$ +jets (MC)	$0.8 \pm 0.3$	$13.7 \pm 2.1$	$0.2 \pm 0.1$
	$tZ, WZ, ZZ, t\bar{t}V$	$1.6 \pm 0.3$	$1.9 \pm 0.4$	$2.6 \pm 0.1$
	Fakes	$3.3 \pm 2.9$	$2.9 \pm 2.8$	$8.1 \pm 5.4$
	<b>TOTAL bkg</b>	<b><math>109.9 \pm 8.5</math></b>	<b><math>131.7 \pm 9.1</math></b>	$200.0 \pm 15.3$
	<b>DATA</b>	<b>117</b>	<b>108</b>	200
VRT_highMET	Flavour-sym method	$48.7 \pm 5.4$	$56.5 \pm 6.3$	$91.5 \pm 10.1$
	$Z(\rightarrow ee, \mu\mu)$ +jets (MC)	$0.0 \pm 0.0$	$0.3 \pm 0.2$	$0.1 \pm 0.1$
	$tZ, WZ, ZZ, t\bar{t}V$	$1.1 \pm 0.2$	$1.5 \pm 0.2$	$1.9 \pm 0.2$
	Fakes	$2.9 \pm 1.7$	$4.8 \pm 3.0$	$5.6 \pm 3.0$
	<b>TOTAL bkg</b>	<b><math>52.7 \pm 5.7</math></b>	<b><math>63.1 \pm 6.7</math></b>	$99.1 \pm 10.5$
	<b>DATA</b>	<b>55</b>	<b>56</b>	99

Table B.24: Estimated number of events for the  $ee$  and  $\mu\mu$  channels in the  $Z$ -side band regions compared to the number of observed data.  $N_{e\mu}$  is taken from data and shown only for completeness. Only statistical errors are shown.



# Bibliography

- [1] C. P. Burgess and G. D. Moore, *The standard model : a primer*. New York: Cambridge University Press, 2007.
- [2] S. P. Martin, *A Supersymmetry primer*, arXiv:hep-ph/9709356 [hep-ph]. [Adv. Ser. Direct. High Energy Phys.18,1(1998)].
- [3] J. Silk et al., *Particle Dark Matter: Observations, Models and Searches*. Cambridge Univ. Press, Cambridge, 2010. <http://www.cambridge.org/uk/catalogue/catalogue.asp?isbn=9780521763684>.
- [4] “The matter-antimatter asymmetry problem.” <https://home.cern/topics/antimatter/matter-antimatter-asymmetry-problem>.
- [5] C. P. Burgess and G. D. Moore, *The standard model : a primer*. New York: Cambridge University Press, 2007. Chapter 10.
- [6] E. Gildener, *Gauge-symmetry hierarchies*, Phys. Rev. D **14** (1976) 1667–1672. <http://link.aps.org/doi/10.1103/PhysRevD.14.1667>.
- [7] S. Weinberg, *Gauge hierarchies*, Physics Letters B **82** no. 3, (1979) 387 – 391. <http://www.sciencedirect.com/science/article/pii/037026937990248X>.
- [8] G. F. Giudice, *Naturally Speaking: The Naturalness Criterion and Physics at the LHC*, arXiv:0801.2562 [hep-ph].
- [9] M. Drees, R. Godbole, and P. Roy, *Theory and phenomenology of sparticles*. World Scientific Publishing Co. Pte. Ltd., 2004.
- [10] ATLAS Collaboration, *Observation of a new particle in the search for the Standard Model Higgs boson with the ATLAS detector at the LHC*, Phys. Lett. **B716** (2012) 1–29, arXiv:1207.7214 [hep-ex].
- [11] CMS Collaboration, *Observation of a new boson at a mass of 125 GeV with the CMS experiment at the LHC*, Phys. Lett. **B716** (2012) 30–61, arXiv:1207.7235 [hep-ex].
- [12] K. Olive and Particle Data Group, *Review of Particle Physics*, Chinese Physics C **38** no. 9, (2014) 090001. <http://stacks.iop.org/1674-1137/38/i=9/a=090001>.

- [13] J. Ellis, J. Hagelin, D. Nanopoulos, K. Olive, and M. Srednicki, *Supersymmetric relics from the big bang*, Nuclear Physics B **238** no. 2, (1984) 453 – 476. <http://www.sciencedirect.com/science/article/pii/0550321384904619>.
- [14] S. Borgani, A. Masiero, and M. Yamaguchi, *Light gravitinos as mixed dark matter*, Phys. Lett. **B386** (1996) 189–197, [arXiv:hep-ph/9605222](https://arxiv.org/abs/hep-ph/9605222) [hep-ph].
- [15] F. Takayama and M. Yamaguchi, *Gravitino dark matter without R-parity*, Phys. Lett. **B485** (2000) 388–392, [arXiv:hep-ph/0005214](https://arxiv.org/abs/hep-ph/0005214) [hep-ph].
- [16] M. Hirsch, W. Porod, and D. Restrepo, *Collider signals of gravitino dark matter in bilinearly broken R-parity*, JHEP **03** (2005) 062, [arXiv:hep-ph/0503059](https://arxiv.org/abs/hep-ph/0503059) [hep-ph].
- [17] E. J. Chun and H. B. Kim, *Axino Light Dark Matter and Neutrino Masses with R-parity Violation*, JHEP **10** (2006) 082, [arXiv:hep-ph/0607076](https://arxiv.org/abs/hep-ph/0607076) [hep-ph].
- [18] K. Choi, E. J. Chun, and K. Hwang, *Axino as a sterile neutrino and R-parity violation*, Phys. Rev. **D64** (2001) 033006, [arXiv:hep-ph/0101026](https://arxiv.org/abs/hep-ph/0101026) [hep-ph].
- [19] E. J. Chun and H. B. Kim, *Nonthermal axino as cool dark matter in supersymmetric standard model without R-parity*, Phys. Rev. **D60** (1999) 095006, [arXiv:hep-ph/9906392](https://arxiv.org/abs/hep-ph/9906392) [hep-ph].
- [20] U. Amaldi, W. de Boer, and H. Furstenau, *Comparison of grand unified theories with electroweak and strong coupling constants measured at LEP*, Phys. Lett. **B260** (1991) 447–455.
- [21] H. Georgi and S. L. Glashow, *Unity of All Elementary-Particle Forces*, Phys. Rev. Lett. **32** (1974) 438–441. <http://link.aps.org/doi/10.1103/PhysRevLett.32.438>.
- [22] J. R. Ellis, S. Kelley, and D. V. Nanopoulos, *Precision LEP data, supersymmetric GUTs and string unification*, Phys. Lett. **B249** (1990) 441–448.
- [23] J. R. Ellis, S. Kelley, and D. V. Nanopoulos, *Probing the desert using gauge coupling unification*, Phys. Lett. **B260** (1991) 131–137.
- [24] C. Giunti, C. W. Kim, and U. W. Lee, *Running coupling constants and grand unification models*, Mod. Phys. Lett. **A6** (1991) 1745–1755.
- [25] P. Langacker and M.-x. Luo, *Implications of precision electroweak experiments for  $M_t$ ,  $\rho_0$ ,  $\sin^2 \theta_W$  and grand unification*, Phys. Rev. **D44** (1991) 817–822.

- [26] Y. Kao and T. Takeuchi, *Single-Coupling Bounds on R-parity violating Supersymmetry, an update*, arXiv:0910.4980 [hep-ph].
- [27] F. D. Steffen, *Dark Matter Candidates - Axions, Neutralinos, Gravitinos, and Axinos*, Eur. Phys. J. **C59** (2009) 557–588, arXiv:0811.3347 [hep-ph].
- [28] P. Nath and R. Arnowitt, *Generalized super-gauge symmetry as a new framework for unified gauge theories*, Physics Letters B **56** no. 2, (1975) 177 – 180. <http://www.sciencedirect.com/science/article/pii/037026937590297X>.
- [29] E. Cremmer, S. Ferrara, L. Girardello, and A. Van Proeyen, *Yang-Mills Theories with Local Supersymmetry: Lagrangian, Transformation Laws and SuperHiggs Effect*, Nucl. Phys. **B212** (1983) 413.
- [30] A. Bartl, W. Porod, D. Restrepo, J. Romao, and J. W. F. Valle, *Neutralino phenomenology at LEP-2 in supersymmetry with bilinear breaking of R-parity*, Nucl. Phys. **B600** (2001) 39–61, arXiv:hep-ph/0007157 [hep-ph].
- [31] F. de Campos, O. J. P. Eboli, M. B. Magro, W. Porod, D. Restrepo, M. Hirsch, and J. W. F. Valle, *Probing bilinear R-parity violating supergravity at the LHC*, JHEP **05** (2008) 048, arXiv:0712.2156 [hep-ph].
- [32] V. A. Mitsou, *R-parity violating supersymmetry and neutrino physics: experimental signatures*, PoS **PLANCK2015** (2015) 085, arXiv:1510.02660 [hep-ph].
- [33] P. Meade, N. Seiberg, and D. Shih, *General Gauge Mediation*, Prog. Theor. Phys. Suppl. **177** (2009) 143–158, arXiv:0801.3278 [hep-ph].
- [34] M. Buican, P. Meade, N. Seiberg, and D. Shih, *Exploring General Gauge Mediation*, JHEP **0903** (2009) 016, arXiv:0812.3668 [hep-ph].
- [35] L. Evans and P. Bryant (editors), *LHC Machine*, JINST **3** (2008) S08001. <http://stacks.iop.org/1748-0221/3/i=08/a=S08001>.
- [36] ATLAS Collaboration, *The ATLAS Experiment at the CERN Large Hadron Collider*, JINST **3** (2008) S08003.
- [37] CMS Collaboration, *The CMS experiment at the CERN LHC*, JINST **3** (2008) S08004. <http://stacks.iop.org/1748-0221/3/i=08/a=S08004>.
- [38] LHCb Collaboration, *The LHCb Detector at the LHC*, JINST **3** (2008) S08005. <http://stacks.iop.org/1748-0221/3/i=08/a=S08005>.

- [39] ALICE Collaboration, *The ALICE experiment at the CERN LHC*, JINST **3** (2008) S08002.  
<http://stacks.iop.org/1748-0221/3/i=08/a=S08002>.
- [40] TOTEM Collaboration, *The TOTEM Experiment at the CERN Large Hadron Collider*, JINST **3** (2008) S08007.  
<http://stacks.iop.org/1748-0221/3/i=08/a=S08007>.
- [41] LHCf Collaboration, *The LHCf detector at the CERN Large Hadron Collider*, JINST **3** (2008) S08006.  
<http://stacks.iop.org/1748-0221/3/i=08/a=S08006>.
- [42] MoEDAL Collaboration, *Technical Design Report of the MoEDAL Experiment*, Tech. Rep. CERN-LHCC-2009-006. MoEDAL-TDR-001, Jun, 2009. <http://cds.cern.ch/record/1181486>.
- [43] MoEDAL Collaboration, *The Physics Programme Of The MoEDAL Experiment At The LHC*, Int. J. Mod. Phys. **A29** (2014) 1430050, [arXiv:1405.7662](https://arxiv.org/abs/1405.7662) [hep-ph].
- [44] C. Eck et al., *LHC computing Grid: Technical Design Report. Version 1.06 (20 Jun 2005)*. Technical Design Report LCG. CERN, Geneva, 2005. <https://cds.cern.ch/record/840543>.
- [45] ATLAS Collaboration, *ATLAS liquid-argon calorimeter: Technical Design Report*, <https://cds.cern.ch/record/331061>.
- [46] ATLAS Collaboration, *Search for supersymmetry at  $\sqrt{s} = 7$  TeV in final states with large jet multiplicity, missing transverse momentum and one isolated lepton with the ATLAS detector*, Tech. Rep. ATLAS-CONF-2012-140, CERN, Geneva, Oct, 2012.  
<https://cds.cern.ch/record/1483511>.
- [47] ATLAS Collaboration, *Further search for supersymmetry at  $\sqrt{s} = 7$  TeV in final states with jets, missing transverse momentum and isolated leptons with the ATLAS detector*, Phys. Rev. **D86** (2012) 092002, [arXiv:1208.4688](https://arxiv.org/abs/1208.4688) [hep-ex].
- [48] ATLAS Collaboration, *Search for new phenomena in final states with large jet multiplicities and missing transverse momentum using  $\sqrt{s} = 7$  TeV pp collisions with the ATLAS detector*, JHEP **11** (2011) 099, [arXiv:1110.2299](https://arxiv.org/abs/1110.2299) [hep-ex].
- [49] ATLAS Collaboration, *Hunt for new phenomena using large jet multiplicities and missing transverse momentum with ATLAS in  $4.7$  fb<sup>-1</sup> of  $\sqrt{s} = 7$  TeV proton-proton collisions*, JHEP **07** (2012) 167, [arXiv:1206.1760](https://arxiv.org/abs/1206.1760) [hep-ex].



- [50] S. Roy and B. Mukhopadhyaya, *Some implications of a supersymmetric model with R-parity breaking bilinear interactions*, Phys. Rev. **D55** (1997) 7020–7029, arXiv:hep-ph/9612447 [hep-ph].
- [51] ATLAS Collaboration, S. Asai, E. Romero, et al., *Search for supersymmetry at  $\sqrt{s} = 7$  TeV in final states with large jet multiplicity, missing transverse momentum and one isolated lepton with the ATLAS detector* (supporting INT note), Tech. Rep. ATL-PHYS-INT-2012-080, CERN, Geneva, Oct, 2012. <https://cds.cern.ch/record/1483520>.
- [52] Y. Grossman and S. Rakshit, *Neutrino masses in R-parity violating supersymmetric models*, Phys. Rev. **D69** (2004) 093002, arXiv:hep-ph/0311310 [hep-ph].
- [53] D. F. Carvalho, M. E. Gomez, and J. C. Romao, *Charged lepton flavor violation in supersymmetry with bilinear R-parity violation*, Phys. Rev. **D65** (2002) 093013, arXiv:hep-ph/0202054 [hep-ph].
- [54] W. Porod, M. Hirsch, J. Romao, and J. W. F. Valle, *Testing neutrino mixing at future collider experiments*, Phys. Rev. **D63** (2001) 115004, arXiv:hep-ph/0011248 [hep-ph].
- [55] ATLAS Collaboration, *Performance of primary vertex reconstruction in proton-proton collisions at  $\sqrt{s} = 7$  TeV in the ATLAS experiment*, Tech. Rep. ATLAS-CONF-2010-069, CERN, Geneva, Jul, 2010. <https://cds.cern.ch/record/1281344>.
- [56] ATLAS Collaboration, *Electron performance measurements with the ATLAS detector using the 2010 LHC proton-proton collision data*, Eur. Phys. J. **C72** (2012) 1909, arXiv:1110.3174 [hep-ex].
- [57] ATLAS Collaboration, *A measurement of the ATLAS muon reconstruction and trigger efficiency using J/psi decays*, Tech. Rep. ATLAS-CONF-2011-021, CERN, Geneva, Mar, 2011. <https://cds.cern.ch/record/1336750>.
- [58] ATLAS Collaboration, *Muon reconstruction efficiency in reprocessed 2010 LHC proton-proton collision data recorded with the ATLAS detector*, Tech. Rep. ATLAS-CONF-2011-063, CERN, Geneva, Apr, 2011. <https://cds.cern.ch/record/1345743>.
- [59] ATLAS Collaboration, *Search for supersymmetry in final states with jets, missing transverse momentum and one isolated lepton in  $\sqrt{s} = 7$  TeV pp collisions using  $1 \text{ fb}^{-1}$  of ATLAS data*, Phys. Rev. **D 85** (2012) 012006, arXiv:1109.6606 [hep-ex]. [Erratum: Phys. Rev.D87,099903(2013)].

- [60] M. Cacciari, G. P. Salam, and G. Soyez, *The Anti- $k(t)$  jet clustering algorithm*, JHEP **04** (2008) 063, [arXiv:0802.1189](https://arxiv.org/abs/0802.1189) [hep-ph].
- [61] M. Cacciari and G. P. Salam, *Dispelling the  $N^3$  myth for the  $k_t$  jet-finder*, Phys. Lett. **B641** (2006) 57–61, [arXiv:hep-ph/0512210](https://arxiv.org/abs/hep-ph/0512210) [hep-ph].
- [62] ATLAS Collaboration, *Jet energy measurement with the ATLAS detector in proton-proton collisions at  $\sqrt{s} = 7$  TeV*, Eur. Phys. J. **C73** no. 3, (2013) 2304, [arXiv:1112.6426](https://arxiv.org/abs/1112.6426) [hep-ex].
- [63] ATLAS Collaboration, *Measurement of the  $b$ -tag Efficiency in a Sample of Jets Containing Muons with  $5 \text{ fb}^{-1}$  of Data from the ATLAS Detector*, Tech. Rep. ATLAS-CONF-2012-043, CERN, Geneva, Mar, 2012. <https://cds.cern.ch/record/1435197>.
- [64] ATLAS Collaboration, *Calibrating the  $b$ -Tag Efficiency and Mistag Rate in  $35 \text{ pb}^{-1}$  of Data with the ATLAS Detector*, Tech. Rep. ATLAS-CONF-2011-089, CERN, Geneva, Jun, 2011. <https://cds.cern.ch/record/1356198>.
- [65] ATLAS Collaboration, *Commissioning of the ATLAS high-performance  $b$ -tagging algorithms in the 7 TeV collision data*, Tech. Rep. ATLAS-CONF-2011-102, CERN, Geneva, Jul, 2011. <https://cds.cern.ch/record/1369219>.
- [66] ATLAS Collaboration, *Performance of Missing Transverse Momentum Reconstruction in Proton-Proton Collisions at 7 TeV with ATLAS*, Eur. Phys. J. **C72** (2012) 1844, [arXiv:1108.5602](https://arxiv.org/abs/1108.5602) [hep-ex].
- [67] ATLAS Collaboration,  *$b$ -Jet Tagging Efficiency Calibration using the System8 Method*, Tech. Rep. ATLAS-CONF-2011-143, CERN, Geneva, Oct, 2011. <https://cds.cern.ch/record/1386703>.
- [68] D0 Collaboration, V. M. Abazov et al.,  *$b$ -Jet Identification in the D0 Experiment*, Nucl. Instrum. Meth. **A620** (2010) 490–517, [arXiv:1002.4224](https://arxiv.org/abs/1002.4224) [hep-ex].
- [69] ATLAS Collaboration, *Measurement of the Mistag Rate with  $5 \text{ fb}^{-1}$  of Data Collected by the ATLAS Detector*, Tech. Rep. ATLAS-CONF-2012-040, CERN, Geneva, Mar, 2012. <https://cds.cern.ch/record/1435194>.
- [70] ATLAS Collaboration,  *$b$ -jet tagging calibration on  $c$ -jets containing  $D^{*+}$  mesons*, Tech. Rep. ATLAS-CONF-2012-039, CERN, Geneva, Mar, 2012. <https://cds.cern.ch/record/1435193>.
- [71] M. Kramer et al., *Supersymmetry production cross sections in  $pp$  collisions at  $\sqrt{s} = 7$  TeV*, [arXiv:1206.2892](https://arxiv.org/abs/1206.2892) [hep-ph].

- [72] G. Cowan, K. Cranmer, E. Gross, and O. Vitells, *Asymptotic formulae for likelihood-based tests of new physics*, Eur. Phys. J. **C71** (2011) 1554, arXiv:1007.1727 [physics.data-an]. [Erratum: Eur. Phys. J.C73,2501(2013)].
- [73] M. Baak et al., *HistFitter software framework for statistical data analysis*, Eur. Phys. J. C **75** no. arXiv:1410.1280, (2014) 153. 35 p. <https://cds.cern.ch/record/1953093>.
- [74] M. Hirsch, M. A. Diaz, W. Porod, J. C. Romao, and J. W. F. Valle, *Neutrino masses and mixings from supersymmetry with bilinear R parity violation: A Theory for solar and atmospheric neutrino oscillations*, Phys. Rev. **D62** (2000) 113008, arXiv:hep-ph/0004115 [hep-ph]. [Erratum: Phys. Rev.D65,119901(2002)].
- [75] ATLAS Collaboration, S. Asai, E. Romero, et al., *Search for Supersymmetry with jets and missing transverse momentum and one lepton at  $\sqrt{s} = 7$  TeV*, Tech. Rep. ATL-PHYS-INT-2011-082, CERN, Geneva, Oct, 2011. <https://cds.cern.ch/record/1387044>.
- [76] W. Porod, *SPheno, a program for calculating supersymmetric spectra, SUSY particle decays and SUSY particle production at  $e^+ e^-$  colliders*, Comput. Phys. Commun. **153** (2003) 275–315, arXiv:hep-ph/0301101 [hep-ph].
- [77] W. Porod and F. Staub, *SPheno 3.1: Extensions including flavour, CP-phases and models beyond the MSSM*, Comput. Phys. Commun. **183** (2012) 2458–2469, arXiv:1104.1573 [hep-ph].
- [78] E. Torro Pastor, *Study of supersymmetric signals with R-parity violation in ATLAS at LHC*. PhD thesis, Valencia U., 2012. [http://roderic.uv.es/bitstream/handle/10550/25802/Thesis\\_EmmaTorro.pdf](http://roderic.uv.es/bitstream/handle/10550/25802/Thesis_EmmaTorro.pdf).
- [79] ATLAS Collaboration, *Search for supersymmetry at  $\sqrt{s}=8$  TeV in final states with jets and two same-sign leptons or three leptons with the ATLAS detector*, JHEP **06** (2014) 035, arXiv:1404.2500 [hep-ex].
- [80] ATLAS Collaboration, *Search for supersymmetry in events with large missing transverse momentum, jets, and at least one tau lepton in 20  $\text{fb}^{-1}$  of  $\sqrt{s} = 8$  TeV proton-proton collision data with the ATLAS detector*, JHEP **09** (2014) 103, arXiv:1407.0603 [hep-ex].
- [81] ATLAS Collaboration, *Search for squarks and gluinos in events with isolated leptons, jets and missing transverse momentum at  $\sqrt{s} = 8$  TeV with the ATLAS detector*, JHEP **04** (2015) 116, arXiv:1501.03555 [hep-ex].

- [82] ATLAS Collaboration, *Summary of the searches for squarks and gluinos using  $\sqrt{s} = 8$  TeV pp collisions with the ATLAS experiment at the LHC*, JHEP **10** (2015) 054, [arXiv:1507.05525 \[hep-ex\]](#).
- [83] M. Dine and W. Fischler, *A Phenomenological Model of Particle Physics Based on Supersymmetry*, Phys. Lett. B **110** (1982) 227.
- [84] L. Alvarez-Gaume, M. Claudson, and M. B. Wise, *Low-Energy Supersymmetry*, Nucl. Phys. B **207** (1982) 96.
- [85] C. R. Nappi and B. A. Ovrut, *Supersymmetric Extension of the  $SU(3) \times SU(2) \times U(1)$  Model*, Phys. Lett. B **113** (1982) 175.
- [86] M. Dine and A. E. Nelson, *Dynamical supersymmetry breaking at low-energies*, Phys. Rev. D **48** (1993) 1277–1287, [arXiv:hep-ph/9303230 \[hep-ph\]](#).
- [87] M. Dine, A. E. Nelson, and Y. Shirman, *Low-energy dynamical supersymmetry breaking simplified*, Phys. Rev. D **51** (1995) 1362–1370, [arXiv:hep-ph/9408384 \[hep-ph\]](#).
- [88] M. Dine, A. E. Nelson, Y. Nir, and Y. Shirman, *New tools for low-energy dynamical supersymmetry breaking*, Phys. Rev. D **53** (1996) 2658–2669, [arXiv:hep-ph/9507378 \[hep-ph\]](#).
- [89] ATLAS Collaboration, *Search for diphoton events with large missing transverse momentum in 7 TeV proton-proton collision data with the ATLAS detector*, Phys.Lett. **B718** (2012) 411–430, [arXiv:1209.0753 \[hep-ex\]](#).
- [90] CMS Collaboration, “Search for supersymmetry in events with photons and missing energy.” CMS-PAS-SUS-12-018, 2012. <http://cdsweb.cern.ch/record/1460385>.
- [91] CMS Collaboration, *Search for supersymmetry in events with a lepton, a photon, and large missing transverse energy in pp collisions at  $\sqrt{s} = 7$  TeV*, JHEP **1106** (2011) 093, [arXiv:1105.3152 \[hep-ex\]](#).
- [92] CMS Collaboration, “SUSY Search in Photon(s)+jets+ $E_T^{\text{miss}}$  final state with the Jet-Gamma Balance method.” CMS-PAS-SUS-12-013, 2012. <http://cdsweb.cern.ch/record/1477716>.
- [93] ATLAS Collaboration, *Search for supersymmetry in events with photons, bottom quarks, and missing transverse momentum in proton-proton collisions at a centre-of-mass energy of 7 TeV with the ATLAS detector*, [arXiv:1211.1167 \[hep-ex\]](#).
- [94] ATLAS Collaboration, “Search for supersymmetry in final states with jets, missing transverse momentum and a  $Z$  boson at  $\sqrt{s} = 8$  TeV with the ATLAS detector.” ATLAS-CONF-2012-152, 2012. <http://cds.cern.ch/record/1493491>.

- [95] P. Meade, M. Reece, and D. Shih, *Prompt Decays of General Neutralino NLSPs at the Tevatron*, JHEP **1005** (2010) 105, arXiv:0911.4130 [hep-ph].
- [96] J. T. Ruderman and D. Shih, *General Neutralino NLSPs at the Early LHC*, JHEP **1208** (2012) 159, arXiv:1103.6083 [hep-ph].
- [97] ATLAS Collaboration, B. H. Hooberman, E. Romero, et al., *Search for supersymmetry in events with a Z boson and large missing transverse momentum with the full 2012 ATLAS dataset (supporting INT note - Z + MET)*, Tech. Rep. ATL-COM-PHYS-2013-1565, Nov, 2013. <https://cds.cern.ch/record/1630804>.
- [98] ATLAS Collaboration, *Search for supersymmetry in events with four or more leptons in  $\sqrt{s} = 8$  TeV pp collisions with the ATLAS detector*, arXiv:1405.5086 [hep-ex].
- [99] A. Djouadi, J.-L. Kneur, and G. Moultaka, *SuSpect: A Fortran code for the supersymmetric and Higgs particle spectrum in the MSSM*, Comput. Phys. Commun. **176** (2007) 426–455, arXiv:hep-ph/0211331 [hep-ph].
- [100] M. Muhlleitner, A. Djouadi, and Y. Mambrini, *SDECAY: A Fortran code for the decays of the supersymmetric particles in the MSSM*, Comput. Phys. Commun. **168** (2005) 46–70, arXiv:hep-ph/0311167 [hep-ph].
- [101] T. Sjostrand, S. Mrenna, and P. Z. Skands, *PYTHIA 6.4 Physics and Manual*, JHEP **0605** (2006) 026, arXiv:hep-ph/0603175 [hep-ph].
- [102] A. Sherstnev and R. Thorne, *Parton Distributions for LO Generators*, Eur. Phys. J. C **55** (2008) 553–575, arXiv:0711.2473 [hep-ph].
- [103] W. Beenakker, R. Hopker, M. Spira, and P. Zerwas, *Squark and gluino production at hadron colliders*, Nucl. Phys. B **492** (1997) 51–103, arXiv:hep-ph/9610490 [hep-ph].
- [104] A. Kulesza and L. Motyka, *Threshold resummation for squark-antisquark and gluino-pair production at the LHC*, Phys. Rev. Lett. **102** (2009) 111802, arXiv:0807.2405 [hep-ph].
- [105] A. Kulesza and L. Motyka, *Soft gluon resummation for the production of gluino-gluino and squark-antisquark pairs at the LHC*, Phys. Rev. D **80** (2009) 095004, arXiv:0905.4749 [hep-ph].
- [106] W. Beenakker et al., *Soft-gluon resummation for squark and gluino hadroproduction*, JHEP **0912** (2009) 041, arXiv:0909.4418 [hep-ph].
- [107] W. Beenakker et al., *Squark and gluino hadroproduction*, Int. J. Mod. Phys. A **26** (2011) 2637–2664, arXiv:1105.1110 [hep-ph].

- [108] “NLL-FAST website.” [http://pauli.uni-muenster.de/~akule\\_01/nllwiki/index.php/NLL-fast](http://pauli.uni-muenster.de/~akule_01/nllwiki/index.php/NLL-fast).
- [109] “PROSPINO website.” <http://www.thphys.uni-heidelberg.de/~plehn/index.php?show=prospino&visible=tools>.
- [110] ATLAS Collaboration, *Electron reconstruction and identification efficiency measurements with the ATLAS detector using the 2011 LHC proton-proton collision data*, Eur. Phys. J. C **74** (2014) 2941, arXiv:1404.2240 [hep-ex].
- [111] ATLAS Collaboration, *Muon reconstruction efficiency and momentum resolution of the ATLAS experiment in proton-proton collisions at  $\sqrt{s} = 7$  TeV in 2010*, Eur. Phys. J. C **74** (2014) 3034, arXiv:1404.4562 [hep-ex].
- [112] ATLAS Collaboration, *Expected Performance of the ATLAS Experiment - Detector, Trigger and Physics*, arXiv:0901.0512 [hep-ex].
- [113] M. Cacciari, G. P. Salam, and G. Soyez, *The Catchment Area of Jets*, JHEP **04** (2008) 005, arXiv:0802.1188 [hep-ph].
- [114] ATLAS Collaboration, *Single hadron response measurement and calorimeter jet energy scale uncertainty with the ATLAS detector at the LHC*, Eur. Phys. J. C **73** no. 3, (2013) 2305, arXiv:1203.1302 [hep-ex].
- [115] ATLAS Collaboration, *Characterisation and mitigation of beam-induced backgrounds observed in the ATLAS detector during the 2011 proton-proton run*, JINST **8** (2013) P07004, arXiv:1303.0223 [hep-ex].
- [116] ATLAS Collaboration, *Performance of primary vertex reconstruction in proton-proton collisions at  $\sqrt{s} = 7$  TeV in the ATLAS experiment*, ATLAS-CONF-2010-069. <http://cds.cern.ch/record/1281344>.
- [117] ATLAS Collaboration, *Pile-up subtraction and suppression for jets in ATLAS*, ATLAS-CONF-2013-083. <http://cds.cern.ch/record/1570994>.
- [118] ATLAS Collaboration, *Measurements of the photon identification efficiency with the ATLAS detector using  $4.9 \text{ fb}^{-1}$  of pp collision data collected in 2011*, ATLAS-CONF-2012-123. <http://cds.cern.ch/record/1473426>.
- [119] ATLAS Collaboration, *Search for squarks and gluinos in events with isolated leptons, jets and missing transverse momentum at  $\sqrt{s} = 8$  TeV with the ATLAS detector*, JHEP **04** (2015) 116, arXiv:1501.03555 [hep-ph].

- [120] ATLAS Collaboration, *Search for squarks and gluinos with the ATLAS detector in final states with jets and missing transverse momentum using  $4.7 \text{ fb}^{-1}$  of  $\sqrt{s} = 7 \text{ TeV}$  proton-proton collision data*, Phys. Rev. **D87** no. 1, (2013) 012008, [arXiv:1208.0949 \[hep-ex\]](#).
- [121] ATLAS Collaboration, A. Chitan et al., *Search for strongly produced supersymmetric particles in decays with at least two leptons at  $\sqrt{s} = 8 \text{ TeV}$  with the ATLAS detector*, Tech. Rep. ATL-COM-PHYS-2013-1539, Nov, 2013. <https://cds.cern.ch/record/1627071>.
- [122] ATLAS Collaboration, *Measurements of normalized differential cross-sections for  $t\bar{t}$  production in  $pp$  collisions at  $\sqrt{s} = 7 \text{ TeV}$  using the ATLAS detector*, Phys. Rev. D **90** (2014) 072004, [arXiv:1407.0371 \[hep-ex\]](#).
- [123] ATLAS Collaboration, *Measurements of top quark pair relative differential cross-sections with ATLAS in  $pp$  collisions at  $\sqrt{s} = 7 \text{ TeV}$* , Eur. Phys. J. C **73** (2013) 2261, [arXiv:1207.5644 \[hep-ex\]](#).
- [124] ATLAS Collaboration, A. Chitan et al., *Search for strongly produced supersymmetric particles in decays with leptons at  $\sqrt{s} = 8 \text{ TeV}$  (supporting INT note - Combination)*, Tech. Rep. ATL-COM-PHYS-2013-1493, Nov, 2013. <https://cds.cern.ch/record/1624335>. (combination INT note, aiming at a SUSY strong production with leptons paper, together with four other analysis-specific INT notes: 1 hard-lepton, 1(2) soft-lepton(s), 2 leptons+Razor, Z+MET.).
- [125] ATLAS Collaboration, A. Chitan et al., *Search for strongly produced supersymmetric particles in decays with leptons at  $\sqrt{s} = 8 \text{ TeV}$  (supporting INT note - 1 hard lepton)*, Tech. Rep. ATL-COM-PHYS-2013-1517, Nov, 2013. <https://cds.cern.ch/record/1626588>.
- [126] ATLAS Collaboration, *Search for top squark pair production in final states with one isolated lepton, jets, and missing transverse momentum in  $\sqrt{s} = 8 \text{ TeV}$   $pp$  collisions with the ATLAS detector*, JHEP **11** (2014) 118, [arXiv:1407.0583 \[hep-ex\]](#).
- [127] ATLAS Collaboration, *Search for squarks and gluinos with the ATLAS detector in final states with jets and missing transverse momentum using  $\sqrt{s} = 8 \text{ TeV}$  proton-proton collision data*, JHEP **09** (2014) 176, [arXiv:1405.7875 \[hep-ex\]](#).
- [128] ATLAS Collaboration, *Measurement of the top quark-pair production cross section with ATLAS in  $pp$  collisions at  $\sqrt{s} = 7 \text{ TeV}$* , Eur. Phys. J. **C71** (2011) 1577, [arXiv:1012.1792 \[hep-ex\]](#).

- [129] ATLAS Collaboration, A. Chitan et al., *Search for strongly produced supersymmetric particles in decays with leptons at  $\sqrt{s} = 8$  TeV (supporting INT note)*, Tech. Rep. ATL-PHYS-INT-2013-017, Oct, 2013. <https://cds.cern.ch/record/1610179>.
- [130] ATLAS Collaboration, Jet-Etmiss Group, “JETENERGYRESOLUTIONPROVIDER, jetresolution package.” <http://twiki.cern.ch/twiki/bin/viewauth/AtlasProtected/JetEnergyResolutionProvider>. (software package used to obtain the Jet Energy Resolution and its uncertainty for AntiKt 0.4/0.6 jets).
- [131] ATLAS Collaboration, *Jet energy resolution in proton-proton collisions at  $\sqrt{s} = 7$  TeV recorded in 2010 with the ATLAS detector*, Eur. Phys. J. **C73** no. 3, (2013) 2306, arXiv:1210.6210 [hep-ex].
- [132] ATLAS Collaboration, *Electron reconstruction and identification efficiency measurements with the ATLAS detector using the 2011 LHC proton-proton collision data*, Eur. Phys. J. **C74** no. 7, (2014) 2941, arXiv:1404.2240 [hep-ex].
- [133] “Egamma group, egammasfclass, egammaanalysisutils package.” [http://twiki.cern.ch/twiki/bin/viewauth/AtlasProtected/EfficiencyMeasurements#Electron\\_efficiencies\\_2011\\_Morio](http://twiki.cern.ch/twiki/bin/viewauth/AtlasProtected/EfficiencyMeasurements#Electron_efficiencies_2011_Morio).
- [134] “Muon combined performance group, muonefficiencycorrections package.” <http://twiki.cern.ch/twiki/bin/viewauth/AtlasProtected/MCPAnalysisGuidelinesRel17MC11a>.
- [135] M. Botje et al., *The PDF4LHC Working Group Interim Recommendations*, arXiv:1101.0538 [hep-ph].
- [136] J. M. Campbell and R. K. Ellis,  *$t\bar{t}W^{+-}$  production and decay at NLO*, JHEP **07** (2012) 052, arXiv:1204.5678 [hep-ph].
- [137] G. Corcella, I. G. Knowles, G. Marchesini, S. Moretti, K. Odagiri, P. Richardson, M. H. Seymour, and B. R. Webber, *HERWIG 6: An Event generator for hadron emission reactions with interfering gluons (including supersymmetric processes)*, JHEP **01** (2001) 010, arXiv:hep-ph/0011363 [hep-ph].
- [138] J. M. Butterworth, J. R. Forshaw, and M. H. Seymour, *Multiparton interactions in photoproduction at HERA*, Z. Phys. **C72** (1996) 637–646, arXiv:hep-ph/9601371 [hep-ph].
- [139] A. L. Read, *Presentation of search results: The  $CL(s)$  technique*, J. Phys. **G28** (2002) 2693–2704. [,11(2002)].
- [140] M. Baak, G. J. Besjes, D. Cte, A. Koutsman, J. Lorenz, and D. Short, *HistFitter software framework for statistical data analysis*, Eur. Phys. J. **C75** (2015) 153, arXiv:1410.1280 [hep-ex].



- [141] ATLAS Collaboration, *Search for supersymmetry in events containing a same-flavour opposite-sign dilepton pair, jets, and large missing transverse momentum in  $\sqrt{s} = 8$  TeV pp collisions with the ATLAS detector*, Eur. Phys. J. **C75** no. 7, (2015) 318, [arXiv:1503.03290](#) [hep-ex]. [Erratum: Eur. Phys. J.C75,no.10,463(2015)].
- [142] G. Barenboim, J. Bernabeu, V. A. Mitsou, E. Romero, and O. Vives, *METing SUSY on the Z peak*, Eur. Phys. J. **C76** (2016) 57, [arXiv:1503.04184](#) [hep-ph].
- [143] V. A. Mitsou, *Conciliating SUSY with the Z-peaked excess*, EPJ Web Conf. **126** (2016) 02021, [arXiv:1512.06166](#) [hep-ph].
- [144] ATLAS Collaboration, *Search for new phenomena in events containing a same-flavour opposite-sign dilepton pair, jets, and large missing transverse momentum in  $\sqrt{s} = 13$  TeV pp collisions with the ATLAS detector*, [arXiv:1611.05791](#) [hep-ex].
- [145] CMS Collaboration, *Search for Physics Beyond the Standard Model in Events with Two Leptons, Jets, and Missing Transverse Momentum in pp Collisions at  $\sqrt{s} = 8$  TeV*, JHEP **04** (2015) 124, [arXiv:1502.06031](#) [hep-ex].
- [146] CMS Collaboration, *Search for new physics in final states with two opposite-sign, same-flavor leptons, jets, and missing transverse momentum in pp collisions at  $\sqrt{s} = 13$  TeV*, JHEP **12** (2016) 013, [arXiv:1607.00915](#) [hep-ex].
- [147] L. Lyons, *Statistics for nuclear and particle physicists*. Cambridge University Press, 1986.
- [148] K. Cranmer, *Practical Statistics for the LHC*, [arXiv:1503.07622v1](#) [physics.data-an].
- [149] G. Cowan, K. Cranmer, E. Gross, and O. Vitells, *Power-Constrained Limits*, [arXiv:1105.3166](#) [physics.data-an].
- [150] ATLAS Collaboration, Statistics Forum, “The  $CL_s$  method: information for conference speakers.” <https://www.pp.rhul.ac.uk/~cowan/stat/cls/CLsInfo.ps>.
- [151] G. Cowan, *Statistical data analysis*. Oxford University Press, 1998.
- [152] ATLAS Collaboration, *Observation of a new particle in the search for the Standard Model Higgs boson with the ATLAS detector at the LHC*, Phys. Lett. **B 716** (2012) 1–29, [arXiv:1207.7214](#) [hep-ex].
- [153] ATLAS Collaboration, “Search for susy in events with photon, jets and missing transverse energy with the atlas detector.” ATL-COM-PHYS-2014-029, 2014. <http://cds.cern.ch/record/1643485>.



# List of Figures

1.1	The presumed schematic structure for Supersymmetry breaking [2]. . . . .	24
2.1	Schematic layout of the CERN accelerator complex. . . . .	31
2.2	Layout of the ATLAS detector. . . . .	34
2.3	Layout of the ATLAS Inner Detector. . . . .	35
2.4	Layout of the ATLAS Calorimeters. . . . .	37
2.5	Layout of the ATLAS Muon System. . . . .	38
3.1	Summary of the fit results in the control regions (left) and validation regions (right). The difference between the observed and predicted number of events, divided by the total (statistical and systematic) uncertainty on the prediction, is shown for each control and validation region. . . . .	53
3.2	Distribution of $m_{\text{eff}}^{\text{inc}}$ in the $t\bar{t}$ validation region for the electron (left) and muon (right) channels. The SM expectation shown here is the output of the final fit. The uncertainty band around the SM expectation combines all statistical and systematic uncertainties except for the multiparton uncertainty. . . . .	53
3.3	Distribution of the jet multiplicity in the electron (left) and muon (right) channels after all selection requirements except for that on the jet multiplicity. The last bin includes all overflows. The SM expectation shown here is the sum of the fitted values for each of the SM background components. The uncertainty band around the SM expectation combines all statistical and systematic uncertainties except for the multiparton uncertainty, which is included only for $N_{\text{jet}} \geq 7$ . . . . .	55
3.4	Distribution of the transverse mass in the electron (left) and muon (right) signal regions after all selection requirements except for that on the transverse mass. The last bin includes all overflows. The SM expectation shown here is the sum of the fitted values for each of the SM background components. The uncertainty band around the SM expectation combines all statistical and systematic uncertainties except for the multiparton uncertainty, which is included only for $m_{\text{T}} > 120$ GeV. . . . .	55

3.5	Distribution of $m_{\text{eff}}^{\text{inc}}$ in the electron (left) and muon (right) signal regions after all selection requirements. The last $m_{\text{eff}}^{\text{inc}}$ bin includes all overflows. The SM expectation shown here is the input to the final fit, and is entirely derived from simulation, normalized to the theoretical cross sections. The uncertainty band around the SM expectation combines the statistical uncertainty on the simulated event samples with the systematic uncertainties on the jet energy scale and resolution, lepton efficiency and resolution, luminosity, multijet background and $b$ -tagging. . . .	56
3.6	Expected and observed 95% CL exclusion limits in the bilinear R-parity violating model. The results are obtained by combining the electron and muon channels. The band around the median expected limit shows the $\pm 1\sigma$ variations on the median expected limit, including all uncertainties except the theoretical uncertainties on the signal. The dotted lines around the observed limit indicate the sensitivity to $\pm 1\sigma$ on these theoretical uncertainties. The thin solid black contours show the LSP lifetime. The result from the previous ATLAS search [59] for this model is also shown (in blue). . . . .	58
4.1	The branching fraction for $\tilde{\chi}_1^0 \rightarrow h\tilde{G}$ and $\tilde{\chi}_1^0 \rightarrow Z\tilde{G}$ processes as function of $\mu$ for GGM grid models characterised by the following parameters: $M_1 = 1\text{TeV}$ , $M_2 = 1\text{TeV}$ , $m(\tilde{g}) = 800\text{GeV}$ , $\tan\beta = 1.5$ (left), $\tan\beta = 30$ (right). . . . .	66
4.2	Example of Feynman diagrams for signal processes, also indicating leptonic $Z$ decays. . . . .	66
4.3	The fraction of the $\tilde{g}\tilde{g}$ processes as function of $\mu$ for GGM grid models characterised by the following parameters: $M_1 = 1\text{TeV}$ , $M_2 = 1\text{TeV}$ , $m(\tilde{g}) = 900\text{GeV}$ , $\tan\beta = 1.5$ . . . . .	67
4.4	Total production cross-section (top) and uncertainty in the cross-section estimation (bottom) for the GGM model with $\tan\beta = 1.5$ . . . . .	71
4.5	Generation efficiency (top) and effective cross-section (bottom) for the GGM model with $\tan\beta = 1.5$ . . . . .	72
4.6	Total production cross-section (top) and uncertainty in the cross-section estimation (bottom) for the GGM model with $\tan\beta = 30$ . . . . .	73
4.7	Generation efficiency (top) and effective cross-section (bottom) for the GGM model with $\tan\beta = 30$ . . . . .	74
4.8	Fraction of total cross section due to gluino–gluino production for the GGM model with $\tan\beta = 1.5$ (top) and GGM model with $\tan\beta = 30$ (bottom). . . . .	76
4.9	Fraction of total cross section due to squark–gluino production for the GGM model with $\tan\beta = 1.5$ (top) and GGM model with $\tan\beta = 30$ (bottom). . . . .	77

4.10	Fraction of total cross section due to squark pair production for the GGM model with $\tan\beta = 1.5$ (top) and GGM model with $\tan\beta = 30$ (bottom). . . . .	78
4.11	Fraction of total cross section due to EW production for the GGM model with $\tan\beta = 1.5$ (top) and GGM model with $\tan\beta = 30$ (bottom). . . . .	79
4.12	Masses of $\tilde{\chi}_1^0$ (top), $\tilde{\chi}_2^0$ (middle) and $\tilde{\chi}_1^+$ (bottom) for the GGM model with $\tan\beta = 1.5$ . . . . .	80
4.13	Masses of $\tilde{\chi}_1^0$ (top), $\tilde{\chi}_2^0$ (middle) and $\tilde{\chi}_1^+$ (bottom) for the GGM model with $\tan\beta = 30$ . . . . .	81
4.14	Branching ratio for $\tilde{\chi}_1^0 \rightarrow h\tilde{G}$ (left) and $\tilde{\chi}_1^0 \rightarrow Z\tilde{G}$ (right) for the GGM model with $\tan\beta = 1.5$ . . . . .	82
4.15	Branching ratio for $\tilde{\chi}_1^0 \rightarrow h\tilde{G}$ (left) and $\tilde{\chi}_1^0 \rightarrow Z\tilde{G}$ (right) for the GGM model with $\tan\beta = 30$ . . . . .	82
4.16	Invariant mass distribution for events containing opposite sign electrons (left) and muons (right) after preselection and $81 \text{ GeV} < m_{\ell\ell} < 101 \text{ GeV}$ cut. The plot labelled “Data/SM” shows the ratio of the distribution from data to that of the total SM background. Only experimental uncertainties are shown. . . . .	91
4.17	$H_T$ distribution for events containing opposite sign electrons (left) and muons (right) after preselection and $81 \text{ GeV} < m_{\ell\ell} < 101 \text{ GeV}$ cut. The plot labelled “Data/SM” shows the ratio of the distribution from data to that of the total SM background. Only experimental uncertainties are shown. . . . .	92
4.18	Leading jet $p_T$ distribution for events containing opposite sign electrons (left) and muons (right) after preselection and $81 \text{ GeV} < m_{\ell\ell} < 101 \text{ GeV}$ cut. The plot labelled “Data/SM” shows the ratio of the distribution from data to that of the total SM background. Only experimental uncertainties are shown. . . . .	92
4.19	Subleading jet $p_T$ distribution for events containing opposite sign electrons (left) and muons (right) after preselection and $81 \text{ GeV} < m_{\ell\ell} < 101 \text{ GeV}$ cut. The plot labelled “Data/SM” shows the ratio of the distribution from data to that of the total SM background. Only experimental uncertainties are shown. . . . .	93
4.20	Leading lepton $p_T$ distribution for events containing opposite sign electrons (left) and muons (right) after preselection and $81 \text{ GeV} < m_{\ell\ell} < 101 \text{ GeV}$ cut. The plot labelled “Data/SM” shows the ratio of the distribution from data to that of the total SM background. Only experimental uncertainties are shown. . . . .	93
4.21	Subleading lepton $p_T$ distribution for events containing opposite sign electrons (left) and muons (right) after preselection and $81 \text{ GeV} < m_{\ell\ell} < 101 \text{ GeV}$ cut. The plot labelled “Data/SM” shows the ratio of the distribution from data to that of the total SM background. Only experimental uncertainties are shown. . . . .	94

- 4.22  $E_T^{\text{miss}}$  distribution for events containing opposite sign electrons (left) and muons (right) after preselection and  $81 \text{ GeV} < m_{\ell\ell} < 101 \text{ GeV}$  cut. The plot labelled “Data/SM” shows the ratio of the distribution from data to that of the total SM background. Only experimental uncertainties are shown. . . . . 94
- 4.23 Jet multiplicity distribution for events containing opposite sign electrons (left) and muons (right) after preselection and  $81 \text{ GeV} < m_{\ell\ell} < 101 \text{ GeV}$  cut. The plot labelled “Data/SM” shows the ratio of the distribution from data to that of the total SM background. Only experimental uncertainties are shown. . . . . 95
- 4.24 Distribution of  $E_T^{\text{miss}}$  in the electron (left) and muon (right) channel in VRZ following the requirement of  $\Delta\phi(\text{jet}_{1,2}, E_T^{\text{miss}}) > 0.4$ . Here the  $Z/\gamma^* + \text{jets}$  background (solid blue) is modelled using  $p_T$ - and  $\phi$ -smeared pseudo-data events. The hatched uncertainty band includes the statistical uncertainty on the simulated event samples and the systematic uncertainty on the jet-smearing estimate due to the jet response function and the seed selection. The backgrounds due to  $WZ$ ,  $ZZ$  or rare top processes, as well as from lepton fakes, are included under “Other Backgrounds”. . . . . 99
- 4.25 Diagram indicating the position in the  $E_T^{\text{miss}}$  versus dilepton invariant mass plane of the SR, the control region CRT, and the two validation regions (VRT and VRTZ) used to validate the side-band fit. VRT and VRTZ have lower  $H_T$  thresholds than CRT and SR. . . . . 111
- 4.26  $E_T^{\text{miss}}$  distribution in VRT\_highHT ( $E_T^{\text{miss}} < 225 \text{ GeV}$ ) and CRT ( $E_T^{\text{miss}} > 225 \text{ GeV}$ ) for the electron (left) and muon (right) channels. The agreement between data and MC is better for lower  $E_T^{\text{miss}}$  values, corresponding to VRT\_highHT. . . . . 112
- 4.27 The observed and expected yields in CRT and the VRs in the  $Z$  boson mass side-bands (*left*) and the  $Z$  boson mass window (*right*) regions. The *bottom* plot shows the difference in standard deviations between the observed and expected yields. The backgrounds due to  $WZ$ ,  $ZZ$  or rare top processes, as well as from lepton fakes, are included under “Other Backgrounds”. . . . . 115
- 4.28  $H_T$  distribution in VRQCD for ee channel (left),  $\mu\mu$  channel (right) and  $e\mu$  channel (bottom). Only fake leptons statistical and systematic errors and data statistical errors are shown. No detector related uncertainties are considered here. . . . . 120
- 4.29  $E_T^{\text{miss}}$  distribution in VRQCD for ee channel (left),  $\mu\mu$  channel (right) and  $e\mu$  channel (bottom). Only fake leptons statistical and systematic errors and data statistical errors are shown. No detector related uncertainties are considered here. . . . . 121

- 4.30 Summary of the agreement between data and prediction in all the analysis regions: CRT, VRT(Z), VRT(Z) with an additional requirement of  $H_T > 600$  GeV (VRT(Z)-highHT), VRT(Z) with a higher  $E_T^{\text{miss}} > 225$  GeV requirement and  $400 < H_T < 600$  GeV (VRT(Z)-highMET), and the signal region (SR). . . . . 130
- 4.31  $\Delta\phi$  between leading jet and  $E_T^{\text{miss}}$  (top) and between the sub-leading jet and  $E_T^{\text{miss}}$  (bottom) in the SRs before the  $\Delta\phi(E_T^{\text{miss}}, \text{jet}) > 0.4$  cut is applied, for electron (left) and muon (right) channel. All detector-related uncertainties are included. Normalization of  $t\bar{t}$  by 0.49 is indicated. . . . . 132
- 4.32  $E_T^{\text{miss}}$  distribution after unblinding in the SRs before (top) and after (bottom) the  $\Delta\phi(E_T^{\text{miss}}, \text{jet}) > 0.4$  cut is applied, for electron (left) and muon (right) channel. All detector-related uncertainties are included. Normalization of  $t\bar{t}$  by 0.49 or 0.52 respectively is indicated. . . . . 133
- 4.33  $H_T$  distribution after unblinding in the SRs before (top) and after (bottom) the  $\Delta\phi(E_T^{\text{miss}}, \text{jet}) > 0.4$  cut is applied, for electron (left) and muon (right) channel. All detector-related uncertainties are included. Normalization of  $t\bar{t}$  by 0.49 or 0.52 respectively is indicated. . . . . 134
- 4.34 Invariant mass distribution after unblinding in the SRs before (top) and after (bottom) the  $\Delta\phi(E_T^{\text{miss}}, \text{jet}) > 0.4$  cut is applied, for electron (left) and muon (right) channel. All detector-related uncertainties are included. Normalization of  $t\bar{t}$  by 0.49 or 0.52 respectively is indicated. . . . . 135
- 4.35 Jet multiplicity distribution after unblinding in the SRs before (top) and after (bottom) the  $\Delta\phi(E_T^{\text{miss}}, \text{jet}) > 0.4$  cut is applied, for electron (left) and muon (right) channel. All detector-related uncertainties are included. Normalization of  $t\bar{t}$  by 0.49 or 0.52 respectively is indicated. . . . . 136
- 4.36 The 95% CL exclusion limit from the combined same-flavour channels in the  $\mu$  versus  $m(\tilde{g})$  plane in the GGM model with  $\tan\beta = 1.5$  (top) and  $\tan\beta = 30$  (bottom). The dark blue dashed line indicates the expected limits at 95% CL and the green (yellow) bands show the  $\pm 1\sigma$  ( $\pm 2\sigma$ ) variation on the expected limit as a consequence of the experimental and theoretical uncertainties on the background prediction. The observed limits are shown by the solid red lines, with the dotted red lines indicating the limit obtained upon varying the signal cross section by  $\pm 1\sigma$ . The region below the grey line has the gluino mass less than the lightest neutralino mass and is hence not considered. The value of the lightest neutralino mass is indicated by the  $x$ -axis inset. . . . . 138
- 6.1 Diseño gráfico del detector ATLAS. . . . . 146

6.2	Límites de exclusión a 95 % CL, esperados y observados en el modelo con bRPV. Los resultados se obtienen al combinar los canales de electrón y muon. La banda amarilla alrededor del límite esperado representa las variaciones de $\pm 1\sigma$ en los límites esperados cuando se incluyen todas las incertidumbres excepto las teóricas de la señal. Las líneas de puntos alrededor del límite observado indican la sensibilidad al variar las incertidumbres teóricas en $\pm 1\sigma$ . Las líneas negras sólidas presentan la vida media de la LSP. El resultado de las búsquedas anteriores en ATLAS [59] se muestran en azul. . . . .	150
6.3	Resumen del acuerdo entre datos y predicción en todas las regiones del análisis. . . . .	152
6.4	Límites de exclusión a 95 % CL para $(ee + \mu\mu)$ para los modelos GGM con $\tan\beta = 1,5$ (arriba) y $\tan\beta = 30$ (abajo). La línea azul de puntos indica los límites esperados, la banda verde (amarilla) muestra la variación a $\pm 1\sigma$ ( $\pm 2\sigma$ ) del límite esperado como consecuencia de las incertidumbres teóricas y experimentales en la predicción del fondo. Los límites observados se presentan mediante las líneas sólidas rojas, siendo las líneas rojas de puntos los límites obtenidos al variar la sección eficaz de la señal en $\pm 1\sigma$ . La región por debajo de la línea gris no se considera en este análisis. El valor de la masa del neutralino más ligero está indicada en el eje $x$ adicional. . . . .	153
A.1	The plot shows the probability of obtaining $x = k$ occurrences when the expected value is $\mu = 2$ (black), 5 (blue) and 10 (red). The function is defined only at integer values of $k$ . The connecting lines are only guides for the eye. . . . .	160
A.2	The plot shows the gaussian pdf curves for different values of the mean, $\mu$ , and standard deviation, $\sigma$ . . . . .	161
A.3	Illustration of a simple hypothesis test. . . . .	166
A.4	The plot shows . . . . .	170
A.5	(a) The observed (solid) 95% CL upper limit on the signal strength as a function of $m_H$ and the expectation (dashed) under the background-only hypothesis. The dark and light shaded bands show the plus/minus one sigma and plus/minus two sigma uncertainties on the background-only expectation. (b) The observed (solid) local $p_0$ as a function of $m_H$ and the expectation (dashed) for a SM Higgs boson signal hypothesis ( $\mu = 1$ ) at the given mass. (c) The best-fit signal strength $\hat{\mu}$ as a function of $m_H$ . The band indicates the approximate 68% CL interval around the fitted value. [152] . . . . .	174
A.6	Illustration of the background-only $p$ -value ( $p_0$ ) definition. . . . .	175
A.7	Illustration of the signal-plus-background $p$ -value ( $p_\mu$ ) and the $1 - p_b$ definitions. . . . .	176



A.8	Illustration of statistical tests of parameter values $\mu$ for the cases of: (left) little sensitivity and (right) substantial sensitivity.	177
B.1	Sketch showing the relative situation of regions SR, CRT, VRT_highHT, VRTZ_highHT. Extrapolation from CRT to VRT_highHT is done in $E_T^{\text{miss}}$ while extrapolation from CRT to SR is done in $m_{\ell\ell}$ .	179
B.2	Sketch showing the relative situation of regions SR, VRTZ, VRTZ_highMET, VRTZ_highHT in the $Z$ -mass window and the analogous regions in the $Z$ -mass side band.	180
B.3	Data-MC comparison in the $m_{\ell\ell}$ distribution for VRTZ+VRT. No normalization factor has been applied to $t\bar{t}$ . Only statistical errors are shown.	182
B.4	Data-MC comparison in the $m_{\ell\ell}$ distribution for SR+CRT. For $t\bar{t}$ , a normalization factor of 0.52 has been applied as suggested by the side-band fit. Only statistical errors are shown.	183
B.5	Data-MC comparison in the $m_{\ell\ell}$ distribution for (VRTZ+VRT)_highHT. No normalization factor has been applied to $t\bar{t}$ . Only statistical errors are shown.	184
B.6	Data-MC comparison in the $m_{\ell\ell}$ distribution for (VRTZ+VRT)_highMET. No normalization factor has been applied to $t\bar{t}$ . Only statistical errors are shown.	185
B.7	$E_T^{\text{miss}}$ distributions in SR without $\Delta\phi$ cuts (top) and SR with $\Delta\phi > 0.4$ (bottom). $Z$ +jet has been estimated with the jet-smearing method. All other sources of background are taken from MC. Left: $ee$ channel. Right: $\mu\mu$ channel.	189
B.8	Reduction (in percentage) on the number of expected events in GGM ( $\tan\beta = 1.5$ ) signal when applying a $\Delta\phi > 0.4$ in SR with respect to the nominal SR expectation, in the $ee$ channel.	191
B.9	Expected exclusion limits in SR before applying the $\Delta\phi(\text{jet}_{1,2}, E_T^{\text{miss}})$ cut (dashed blue line with yellow uncertainty band) compared to expected exclusion in SR with $\Delta\phi > 0.4$ (green dashed line with green dotted uncertainty lines). Upper plots: GGM with $\tan\beta = 1.5$ ; Bottom plots: GGM with $\tan\beta = 30$ ; Left: $ee$ channel; Right: $\mu\mu$ channel.	194



# List of Tables

1.1	The fermions of the Standard Model listed with their chirality, spin and electric charge. . . . .	17
1.2	The bosons of the Standard Model listed with their spin and electric charge. . . . .	17
1.3	The undiscovered particles in the Minimal Supersymmetric Standard Model (with sfermion mixing for the first two families assumed to be negligible). Anti-sfermion fields have not been listed.	23
3.1	Overview of the selection criteria for the signal and control regions in this analysis. The $p_T$ selections for leptons are given for electrons (muons). All mass and momentum requirements are in units of GeV. $\ell_1$ is the leading lepton, $\ell_2$ the subleading lepton and $m_{\ell\ell}$ the invariant mass of the two leading leptons. .	46
3.2	Overview of the selection criteria for the validation regions in this analysis. The $p_T$ selections for leptons are given for electrons (muons). All mass and momentum requirements are in units of GeV. $\ell_1$ is the leading lepton and $\ell_2$ the subleading lepton. . . . .	52
3.3	The observed numbers of events in the electron and muon signal regions, and the background expectations from the fit. The inputs to the fit are also shown; these consist of the data-driven multijet background estimate and the nominal expectations from simulation (MC), normalized to theoretical cross sections. The errors shown are the statistical plus systematic uncertainties on the mean of the Poisson function describing the background probability density. . . . .	54
4.1	Overview over all signal, control, seed and validation regions used in this analysis. More details are given in the text in the specific sections. The $E_T^{\text{miss}}$ significance and the SoftTerms fraction $f_{\text{ST}}$ needed in the seed regions for the jet smearing method are defined in Section 4.6.1. The dilepton pair flavour is denoted as either SF for same flavour or OF for opposite flavour.	63

4.2	Parameters of the GGM models used for the signal production. The constraint $c\tau_{\text{NLSP}} < 0.1$ mm is fulfilled for all input values of $\mu > 120$ GeV. . . . .	66
4.3	SUSY particle mass spectrum for the higgsino-like NLSP GGM model which is characterised by the following parameters: $M_1 = 1\text{TeV}$ , $M_2 = 1\text{TeV}$ , $\tan\beta = 1.5$ , $c\tau_{\text{NLSP}} < 0.1$ mm, $\mu = 200\text{GeV}$ , $m(\tilde{g}) = 700\text{GeV}$ . . . . .	68
4.4	Summary of the electron selection criteria. The signal selection requirements are applied on top of the baseline requirements. .	84
4.5	Summary of the electron selection criteria. The signal selection requirements are applied on top of the baseline requirements. .	85
4.6	Summary of the jet selection criteria. The signal selection requirements are applied on top of the baseline requirements. . .	86
4.7	Summary of the overlap removal (OR) requirements. . . . .	87
4.8	Pre-selection cuts common to all the regions used in this analysis. The upper part of the table shows cuts which are common to several SUSY analyses, whereas the bottom part shows the cuts which are designed for this analysis only. . . . .	88
4.9	Cuts defining the signal region. . . . .	90
4.10	Main background descriptions and their nominal estimation methods. The $Z + \text{jets}$ and Drell-Yan backgrounds differ only in the invariant mass of the leptons, where the former considers only $m_{\ell\ell} > 40$ GeV while for the later $m_{\ell\ell} < 40$ GeV. . . . .	96
4.11	Number of $Z/\gamma^* + \text{jets}$ background events estimated in the signal region (SR) using the jet smearing method. This is compared with the prediction from the SHERPA MC simulation. The quoted uncertainties include those due to statistical and systematic effects (see Sect. 4.7). . . . .	99
4.12	Contribution of the subtracted flavour non-symmetric processes in $\text{CRe}\mu$ estimated from MC or with the matrix method. The lower part of the table shows the number of data events, the total sum of the flavour non-symmetric processes and the result of subtracting these two numbers, $N_{e\mu}^{\text{data,corr}}$ , in $\text{CRe}\mu$ . The first error gives the statistical uncertainty. The second one corresponds to the experimental systematic uncertainties (theoretical uncertainties are not included). . . . .	101
4.13	Trigger efficiency factors. . . . .	101
4.14	Background composition in VRZ estimated from MC directly. The first error corresponds to statistical uncertainties. The second one gives the experimental uncertainties. . . . .	103
4.15	Number of $ee$ and $\mu\mu$ events and the values of $k_{ee}$ and $k_{\mu\mu}$ estimated from data in the validation region VRZ for several cuts on $E_T^{\text{miss}}$ . . . . .	103

4.16	Number of $ee, \mu\mu$ events and the values of $k_{ee}, k_{\mu\mu}$ and their statistical error estimated from data and MC in validation region VRZ. Values for three different zones of the detector (barrel-barrel, barrel-endcap, endcap-endcap) are given. The Global $k_{ee}, k_{\mu\mu}$ values are calculated without discriminating in barrel/endcap zones. For the MC estimates, the first uncertainty shown corresponds to the statistical error, the second one to the experimental systematic uncertainties. For the data estimates the second uncertainty is due to the $E_T^{\text{miss}}$ dependence of the $k$ factors. . . . .	104
4.17	Summary of data-driven estimation of dileptonic $t\bar{t}$ , WW, Wt and $Z \rightarrow \tau\tau$ backgrounds in SR. The first uncertainty shown corresponds to the statistical error, the second one to the experimental systematic uncertainties. The third number corresponds to the uncertainty due to the dependency of $k_{ee}, k_{\mu\mu}$ on $E_T^{\text{miss}}$ . . . . .	105
4.18	Summary of closure test for the estimation of dileptonic- $t\bar{t}$ , WW, Wt and $Z \rightarrow \tau\tau$ backgrounds in SR. The first uncertainty shown corresponds to the statistical error, the second one to the experimental systematic uncertainties. The third number corresponds to the uncertainty due to the dependency of $k_{ee}, k_{\mu\mu}$ on $E_T^{\text{miss}}$ , as detailed in Section 4.6.2.3. The bottom part of the table shows the summary of direct MC estimation of dileptonic- $t\bar{t}$ , WW, Wt and $Z \rightarrow \tau\tau$ backgrounds in SR. . . . .	106
4.19	Background fit results in the electron channel for an integrated luminosity of $20.3 \text{ fb}^{-1}$ . Nominal MC and data-driven expectations are given for comparison. The uncertainties shown are statistical + systematic. . . . .	108
4.20	Background fit results in the muon channel for an integrated luminosity of $20.3 \text{ fb}^{-1}$ . Nominal MC and data-driven expectations are given for comparison. The uncertainties shown are statistical + systematic. . . . .	109
4.21	Background fit results in the SF channel (ee and $\mu\mu$ combined) for an integrated luminosity of $20.3 \text{ fb}^{-1}$ . Nominal MC and data-driven expectations are given for comparison. The uncertainties shown are statistical + systematic. . . . .	110
4.22	Final estimates for flavour-symmetric backgrounds from the flavour-symmetry method compared to the estimates from the side-band fit. The contribution of $Z \rightarrow \tau\tau$ to the fit is negligible. All sources of uncertainty are considered in the shown errors. . . . .	111
4.23	Background fit results from VRT in the the SR, VRT and VRTZ for an integrated luminosity of $20.3 \text{ fb}^{-1}$ . The uncertainties shown are statistical + systematic. VRT has been used as control region to normalize $t\bar{t}$ , while VRTZ is used as validation region. . . . .	113

4.24	Summary of the $t\bar{t}$ normalization factors ( $\mu_{Top}$ ) found in three different Control Region selections. . . . .	113
4.25	Estimated number of events for the $ee$ and $\mu\mu$ channels in the $Z$ -window regions compared to the number of observed data. $N_{e\mu}$ is taken from data and shown only for completeness. Only statistical errors are shown. . . . .	115
4.26	Estimated number of events for the $ee$ and $\mu\mu$ channels in the $Z$ -sideband regions compared to the number of observed data. $N_{e\mu}$ is taken from data and shown only for completeness. Only statistical errors are shown. . . . .	116
4.27	Definition of the fake lepton enriched validation region. The dilepton pair electric charge sign is denoted as SS for same sign. More details about the selection are given in the text . . . . .	119
4.28	Number of fake lepton events in SR, CRe $\mu$ , CRT, VRT and VRTZ estimated with the Matrix Method. The uncertainties shown are statistical and systematic added quadratically. . . . .	122
4.29	Maximum signal contamination in control and validation regions. . . . .	125
4.30	Summary of uncertainties. . . . .	127
4.31	Overview of the dominant sources of systematic uncertainty on the background estimate in the signal region for the SF channel. Their relative values with respect to the total background expectation are shown in %. . . . .	128
4.32	Final background estimation in SRs after applying a $\Delta\phi(\text{jet}_{1,2}, E_T^{\text{miss}}) > 0.4$ cut, using the flavour-symmetry method. All sources of uncertainties are considered in the shown errors. . . . .	129
4.33	Total Background expectation for SRs . . . . .	130
4.34	Breakdown of upper limits for SR-Z. . . . .	139
4.35	95% confidence level expected and observed upper limits on the contribution of BSM physics events to the signal regions, $CL_B$ values, the $p_0$ -value for the observed result, and the corresponding Gaussian significance based on the combined fit background estimation. The expected upper limit on number of events is shown with the $1\sigma$ uncertainties. . . . .	139
B.1	Number of dileptonic- $t\bar{t}$ events in VRZ.Zsideband per barrel-endcap region <b>before applying any correction factor</b> . Uncertainties are statistical only. . . . .	181
B.2	Number of dileptonic- $t\bar{t}$ events in VRZ.Zsideband per barrel-endcap region <b>after correcting</b> $N_{\mu\mu}, N_{e\mu}$ <b>with</b> $k_{ee}$ <b>and</b> $\alpha$ ( $N_{ee}^{MC}$ is taken as reference). Uncertainties are statistical only. . . . .	181
B.3	Data/MC ratios for different regions in the low $m_{\ell\ell}$ -sideband, $m_{\ell\ell} < 81$ GeV; the $m_{\ell\ell}$ -window, $81 < m_{\ell\ell} < 101$ GeV; and the high $m_{\ell\ell}$ -sideband, $m_{\ell\ell} > 101$ GeV. In each of the regions, the normalization factor applied to $t\bar{t}, t\bar{t}\text{-Norm}$ , is also given. Only statistical errors are shown. . . . .	186

B.4	Summary of data-driven estimation of $t\bar{t}$ , WW, Wt and $Z(\tau\tau) + j$ backgrounds in SR for several cut values on $\Delta\phi(\text{jet}, E_T^{\text{miss}})$ . The first uncertainty shown corresponds to the statistical error. The second one, to the detector systematic uncertainties. The third number corresponds to the uncertainty due to the dependency of $k_{ee}$ , $k_{\mu\mu}$ on $E_T^{\text{miss}}$ . . . . .	187
B.5	Z+jets estimation from the jet smearing method and from direct MC in SR before and after applying the $\Delta\phi > 0.4$ cut. . . . .	188
B.6	MC-estimated backgrounds and fake leptons estimation in SR <sub>ee</sub> for different $\Delta\phi$ cuts. Only statistical and detector systematic uncertainties are included in this table. . . . .	190
B.7	MC-estimated backgrounds and fake leptons estimation in SR <sub>mm</sub> for different $\Delta\phi$ cuts. Only statistical and detector systematic uncertainties are included in this table. . . . .	190
B.8	Final background estimation in SR <sub>ee</sub> and signal MC expectations and expected significance for different $\Delta\phi$ cut values. The signal expected significance is also shown. . . . .	191
B.9	Final background estimation in SR <sub>mm</sub> and signal MC expectations and expected significance for different $\Delta\phi$ cut values. The signal expected significance is also shown. . . . .	192
B.10	Final background estimation in SR with no $\Delta\phi$ cut using the flavour-symmetry method. All sources of uncertainties are considered in the shown errors. . . . .	193
B.11	Final background estimation in SR after applying a $\Delta\phi(\text{jet}_{1,2}, E_T^{\text{miss}}) > 0.4$ cut, using the flavour-symmetry method. All sources of uncertainties are considered in the shown errors. . . . .	193
B.12	Final background estimation in SR according to the side-band fit method. All sources of uncertainties are considered in the shown shown errors. . . . .	195
B.13	Final background estimation in SR with $\Delta\phi > 0.4$ according to the side-band fit method. All sources of uncertainties are considered in the shown errors. . . . .	195
B.14	Final estimates for flavour-symmetric backgrounds from the flavour-symmetry method compared to the estimates from the side-band fit. The contribution of $Z \rightarrow \tau\tau$ to the fit is negligible. All sources of uncertainty are considered in the shown errors. . . . .	196
B.15	Summary of closure test for the estimation of $t\bar{t}^{2l}$ , WW, Wt and $Z \rightarrow \tau\tau$ backgrounds in SR. The first uncertainty shown corresponds to the statistical error, the second one to the experimental systematic uncertainties. The third number corresponds to the uncertainty due to the dependency of $k_{ee}$ , $k_{\mu\mu}$ on $E_T^{\text{miss}}$ , as detailed in Section 4.6.2.3. The bottom part of the table shows the summary of direct MC estimation of $t\bar{t}^{2l}$ , WW, Wt and $Z \rightarrow \tau\tau$ backgrounds in SR. . . . .	197

B.16	Background fit results in the electron channel, obtained with the discovery fit configuration for an integrated luminosity of $20.3 \text{ fb}^{-1}$ . The uncertainties shown are statistical + systematic.	198
B.17	Background fit results in the electron channel, obtained with the discovery fit configuration for an integrated luminosity of $20.3 \text{ fb}^{-1}$ . The uncertainties shown are statistical + systematic.	199
B.18	Background fit results in the electron channel, obtained with the discovery fit configuration for an integrated luminosity of $20.3 \text{ fb}^{-1}$ . The uncertainties shown are statistical + systematic.	200
B.19	Background fit results, obtained with the discovery fit configuration for an integrated luminosity of $20.3 \text{ fb}^{-1}$ . The uncertainties shown are statistical + systematic. VRT has been used as control region to normalize $t\bar{t}$ . VRTZ_highHT is used as validation region.	201
B.20	Summary of the $t\bar{t}$ normalization factors ( $\mu_{Top}$ ) found in three different selections of the Control Region.	201
B.21	Total Background expectation for SRs	202
B.22	95 % confidence level expected and observed upper limits on the contribution of BSM physics events to the signal regions, the $p_0$ -value for the observed result, and the corresponding Gaussian significance. The expected upper limit on number of events is shown with the $1\sigma$ uncertainties. No cut on the opening angle between jets and the $E_T^{\text{miss}}$ is applied.	202
B.23	Estimated number of events for the $ee$ and $\mu\mu$ channels in the $Z$ -window regions compared to the number of observed data. $N_{e\mu}$ is taken from data and shown only for completeness. Only statistical errors are shown.	202
B.24	Estimated number of events for the $ee$ and $\mu\mu$ channels in the $Z$ -side band regions compared to the number of observed data. $N_{e\mu}$ is taken from data and shown only for completeness. Only statistical errors are shown.	203



